Large Scale Antenna Array for GPS Bistatic Radar

Chow Yii Pui

Thesis submitted for the degree of

Doctor of Philosophy

School of Electrical and Electronic Engineering
Faculty of Engineering, Computer and Mathematical Sciences
The University of Adelaide
South Australia

July 2017

Contents

Abstract

GPS passive bistatic radar uses signals transmitted by navigation satellites to perform target detection. This research aims to develop a ground-based receiver that detects the reflected GPS signals from air targets. The main challenge for GPS bistatic radar is the difficulty in detecting the extremely weak power GPS signal reflections from a target since GPS satellites are located at very high altitudes and transmit signals at relatively low power levels.

The research in this thesis investigates the minimum power of the reflected GPS signal that can be reliably detected by applying several techniques for enhancing the receiver detection performance. The proposed techniques for GPS bistatic radar target detection model include: using a large scale antenna array at the receiver, applying long coherent integration times for the captured data and non-coherently summing the power returns of targets from multiple satellites or receivers. This detection model requires the radar system to incorporate the signal information from a large number of receiving channels and non-cooperative transmitters to perform air target detection.

This research also incorporates additional techniques at the pre-detection stage that are essential for the target detection model. Among these techniques include: direct-path GPS signals acquisition that obtains the Doppler frequency component and C/A code pattern from each satellite, array calibration that realigns the inter-element phase errors and orientation of phased-array receiver using the GPS system, and direct-path signal interference cancellation.

The GPS bistatic radar target detection performance was initially investigated using the results produced by computer simulations. Then, a prototype phased-array GPS bistatic radar receiver was built to capture target reflections from an aircraft and investigate the detection performance of the system experimentally. The system was able to successfully detect and locate the position of a nearby aircraft, which demonstrates that the techniques introduced for GPS bistatic radar in this thesis do work in practice. The experimental results also provide a benchmark that can be used to estimate the scale of the receiver required for detecting objects at a greater distance.

Declaration

I certify that this work contains no material which has been accepted for the award of any other degree or diploma in my name, in any university or other tertiary institution and, to the best of my knowledge and belief, contains no material previously published or written by another person, except where due reference has been made in the text. In addition, I certify that no part of this work will, in the future, be used in a submission in my name, for any other degree or diploma in any university or other tertiary institution without the prior approval of the University of Adelaide and where applicable, any partner institution responsible for the joint-award of this degree.

I give consent to this copy of my thesis when deposited in the University Library, being made available for loan and photocopying, subject to the provisions of the Copyright Act 1968.

I also give permission for the digital version of my thesis to be made available on the web, via the University's digital research repository, the Library Search and also through web search engines, unless permission has been granted by the University to restrict access for a period of time.

I acknowledge the support I have received for my research through the provision of an Australian Government Research Training Program Scholarship.

Signature:

Date:

Acknowledgements

Firstly, I would like to thank my first co-supervisor, Mr. Matthew Trinkle, for being willing to spend his precious time with me together investigating the problems addressed in my research and accompany me during the excursions to perform the air target detection experiments. He is also the person who introduced me to study the topic of GPS bistatic radar. I had learnt a lot of skills in RF electronic system, PCB and FPGA designs from him since I did my undergraduate honours project under his supervision. These knowledges are potentially useful for my future career in the electrical and electronic engineering field.

Besides, I would like to thank my second co-supervisor, Prof. Doug Gray, for admitting me as a student member of the Adelaide Radar Research Centre (ARRC), which granted me access to the radar laboratory and numerous resources for designing, testing and building the experimental GPS bistatic radar receiver for my research. Besides, he has provided much useful feedback that greatly improved the writing quality of my thesis.

Also, I would like to thank my principal supervisor, Dr. Brian Ng, for his role in supervising and managing my PhD candidature during these years. He provided useful information and advice before I started writing this thesis. He also encouraged me when I at times lost concentration in writing the thesis.

There are several staff members at the School of Electrical and Electronic that I am indebted for their assistance and advice. Mr. Danny di Giacomo provided me with a wide range of electronic components suitable for my experimental receiver and placed orders when components were required. Mr. Pavel Simcik helped me to fabricate PCBs for several modules in the system. Ian Linke provided materials for building the receiver’s structure and performed safety inspection for its worthiness in mounting on a car prior to performing the field test. Ms. Rose-Marie Descalzi managed the paperwork and expenses for my travel to conferences.

In addition, I would like to thank Dr. Abraham du Plooy from Opt-Osl Systems for fabricating the phased-array elements for the radar receiver. Besides, I would like to thank Dr.

James Palmer from DSTO for his invitation to present my research outcome at several passive bistatic radar workshops. These workshops further stimulate my interest in the development work of passive bistatic radar. I had also learnt some useful knowledge related to my research by sharing with other attendees.

I also treasured my friendship with my fellow colleagues, Ruiting Yang, Zili Xu, Kai Yu and Yuexian Wang. We love to share both our work and life together while helping each other when needs arose.

There are also a few distant but sincere friends, Keyi Lu, Sieng Yii Tiong, Maggie Jing Li and Amg Chong Ngu whom I truly appreciated for their concern regarding the progress of my PhD study when they sent me birthday greetings every year.

Lastly, I would like to utterly thank my wife for her truly great love and care since our relationship began, and also my parents for their unconditional love in raising me up and teaching me well. May the success and achievement from my research glorify the name of my Heavenly Father.

List of Figures

List of Tables

Abbreviations

2-D/3-D	Two/Three-dimensional space
ADC	Analogue-to-digital converter
ARM	Anti-radiation missile
AWGN	Additive white Gaussian noise
BCAF	Cross ambiguity function (Beamformer)
BDS	BeiDou navigation satellite system
BPSK	Binary phase-shift keying
C/A	Coarse/acquisition
CAF	Cross ambiguity function
CCAF	Cross ambiguity function (Combined elements)
CDF	Cumulative distribution function
CDMA	Code division multiple access
CFAR	Constant false alarm rate
CRPA	Controlled radiated pattern antenna
CW	Continuous wave
DAB	Digital audio broadcasting
DOA	Direction-of-arrival
DOP	Dilution of precision
DSI	Direct-path signal interference
DSP	Digital signal processor
DSSS	Direct-sequence spread spectrum
DVB-S	Digital video broadcasting-Satellite
DVB-T	Digital video broadcasting-Terrestrial
ECM	Electronic countermeasure
EIRP	Effective isotropic radiated power
FDOA	Frequency-difference-of-arrival

FFT	Fast Fourier transform
FIFO	First in, first out
FM	Frequency modulation
FPGA	Field-programmable gate arrays
FRPA	Fixed radiated pattern antenna
GEMS	GNSS environment monitoring system
GNSS	Global navigation satellite system
GPS	Global Positioning System
GSM	Global system for mobile communications
HDOP	Horizontal dilution of precision
IF	Intermediate frequency
JPALS	Joint precision approach and landing system
LEO	Low Earth orbit
LHCP	Left-hand, circularly polarized
LNA	Low noise amplifier
LOS	Line-of-sight
LP	Linearly polarised
LSE	Least squares estimator
MCE	Monte Carlo experiments
MEO	Medium Earth orbit
MIMO	Multiple-input & multiple-output
MISO	Multiple-input & single-output
MMSE	Minimum mean square error
MSE	Mean squared error
MVDR	Minimum variance distortionless response
PBR	Passive bistatic radar
P	Precision
PC	Personal computer
PDF	Probability density function
PDOP	Position dilution of precision
PLL	Phased-locked loop
PMR	Passive MIMO radar
PRN	Pseudo-random noise
RCS	Radar cross-section

RF	Radio frequency
RHCP	Right-hand, circularly polarised
RMSE	Root-mean-square error
SDRAM	Synchronous dynamic random access memory
SISO	Single-input & single-output
SNR	Signal-to-noise ratio
SV	Space vehicle
TBD	Track-before-detect
TDOA	Time-difference-of-arrival
TOA	Time-of-arrival
UERE	User equivalent range error
VDOP	Vertical dilution of precision
VHDL	VHSIC hardware description language
VHSIC	Very high speed integrated circuit

Symbols

x^*	complex conjugate
x^T	transpose
x^H	Hermitian/conjugate transpose
$f(t)$	continuous function
$f(k)$	discrete function
$n(t)$, $n(k)$	white noise
$\boldsymbol{a}$	array steering vector
b	receiver index
c	speed of light
f_B	signal bandwidth
f_0	signal carrier frequency
f_D	direct-path signal Doppler frequency
f_δ	target Doppler frequency
$\mathscr{f}$	function of Doppler frequency
j	complex number
k	sample index
$\mathscr{k}$	Boltzmann constant
$\Bbbk$	data sub-block time frame index
l	transmitter/satellite index
m	antenna element index
$\mathfrak{m}$	multipath signal index
n	noise
$\boldsymbol{p}$	position vector
$\boldsymbol{u}$	coordinate of sensor’s element relative to reference
$\boldsymbol{v}$	velocity vector
$\boldsymbol{w}$	weigh vector

B	number of base stations/receiver sites
$\mathrm{C}(t)$, $\mathrm{C}(k)$	PRN code sequence
$\mathcal{C}(k,\boldsymbol{p}_{\delta})$	function of PRN code sequence
$\mathrm{E}(H)$	expectation of random variable
G	gain
$\mathcal{H}$	hypothesis of a statistical model
I	identity matrix
K	number of samples
$\mathbb{K}$	total number of data sub-blocks
$\bar{K}$	size of each data sub-block
L	number of illuminators/satellites
M	number of antenna elements
$\mathfrak{M}$	number of multipath signals
$\mathcal{N}$	number of Monte Carlo experiments
P_{x}, P_{y}, P_{z}	position search range in x, y and z dimensions
$\mathbb{P}$	probability
$\mathcal{P}$	subspace projection of signals
P_{R}	receiving power at the receiver
P_{T}	transmitting power of illuminator
R_{D}	direct propagation path
R_{T}	transmitter-to-target/transmission path
R_{R}	receiver-to-target/reflected path
$\mathcal{R}(t)$, $\mathcal{R}(k)$	Cross-correlation function
RX	receiver
TX	transmitter
V_{x}, V_{y}, V_{z}	velocities search range in x, y and z dimensions
V	velocity magnitude
Γ	Gamma function
Λ	chi-squared distribution non-centrality parameter
α	number of beams
β	bistatic angle
γ	lower incomplete Gamma function
δ	target index

ϵ	inter-element phase error
θ	azimuth angle
λ_0	signal wavelength
ρ	pseudorange
ψ	target velocity aspect angle
μ	signal amplitude
σ	noise amplitude
σ_B	bistatic radar cross section
τ	detection threshold
ϕ	elevation angle

Publications

1. C. Pui, M. Trinkle, “GPS Bistatic Radar Research and Experimental Results”, in Progress in Radar Research (PIRR) Workshop, Adelaide, Australia, 2011.
2. C. Pui, M. Trinkle, “GPS Bistatic Radar for Target Detection and Estimation using Antenna Arrays”, in International Global Navigation Satellite Systems (IGNSS), Sydney, Australia, 2011.
3. C. Pui, M. Trinkle, “Experimental Results Investigating the Feasibility of GPS Bistatic Radar for Target Detection and Estimation”, in Proceedings of the 24th International Technical Meeting of The Satellite Division of the Institute of Navigation (ION GNSS 2011), Portland, OR, September 2011, pp. 3165-3171.
4. C. Pui, M. Trinkle, B. Ng, “Passive Bistatic Radar for Aircraft Detection using GPS as a Source of Opportunity”, in Defence Science Institute (DSI) Passive Radar Workshop, Melbourne, Australia, 2013.
5. C. Pui, M. Trinkle, B. Ng, “Aircraft Detection Experimental Results for GPS Bistatic Radar using Phased-array Receiver”, in International Global Navigation Satellite Systems (IGNSS), Gold Coast, Australia 2013.
6. C. Pui, M. Trinkle, “GPS Bistatic Radar using Phased-array Technique for Aircraft Detection”, in Proceedings of IEEE International Conference on Radar, Adelaide, Australia, 2013, pp. 274-279.
7. C. Pui, M. Trinkle, B. Ng, “Progress in GPS Bistatic Radar for Air Target Detection”, in Progress in Radar Research (PIRR) Workshop, Adelaide, Australia, 2014.
8. C. Pui, M. Trinkle, “Aircraft Detection using GPS Bistatic Radar incorporating MIMO Techniques”, in IEEE Two-Day Workshop on Passive Radar, Adelaide, Australia, 2015.

CHAPTER 1

Introduction

1.1 Problem Description

Bistatic radars have been developed and commonly used for aircraft detection before and during World War II [1]. As opposed to monostatic (conventional) radars that perform target detection using collocated transmitters and receivers, bistatic radars use receivers that are widely separated from the transmitters. Although there is no standard definition for the required separation between the transmitter and receiver sites, Skolnik defined the separation distance for bistatic radar to be “comparable to the target distance” [2] and also gave examples of separation distances from a few miles to hundreds of miles for air targets and hundreds to thousands of miles for satellite targets. Both types of the aforementioned radars are illustrated in Figure 1.1. A bistatic radar can also be further expanded to become a multistatic radar if multiple widely separated transmitting or receiving elements are utilised in the system.

There are two basic classes of bistatic radars: active and passive. Active radars use their own transmitters to emit radio frequency (RF) signals and capture target reflections with receivers at one or multiple separated locations. Therefore, active bistatic radars can be operated in monostatic, bistatic or multistatic modes. The characteristics of the signal emissions (e.g. frequency, timing) can be varied by the radar operators based on the target properties. Passive radars (also known as passive coherent location) are exclusively operated in bistatic mode and they use only receivers to capture target reflections that are illuminated by transmitters of opportunity, which are non-cooperative sources that are designed to transmit signals for other purposes, but may also be suitable for bistatic operation. Hence, this kind of radar is termed “passive bistatic radar” (PBR) and such systems do not require dedicated

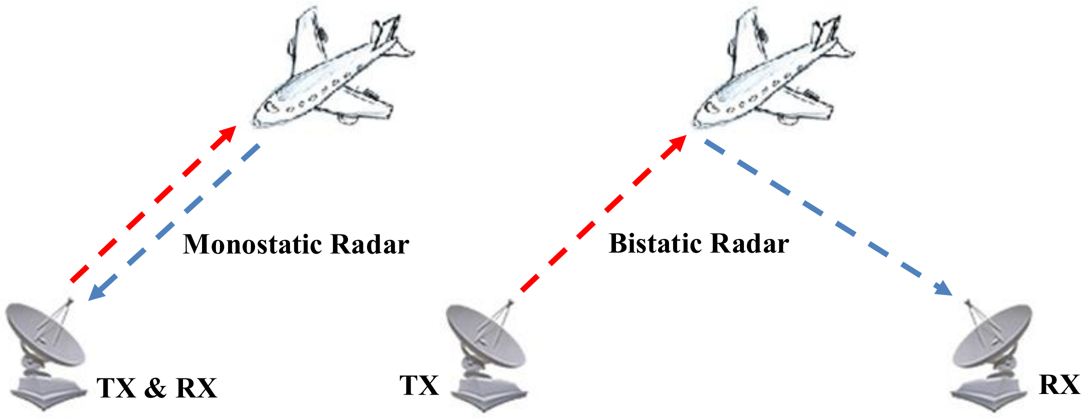

Figure 1.1: Illustration of monostatic radar vs. bistatic radar.

transmitters to be built as they perform target detection using RF signals emitted from existing sources. This means that the processing of PBR signals requires some knowledge about the transmitters such as their position and the signal characteristics including timing, frequency and modulation.

The study reported here is performed primarily for PBR, but may also be applicable for active bistatic radar. The simplest PBR system requires at least a single element in a land-based or airborne receiver to detect and capture direct-path signals from one illuminator and line-of-sight (LOS) scattered signals from the target. These scattering signals are generally transmitted from communication or broadcasting stations that can be land-based or space-based. The diagram of a PBR environment (not to scale) is illustrated in Figure 1.2.

The PBR system initially performs target detection using a Doppler-delay search technique. The delay information between these two signals is then extracted to perform range estimation for the target. To estimate the location of target, the PBR system typically uses trilateration, based on multiple range estimates. These can be obtained by either having multiple transmitters and a single receiver or a single transmitter with multiple widely separated receivers. To enhance the precision of the localisation solution of PBR, a phased-array receiver can be utilised by the system to estimate the direction-of-arrival (DOA) of the target, which can be included in the position solution.

This study seeks to experimentally evaluate the possibility of using signals transmitted by Global Positioning System (GPS) to implement a PBR system for airborne target detection and determine experimentally the detection ranges that can be expected from such a system. Several techniques for extending the range of the system will also be introduced and tested experimentally. The GPS satellites are potential illuminators of opportunity for the aforementioned system as they continuously broadcast orthogonal navigation signals from each

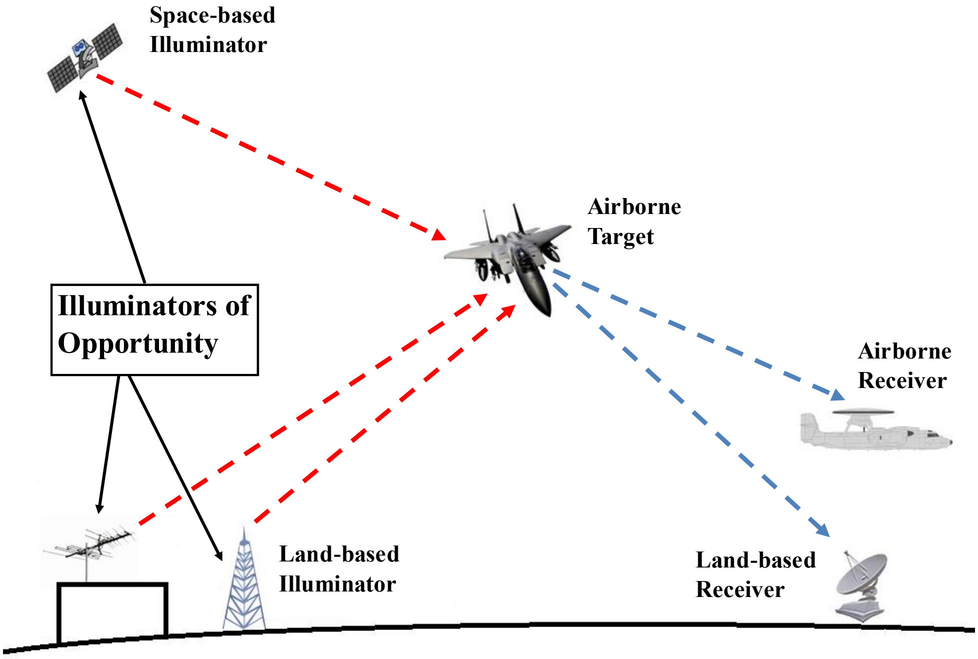

Figure 1.2: The PBR airborne target detection environment.

satellite. But since these illuminators are space-based and the received transmission signal is weak, a high antenna gain is required to achieve detection of an airborne target at a reasonable distance. To obtain a high antenna gain in multiple directions, a phased-array is used for the experimental PBR system. The maximum array gain is limited by the number of antenna elements. Part of this study aims to determine the number of antenna elements required to detect a target at a given distance. Ideally the receiver array should also be portable so that it can be rapidly deployed, easily rotated and tilted (The design details will be covered in Chapter 5) to obtain the best orientation for optimum signal reception of the scattered signals from air targets. The orientation of the array needs to be accurately known to get an accurate target bearing and techniques for automatically estimating the orientation of the array as well as the array phased errors are also developed. The primary objective for the development of this PBR system is to develop a Multiple-input & multiple-output (MIMO) PBR technique that improves the detection range by combining the signal power from all available (i.e. within LOS of target and receiver) GPS satellites and all elements in the array in a single detector. This method essentially performs target localisation and tracking as part of the detection. The detection performance of PBR using this method is believed to outperform the trilateration method since the latter processes target information using the illuminators independently. This detection method forms the basis for the work described in this thesis. The main issues addressed in this thesis are described as follows:

- Feasibility of PBR using GPS satellites to detect aircraft is studied by considering the power budget in a typical scenario. This gives an estimate of the number of antenna elements required in the receiver array for detecting a target at a given distance;
- Development of array calibration methods. The GPS satellites are good calibration sources since the direct-path signal information from the illuminators of opportunity are stored in the PBR system after acquisition and can be reused to perform array calibration;
- Signal processing techniques for detecting weak reflections from the aircraft. Typically each GPS signal is extracted independently from all others. However weaker signals can be extracted if combined detection is performed on all signals simultaneously based on a physical propagation model. Such a detection algorithm has been developed and tested on real data in this thesis.

1.2 Outline of Thesis and Main Contributions

C**hapter 2** gives an overview of PBR and GPS bistatic radar, particularly the historical background and applications. The chapter also focuses mainly on target detection techniques applied in GPS bistatic radars as well as identifying the areas that required further research.

In **Chapter 3**, the target detection and parameter estimation model for GPS bistatic radar using a phased-array technique are developed. The main model parameters are explored by MATLAB simulations based on a 32-element phased-array receiver. Furthermore, a comparison between 2-D and 3-D antenna array calibration techniques using GPS signals is also presented. **The main contributions are:**

(a) An implementation of a phased-array technique for estimating the direction-of-arrival (DOA) of targets in a GPS bistatic radar receiver which increases the accuracy and efficiency over existing target localisation techniques;

(b) Development of a calibration technique to determine the attitude of the antenna array (rotation and tilt) and the phase error of each antenna element using the GPS signals as calibration sources;

In **Chapter 4**, the feasibility of implementing MIMO radar detection techniques for GPS bistatic radars are investigated. Initially, a Multiple-input & single-output (MISO) model is used where the phased-array receiver can be treated as a single sensor and the GPS satellites are widely separated transmitters. The signals from all satellites are combined non-coherently at the receiver prior to detection to improve the detection performance. A MIMO model is also used with multiple GPS satellites and widely separated ground-based phased-array receivers. The performance of target detection and location estimation using this model is investigated in detail using MATLAB simulations. **The main contribution is:**

Development of the MISO and MIMO detection model for GPS bistatic radar receiver with improved tracking and detection of target reflections by combining the power of multiple satellite signals at multiple receivers prior to detection.

In **Chapter 5**, an experimental system is designed to collect data from aircraft detection experiments. This data is used to compare the detection performance of conventional phased-array and MIMO techniques. The use of real signals also required a number of additional challenges to be overcome, such as the need to cancel the GPS direct-path signals which are much stronger than the weak target returns. **The main contributions are:**

(a) Designed, constructed and tested a phased-array GPS bistatic radar receiver with specification that suits the requirement for experimental works performed in this chapter.

(b) Provide predictions of the range at which aircraft can be detected for a given phased-array size based on the results from an aircraft detection experiment.

(c) Use of a polynomial regression technique to model the time-varying Doppler components within a certain signal length to improve the accuracy of Doppler estimation for direct-path signal;

(d) Applying a Wiener filter for GPS bistatic radar to estimate and remove the direct-path signal interferences and their multipath components;

(e) Experimentally evaluate the feasibility of a GPS bistatic radar utilising phased-array receiver for air target detection and parameter estimation using the techniques given in Chapters 3 and 4;

Chapter 6 concludes the work described in this thesis and discusses future work that can be carried out to increase the aircraft detection capability of GPS bistatic radars.

The MATLAB programming codes for running the simulations and processing the experimental data were stored in the cloud link as follows:

https://1drv.ms/f/s!AtEyVIJaRqJAvWUeyJxrximihhFq

CHAPTER 2

GPS Bistatic Radar Background for Target Detection

2.1 Introduction

In this chapter, the background of PBR and GPS bistatic radars will be presented. Section 2.2 will present the historical background and advantages of PBR for target detection. To motivate the reader, several examples of illuminators of opportunity that have been studied or utilised for detecting airborne targets in the literature will also be provided in this section. Section 2.3 will briefly compare the performance of various illuminators for PBR from the aspects of their transmission power, ambiguity performance and coverage. Section 2.4 will present the history and a brief technical background of GPS. Previously proposed ideas and applications using GPS as the illuminator of opportunity for PBR will be reviewed in Section 2.5. The advantages and issues of GPS bistatic radar along with the literature review of some potential techniques to perform airborne target detection will be discussed in Section 2.6. Furthermore, the discussion regarding of techniques and outlines outstanding which research areas presented in this chapter that will be further studied and addressed in the following chapters of this thesis will be made in Section 2.7. The chapter ends with a conclusion in Section 2.8

2.2 Background of Passive Bistatic Radar

The earliest PBR and also British radar experiment was performed by Sir Robert Watson Watt and Arnold Wilkins at Daventry, United Kingdom in 1935. This experiment demonstrated the capability of a PBR system to detect aircraft using broadcast signals from the BBC empire shortwave station as the illuminator of opportunity and captured the reflections from a Heyford biplane bomber that was about eight miles away from the receiver [1, 3]. Radar quickly evolved from a passive to active system since the radar detection performance using the reflections from continuous wave (CW) illuminators of opportunity is greatly affected by the much stronger direct-path signal [3].

Before the end of World War II, most of the radar developments were in the area of active CW bistatic radar. Examples of operational bistatic radar systems included the “Chain Home” system by the United Kingdom, the “electromagnetic barrier” system by France, “RUS-1” by the Soviet Union and “Type-A” by Japan [4]. Germany on the other hand developed and operated a PBR system called “Klein Heidelberg” that used the previously mentioned “Chain Home” system as the illuminator of opportunity to warn about the presence of incoming attacks from enemy bombers [4].

Research and development work on the bistatic radar had also been carried by the United States during the same era, but their efforts were soon diverted to focus on monostatic radar with the introduction of the duplexer in 1936. Monostatic radars intrinsically have fewer geometric complexity and lower cost due to the advantage of using the transmitting and receiving antennas at a common location. Due to these advantages, the development of bistatic radar was halted after World War II with all the efforts being focused on monostatic radar.

Although the development of bistatic radar revived in the early 1950s with the emergence of new radar applications that required bistatic operation, it was not until the 1970s that significant work was carried out for this kind of radar. New bistatic radar applications included semi-active homing missiles, forward scatter fence and multistatic radars in military applications [4, 5]; atmospheric and ocean observation, planetary exploration and traffic precollision sensors in civilian applications [4, 5]. Furthermore, the introduction of new threats such as retrodirective jammers and attacks by anti-radiation missiles (ARM) during the 1970s significantly increased the importance of bistatic radar as it has the benefit of locating transmitters at places which have less potential threats.

The idea of PBR was also revived as a result of the resurgence of bistatic radar systems. The target detection scenario of a PBR is similar to an active bistatic radar in terms of geometry. From a military perspective, it is difficult to detect the presence of PBR as the system virtually does not transmit an RF signal and the location of its receiver is unknown [6, 7, 8], hence having the key advantage of reducing the possibility of electronic countermeasure (ECM) attacks against it. In addition, [8] explained that while stealth aircrafts are specifically designed to counter X-band monostatic radar, PBR can be a potential anti-stealth technology by utilising illuminators of opportunity which are generally communication signals and are broadcast at lower frequency bands where stealth techniques are less likely to be effective. Moreover, the signal reuse advantage of PBR helps to alleviate the spectral congestion issue which is increasing with time due to the rising number of transmission sources and therefore benefits military operations in areas that are highly populated with broadcasting sources [9].

In the 1980s, the development of PBR was performed by IBM using the history of Doppler-shift from analogue television signals to track aircraft in non-realtime. Following this Lockheed-Martin used frequency modulation (FM) radio broadcast signals, but the poor ambiguity function and dynamic range of these signals were criticised for being unable to support aircraft detection and tracking [3]. However, the capability of PBR for air target detection and tracking became more promising following increases in computational performance and cost reduction for hardware such as analogue-to-digital converters (ADC) and digital signal processors (DSP) as predicted by the Moore’s law [3, 9]. The timing and synchronisation between the illuminator of opportunity and receiver of PBR are also no longer problematic with the introduction of GPS technology. As indicated by [10], PBR technologies for aircraft detection exceeding 100 km using FM radio signals were already available in military application, such as “Silent Sentry” by Lockheed Martin and “Homeland Alerter 100” by Thales. From the above application examples, it is found that the PBR of this era commonly used analogue modulated illuminators of opportunity.

In the first decade of the 21st century, many studies for air target detection PBR have focused on utilising digital transmitters as illuminators of opportunity with the expansion of availability of such formats. In the literature, schemes based on Digital Video Broadcasting-Terrestrial (DVB-T) stations [11, 12], Digital Audio Broadcasting (DAB) stations [11, 13] and cellular basestations [14] are discussed. There are also experimental results for PBR utilising Wi-Fi networks presented by Falcone *et al*. [15] for short-range land target detection such as vehicles and running people and Chetty *et al*. [16] for indoor target detection. The characteristics of all potential land-based illuminators of opportunity in terms of frequency, bandwidth, transmission power and modulation type were summarised in [6, 10].

The feasibility of low Earth orbit (LEO) space-based illuminators of opportunity for mid-range aircraft surveillance are also investigated [17]. The illuminators investigation included remote sensing satellites such as TerraSAR-X, Radarsat-2 and Cosmo-SkyMed; communication satellites such as Sirius-Xm, Eutelsat W2A and Inmarsat I-4 EMEA. From the study, the argument has been made that the CW transmissions of communication satellites are more reliable than the remote sensing counterparts that use burst transmissions.

2.3 PBRs Performance Comparison

The detection performance of PBR systems in terms of target resolution and ambiguity function is usually less optimal or inferior to their active counterparts. This is because the transmit waveforms for active radars are carefully designed for target detection while the signal characteristics of illuminators for PBR are typically designed for applications such as communications, broadcasting or navigation. However, the advantages previously mentioned such as stealth and the possibility of utilising the spatial diversity of a large number of illuminators to exploit the reflections of a target from many angular aspects affirm the potential of PBR as a complementary asset for target detection.

It is unclear whether the cost of building an active or PBR system is lower. PBR does not require any cost for building a transmitter due to its use of signals from other sources. However, the receiver of a PBR requires more computational power. In comparison with their active counterparts, the absence of directional control mechanisms for the illuminators of opportunity renders PBR no flexibility over the transmitter-to-target propagation path and therefore requires the receiver to perform all the signal processing tasks. In comparison with the monostatic radar, the PBR requires more processing in solving the higher complexity bistatic geometry. In addition, the PBR system requires a direct-path signal interference (DSI) suppressing module since the direct-path signals transmitted by the illuminators of opportunity must be acquired as a time reference for the target searching process, but will eventually act like interferences at the target detection stage.

The performance comparison for PBR’s illuminators is usually assessed in terms of power density at the target, ambiguity performance and coverage. Firstly, a comparison of the performance of PBR for analogue and digital modulated illuminators was made by Griffiths [18, 19], where it was shown that analogue modulation is superior to the digital counterpart in target detection ranges due to the higher effective isotropic radiated power (EIRP). However, analogue modulation has poorer ambiguity performance since its modulation is highly reliant on the contents of the broadcast. Likewise, digital modulation is more constant in time and its noise-like characteristic makes such formats independent of the contents of the broadcast. On the other hand, the availability and spatial diversity of illuminators for a PBR system within an air or ground surveillance area are the most important factors in assessing the performance of PBR in terms of coverage. Clearly, having more widely separated transmitters available in the surveillance area will increase the target detection reliability of PBR system since the receiver will less likely be shaded by geometric factors, such as the body attitude of targets and geographical obstacles, from capturing the target reflections.

The performance for PBR using space-based illuminators will also be discussed. Initially the concept of using space-based transmitters such as communication [20] and navigation [21] satellites as the illuminators of opportunity for PBR to perform target detection was considered. The space-based illuminators are usually designed to transmit sufficient power to establish communication links with the receivers on Earth [22]. But in terms of target detection performance, the power density at the target given by these illuminators might not be as good as the land-based illuminators since the majority of the signal power is lost during the signal propagation between space and Earth.

Modern satellite systems such as Digital Video Broadcast-Satellite (DVB-S) and Global Navigation Satellite System (GNSS) are designed to transmit digital modulated CW signals. Therefore, PBR systems that utilise these types of illuminators for target detection have similar ambiguity functions as land-based digital modulated illuminators.

In terms of the coverage of a PBR system, land-based and geostationary space-based illuminators of opportunity are able to provide constant coverage within the surveillance area since they are stationary. However, both types of illuminators of opportunity are not necessarily built in large numbers since they are designed to fulfill the demand of land-based applications within a given area and are also more localised. Other space-based illuminators such as the earth orbiting satellites are not able to provide continuous coverage due to their intermittent appearance over a given area [22]. However, earth orbiting satellite systems for navigation such as GPS rely on large numbers of satellites in its constellation ensuring continuous and uninterruptible coverage in all areas, populated or otherwise. In the case of GPS, this means that more than four satellites are typically within LOS anywhere on Earth. The utilisation of this kind of illuminator of opportunity to perform target detection for PBR is the major work reported in this thesis.

2.4 Background of GPS

GPS is the first GNSS in the world established by the U.S. government in the 1960s. It currently consists of 32 satellites in its constellation to form global coverage for users to precisely keep track of their position and time. This system was initially designed for military applications where precise positioning and timing were primary concerns for transportation and weapons.

Following the concern about the fatal shooting down incident of a civilian airliner, Korean Airlines 007, by a Soviet interceptor due to its mistaken violation of their airspace, GPS became accessible to the public in the 1980s [23] providing higher navigation capability to all forms of transportation and better response to distress calls. Although the precision of current GPS for civilian applications is inferior to those utilised by the military, the ongoing modernisation program for this system by the U.S. government such as adding new civilian signals and frequencies to the future GPS satellites will eventually make its precision of positioning comparable with the military GPS signals [24].

GPS satellites are located at around 20,000 km above the ground [25, 26] in the medium Earth orbit (MEO) region. As of the current system (i.e. Block IIA, IIR, IIR-M and II-F), the satellites are equipped with transmitters that continuously broadcast right-hand, circularly polarised (RHCP), direct-sequence spread spectrum (DSSS) signals using a binary phase-shift keying (BPSK) modulation technique in two frequency bands: L1 at 1.57542 GHz and L2 at 1.2276 GHz. Therefore, the GPS signal occupies a larger bandwidth after the modulation process [25, 26, 27]. This signal is modulated with two types of biphase pseudo-random noise (PRN) codes (i.e. consists of ±1) and a 50 Hz bit rate navigation message. The first type of PRN sequence is called Coarse/Acquisition (C/A) codes that are produced at a chip rate of 1.023 MHz and a cycle period of 1 ms with the purpose of assisting GPS receivers in the initial acquisition stage. The second type is called the precision (P) codes that are produced at a chip rate of 10.23 MHz and a cycle period of approximately a week with the purpose of providing higher ranging accuracy. But to restrict public access, the P codes are encrypted with Y codes. As a result, the name of this encrypted sequence is termed the P(Y) code. The PRN codes between the GPS satellites are also designed to have minimal correlation with each other such that their signals can be acquired by a GPS receiver individually using the code division multiple access (CDMA) method.

The transmission power of a GPS satellite is relatively small among other space-based transmitters. The EIRP for L1 signals is around 500 Watts [28, 29]. The available direct-path signal power on Earth's surface will be reduced by the long propagation path to approximately -155 dBW according to the Friis equation as

$$P_{\mathrm{D}} = P_{\mathrm{T}} G_{\mathrm{R}} G_{\mathrm{T}} \left(\frac{\lambda_0}{4\pi R_{\mathrm{D}}} \right)^2 \tag{2.1}$$

where P_{D} is the available power on Earth's surface, P_{T} is the transmission power of a GPS satellite of 500 Watts, G_{R} and G_{T} is the gain of transmitter and receiver, λ_0 is the wavelength of L1-band signal of 0.19 metres and R_D is the direct-path signal's propagation path of 20,000 × 10^3 metres.

A GPS receiver requires the pseudorange information from at least 4 satellites to determine the 3-D position using the trilateration method, but can be reduced to 3 if the clock of the receiver is synchronised with the satellites [26]. The pseudorange determined by a GPS satellite can be written as

$$\begin{aligned}\rho_l &= ct_{Dl} \\ &= \sqrt{(x_{Sl}-x_R)^2+(y_{Sl}-y_R)^2+(z_{Sl}-z_R)^2}\end{aligned} \tag{2.2}$$

where t_{Dl} is the propagation time of GPS signal between l^{th} satellite and receiver, (x_{Sl}, y_{Sl}, z_{Sl}) and (x_R, y_R, z_R) are the 3-D positions of the l^{th} satellite and the receiver respectively. As previously mentioned, the exact position of the receiver can be determined using pseudorange information from 3 satellites. If pesudorange information from L satellites is given (for $L \geq 3$), an optimum position of the receiver can be estimated using a suitable optimisation algorithm as

$$(\hat{x}, \hat{y}, \hat{z}) = \underset{x_R, y_R, z_R}{\arg\min} \sum_{l=1}^{L} \sqrt{(x_{Sl}-x_R)^2+(y_{Sl}-y_R)^2+(z_{Sl}-z_R)^2} \tag{2.3}$$

2.4.1 GPS Signal Detection Techniques

A typical GPS receiver captures and downconverts GPS signals using an omni-directional, RHCP receiving antenna and IQ demodulator respectively as shown in Figure 2.1. It is not possible to detect the GPS L1 signal directly without applying any further signal processing techniques after demodulation. Firstly, the input signal-to-noise ratio (SNR) of a signal at a receiver is defined as

$$\mathrm{SNR}_{in} = \frac{P_{in}}{\hbar \mathrm{T_A} f_B} \tag{2.4}$$

where, $\hbar$ is the Boltzmann constant of 1.38 × 10^{-23} $\mathrm{m^2\ kg\ s^{-2}\ K^{-1}}$, $\mathrm{T_A}$ is the temperature of the receiver, which is usually assumed to be at room temperature of around 296 degrees Kelvin, f_B is the input bandwidth of the receiver and P_{in} is the power of the input signal. The input SNR of GPS signals captured by a unity gain receiver with 2.5 MHz bandwidth on the Earth's surface is around -15 dB or lower.

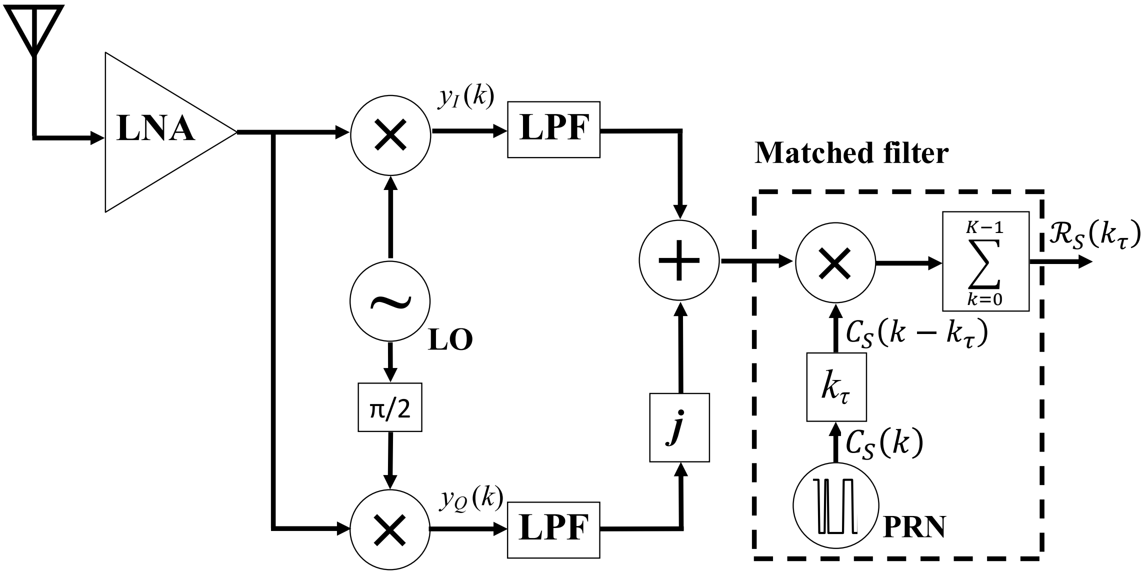

Figure 2.1: A typical block diagram of GPS receiver.

A matched filter can be applied to the demodulated GPS signal by cross-correlating with a replica of the PRN code to extract the desired GPS satellite signal from the additive white Gaussian noise (AWGN) and to discriminate it from the signals transmitted by all other GPS satellites. The discrete form of the cross-correlation function between GPS signals from L satellites that are within the LOS coverage of receiver plus noise and the locally generated C/A code sequence for the desired satellite is defined as

$$\mathcal{R}_s(k_\tau) = \sum_{k=0}^{K-1} \left\{ C_s(k-k_\tau) \cdot \left(\mu_s C_s(k-k_s) + \sigma_n n(k) + \sum_{l=1}^{L-1} \mu_l C_l(k-k_l) \right) \right\} \tag{2.5}$$

where $C_s(k)$ and $C_l(k)$ are bi-phase binary C/A code sequences of the desired and non-desired GPS signals respectively that are within LOS, μ_s and μ_l are the amplitudes of the desired and other satellites signals respectively, k_τ is the sample (i.e. discrete time) lag, $n(k)$ is assumed to be the AWGN with a statistical characteristic of $N(0, \sigma_n{}^2)$. When $k_\tau = k_s$ (i.e. the desired C/A code at the input of receiver is aligned with the locally generated sequence), the cross-correlation value is denoted as

$$\mathcal{R}_{sl}(k_s) = K + \sum_{k=0}^{K-1} \left\{ C_s(k-k_s) \cdot \left(\sigma_n n(k) + \sum_{l=1}^{L-1} \mu_l C_l(k-k_l) \right) \right\} \tag{2.6}$$

such that the ideal output SNR of the matched filter becomes

$$\mathrm{SNR}_{out} = \frac{K^2 {\mu_s}^2}{K{\sigma_n}^2 + K^2\left(C_s(k-k_s)\sum_{l=1}^{L-1} {\mu_l}^2 C_l(k+k_l)\right)^2} \tag{2.7}$$

If C_s and C_l are both perfectly uncorrelated $\forall\, l$, then $C_s(k-k_s)\sum_{l=1}^{L-1}\big(C_l(k-k_l)\big) = 0$. This means that the longer the integration applied in the matched filter, the higher the output SNR that will be achieved. In practice, the isolation between two GPS signals is only around 24 dB or less [26]. Therefore, the desired GPS signal can be successfully recovered from noise to meet the minimum sensitivity requirement of the receiver if a sufficiently long integration is applied for the matched filter and the power ratio of the desired to non-desired signals is sufficiently large.

A more efficient correlation that implements a parallel search technique has also been suggested in [30, 31, 32] to reduce the complexity of the detection process. This parallel search technique performs correlation using the circular convolution approach, thereby eliminating the requirement of the code shifting process in the linear search technique. Since a GPS receiver processes discrete time signals, the correlation can be achieved by multiplying the fast Fourier transform (FFT) of both the input GPS signal and the locally generated C/A code sequence together, followed by the inverse FFT of the product outcome.

Secondly, the GPS satellites are always in motion since they are orbiting the Earth. As a result, this motion causes Doppler shifts in the GPS signal’s carrier frequency. The Doppler frequency is defined as

$$f_D = \left(\frac{V_{\mathrm{TX}}}{\lambda_0}\right)\cos\psi_{\mathrm{TX}} - \left(\frac{V_{\mathrm{RX}}}{\lambda_0}\right)\cos(\pi-\psi_{\mathrm{RX}}) \tag{2.8}$$

where V_{TX} and V_{RX} is the magnitude of velocity for transmitter and receiver respectively, λ_0 is the wavelength of the propagating signal, ψ_{TX} and ψ_{RX} are the respective angles of motion relative to the direct-path signal propagation path. Depending on the DOA of the satellite from the receiver, the variation of frequency for a GPS direct-path signal due to the Doppler shift for a stationary receiver (i.e. $V_{\mathrm{RX}} = 0$) can lie between ±4kHz [26, 33].

For a GPS receiver, the in-phase and quadrature phase output of the demodulator in the presence of Doppler frequency is written as

$$\begin{aligned} y_{\mathrm{I}}(k) &= \mu_S\, C_S(k-k_S)\cos(2\pi(f_0+f_D)k)\cos(2\pi f_0 k) + n_{\mathrm{I}}(k) \\ &= \frac{\mu_S}{2} C_S(k-k_S)[\cos(2\pi f_D k) + \cos(2\pi(2f_0+f_D)k)] + n_{\mathrm{I}}(k) \end{aligned} \tag{2.9}$$

$$\begin{aligned} y_{\mathrm{Q}}(k) &= \mu_S\, C_s(k-k_S)\cos(2\pi(f_0+f_D)k)\sin(2\pi f_0 k)+n_{\mathrm{Q}}(k) \\ &= \frac{\mu_S}{2}C_s(k-k_S)\{\sin(2\pi f_D k)+\sin(2\pi(2f_0+f_D)k)\} \\ &\quad + n_{\mathrm{Q}}(k) \end{aligned} \tag{2.10}$$

The $2f_0$ component in (2.9) and (2.10) can be removed by a filter. When the cross-correlation between the demodulated GPS signal and the locally generated C/A codes are calculated over K lags, the output of the matched filter becomes

$$\begin{aligned} y_{corr}(k) &= \frac{1}{K}\sum_{k=0}^{K-1} C_s(k-k_\tau)\{y_{\mathrm{I}}(k)+jy_{\mathrm{Q}}(k)\} \\ &= \frac{\mu_S}{2}\mathcal{R}_s(k_\tau)\left\{\frac{\sin(2\pi f_D K)}{2\pi f_D K}+j\left(1-\frac{\cos(2\pi f_D K)}{2\pi f_D K}\right)\right\}+\mathcal{R}_n(k_\tau) \end{aligned} \tag{2.11}$$

where

$$\begin{aligned} \mathcal{R}_s(k_\tau) &= \frac{1}{K}\sum_{k=0}^{K-1} C_s(k-k_\tau)\{C_s(k-k_S)+jC_s(k-k_S)\} \\ \mathcal{R}_n(k_\tau) &= \frac{1}{K}\sum_{k=0}^{K-1} C_s(k-k_\tau)\{n_{\mathrm{I}}(k)+jn_{\mathrm{Q}}(k)\} \end{aligned} \tag{2.12}$$

As shown in (2.7), the SNR of a GPS signal at the output of a matched filter will increase linearly with the increase of the integration length, *K*. However, the effectiveness of the improvement when increasing the length of integration will be limited by the size of the Doppler frequency component, f_D, as shown in (2.11). This means that using integration times beyond a certain length will result in further reduction of SNR due to integration loss. To resolve this issue, the Doppler frequency component needs to be identified and removed using a discrete linear search algorithm for Doppler offsets along with the cross-correlation technique as illustrated in Figure 2.2. If the Doppler is completely removed and both the input and locally generated C/A codes are aligned to each other (i.e. $k_\tau = k_S$), no attenuation occurs and $y_{corr}(k) = \mu_S/2$. This code-Doppler search algorithm is also experimentally demonstrated by a GPS signal acquisition result in Figure 2.3, where the presence of the signal was located at Doppler offset of 1,900 Hz and sampled code phase of 2,866 using an integration period of 5 milliseconds and Doppler resolution of 50 Hz.

The output of the matched filter after performing Doppler removal can be denoted as

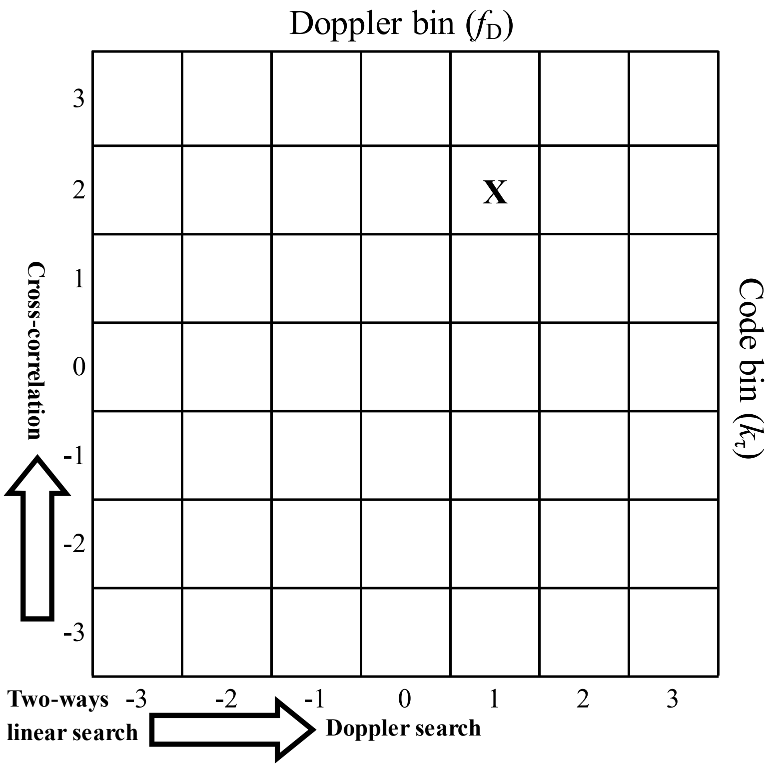

Figure 2.2: The illustration of discrete linear code-Doppler search algorithm. The 'X' symbol in the grid indicates the code-Doppler location of a GPS signal.

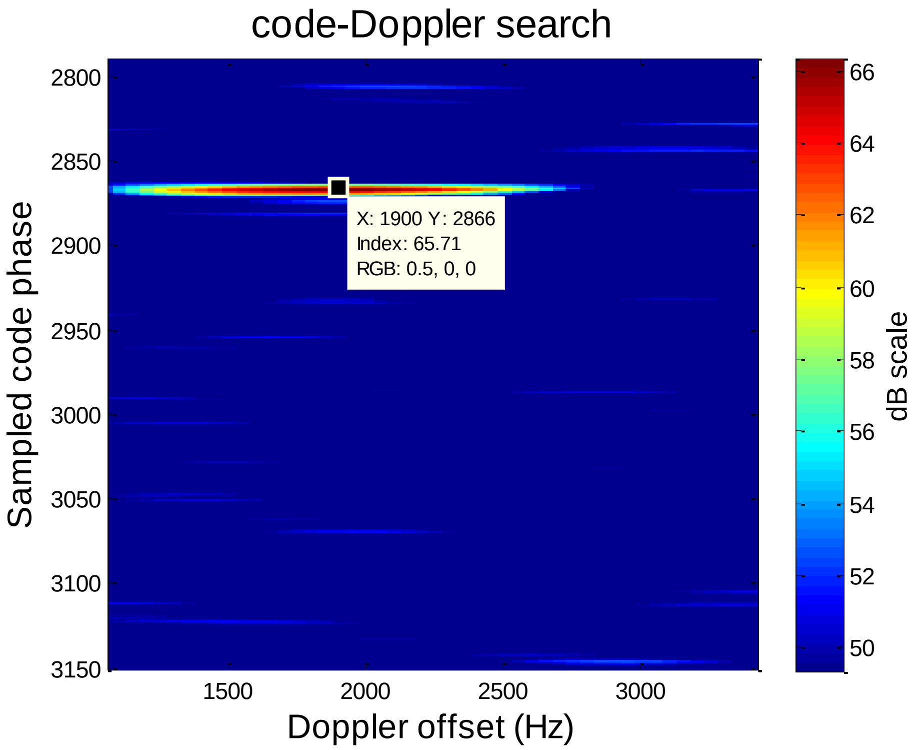

Figure 2.3: A down-converted GPS signal located at Doppler offset of 1,900 Hz and sampled code phase of 2,866 is sampled at 4.167MHz and detected using code-Doppler search for an integration period of 5 milliseconds and Doppler resolution of 50 Hz.

$$\begin{aligned} y_{corr}(k) &= \frac{1}{K}\sum_{k=0}^{K-1}\left\{y_{\mathrm{I}}(k) + j\,y_{\mathrm{Q}}(k)\right\}\cdot e^{-j2\pi f_{\Delta}k} \\ &= \frac{\mu}{2}R_s(k_\tau)\left\{\frac{e^{j2\pi(f_D-f_\Delta)K}}{2\pi(f_D-f_\Delta)K}-1\right\}+R_n(k_\tau)\,e^{-j2\pi f_\Delta k} \end{aligned} \tag{2.13}$$

where f_Δ is a Doppler bin.

From (2.13), the discrete Doppler search might result in a residual error between the Doppler frequency of the captured GPS signal and the nearest Doppler bin value. Therefore the integration result becomes more sensitive to the residual Doppler error as the integration time, *K*, is increased. This means that longer integration times will require a higher Doppler search resolution resulting in a higher complexity search.

2.5 GPS Bistatic Radar Detection Applications

A PBR system that utilises GPS satellites as illuminators of opportunity to perform target detection can be termed a "GPS bistatic radar" and it is classified as a subclass of passive GNSS radar. The earliest idea of proposing this kind of PBR based on the specular reflection detection model was patented to Tsui *et al.* [21] in 1993. This patent proposed a detection approach using a directional antenna to point at a target and a signal processing technique to improve the detection performance of the receiver such that the time-of-arrival (TOA) of target reflection can be acquired to determine the position of a target if 4 satellites were utilised, or the pseudorange of a target if only one satellite is available.

In the following year, a target detection scheme for GPS bistatic radar was reported by Koch *et al.* [34] which used the forward scatter path detection approach. This detection approach identifies the presence of targets when they appear in between the baseline of PBRs. Air targets such as civilian and military aircraft and space targets such as the Russian MIR space station were chosen as the targets of interest in this detection scenario and a receiver that detected the signals from the target using a 10 dBi tracking antenna and integration process were also utilised to improve the target signature. This experiment demonstrated target detection by monitoring the received SNR of GPS signals from various satellites and identifies the presence of a target by a reduction in SNR due to blockage of the direct path. However, these initial attempts do not appear to have any follow-on work due to the difficulty of reliable target detection due to the weak power GPS signals [35]. This approach also lacks the capability of determining the position of the detected target since no target information regarding its pseudorange and DOA from the receiver is acquired.

The air target detection technique for GPS bistatic radar similar to [21] was further extended by McIntosh [36] in 2001. This patent provided more comprehensive methods such as extracting the GPS Doppler offsets and code delay information of target reflection with respect to the GPS direct-path signal using a linear range-Doppler search approach to identify the presence of an air target and using the time-difference-of-arrival (TDOA) between the direct-path signal and target reflection to localise the target. However, no follow-on work has been performed to analyse the feasibility of this proposed idea.

Another idea of utilising GPS bistatic radar for detecting helicopters using the forward scatter technique has been proposed by Clemente and Soraghan [37]. While the forward scatter detection approach lacks the capability of extracting Doppler information from a moving target, this idea suggested detecting a helicopter that is located near to the forward scattering region. The radar signature from its rotating blades can be acquired using micro-Doppler analysis which is usually performed on a target where some parts of its body are creating an additional motion relative to its main body that yields an offset to the main Doppler shift and this offset is not necessarily constant. This idea is inspired by Thayaparan *et al*. [38] where the analysis of the moving blades of a helicopter was performed using a wavelet transform to observe the time varying Doppler shift.

GPS bistatic radar has also been proposed and investigated in later years for remote sensing applications, such as altimetry [39, 40, 41], forward scatter wind speed measurement [42], oceanography [43], sea ice cover measurement [44] and soil moisture [45, 46]. Brown *et al*. [47] developed a phased-array receiver that contained 109 elements for a GPS bistatic radar that can be mounted on an aircraft to perform remote sensing application and is claimed to be superior over a single receiving element in terms of detection reliability since it is able to track GPS signal reflections robustly with minimal clutter using digital beamforming. Moreover, a study of applying the inverse synthetic aperture techniques (ISAR) to GPS bistatic radar in imaging applications has been made by [48, 49] for the case where the illuminator is moving and a stationary receiver is employed.

2.6 GPS Signal Air Target Detection for Passive Bistatic Radar

From a military perspective, the space-based illuminators of opportunity are strategically superior to the land-based counterparts as their deployment altitude provides a sanctuary to them. Hence, their operation cannot be disabled without highly advanced armaments such as physical attack using anti-satellite weapons or access denial using an electronic jammer. In fact, the orbiting GPS satellites at MEO are even safer from threats than many potential space-based illuminators of opportunity such as the communication satellites that are stationed at LEO. In addition, GPS bistatic radar has the advantage of a relatively large number of widely separated illuminators and being globally available.

As the newer GPS satellite generation Block IIR & IIR-M have replaced most of the previous generation Block I and Block IIA satellites, the reliability of the system has significantly improved, and therefore, offers greater potential to be used as illuminators of opportunity for PBR. Also, the new GPS Block III satellites will be launched in the near future which are designed to transmit L5-band signals (operated at 1.17645 GHz) that have higher power than the current L1 and L2 signal, hence increasing the reliability of GPS bistatic radar in terms of detection performance.

Moreover, the operational coverage of navigation systems can be further expanded if GPS is incorporated with the constellation of other GNSS such as the Russian GLONASS that was rejuvenated in recent years and the systems where ongoing deployment are made for global coverage such as the European GALILEO and Chinese BeiDou Navigation Satellite System (BDS). GNSS interoperability using a common receiver has been studied by Rizos [50] and this approach has benefits in the area of positioning since the increased number of navigation satellites provide higher geometrical diversity and coverage that allows the receiver to acquire and process more navigation parameters, hence improving the positioning accuracy with the reduction of position dilution of precision (PDOP) [51]. This implies that the implementation of such a technique can also benefit PBR in terms of the accuracy of localising a target, assuming that the interoperability issues at the receiver are resolved. However, the availability of multiple GNSS constellations for PBR can only be guaranteed if their access can be consistently provided by the individual nations.

Since the GPS signal structure is designed for ranging and positioning purposes, these signals can be potentially utilised by PBR to perform localisation of the target of interest using similar positioning methods as in a conventional GPS receiver by exploiting both the direct-path signals and reflections from the target. The greatest challenge of GPS bistatic radar for aircraft detection is the low transmission power and the high direct path propagation loss. The additional reflected path between the target and the receiver will also further attenuate the available power. However, this is not always the case since the radar cross section (RCS) of target is another crucial factor that affects the signal power of target reflection. In addition, Mojarrabi *et al.* [52] suggested that land and sea clutter could become a real problem for GPS bistatic radar when performing air target detection since the power of the land or sea clutter is typically 20 dB below the direct-path signal and will easily mask weak signal returns.

To detect the weak reflections from a target, the sensitivity of a receiver for GPS bistatic radar should be much higher than a conventional GPS navigation receiver. The signal processing gain using coherent and non-coherent integration (i.e. pre and post square-law detection respectively) for increasing the detection performance of GPS receivers has been discussed by different authors for GPS signal acquisition. As suggested by Liu *et al*. [53], both integration techniques can be applied directly to GPS bistatic radar to improve the sensitivity of the receiver for target detection.

The clutter problem can also be mitigated by employing high directional antennas at the receiver of GPS bistatic radars and pointing it at the area of interest, such as the patch of sky that an air target is likely to occupy. In that case, the signals that appear outside the beamwidth of the antenna such as surface clutter can be greatly reduced. A narrow beamwidth can be achieved by using a large scale antenna array with many receiving elements that implement a phased-array technique so that the desired signal from a certain DOA captured by each element can be aligned in-phase and summed together. This technique also increases the SNR of the desired signal by a factor equal to the number of elements in the array and is the main hypothesis of this project.

2.6.1 Coherent Integration

Coherent integration performs a phasor sum of the input signal after aligning each sample to have the same phase. The phase and frequency of the signals before integration must be stable to avoid integration loss. An ideal coherent integration will result in improving the SNR by a factor of the number of integrations performed. It is generally implemented in GPS receivers using the correlation technique as shown in (2.5) to improve the SNR of weak input signals to a detectable level.

A GPS receiver for indoor application might experience very poor signal reception due to obstacles such as walls or windows that result in further reduction of the signal power. Pany *et al*. [54] indicated that the GPS signal power in an indoor environment can be reduced to as low as 10 dB-Hz. Therefore, that author suggested using extremely long coherent integration times and demonstrated that a GPS receiver that applied coherent integration up to 2 seconds can achieve a 10 dB higher sensitivity than an ordinary GNSS receiver that only used a coherent integration time of not more than a few dozens of milliseconds. The author also explained that long coherent integration helps with rejecting the multipath signals if their Doppler frequencies differ with the direct-path signal which can also be seen from (2.11). This process also avoids the squaring loss that is encountered when using a non-coherent integration process for a very weak signal. However, the long integration process is susceptible to frequency variations in the signal. Hence a GPS receiver that implements such process must use stable oscillator. Also, the linear Doppler search process is only able to identify and remove the Doppler frequency of the GPS direct-path signal at the receiver properly if it is constant over the integration period.

2.6.2 Non-coherent Integration

The non-coherent integration technique sums the amplitude of the signal which renders it immune to phase misalignment between samples. This technique is also commonly applied by radar systems to add multiple pulses at the post-detector. However, the SNR improvement depends on the input SNR at the square-law detector. According to an analysis performed by Barton [55], the worst non-coherent integration gain (i.e. input SNR below a certain level) is equal to the square root of the number of integrations. Toomay [56] also showed the non-coherent integration gain to be in between the square root and linear factor of the number of integrations. Therefore, this integration process is usually applied after coherent integration to maximise the overall SNR.

Another study was made by Glennon *et al*. [35] in 2006 to investigate the feasibility of GPS bistatic radar to perform target detection theoretically based on a series of power budget estimations. This study also considered improving the input SNR of the target reflections by non-coherently integrating GPS signals of multiple satellites from the target which can improve the overall SNR by at least the square root of the total number of satellites applied in the detection scheme, assuming uniform power density of signals at the reflection point.

2.6.3 Radar Cross-section

Radar cross-section (RCS) is a factor that characterises the amount of reflected energy from a scatterer. Compared to the monostatic counterpart, modelling of bistatic target RCS is more complicated due to the additional geometrical factors such as the bistatic angle and the shape of the target. For a multi-static PBR that utilises multiple widely separated illuminators of opportunity, the RCS of a single target varies with the bistatic angle. The variations are classified into three regions: pseudo-monostatic, bistatic and forward scatter.

The pseudo-monostatic region usually occurs when the bistatic angle is small and its bistatic RCS is comparable to the monostatic counterpart. As demonstrated by Skolnik [57], the boundary of this region is determined by the physical size of the target. This is demonstrated by comparing the scattering behaviour of two ideal conducting spheres and showing that the RCS of the larger sphere that lies in the optical scattering region behaves like a monostatic scatterer with minor fluctuations up to a higher bistatic angle than the smaller sphere that lies in the Mie scattering region.

Since a large aircraft is much larger than the wavelength of GPS signal, this kind of target should lie within the optical scattering region for a GPS bistatic radar. However, the boundary of the pseudo-monostatic region for such a target can no longer assumed to be the same as a conducting sphere due to the higher shape complexity. In fact, Ewell and Zehner [58] studied the bistatic RCS of 4 coastal freighters using an X-band radar and found that the RCS reduces compared to the monostatic case when the bistatic angle exceeds 10 degrees. The reduction of RCS in the bistatic region is due to issues such as retroreflection of energy to the transmitter and shadowing as explained by Willis [1]. To avoid this loss in RCS, it is important for GPS bistatic radars to perform detection using multiple transmitters so that there is a better chance of getting a large RCS due to the reflection geometry.

The bistatic geometry of the target will move into the forward scatter region when an air target approaches the bistatic baseline (i.e. $\beta \approx 180°$). The characteristic of target in this region is explained by Kock [59] using an analogy that describes the target as an opaque screen object and its area is identical to an aperture. According to Babinet's principle, when the screen and aperture are illuminated by a common source that has a much smaller wavelength, the diffraction field pattern for both objects will become identical. In that case, the bistatic RCS of a smooth or complex shaped target can be denoted as

$$\sigma_{\mathrm{B}} = \frac{4\pi A^2}{{\lambda_0}^2} \tag{2.14}$$

where A is the silhouette (shadow) area of the target that has the same size as the aperture and λ_0 is the wavelength of the L1-band signal. Hence the bistatic RCS will be maximised in this region.

However, in the forward scatter region, the target will produce little to no Doppler shift and delay compared to the direct-path signal. Hence, the target signature cannot be easily discriminated from the direct-path signal using the Doppler-delay search process. For this reason, the forward scatter target might not produce useful information in the detection process.

2.6.4 Phased-array Technique

A GPS receiver is highly susceptible to jamming by interfering sources since GPS satellites broadcast signals that are extremely weak when they reach the Earth's surface. To mitigate the jamming issue, Kaplan [26] suggested using a relatively high cost Controlled Radiated Pattern Antenna (CRPA) over a Fixed Reception Pattern Antenna (FRPA) design. CRPAs use beamforming techniques to steer a beam in the direction of GPS satellites for optimal signal reception and nulls in the directions of interfering sources or multipath signals for anti-jamming protection. This implementation also requires the DOAs of all the GPS satellites within LOS to be known.

Phased-array techniques do not seem to have been widely considered in relation to PBR for target detection, possibly due to the high development cost when a large scale antenna array is considered for the receiver. The advantage of beamforming for a phased-array DVB-T PBR receiver for observing multiple directions simultaneously has been mentioned by Palmer *et al.* [60]. A DVB-T PBR receiver with an antenna array to search for low-flying and low-observable targets was developed by Knott *et al.* [61] and Poullin *et al.* [62]. The array processing techniques performed by these receivers include searching for signals and using adaptive null-steering methods to minimise the reception from the DOA of direct-path signals, which is a common problem for all PBRs.

Applying phased-arrays to PBR has many benefits. Firstly, multiple directions can be searched simultaneously. Secondly, the receiver's output SNR is increased by the factor of the number of elements. This is especially beneficial to GPS bistatic radar that has comparatively much weaker transmission signals among other PBRs. However, having more antenna elements also means higher cost and processing power.

2.6.5 MIMO Radar Technique

The MIMO concept first emerged into the area of communications in the early 1990s [63, 64]. Researchers were looking for techniques that employ multiple transmitters and receivers to improve the quality of service for wireless systems in terms of channel capacity and reliability equivalent to the wired counterparts [63, 65]. Until today, the MIMO technique has been widely applied in commercial communication applications such as mobile phones that use the 4G LTE standard and wireless networking that use the IEEE 802.11n and 802.11a/c standards.

In the 2000s, MIMO techniques attracted radar researchers to exploit its potential for radar networks that also consist of multiple transmitters and receivers. While the scope of radar systems is distinct to the communication system, the basic operation of both systems that implement the MIMO technique is similar, in the way that each element of the transmit array transmits independent waveforms [64, 66]. Hence, the MIMO radar system is distinct to the phased-array counterpart that also uses multiple transmitting elements but only transmits common weight-adjusted signals. The two main directions of MIMO radar that were being investigated are the coherent MIMO [67, 68] and non-coherent (also known as statistical) MIMO [69, 70, 71, 72] radars. The performance of these two kinds of MIMO radar systems are popularly compared with their phased-array radar counterparts to demonstrate the superiority of the MIMO technique as a worthy successor or complement to the phased-arrays.

Coherent MIMO radar requires the transmitting and receiving array elements to be closely separated and collocated so that the target is in the far field region of the system [67]. This method works by transforming the physical positions of transmit and receive array into a virtual array. As a result, the effective aperture of the virtual array becomes larger than the phased-array counterpart [67, 73] that can only apply the beamforming process using the physical elements. From the literature, the coherent MIMO radar technique has superior angular resolution [74, 75], better minimum detectable velocity for applications such as the Ground Moving Target Indicator [73], and can identify more targets [74, 76]. In addition, the capability of coherent MIMO to transmit multiple probing signals enables the radar system to better perform radar imaging and parameter estimation.

There are two kinds of MIMO techniques that can process the acquired target information using the non-coherent approach: spatial and frequency [77]. The spatial MIMO radar uses widely separated transmit and receive arrays [67, 72]. This kind of configuration allows each transmitting-receiving pair to obtain the scattering response of a target from different aspect angles. This angular diversity characteristic makes MIMO radar superior to monostatic radar when it comes to the exploitation of target scintillation [72] and the mitigation of target fading [66]. Hence, the MIMO technique can better exploit the RCS diversity of a target [71], estimate the Doppler of slow-moving targets [78] and provide high resolution target localisation [79]. On the other hand, the frequency diverse MIMO radar [77] utilises multiple collocated transmitting antennas to illuminate the target with signals at different frequencies. This kind of configuration allows the radar to combine both the beamforming and frequency diversity MIMO techniques to perform target detection and estimation [72, 80]. Hence, the frequency diverse MIMO radar improves the SNR of target return at the desired direction while mitigating the effect of target fluctuation. While the frequency MIMO radar lacks the spatial diversity advantage of the spatial MIMO radar, it is superior in terms of improving the SNR of target if the latter only employs isotropic sensors [80].

The non-coherent MIMO radar is similar to the multistatic radar as both systems cooperatively process the signals captured by multiple receiving sites. However, there is a difference between both systems in the processing technique for the captured data. In general [66], a multistatic radar system operates each transmitting or receiving site independently. Then, the initial data processing outcome from each receiving site is incorporated into the central processor of the radar system via a communication link for the ultimate decision making process of target detection and parameter estimation. In contrast, the MIMO radar technique yields a higher level of cooperation as the system jointly processes the signals at both the transmitting and receiving sites.

The performance of the MIMO radar is also compared to other distributed radar systems such as the netted radar [77]. From this study, it is assumed that when the phase information of a target is not available to the radar, the probability of detection for a MIMO radar using a non-coherent technique outperforms the netted radar counterpart by a large margin at low input SNR. Also, in comparison with the netted radar that applies a unique algorithm to perform phase alignment at all receiving sites, the performance of MIMO radar is slightly inferior at very low input SNR. However, the non-coherent processing for MIMO radar has comparatively lower computational complexity than the phase alignment process.

Since the PBRs do not have transmitting capability, there are limited MIMO radar techniques that can be implemented on such systems. Furthermore, as most of the target detection and estimation techniques for PBRs are still immature at current stage, the majority of the researchers focus on PBRs using the traditional bistatic or multistatic techniques. However, the spatial MIMO radar technique seems to be a promising solution for the PBRs as many illuminators of opportunity are widely separated and large in number. For instance, there are studies investigating the performance of DVB-T based passive MIMO radar (PMR) [81, 82, 83]. In addition, a study which investigates the technique that allows PMR to perform localisation without the reference information from the direct-path signal has been reported [84]. This technique is useful in the case where the receiver in the system is experiencing difficulty in acquiring the direct-path signals. Besides, the author demonstrated that the detection performance and target resolution of PMR improved as the number of transmitters and receivers increased.

2.7 Proposed Research

The potential techniques proposed in Section 2.6 serves to demonstrate the feasibility of detecting air targets using GPS bistatic radar based on the actual experimental results. These results are presented in Chapter 5 of this thesis and can be used as a benchmark to determine the scale of antenna array that may be required to detect air targets at a more realistic distance. The key challenge of this research project is the detection of very weak GPS signal powers. These potential techniques have been applied in this thesis to overcome this challenge by improving the SNR of the extremely weak reflected GPS signals to a desired detectable level. Among the two main outcomes of this research are the implementation of phased-array and MIMO radar techniques that will be described in Chapters 3 and 4. The proposed designs for GPS bistatic radar implementing these techniques are illustrated in Figure 2.4. This section also addresses the research gaps for GPS bistatic radar and how these techniques can fulfil these requirements.

2.7.1 Coherent Integration

Long coherent integration periods were used to avoid squaring loss. The GPS bistatic radar can also apply code-Doppler search implementing long coherent integration process as shown in

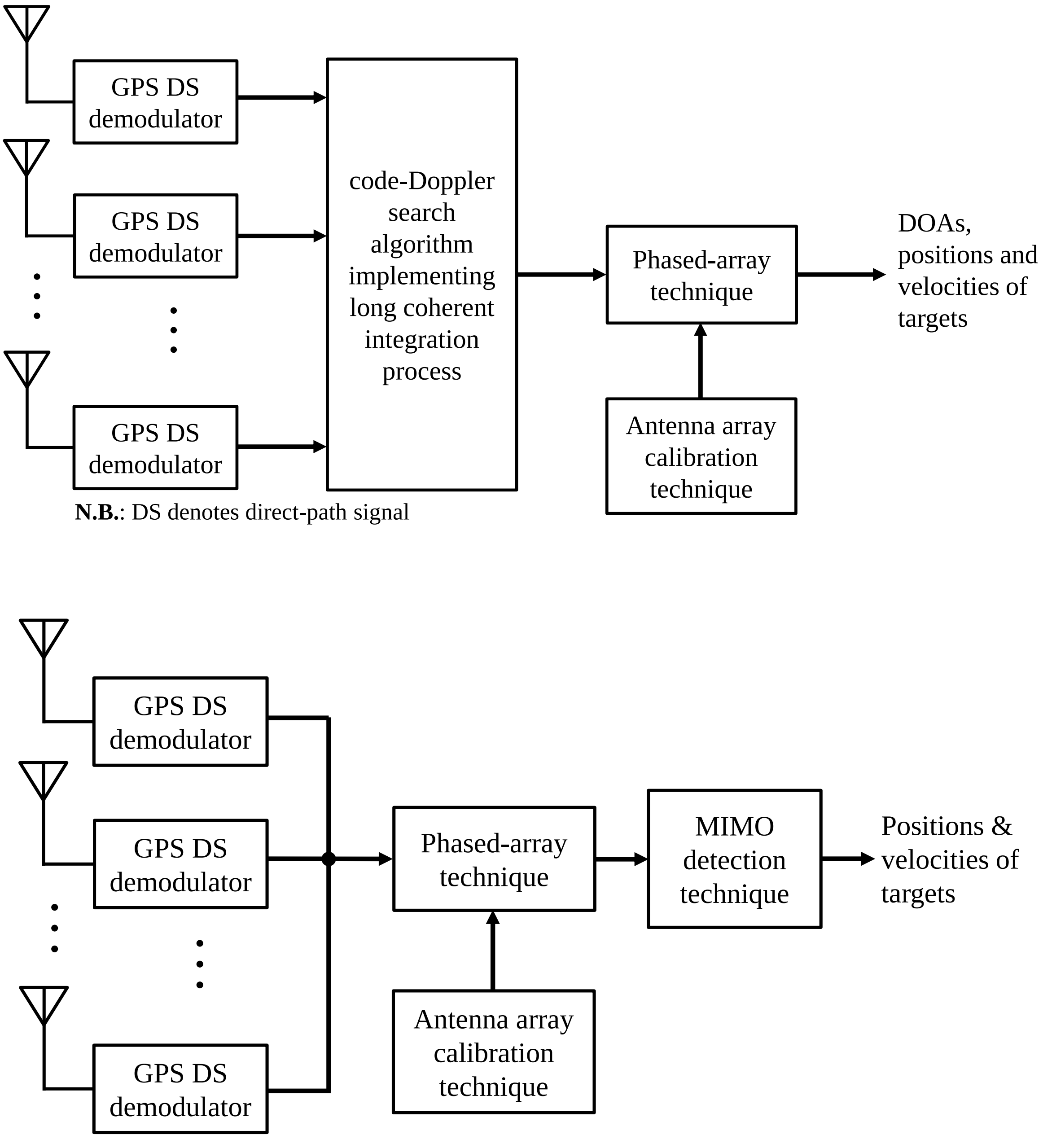

N.B.: DS denotes direct-path signal

N.B.: DS denotes direct-path signal

Figure 2.4: Schematic of the proposed phased array (Top) and MIMO radar (Bottom) designs for GPS bistatic radar in performing air target detection and parameters estimation.

(2.5) to increase the sensitivity of the receiver while obtaining Doppler frequency offset and code delay of the targets relative to the direct-path signal. These information allow the location and velocity of targets to be determined. However, the maximum effective integration time is limited by the variations in Doppler due to the target trajectory and needs to be carefully selected to minimise integration loss. Hence, the sensitivity of the receiver needs to be supplemented by the phased-array processing technique to improve the SNR of the target reflections to a designated level. Moreover, a tracking algorithm is also provided by the MIMO radar technique to minimise the variations in Doppler due to the target trajectory.

2.7.2 Phased-array Technique

The design of a GPS bistatic radar system using a phased-array receiver has not received much attention in the literature. The study of the performance of GPS bistatic radar carried out by Glennon *et al*. [35] provided an example of an air target detection scenario using a horn antenna with 15 dB gain. This example seems to neglect the issue of searching for the DOA of the target scattering signal as no steering mechanism was presented. In the analysis of air target detection using low Earth orbit communication signals, Cherniakov [85] suggested the use of an antenna with a relatively large effective area and narrow beamwidth. This suggestion most likely referred to the use of a single high gain and directivity element. Tsui *et al*. [21] suggested that the range and position of a target can be acquired by a directional antenna which is steered at it, but the steering technique of this directional antenna is not described.

From the direct-path signal acquisition perspective, steering the beams of the antenna array at the illuminators of opportunity where their DOAs are known might be a redundant process. It is because these broadcasts are sufficiently robust, hence allow the signal information to be acquired with ease by a receiver that utilised an omnidirectional antenna and implemented signal processing module that provide sufficient gain to improve these signals to a useful level. However, adding the array processing part for a PBR receiver will further increase the SNR of the captured direct-path signals which will result in signal information being acquired with higher accuracy. This approach is particularly useful when pointing the beam at the DOA of the desired direct-path signal while discriminating against the stronger broadcasts from other illuminators that might distort or corrupt the information from the desired signal if the acquisition process is interfered with.

A large scale antenna array with 32 dual-polarised elements was constructed and used to improve the SNR by virtue of the array gain. An array calibration algorithm was also developed in Chapter 3 to determine the phase errors and array orientation to maximise SNR for the array and provide an accurate DOA estimate of the target. The performance of the air target detection using the phased-array technique will be investigated by simulations and experimental results.

2.7.3 MIMO Radar Technique

While the MIMO technique was investigated to improve the detection and parameter estimation performance of a radar system, this technique is still not widely applied in the area of PBRs. Therefore, there is still a significant gap in implementing MIMO radar technique for PBR systems at the current stage. The MIMO radar detection technique can potentially be applied to improve the performance of GPS bistatic radars from different aspects. For instance, the target reflections from multiple GPS satellites can be added non-coherently prior to detection to further improve the SNR. Glennon [35] suggested this non-coherent MIMO technique rather than coherent addition, as the phase coherence of the reflected signals is likely to be distorted by a diffuse reflection process from a large target. However, the author did not provide details about the implementation of this integration technique in practice and Chapter 4 in this thesis addresses this gap.

In addition, the inherently poor satellite transmission power and air target motion may affect the conventional detection process when long signal integration periods are applied. Therefore, the GPS MIMO radar system can be supplemented by the track-before-detect (TBD) technique to track target motion while improving the radar detection performance.

The main objective of applying the MIMO radar technique along with the phased-array technique is to integrate the matched filters output of target reflections from multiple satellites so that the final SNR can be improved by the non-coherent integration gain. This solution is proposed to bridge the gap in [35] where the idea of combining the output from all the available satellites was presented. This technique is particularly useful for GPS bistatic radar where the power budget for target reflections is limited by the low satellites transmission power.

2.8 Conclusion

The historical background of bistatic radar and its further development into PBR was initially covered in this chapter. The PBR was found to be a potential option to perform air target detection since that many types of illuminators of opportunity can be used in this modern age to fulfil its requirement. A performance comparison between different types of illuminators for PBR has also been studied. Among this study, the space-based illuminators of opportunity such as the GPS satellites were found to be advantageous in having continuous and uninterruptible coverage globally. Therefore, the GPS bistatic radar has been selected as the main PBR research topic in this thesis.

A brief history and technical background in terms of GPS signal acquisition and forming the navigation solution has been reviewed. Similarly, the air target localisation technique for GPS bistatic radar will also be based on the linear code-Doppler search technique used for acquiring GPS signals. Modifications of these techniques when searching targets will be further discussed in Chapter 3.

The idea of using GPS bistatic radar for air target detection was also studied by other researchers in the past. However, this idea appears to have no follow-on work due to the inherently poor satellite transmission power that poses a great challenge for air target detection. Hence, a literature review was made to investigate the advantages and issues of GPS bistatic radar along with of some potential techniques to perform airborne target detection. This chapter ends up with specifying the research problem and proposing solutions to fill up the gaps of GPS bistatic radar for air target detection, which enable the development of the following chapters for this thesis.

CHAPTER 3

Feasibility of Target Detection using Phased-array Technique

3.1 Introduction

This chapter investigates the factors affecting the performance of GPS bistatic radar for air target detection. The minimum detectable scattered power will be analysed when several techniques are used to enhance the detection performance including the use of large scale antenna arrays and increasing the integration periods of the matched filter in the radar receiver. Hence, the proposed target detection model for GPS bistatic radar using the phased-array technique and the array calibration model due to the inter-channel phase errors and attitude of the antenna array will be presented. The target detection and location estimation performance for GPS bistatic radar will also be investigated using the results from simulation processes.

Section 3.2 presents the target detection and statistical models for GPS bistatic radar. Section 3.3 covers the background of phased-array antennas and discusses the feasibility of implementing this technique for GPS bistatic radar. A calibration technique for GPS bistatic radar will be described in Section 3.4 to resolve several issues that will be encountered by a phased-array receiver such as phase misalignment and determination of the attitude of the antenna array. In Section 3.5, signal processing techniques for performing target detection and position estimation are presented and analysed by simulation to examine the capabilities and limitations of GPS bistatic radar. This includes both the target detection and parameter estimation algorithms using phased-array receiving antennas. This chapter will be concluded in Section 3.6.

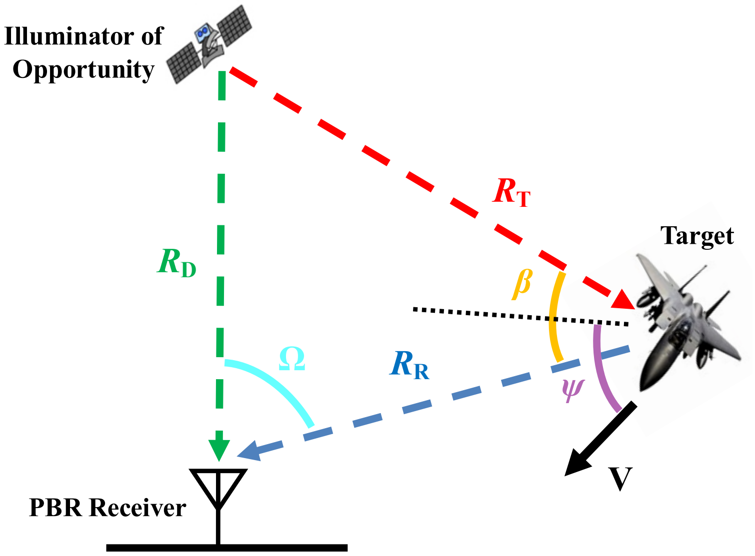

Figure 3.1: Target detection scenario of a bistatic radar (not to scale).

3.2 Estimation of Parameters for GPS Bistatic Radar

An initial assessment of the feasibility of a GPS bistatic radar system is obtained by the available power using the radar equation in (3.1) based on the scenario illustrated in Figure 3.1.

$$P_R = \frac{P_T G_R G_T \sigma_B}{(4\pi)^3} \left(\frac{\lambda_0}{R_T R_R} \right)^2 \tag{3.1}$$

where P_R is the available power of a signal scattered by the target at the radar receiver, P_T is the L1-band signal transmission power of GPS satellite, G_R and G_T are the gain of receiver and transmitter respectively, σ_B is the bistatic radar cross-section of a target, λ_0 is the wavelength of the L1-band signal, R_T is the transmitter-to-target range, R_R is the receiver-to-target range (also known as the reflected path). As indicated in Figure 3.1, the bistatic angle β is the angular separation between the R_T and R_R, Ω is the angular separation between R_D and R_R, and ψ is the target velocity aspect angle.

3.2.1 Power Measurement of Target Scattering

The performance of a radar system can be measured in terms of target detection range. As derived from (2.1) and (3.1), the relative relationship between the power of the target return and the direct-path signal, P_R and P_D, respectively, incident on the antenna of a common bistatic radar receiver is given by

$$\frac{P_\mathrm{R}}{P_\mathrm{D}} = \frac{\sigma_\mathrm{B} {R_\mathrm{D}}^2}{4\pi {R_\mathrm{T}}^2 {R_\mathrm{R}}^2} \tag{3.2}$$

For an omni-directional receive antenna, the SNR of the target scattering signal captured by a bistatic radar receiver in a white noise only environment is given in as

$$\mathrm{SNR}_\mathrm{tgt} = \frac{P_\mathrm{R}}{N_\mathrm{WGN}} = \frac{P_\mathrm{D}\sigma_\mathrm{B} {R_\mathrm{D}}^2}{4\pi {R_\mathrm{T}}^2 {R_\mathrm{R}}^2 (\mathscr{k} T_\mathrm{A} f_\mathrm{B})} \tag{3.3}$$

For a fixed receiver bandwidth and target RCS, typical ranges R_T and R_R in the GPS scenario cause significant reduction in the $\mathrm{SNR}_\mathrm{tgt}$. In the case of a space-based PBR, R_T will be much greater than R_R due to the significant difference between the altitudes of the Earth orbiting illuminators that are deployed in the thermosphere or above (i.e. exceeding 100km) and tropospheric aircraft such as an airliner and a helicopter or low stratospheric aircraft such as a military airplanes (i.e. less than 30km). In the case of GPS bistatic radar, the altitude difference between the satellites and the target is even greater than those illuminators of opportunity at LEO. Therefore, range R_T can be approximated to be equal to the range R_D. Hence, the distance of target from a radar receiver, R_R, becomes the sole factor that contributes to the reduction of $\mathrm{SNR}_\mathrm{tgt}$ with respect to the power level of a direct-path signal. The $\mathrm{SNR}_\mathrm{tgt}$ under this approximation is shown as

$$\mathrm{SNR}_\mathrm{tgt} = \frac{P_\mathrm{D}\sigma_\mathrm{B}}{4\pi {R_\mathrm{R}}^2 (\mathscr{k} T_\mathrm{A} f_\mathrm{B})} \qquad R_\mathrm{D} \approx R_\mathrm{T} \gg R_\mathrm{R} \tag{3.4}$$

While the power level of a GPS signal reaching the Earth's surface from (2.1) is estimated to be around −155 dBW, a conventional GPS receiver is usually designed to have a minimum input power sensitivity of −160 dBW to guarantee steady GPS services most of the time. This figure can be used as a benchmark to estimate the sensitivity requirement of a GPS bistatic radar receiver to detect a target at any given range, R_R. The power level (3.2) and SNR (3.4) resulting from scattered GPS signals from a target with varying RCS and distance is summarised in Figure 3.2 and shows that the received power of a target return is significantly lower than the direct-path signal. Therefore, the radar receiver must be designed to provide sufficient gain to improve the SNR to achieve a given detection performance.

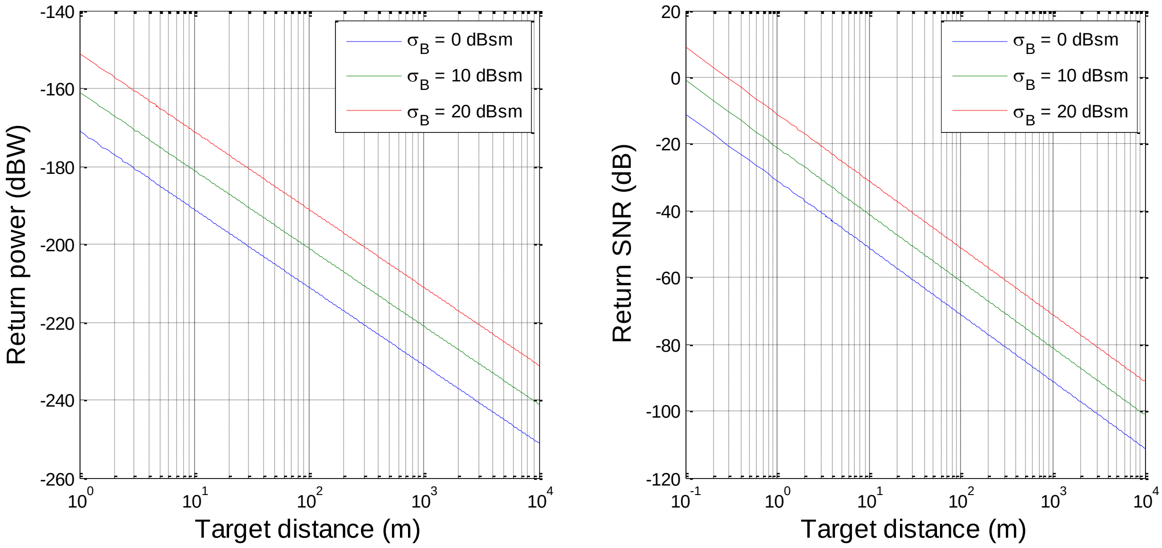

Figure 3.2: Estimated return power (Left) and SNR (Right) of various RCS targets.

The remainder of this section establishes the SNR required for a specified target detection probability by considering the probability density function (PDF) of the signal and noise at the output of a matched filter. Referring to (2.6), the PDF of a desired GPS signal in AWGN (neglecting non-desired signals) at the output of matched filter can be modelled as a normal distribution with a mean, μ, and variance, σ^2, each being determined by the output signal and noise power respectively. Two hypotheses $\mathcal{H}_0$ and $\mathcal{H}_1$ are defined as the absence and presence of desired signal at the output of the matched filter respectively after a squaring operation respectively. The PDF of the squared matched filter outputs under $\mathcal{H}_0$ and $\mathcal{H}_1$ is a standard and non-central chi-squared distribution respectively. The theoretical detection performance of the GPS bistatic radar receiver will be analysed using a likelihood ratio test that ensures a constant false alarm rate (CFAR) for a receiver with a fixed detection threshold τ. The likelihood ratio test [86] is given by

$$\log \frac{p(y;\mathcal{H}_1)}{p(y;\mathcal{H}_0)} \underset{\mathcal{H}_0}{\overset{\mathcal{H}_1}{\gtrless}} \tau \tag{3.5}$$

The probability of false alarm, $\mathbb{P}_{\mathrm{FA}}$, for a given τ, can be obtained from the cumulative distribution function (CDF) of the squared matched filter output under $\mathcal{H}_0$ as

$$\mathbb{P}_{\mathrm{FA}} = \frac{\gamma\left(\frac{L}{2},\frac{\tau}{2}\right)}{\Gamma\left(\frac{L}{2}\right)} \tag{3.6}$$

where $\gamma\left(\frac{L}{2},\frac{\tau}{2}\right)$ is the lower incomplete Gamma function, $\Gamma\left(\frac{L}{2}\right)$ is the Gamma function and L is the number of cumulative sums of normal distribution outputs. This corresponds to non-coherently adding several squared matched filter outputs, either from different satellites or time-delayed squared outputs from the same satellite.

While the CFAR should be set to be as low as practical to minimise the occurrence of false detections, this process will necessarily involve a trade-off against the probability of detection, $\mathbb{P}_{\mathrm{D}}$, which is given by

$$\mathbb{P}_{\mathrm{D}} = 1 - \left(1 - Q_{\frac{L}{2}}\left(\sqrt{\Lambda}, \sqrt{\tau}\right)\right) = Q_{\frac{L}{2}}\left(\sqrt{\Lambda}, \sqrt{\tau}\right) \tag{3.7}$$

where $Q_{L/2}\left(\sqrt{\Lambda}, \sqrt{\tau}\right)$ is the Marcum Q-function and Λ is the non-centrality parameter of the non-central chi-squared distribution of the squared matched filter output under $\mathcal{H}_1$ and can be linked to the SNR at the output of the matched filter as

$$\Lambda = \sum_{l=1}^{L} \left(\frac{\mu_l}{\sigma_l}\right)^2 = \sum_{l=1}^{L} \mathrm{SNR}_l \tag{3.8}$$

where μ_l and σ_l are the post matched filter amplitudes of the l^{th} signal and noise respectively.

In this chapter, L is assumed to be 1 as it is considered that the detection is based on a single satellite signal and coherent integration is performed over the entire data block to maximise the resulting SNR at the output of the matched filter. The case where multiple matched filter outputs are added non-coherently to improve the final SNR using a MIMO technique will be analysed in Section 4.3.1. Hence, based on (3.6) to (3.8), the probability of detection for a given CFAR can be obtained as a function of input SNR as shown in Figure 3.3. From the figure, it is indicated that an SNR above 11.7 dB is required at the output of the matched filter for a detection performance corresponding to a $\mathbb{P}_{\mathrm{D}}$ of 90% and a $\mathbb{P}_{\mathrm{FA}}$ of 1%. This performance requirement is reasonably high for an experimental 32-element phased-array GPS bistatic radar receiver due to the limited size of the system and transmission power from the illuminating sources. Usually, an SNR above 13 dB is required for reliable detection or 15 dB for tracking [87], hence requires a $\mathbb{P}_{\mathrm{FA}}$ of 1% for the same $\mathbb{P}_{\mathrm{D}}$. The detection performance can be improved to fulfil military standard requirement if an adequately powerful system (i.e. larger number of elements in the antenna array) is utilised for target detection or tracking in practice.

The output SNR related to the overall receiver gain and loss, G_{R} and G_{LOSS} respectively, is required to detect a fixed size target δ at a given distance can be written as

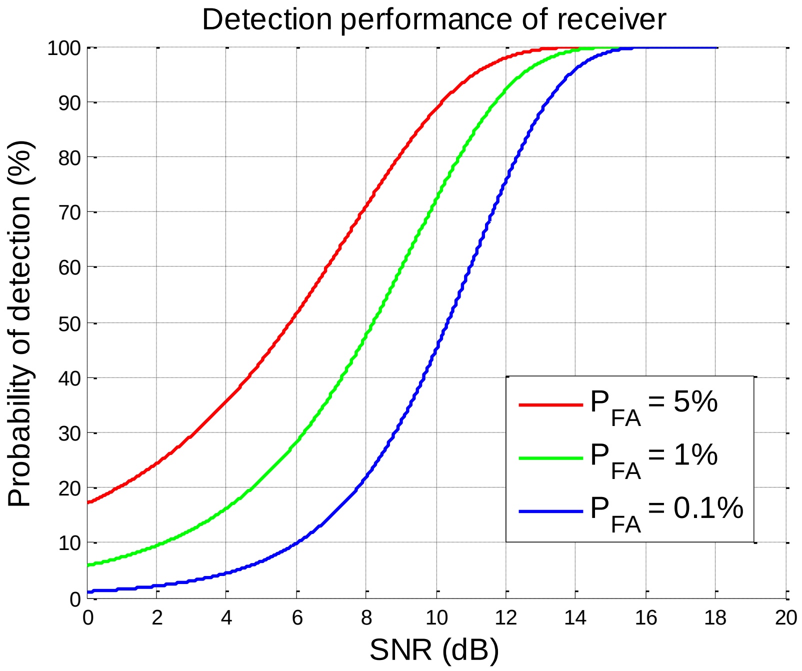

Figure 3.3: Given a certain CFAR, a higher SNR of the input signal results in an improvement of receiver performance in terms of probability of detection.

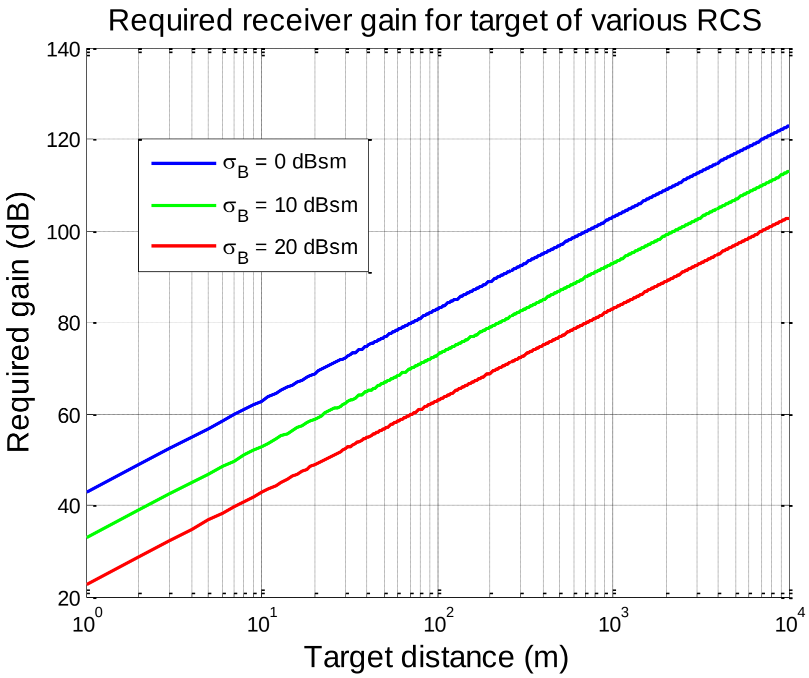

Figure 3.4: Required GPS bistatic radar receiver gain for detecting targets of various RCS, σ_B, while satisfying detection performance of $\mathbb{P}_D = 90\%$ and $\mathbb{P}_{FA} = 1\%$.

$$\mathrm{SNR_{out}} = \mathrm{SNR}_{\delta}\frac{G_{\mathrm{R}}}{G_{\mathrm{LOSS}}} \tag{3.9}$$

Hence, the maximum target detection range can be derived from (3.4) and (3.9) as

$$R_{\mathrm{R}} = \sqrt{\frac{P_{\mathrm{D}}\sigma_{\mathrm{B}}G_{\mathrm{R}}}{4\pi(\mathscr{k}\mathrm{T_A}f_{\mathrm{B}})G_{\mathrm{LOSS}}\mathrm{SNR_{out}}}} \tag{3.10}$$

Using the above detection performance case, the required gains for the radar receiver to detect targets of various RCS at different ranges are summarised in Figure 3.4.

3.3 Background of Phased-array Technique

Since the power levels of GPS signal returns from a target are expected to be extremely weak, a high gain antenna must be utilised by the receiver of a GPS bistatic radar to feasibly perform target detection. Due to the law of conservation of energy, increasing the gain of an antenna will result in reduced coverage. High gain antennas are commonly used by a radar transmitter, receiver or transceiver to provide adequate performance for detecting weak target returns. Examples include a single high-gain antenna such as the parabolic, horn and yagi antenna, or an antenna that is composed by an array of elements, known as a phased-array. Also due to their narrow beamwidth, directional antennas can help a radar system to discriminate signal returns from different directions. However, a beam steering mechanism usually needs to be used with this type of antenna to give the capability of scanning for targets across all directions of interest.

The traditional method of scanning the beam is to mechanically rotate the antenna (i.e. using a motor drive). Electronic scanning broke with tradition by using programmable phase shifters on each antenna element in a phased-array system to steer the beam electronically. While phased-array techniques had already been used in radio transmitters and radars since World War II, the first electronically scanned array radar was believed to be developed by Lincoln lab in the 1950s [88]. It used a 5000-element planar array in a UHF radar with diode-switched phase shifters to perform satellite detection and tracking.

Currently, the electronically scanned array technique has become widely applied in modern military radars, mainly due to its advantages such as

(i) Flexibility in beam pattern synthesis: The shape of the beam pattern is a function of the phase shifter and amplitude setting at each antenna element. It can be optimised to receive signals from certain directions (i.e. beam steering) and reject signals from other directions (i.e. null steering);

(ii) Increased tolerance to component failure as the system will still function if some channels fail;

(iii) Faster beam scanning due to the rapid advance in performance of DSPs and RF components that allow rapid switching.

(iv) Fast beam switching allows multiple functions, such as tracking and surveillance, to be carried out simultaneously.

The overall performance of an electronically scanned array receiver improves with the number of elements. More elements give better control over the beam pattern and SNR detection performance. But this comes at an increased cost due to

(i) More components such as antennas and front-ends;

(ii) Higher processing power in the receiving platform to control the electronic steering mechanism of the array or perform array processing digitally.

Due to its higher cost, this technique is less common in commercial communication or radar applications.

3.3.1 Phased-array Receiver for PBR

Phased-array receivers can be applied to each receiver site of a PBR. Steering a beam in a given direction using phased-array techniques requires controlling the phase of an incoming or departing signal at each element in an array such that the overall beam pattern can be adjusted to focus on a desired direction while attenuating others. As illustrated in Figure 3.5, when a plane wave signal from an illuminating source arrives at the array from a certain DOA, $\boldsymbol{\kappa}_s$ as a function of azimuth angle, θ_s, and elevation angle, ϕ_s, it will have different phase on each element due to the difference in the time-of-arrival. For the special case of a simple plane wave incident upon the array which consists of the incoming signal, $s(k)$, and the AWGN, $n(k)$, with an amplitude of μ_m and σ_n respectively, the input signal model at the m^{th} element becomes

$$x_m(k, \boldsymbol{\kappa}_s) = a_m(\boldsymbol{\kappa}_s)\big(\mu_m s(k) + \sigma_n n(k)\big) \tag{3.11}$$

where $a_m(\boldsymbol{\kappa})$ is the spatial phase factor in the case of a 2-D planar array for plane wave signals, such that

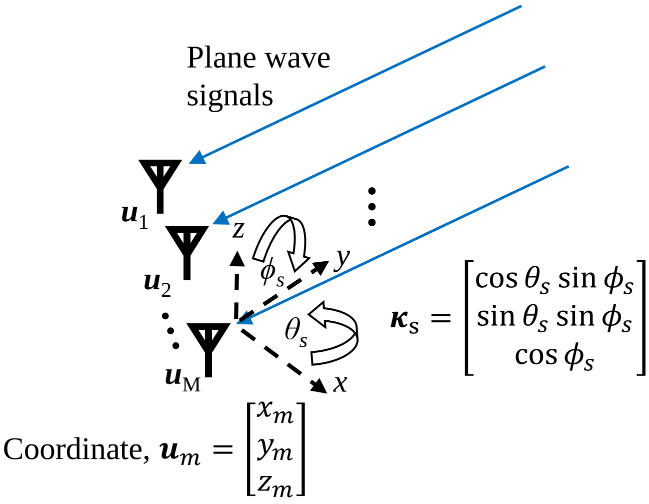

Figure 3.5: Illustration of the arrival of plane wave signals at antenna array.

$$a_m(\boldsymbol{\kappa}_s) = \exp(j\boldsymbol{\kappa}_s{}^{\mathrm{T}}\boldsymbol{u}_m) = \exp\left(j\frac{2\pi}{\lambda_0}\begin{bmatrix} \cos\theta_s \sin\phi_s \\ \sin\theta_s \sin\phi_s \\ \cos\phi_s \end{bmatrix}^{\mathrm{T}}\begin{bmatrix} u_{mx} \\ u_{my} \\ u_{mz} \end{bmatrix}\right) \tag{3.12}$$

where $\boldsymbol{u}_m$ is the 3-D position, relative to the origin in the array (usually the array center), at the m^{th} receiver.

A phased-array receiver forms a complex weighted sum of the antenna outputs. Hence, the output beam of an M-element array, also known as the “beamformer”, becomes

$$\begin{aligned} y(k,\boldsymbol{\kappa}) &= \sum_{m=1}^{M} a_m{}^{*}(\boldsymbol{\kappa}) x_m(k,\boldsymbol{\kappa}_s) \\ &= \boldsymbol{a}^{\mathrm{H}}\boldsymbol{x} \end{aligned} \tag{3.13}$$

where $\boldsymbol{a} = [a_1(\boldsymbol{\kappa}) \quad a_2(\boldsymbol{\kappa}) \quad \cdots \quad a_M(\boldsymbol{\kappa}) \ ]^{\mathrm{T}}$ are the complex weighting coefficients, also known as the beamformer weights.

The choice of $\boldsymbol{a}$ depends on the beamformer design. Initially, the signals can be added in phase from the direction of the beam using the conventional beamformer. The output power of the conventional receiver can be expressed as

$$P_{conv}(\boldsymbol{\kappa}) = E\{y^2(k,\boldsymbol{\kappa})\} = \boldsymbol{a}^{\mathrm{H}}E\{\boldsymbol{x}\boldsymbol{x}^{\mathrm{H}}\}\boldsymbol{a} = \boldsymbol{a}^{\mathrm{H}}\mathbf{Q}_x\boldsymbol{a} \tag{3.14}$$

where $\mathbf{Q}_x$ is the covariance matrix of the receiver outputs.

The phased-array receiver is able to search and identify the DOAs of multiple input signals simultaneously by forming multiple beams across all directions of interest. This is achieved by creating $P_{conv}(\boldsymbol{\kappa})$ over a grid of steering directions. The full DOA search range of a 2-D planar array is between ±180 degrees in azimuth and 0 to 90 degrees in elevation. The complexity of the DOA search will become higher if the numbers of beams and elements increase. A larger aperture results in higher directivity, which gives better signal discrimination but also requires more beams.

The conventional beamformer can be used to improve the SNR of incoming signals and discriminate between them based on their DOA. If the signal on each element has the same amplitude (i.e. $\mu_m = \mu \;\forall\, m$), then the beam output when the array is steered at the signal direction (i.e. $\boldsymbol{\kappa} = \boldsymbol{\kappa}_s$) is given by

$$y(k) = M\,\mu_m + \sum_{m=1}^{M} n(k) \tag{3.15}$$

In this case, the beamformer output power can be expressed as

$$\begin{aligned} E\{|y(k)|^2\} &= M^2\mu^2 + \boldsymbol{a}^{\mathrm{H}} E\{|y(k)|^2\}\boldsymbol{a} \\ &= M^2\mu^2 + \boldsymbol{a}^{\mathrm{H}}\sigma^2\mathbf{I}\boldsymbol{a} \\ &= M^2\mu^2 + M\sigma^2 \end{aligned} \tag{3.16}$$

The final SNR can be improved by a factor, known as the array gain, G_{ARR}. Hence, the SNR of the beamformer output is given as

$$\mathrm{SNR}_{\mathrm{out}} = \frac{M^2\mu}{M\sigma} = G_{\mathrm{ARR}}\mathrm{SNR}_{\mathrm{in}} \tag{3.17}$$

The conventional beamformer can also discriminate between multiple incoming signals from different DOAs, provided the angular separation is larger than the beamwidth of the array beam pattern. If higher angular resolution is required for a fixed number of receivers, higher resolution techniques such as the minimum variance distortionless response (MVDR) or Capon beamformer [89] could be applied. MVDR formulates the search problem to that of minimising the output power subject to unity gain constraint in a clear steering direction κ, expressed as

$$\mathbf{w}^{\mathrm{H}}(\kappa)\boldsymbol{a}(\kappa) = 1 \tag{3.18}$$

By applying the Lagrange multipliers, the weights for the MVDR beamformer become

$$\mathbf{w}(\kappa) = \frac{\mathbf{Q}^{-1}\boldsymbol{a}(\kappa)}{\boldsymbol{a}^{\mathrm{H}}(\kappa)\mathbf{Q}^{-1}\boldsymbol{a}(\kappa)} \tag{3.19}$$

where $\mathbf{Q}$ is the covariance matrix of the receiver outputs. The beamformer output power can be shown to be given by

$$P_{\mathrm{mvdr}}(\kappa) = \frac{1}{\boldsymbol{a}^{\mathrm{H}}(\kappa)\mathbf{Q}^{-1}\boldsymbol{a}(\kappa)} \tag{3.20}$$

3.3.2 Null-Steering

Phased-arrays can not only be used to steer beams at signals, but also nulls in undesired directions. A typical beam pattern of an antenna array that implements the beam and null-steering technique is shown in Figure 3.6. By using the minimum-norm solution shown in (3.21), the null-steering beam pattern can be designed by determining the weight vector for an *M*-element receiving array as

$$\boldsymbol{U}\,\boldsymbol{w} = \begin{bmatrix} \mathbf{a}^{\mathrm{H}}(\boldsymbol{\kappa}_0) \\ \mathbf{a}^{\mathrm{H}}(\boldsymbol{\kappa}_{i1}) \\ \vdots \\ \mathbf{a}^{\mathrm{H}}(\boldsymbol{\kappa}_{i\mathrm{N}}) \end{bmatrix} \boldsymbol{w} = \begin{bmatrix} 1 \\ 0 \\ \vdots \\ 0 \end{bmatrix} \tag{3.21}$$

where $\boldsymbol{a}(\boldsymbol{\kappa}_0)$ is the steering vector for the desired direction and has unity gain and $\boldsymbol{a}(\boldsymbol{\kappa}_i)$ are the non-desired directions which have zero gain, provided that $\mathrm{N} \leq M - 1$ and $\boldsymbol{\kappa}_0 \neq \boldsymbol{\kappa}_i$ to avoid contradiction. Defining the vector, $\boldsymbol{\gamma}$, by

$$\boldsymbol{\gamma} = (\boldsymbol{U}\boldsymbol{U}^{\mathrm{H}})^{-1}[1 \quad 0 \quad \cdots \quad 0]^{\mathrm{T}} \tag{3.22}$$

Hence, the weight vector, $\boldsymbol{w}$ can be shown to be given by

$$\mathbf{w} = \boldsymbol{U}^{\mathrm{H}}\boldsymbol{\gamma} \tag{3.23}$$

3.3.3 Discussion of Phased-array Technique for GPS Bistatic Radar

The performance of MVDR is superior to the conventional beamformer in most applications. However, for a GPS bistatic radar, the target return that is captured by the receiver is generally

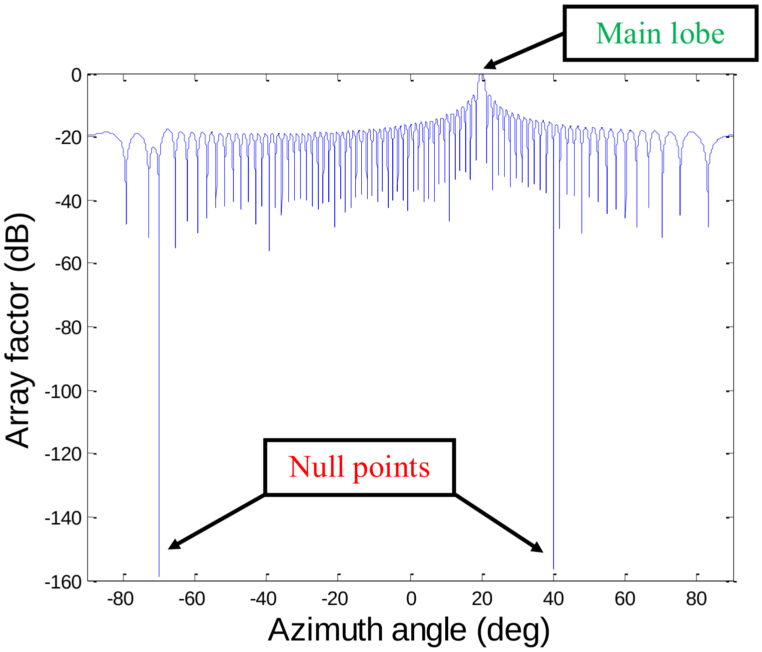

Figure 3.6: Beam pattern of a 8-element ULA showing 2 null directions using the null-steering technique.

noise dominated even after applying long period cross-correlation technique. In that case, the MVDR weights become the same as those for the conventional beamformer and its search process is computationally less efficient than the conventional counterpart. Therefore, the conventional beamforming techniques are more suitable for GPS bistatic radar to perform target searching as there is no benefit in using MVDR.

Phased-arrays can be used to remove the DSI, which is much stronger than the target return by using null-steering technique. This is particularly suited to systems that use ground based illuminators which have a large angular separation from air targets. However in the case of a space-based PBR such as a GPS bistatic radar, there is a high possibility that the DOAs of air targets will coincide with the illuminators, which means that the receiver will not able to search for targets that appear at these directions if the null-steering technique is applied. It also wastes degrees of freedom distorting the beam pattern and amplifying the thermal noise which result in the reduction of receiver’s output SNR. Therefore in this thesis the DSI cancellation process has been performed using a time-domain processing filter rather than the null-steering method.

3.4 Antenna Array Calibration Technique

The full array gain will only be achieved if the array has no gain or phase errors and the positions of the elements are known accurately. In practice, non-idealities in electronic circuits and cable lengths may affect the phase shifts in an antenna array by a factor of $\boldsymbol{\varepsilon} = [\varepsilon_1\ \varepsilon_2\ \dots\ \varepsilon_M]^T$, where ε_m is the multiplicative error contained in the received signal at the mth element relative to the reference channel of the array shifted by a phase of φ_m. Hence, the output of the conventional beamformer in the presence of phase errors becomes

$$y(k) = \sum_{m=1}^{M} \mu_m s_m(k, \boldsymbol{\kappa}_s)\, \epsilon_m a_m(\boldsymbol{\kappa}_s)^* + n_m(k) \tag{3.24}$$

where

$$\epsilon_m = \exp(j\varphi_m) \tag{3.25}$$

The expression in (3.24) implies that the signals of all elements in the array will no longer be coherently summed due to the introduction of phase errors at each channel. Typically a known calibration signal can be used to measure the phase error in the array.

3.4.1 Background

The traditional method of estimating phase errors in an antenna array is to use a signal generator that splits a given signal coherently and send each output to all the front-ends in the array. This method also requires the signal splitter to be properly calibrated. Then, the phase error can be determined from the phase difference between the signals at each channel. However, this method assumes that the phase errors in the array will remain fixed and it must be performed prior to the operation of the system.

In practice, the phase parameters of the array system might be time-varying, especially for space based and airborne applications where significant changes to ambient conditions may affect the behaviour of the system. Therefore, these applications require a calibration technique that can monitor the phase condition of the system continuously to ensure that these parameters can be compensated during operation.

Online calibration can be achieved by transmitting a calibration signal [90, 91]. Typically the directions of the calibration sources are not known and need to be estimated as part of the calibration process. Techniques for calibrating mutual coupling, positions errors and array phase errors have been studied in [92].

For the case of GPS bistatic radar, the directions of the GPS signal sources are known but the attitude of the array needs to be determined. A number of calibration algorithms have been introduced in the literature for calibrating GPS receiving arrays. Backén *et al.* [93] provided an algorithm for gain-phase calibration in each channel of a 7-element GPS antenna array system using a least squares estimator (LSE) model that incorporates the positions of all available satellites. Xu *et al.* [94] extended the antenna array calibration process to incorporate estimation of the array orientation and mutual coupling effects using the maximum-likelihood method to further mitigate these errors. This algorithm was applied by Trinkle *et al.* [95] to calibrate the phase error in each channel of a circular array configuration receiver error for a GNSS Environment Monitoring System (GEMS) as well as to determine the 2-D orientation change of the receiving array (i.e. yaw angle variation from reference axis).

Attitude determination using GPS signals has also been applied for the Joint Precision Approach and Landing System (JPALS) of an aircraft carrier [96] using the array calibration technique proposed by De Lorenzo *et al.* [97]. This technique is described as being able to determine the 3-D orientation of a GPS antenna array using a search-based ambiguity resolution algorithm for the case where the separation between antennas is multiple numbers of wavelengths apart.

Phased-arrays for the GPS bistatic radar would typically use relatively small inter-elements spacings (i.e. inter-element spacing not exceeding one wavelength of carrier signal). Therefore, the calibration technique for this type of antenna array does not require the ambiguity resolution search. However, the antenna array calibration technique must be able to determine the 3-D orientation since the plane of the antenna array is likely to be tilted at an optimum angle for signal reception of the receiver from the patch of sky that is likely occupied by the air targets. Hence, a calibration technique that determines the phase errors and the 3-D orientation of an antenna array using GPS signals will be discussed in the following section.

Note that in the absence of an algorithm to determine the attitude of the array panel, the alignment can be made with the aid of a magnetic compass and a levelling tool for measuring orientation and tilt angles respectively. However, using a compass to determine the orientation angle will suffer from magnetic declination (i.e. an error in the angle between the true and magnetic North). Since this declination varies with time and location, it would need to be precisely acquired during calibration of the phased-array system.

3.4.2 Phase Error Calibration for GPS Bistatic Radar

The following two sections describe an array calibration algorithm that incorporates estimation of the 3-D orientation of the phased-array, including both the yaw and pitch angles. The assumed 3-D array geometry is shown in Figure 3.7 and Figure 3.8. A yaw angle, θ_e, is defined as a rotation about the *z*-axis, while a pitch angle, ϕ_e, is defined as a rotation about the *x*-*y* plane. Note that the array could be further rotated about its normal axis (roll angle) but this parameter is not included in this study as the array panel was unlikely to be rotated in this dimension for experiments carried out in this work, due to it being mounted on the roof of a stationary vehicle.

The direct-path signals from the LOS GPS satellites can be utilised by a phased-array GPS bistatic radar receiver as the signal sources to provide solutions for the calibration process. The receiver must perform long coherent integration of the GPS signals at each array channel individually to minimise noise fluctuations during the phase estimation.

The measured phase of signal at the m^{th} channel relative to the reference channel (i.e. m = 1), ξ_{lm}, can be modelled as the product of the phase error, ε_m, and a spatial phase factor corresponding to the DOA of l^{th} GPS satellite, $a_m(\boldsymbol{\kappa}_l)$, and is given by

$$\xi_{lm} = \epsilon_m a_m(\boldsymbol{\kappa}_l) \tag{3.26}$$

If only a single signal source is used to perform calibration, then the phase error at m^{th} channel, ε_m, can be estimated directly from (3.26). Applying multiple signal sources for array calibration will result in redundant channel phase error estimates. In this case, the least squares estimator (LSE) can be applied to provide an optimised solution that minimises the sum of the squares of errors from the estimated phase errors at the m^{th} channel as

$$\epsilon_m = \left(\mathbf{X}_m{}^{\mathrm{T}}\mathbf{X}_m\right)^{-1}\mathbf{X}_m{}^{\mathrm{T}}\boldsymbol{\xi}_m \tag{3.27}$$

where $\mathrm{X}_m = [a_m(\boldsymbol{\kappa}_1)\ a_m(\boldsymbol{\kappa}_2)\ ...\ a_m(\boldsymbol{\kappa}_L)]^{\mathrm{T}}$ and $\boldsymbol{\xi}_m = [\xi_{1m}\ \xi_{2m}\ \ldots\ \xi_{Lm}]^{\mathrm{T}}$ for L calibrating sources.

To apply (3.26) and (3.27), the location of the l^{th} GPS satellite and the radar receiver must be known such that $a_m(\boldsymbol{\kappa}_l)$ can be precisely determined. In practice, the location of radar receiver can be acquired using the position information estimated by a conventional GPS receiver that is co-located with the system. From Figure 3.9, the DOAs of GPS satellites can be acquired from the ephemeris given by an advanced satellite tracking algorithm developed by NASA/NORAD called “JSatTrak” [98] based on the accurate location of the receiver and time of the calibration process.

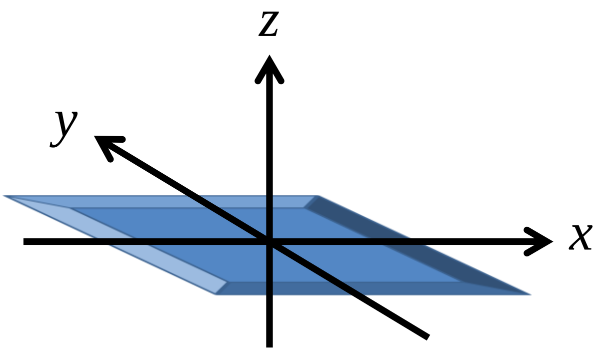

Figure 3.7: Geometry of phased-array antenna panel in 3-D coordinates.

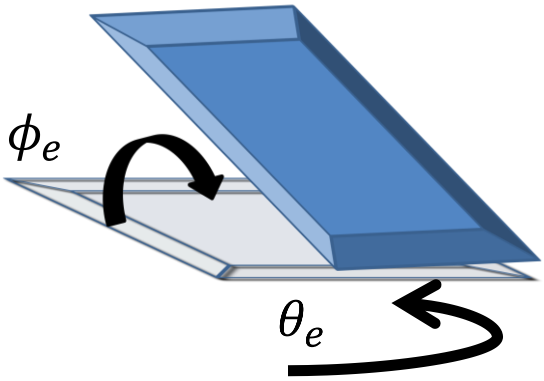

Figure 3.8: Orientation of phased-array panel with respect to the original configuration.

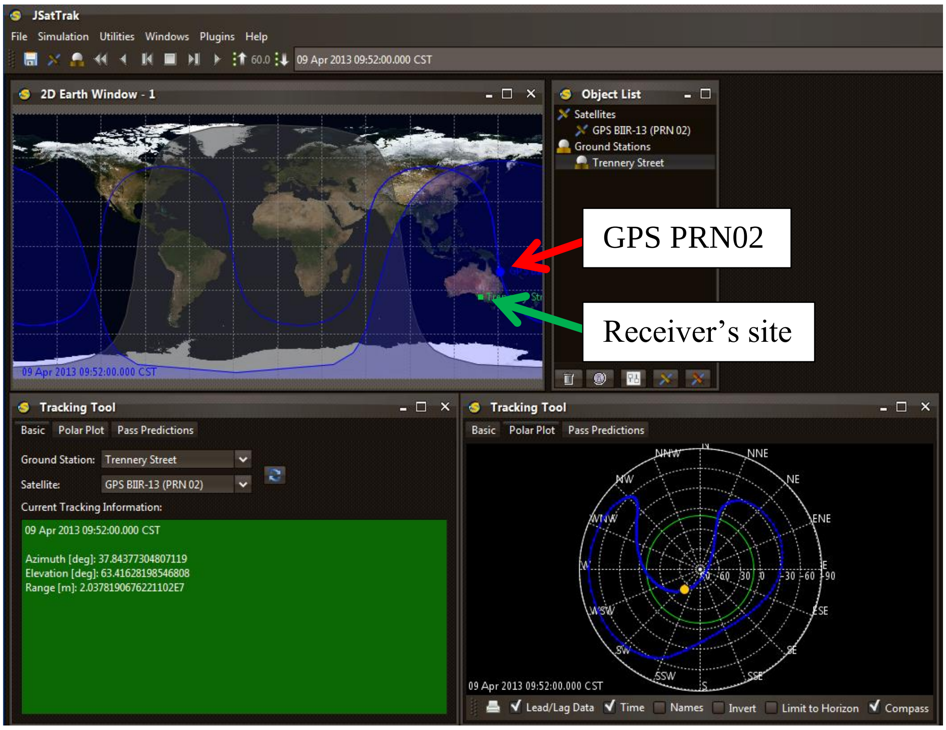

GPS PRN02

Receiver's site

Ground Station: Trennery Street
Satellite: GPS BIIR-13 (PRN 02)
Current Tracking Information:

09 Apr 2013 09:52:00.000 CST

Azimuth [deg]: 37.84377304807119
Elevation [deg]: 63.41628198546808
Range [m]: 2.0378190676221102E7

Figure 3.9: Satellite tracking program "JSatTrak" showing the orbit (Top), range, azimuth and elevation angles information (Bottom Left) and polar plot (Bottom Right) of GPS PRN02 from a receiver position near Adelaide airport (Courtesy Shawn Gano).

3.4.3 Attitude Calibration of Receiving Array for GPS Bistatic Radar

A previous GPS array calibration technique applied in [94] assumed that the array was horizontal and only the orientation was unknown. This calibration is carried out by compensating for the orientation error, θ_e, in the spatial phase factor of the l^{th} calibration source, $a_{lm}(\boldsymbol{\kappa}_l)$, as follows

$$a_{lm}(\boldsymbol{\kappa}_l) = \exp\left(j\frac{2\pi}{\lambda_0}\begin{bmatrix}\cos(\theta_l-\theta_e)\sin\phi_l \\ \sin(\theta_l-\theta_e)\sin\phi_l \\ \cos\phi_l\end{bmatrix}^{\mathrm{T}} \boldsymbol{u}_m \right) \tag{3.28}$$

This model is suitable for ground based omni-directional arrays that typically use multiple elements and scan for interferences on ground level. For arrays searching for air targets that use patch antennas, the array might be tilted to get a better return from the direction of target returns. Hence, there is a need to estimate both the yaw and pitch angles of the array defined in Figure 3.8.

In the case where the attitude of antenna array is altered by an angle about the y-axis, ϕ_e, the position of m^{th} element relative to the origin of array will become

$$\boldsymbol{u}'_m = \begin{bmatrix} u'_{mx} \\ u'_{my} \\ u'_{mz}\end{bmatrix} = \begin{bmatrix}\sqrt{{u_{mx}}^2+{u_{mz}}^2}\cos(\phi_e+\phi') \\ u_{my} \\ \sqrt{{u_{mx}}^2+{u_{mz}}^2}\sin(\phi_e+\phi')\end{bmatrix} \tag{3.29}$$

for $$\phi' = \begin{cases} 2\arctan\dfrac{u_{mz}}{\sqrt{{u_{mx}}^2+{u_{mz}}^2}+u_{mx}}, & u_{mx}>0 \text{ or } u_{mz}\neq 0 \\ \pi, & u_{mx}<0 \text{ and } u_{mz}=0\end{cases}$$

In the presence of yaw angle that corresponds to the rotation of the pitched antenna array about the z-axis, θe, the position of m^{th} element relative to the origin of array will become

$$\boldsymbol{u}''_m = \begin{bmatrix} u''_{mx} \\ u''_{my} \\ u''_{mz}\end{bmatrix} = \begin{bmatrix}\sqrt{{u'_{mx}}^2+{u'_{my}}^2}\cos(\theta_e+\theta') \\ \sqrt{{u'_{mx}}^2+{u'_{my}}^2}\sin(\theta_e+\theta') \\ u'_{mz}\end{bmatrix} \tag{3.30}$$

for $$\theta' = \begin{cases} 2\arctan\dfrac{u_{my}}{\sqrt{{u_{mx}}^2 + {u_{my}}^2} + u_{mx}}, & u_{mx} > 0 \text{ or } u_{my} \neq 0 \\ \pi, & u_{mx} < 0 \text{ and } u_{my} = 0 \end{cases}$$

While this approach could be extended to also determine the roll angle corresponding to the rotation of the antenna array about the normal of the array, this step was not required for the land-based radar receiver. This kind of rotation is more likely to occur on a phased-array system that is onboard a flying aircraft.

The expression for the spatial phase factor of the m^{th} element for the l^{th} calibrating source in the presence of orientation variation of ϕ_e and θ_e becomes

$$a_{lm}(\boldsymbol{\kappa}_l) = \exp\left(j\frac{2\pi}{\lambda_0}\begin{bmatrix}\cos\theta_l \sin\phi_l \\ \sin\theta_l \sin\phi_l \\ \cos\phi_l\end{bmatrix}^{\mathrm{T}} \begin{bmatrix} u''_{mx} \\ u''_{my} \\ u''_{mz}\end{bmatrix}\right) \tag{3.31}$$

Since the orientation angles of the antenna array are unknown, an iterative search over (3.31) that corresponds to $\boldsymbol{u}''_m$ across all possible ϕ_e and θ_e must be performed in the LSE calibration model (3.27). The final outcomes of both the phase errors, $\boldsymbol{\varepsilon}$, and positions of elements, $\boldsymbol{u}''$, relative to the reference element for the antenna array is determined by the ϕ_e and θ_e values that correspond to the smallest least-squares error based on the sum of least-square errors of all channels in the array as

$$(\hat{\boldsymbol{\epsilon}}, \hat{\boldsymbol{u}}'') = \underset{\phi_e, \theta_e}{\arg\min} \sum_{m=1}^{M} \sum_{l=1}^{L} (\xi_{lm} - X_{lm}\epsilon_m)^2 \tag{3.32}$$

Assuming the search step size of 1°, the iterative search space will not be extremely large as it is bounded by angles between ±90° for ϕ_e and ±180° for θ_e. Hence, this search solution can be feasibly applied for the array calibration if adequate computational power is provided for the radar receiver. The summary of the attitude calibration process for a receiving array incorporating the LSE for determining the inter-channel phase errors is illustrated using a flowchart in Figure 3.10.

3.5 Target Verification and Identification Process

The modulation information of the direct-path signal typically needs to be obtained before target detection in PBR systems. The scattered signals are correlated with this information as

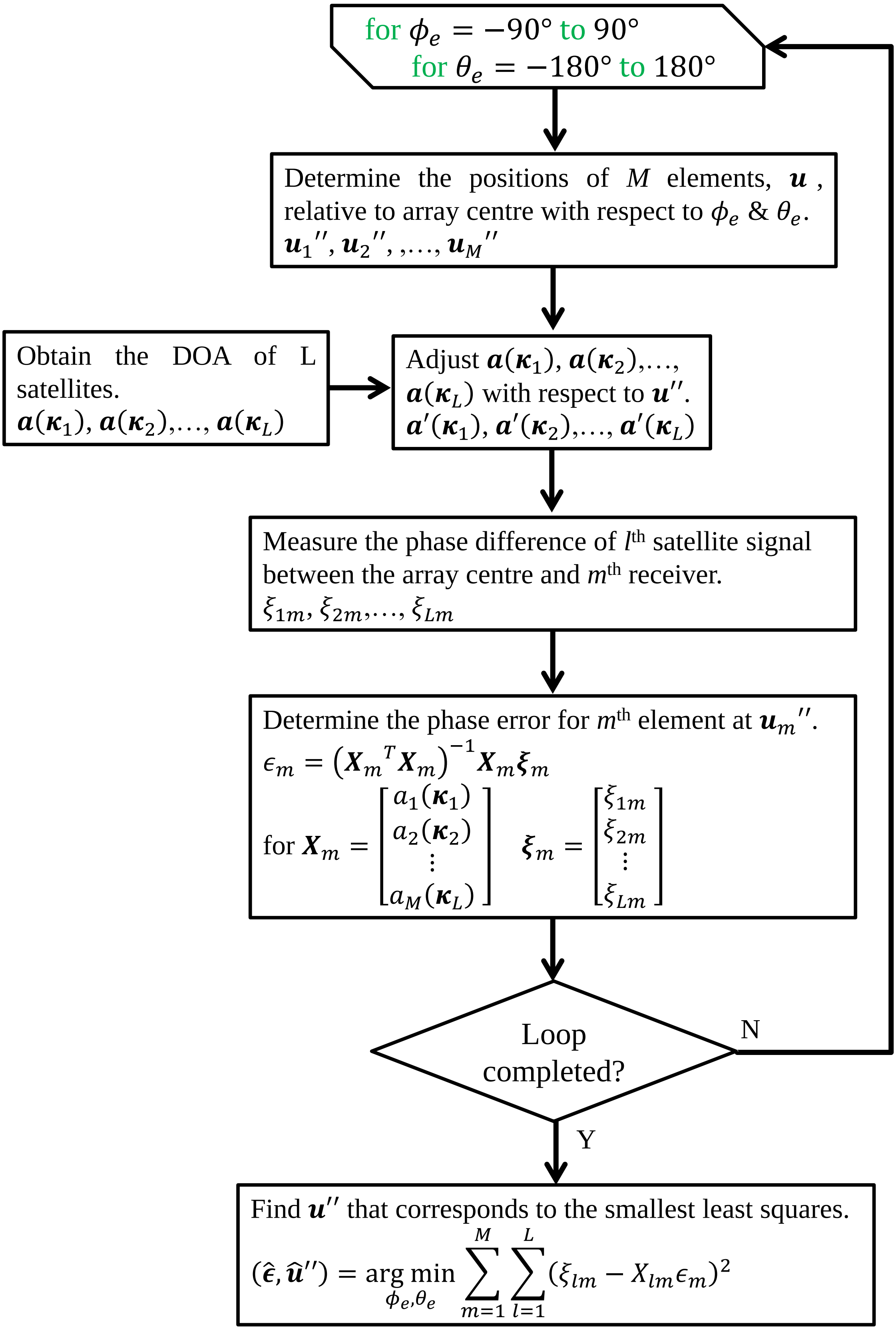

Figure 3.10: Flowchart of the attitude calibration process for a receiving array incorporating the LSE for determining the inter-channel phase errors.

they are delayed in time due to the additional propagation path and shifted in frequency as a result of the additional Doppler shift due to the target's motion. While air target detection approaches using GPS bistatic radar have been proposed by [21, 36], the implementation of a phased-array technique in this area is novel. Hence, the contribution of array processing techniques for GPS bistatic radar will be discussed in this section. Assuming that the Doppler and code phases of direct-path signals are acquired successfully, the methods of performing target detection for a phased-array GPS bistatic radar involve target scattering signal scanning and parameter estimation.

In this thesis, the term 'phased-array technique' will refer to a two stage target position estimation process, where a phased-array is used initially to steer a beam at the target. Then, the target reflection from each GPS satellite is detected independently using a code-Doppler search. This is in contrast to the 'MIMO techniques' discussed in Chapter 4, which jointly process the target reflections from all GPS satellites in the detection process.

3.5.1 Target Detection Modelling

This section introduces the mathematical model for the bistatic radar configuration assumed in the remainder of this thesis. Based on the geometry of a bistatic triangle that is formed by the direct propagation and target scattered path as illustrated in Figure 3.1, the target scattering signals always appear as a delayed version of the direct-path signal as $R_D < R_T + R_R$. In the case of GPS bistatic radar, the relationship between the modulation content of the δ^{th} target, $C_\delta(k)$, and the direct-path and scattered signal can be expressed as

$$C_\delta(k) = C_D(k - k_\delta) \tag{3.33}$$

Apart from the propagation delay, the motion of the air target also results in a change in displacement relative to the transmitter, R_{TX}, and receiver, R_{RX}, in time. Hence, these factors vary the Doppler shift of the scattered signal relative to the direct-path signal. Therefore, in a bistatic radar detection case where both the transmitter and receiver are stationary, the Doppler frequency of the target is denoted as

$$f_\delta = \frac{1}{\lambda_0}\frac{d}{dt}(R_{TX} + R_{Rx}) = \frac{2V}{\lambda_0}\cos\psi\cos\left(\frac{\beta}{2}\right) \tag{3.34}$$

where the target velocity can be expressed by its magnitude, V, and aspect angle relative to the bistatic bisector, δ, shown in the illustration in Figure 3.1.

In the case of non-stationary transmitters such as GPS satellites, the motion of the transmitter also contributes to the Doppler shift of the scattered target signal. As a result, the Doppler frequency of the received target return consists of three Doppler frequency components as follows

$$f_\delta' = f_{\delta-TX} + f_{\delta-RX} + f_{TX-\delta} \tag{3.35}$$

where $f_{\delta-TX}$ and $f_{\delta-RX}$ are the Doppler shifts due to the motion of target in relation to the transmitter and receiver respectively while $f_{TX-\delta}$ is the Doppler shift due to the motion of the transmitter in relation to the target position. It should be noted that $f_{TX-\delta}$ cannot be predicted unless the orbital model of GPS satellites are known precisely. To simplify the problem, $f_{TX-\delta}$ can be approximated by the Doppler frequency of the direct-path signal, f_D, relative to the receiver as the angles of the targets and receiver relative to any GPS satellite are almost the same since both the direct-path and transmitter-to-target path is several orders of magnitude larger than the target-to-receiver path. As a result, the Doppler frequency of the target scattering signal in a GPS bistatic radar detection case can be modelled as

$$f_\delta' \approx f_D + f_\delta = f_D + \frac{2V}{\lambda_0}\cos\psi\cos\left(\frac{\beta}{2}\right) \tag{3.36}$$

Therefore, f_δ becomes the frequency-difference-of-arrival (FDOA) between the direct-path and scattered signal.

By incorporating both the propagation delay and Doppler shift of the target scattering signal relative to direct-path signal of the l^{th} satellite, the relationship between both of these signals can be expressed using the ambiguity function as

$$\mathcal{R}_l(k_{\delta l}, f_{\delta l}) = \sum_{k=0}^{K-1} C_l(k)\, {C_l}^{\mathrm{H}}(k - k_{\delta l}) \exp(j2\pi f_{\delta l} k) \tag{3.37}$$

Given the above relationship, a series of matched filters that consist of the locally generated PRN code (3.33) and a limited range of Doppler frequencies can be applied to cross-correlate with the demodulated input signals across different sample delays to form a cross ambiguity function (CAF). However, the sole reliance on the matched filter technique might not provide sufficient SNR to reach the minimum sensitivity requirement of the receiver without using a high gain antenna model. Hence, the array processing technique can serve as a viable solution to further increase the SNR of the target.

For an *M*-element phased-array receiver, the CAF is generated individually for each element. The conventional beamforming technique can be implemented into the cross ambiguity function by applying the conventional beamformer to each Doppler frequency and sampled code delay bin. A decision has to be made on the choice of the steering vector that corresponds to the highest beampower in each bin to generate a "combined elements cross ambiguity function" (CCAF) from the l^{th} satellite detection, which is denoted as

$$\mathcal{R}_{Cl}(k_\delta, f_\delta) = \max\Big(\mathbf{A}^{\mathrm{H}}\boldsymbol{\mathcal{R}}_l(k_{\delta l}, f_{\delta l})\Big) \tag{3.38}$$

where

$$\mathbf{A} = \begin{bmatrix} \mathrm{a}_1(\boldsymbol{\kappa}_1) & \mathrm{a}_1(\boldsymbol{\kappa}_2) & \ldots & \mathrm{a}_1(\boldsymbol{\kappa}_\alpha) \\ \mathrm{a}_2(\boldsymbol{\kappa}_1) & \mathrm{a}_2(\boldsymbol{\kappa}_2) & \cdots & \mathrm{a}_2(\boldsymbol{\kappa}_\alpha) \\ \vdots & \vdots & \ddots & \vdots \\ \mathrm{a}_M(\boldsymbol{\kappa}_1) & \mathrm{a}_M(\boldsymbol{\kappa}_2) & \ldots & \mathrm{a}_M(\boldsymbol{\kappa}_\alpha) \end{bmatrix} \qquad \boldsymbol{\mathcal{R}}_l(k_{\delta l}, f_{\delta l}) = \begin{bmatrix} \mathcal{R}_{l1}(k_{\delta l}, f_{\delta l}) \\ \mathcal{R}_{l2}(k_{\delta l}, f_{\delta l}) \\ \vdots \\ \mathcal{R}_{lM}(k_{\delta l}, f_{\delta l}) \end{bmatrix} \tag{3.39}$$

where α is the number of beams applied for the DOA search.

As only the maximum value for each Doppler and delay bin is taken over all possible angles, there is a possibility of stronger targets masking weaker ones with the same Doppler and delay. Choosing multiple widely separated transmitters and receivers can overcome this ambiguity. Alternatively, this issue could also be addressed by handling multiple detections over all possible angles in each Doppler and delay bin.

3.5.2 Simulation Example of Target Detection

A simulation was performed using the GPS bistatic radar target detection model in the previous section to search for an air target. This scenario was set up to include a GPS transmitter and an air target that are around 20,000 km and 200 m away from a ground based receiver, respectively. The target is flying towards an arbitrary direction at a constant velocity of 300 m/s and DOA of $[\theta; \phi] = [45; 54.7]°$ from the receiver. Note that the 200 m target distance nearly reaches the detection range limit of the experimental 32-element phased-array receiver described in Chapter 5. The size of a radar receiver can be increased to detect targets from much greater, yet practical ranges.

The model of the input signal at the receiver, x(k), consists of the demodulated direct-path signal, the target scattering signal that is shifted in time and frequency relative to the former as a result of propagation delay and Doppler shift respectively and AWGN.

$$x(k) = \mu_D\, C(k) + \mu_\delta\, C(k - k_\delta) \exp\left(j2\pi \frac{f_\delta}{f_s} k\right) + n(k) \tag{3.40}$$

where k_δ is the TDOA between the scattered and direct-path signal, Δt, rounded to the nearest sample.

$$\begin{aligned}\Delta t &= \frac{1}{c}(R_T + R_R - R_D) \\ &= \frac{|\boldsymbol{p}_{TX} - \boldsymbol{p}_\delta| + |\boldsymbol{p}_{RX} - \boldsymbol{p}_\delta| - |\boldsymbol{p}_{TX} - \boldsymbol{p}_{RX}|}{c}\end{aligned} \tag{3.41}$$

where $\boldsymbol{p}_{TX}$, $\boldsymbol{p}_{RX}$ and $\boldsymbol{p}_\delta$ are the 3-D position of transmitter, receiver and target respectively expressed in Cartesian form, such that

$$\boldsymbol{p} = \begin{bmatrix} p_x \\ p_y \\ p_z \end{bmatrix} \tag{3.42}$$

For a discrete process, this TDOA was rounded to the nearest sample delay, such that

$$k_\delta = \left\lfloor \frac{\Delta t}{f_s} + 0.5 \right\rfloor \leq 0 \tag{3.43}$$

The FDOA, f_δ, between the direct-path and scattered signal can be estimated using model (3.34).

In the simulations, the sampling rate was set to 4 times the C/A code chipping rate, i.e. 4.092 MHz. The initial simulation investigates the effect of varying the integration time on the properties of the CAF. As such, the target RCS and propagation loss are not included in the model and the scattered signal is set to be 10 dB lower than the direct path signal. In practice, it will be much lower and a DSI removal technique is required.

The Doppler search process was performed at a frequency resolution of 1 Hz from −1.5 to 1.5 kHz and a range resolution of 1 sample bin from 0 to 20 sample delays. To reduce the complexity of the search process, a downsampling process was applied to the input data using a decimator to reduce the bandwidth to be just larger than the highest frequency search range to avoid aliasing. A Hanning window function was also applied to the input data to suppress sidelobes that might distort the much weaker target return at small frequency and time offsets.

Three integration periods were considered consisting of 10, 30 and 100 C/A code periods with only a single receive antenna used. As observed from Figure 3.11, longer integration times give better Doppler resolution which help separate the target return from the direct path signal in frequency.

In practice, a radar is designed to detect targets at much further distances than the scenario for this simulation. Hence, the target returns are most likely much further apart in both time and Doppler and can be more readily separated. However, a higher frequency resolution is still important in the case of multipath or multiple targets with similar delays. Thus larger integration times not only improve the SNR of the target, but also help discriminating between targets and DSI or other targets.

Next, a more realistic scenario were considered which was more similar to the target detection experiments that were performed. The SNR was adjusted to model a target with an RCS of 100 m^2 at 200 m from the receiver, which uses antenna elements with a gain of 8 dBi. Two simulation cases with different target SNR were made and tabulated in Table 3.1.

Particular	Direct-path SNR (dB)	Target SNR (dB)
Sim 1	−20	−52
Sim 2		−30

Table 3.1: List of simulation cases using different expected target SNR.

For the Sim 1 case, the expected SNR of the scattered signal is −52 dB and it is 32 dB below the direct-path signal. For such a low SNR level, the integration gain alone was not sufficient to detect the target and an array was used to increase the SNR. Hence, a 32-element antenna array equivalent to the experimental hardware layout configuration as described in Chapter 5 was simulated. The attitude of antenna array is also set to an elevation of 45 degrees and an orientation angle of −30 degrees. The array processing technique was implemented by applying conventional beamforming to each frequency and sample delay bin of the CAFs from all elements. The beamformer output at the DOA that corresponds to the highest beampower was used to form the CCAF. This DOA information is also useful for further processing that can exploit the direction estimate of the target from the receiver.

A comparison has been made between the correlation results of single element and 32-element receiver at the 1st sample delay in Figure 3.12. It can be observed that the former only shows the direct-path signal return and no other return can be identified due to the relatively strong background noise. In contrast, the latter result shows a significant reduction of background noise as well as a target return at −170 Hz. To further demonstrate that the search process works properly, the output beampower that corresponds to the frequency and sample delay bin of the

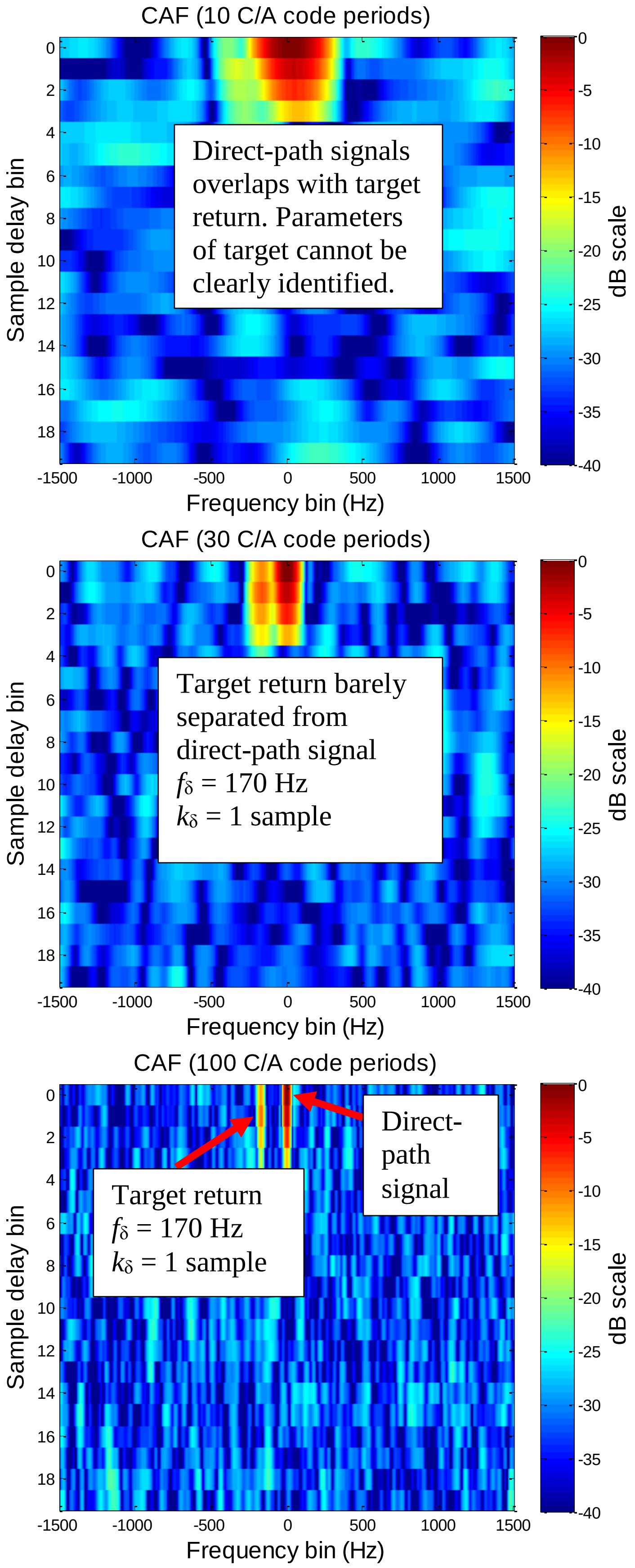

CAF (10 C/A code periods)

Direct-path signals overlaps with target return. Parameters of target cannot be clearly identified.

CAF (30 C/A code periods)

Target return barely separated from direct-path signal
f_δ = 170 Hz
k_δ = 1 sample

CAF (100 C/A code periods)

Target return
f_δ = 170 Hz
k_δ = 1 sample

Direct-path signal

Figure 3.11: Normalised CAF of GPS bistatic radar from simulation search process using integration process of 10, 30 and 100 C/A code periods (Top to bottom).

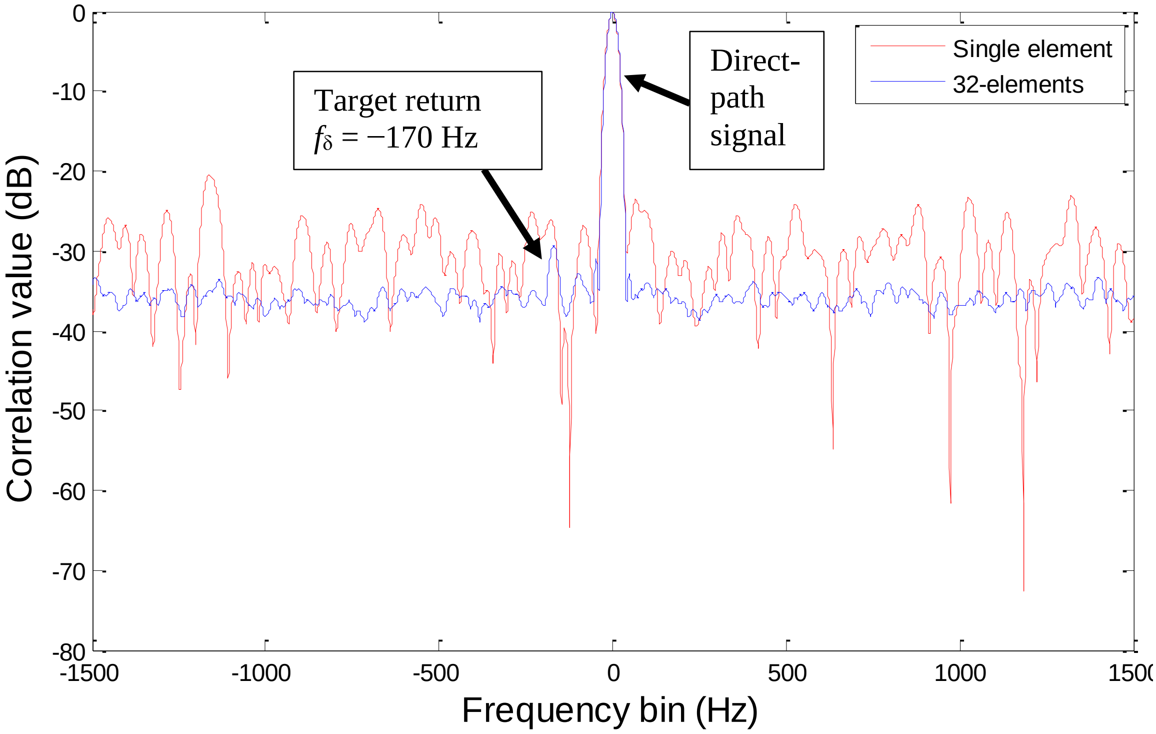

Figure 3.12: Correlation value at 1st sample delay vs. frequency difference at output of single element vs. 32-element receiver.

target is also extracted as shown in Figure 3.13. This result indicates the highest return appears at the DOA of the target. However, the CCAF result from Figure 3.14 shows other correlations corresponding to the sidelobes of the direct-path signal which have power levels comparable to the target return.

For the Sim 2 case, the target power was altered to be −10 dB below the direct-path signal while retaining the same noise level. As shown in Figure 3.15, the CCAF result indicates no correlation other than direct-path signal which is significantly stronger than the target return. This analysis suggested that it is essential to remove or reduce the direct-path signals broadcast by all GPS satellites using a signal cancellation technique to prevent these components from interfering with the target return or appearing as false targets.

There are other conditions such as fluctuation of target RCS at different angles, multiple GPS satellites and variation of target location across time that leads to a changing Doppler shift and power return. These are not included in the simulation as these factors increase complexity without adding further insight into the problems caused by the direct-path signal. The analytical work of real target detection for GPS bistatic radar will be carried in Chapter 5 along with the signal cancellation technique that is previously proposed.

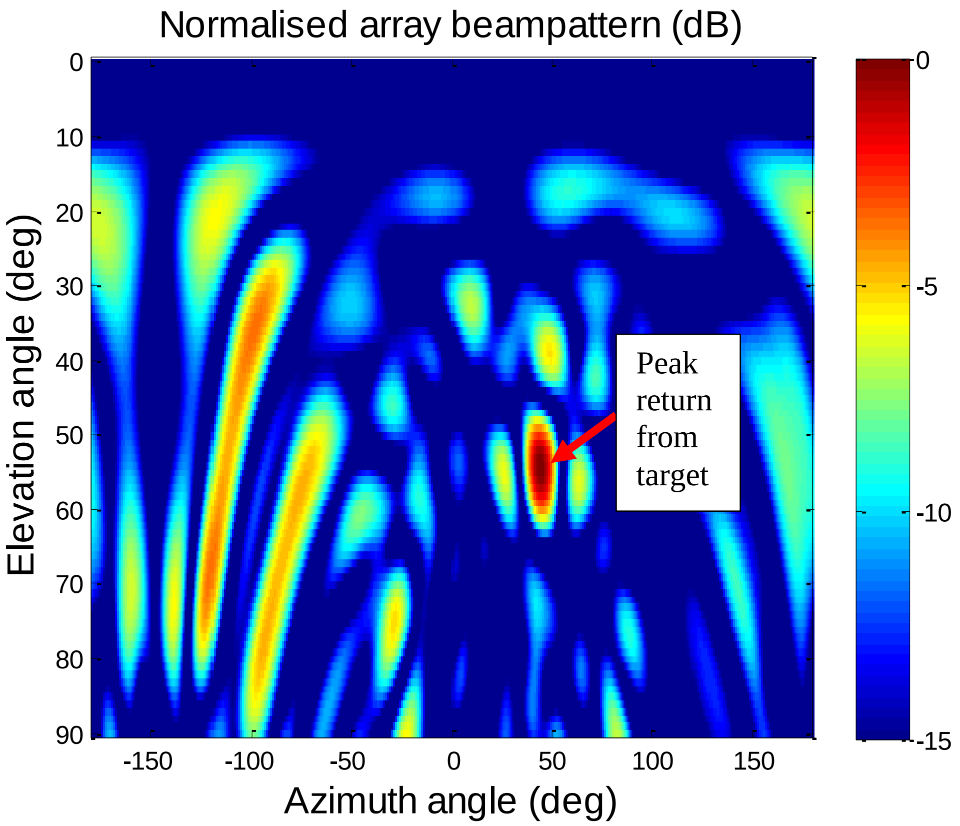

Figure 3.13: Beampower of 32-element receiver for target scattering signal at $f_\delta = -170$ Hz and $k_\delta = 1$. The maximum power appears at a target DOA of $\theta_\delta = 54°$ and $\phi_\delta = 45°$.

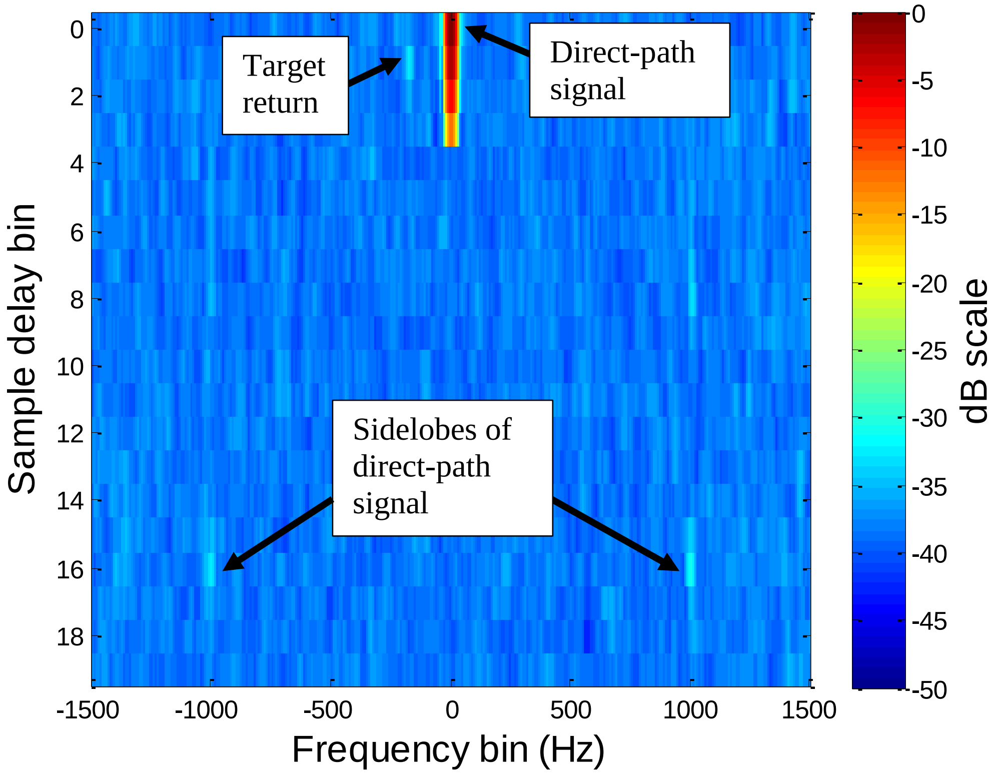

Figure 3.14: CCAF from a GPS bistatic radar single target detection scenario (Sim 1).

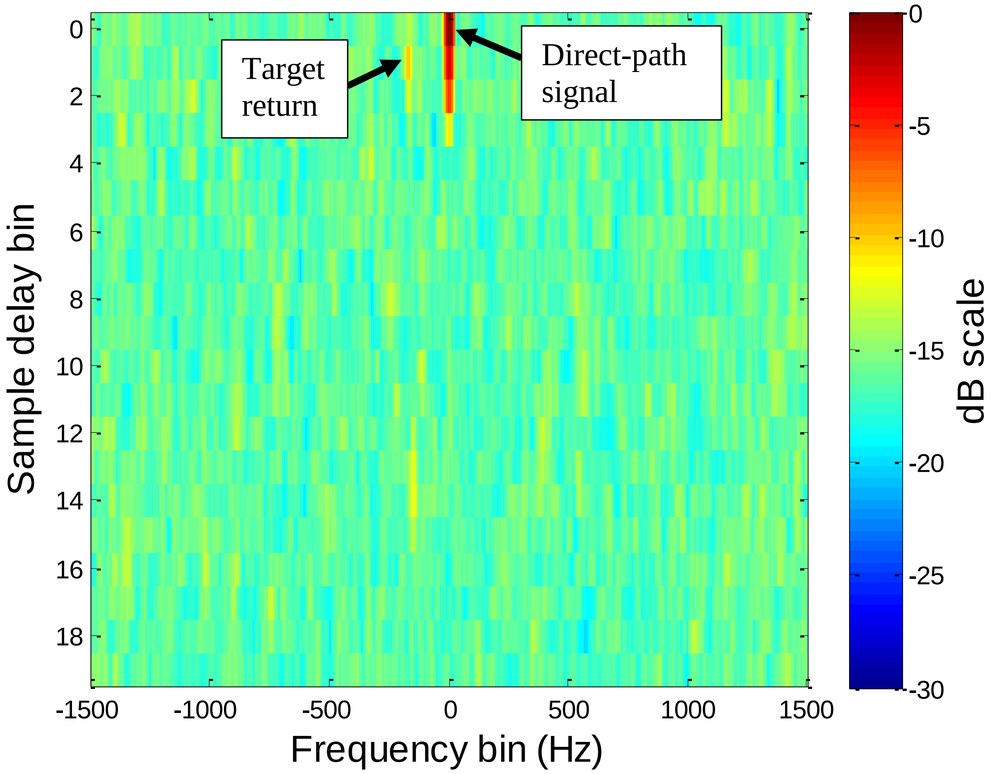

Figure 3.15: CCAF from a GPS bistatic radar single target detection scenario (Sim 2).

3.5.3 Target Parameter Estimation

This section considers how the Doppler and TDOA measurements from multiple CCAFs can be used to determine the target position and velocity. However, the TDOA and FDOA of a target return obtained from correlating every satellite will not be considered since these parameters are determined by individual geometric conditions of each satellite. As a matter of fact, the combined target parameter estimation process will become more challenging when multiple targets appear within the search range of the receiver, since this would result in multiple returns in each CCAF.

When a high correlation value in the CCAF is positively identified as a target return, the corresponding sample delay and frequency difference relative to the direct-path signal return can be used for estimating the range and velocity of the target. The same parameters obtained from the correlation process of multiple transmitters can be used to estimate the position and velocity of the target.

The parameters for each return must be associated with the correct target prior to being combined for individual target parameter estimation. The signal DOA can be used to identify which target the signal belongs to. This DOA can be obtained from the direction of the maximum beampower in the CCAFs (3.38). In the case where multiple targets appear at a common direction and velocity relative to the receiver, TDOA readings can be used to separate targets since the TDOA for targets closer to the receiver will always be smaller, unless the forward scatter geometry condition is approached.

When the targets are independently identified, they can be tracked separately by steering the beam of the antenna array to the direction of each target individually, followed by performing another correlation process. This technique suppresses the power level of the direct-path signals and other target returns that are located outside the coverage of the main beam such that the designated target can be tracked more precisely. The signals that share the same DOA as the designated target will still appear, and need to be discriminated by their sample delays and FDOAs.

The correlation process performed by the l^{th} satellite yields the "beamformer cross ambiguity function" (BCAF) that is expressed as

$$\mathcal{R}_{Bl}(k_{\delta l}, f_{\delta l}) = \boldsymbol{w}_{\delta}{}^{\mathrm{H}} \boldsymbol{R}_{l}(k_{\delta l}, f_{\delta l}) \tag{3.44}$$

where $\boldsymbol{w}_{\delta}$ represents the weight vector adjusted for the beamformer to steer at the designated target utilising either the conventional (3.12), MVDR (3.19) or null-steering (3.23) technique. The comparison of various beamforming techniques in tracking the target will be analysed by simulation at Section 3.5.4.

To estimate the location of target, its corresponding sample delay information obtained from all the BCAFs can be applied to model (3.41) to form simultaneous non-linear equations. Therefore, the accuracy of position estimates using these parameters is limited by the sampling rate of the ADC and the final SNR. Solving each of these equations yields the ambiguity of target location within an ellipsoid.

Two main cases will be considered: (i) less than or equal to 3 transmitters and, (ii) more than 3 transmitters.

For the case where the results from less than or equal to 3 transmitters are available, the target location based solely on TDOA becomes ambiguous. The position estimating process can be assisted by the DOA information from the beamformer to eliminate the ambiguity problem, similar to the position estimating process of the monostatic counterpart.

The target-to-receiver range can be obtained from one or more TDOA measurements as follows. Referring to the bistatic radar triangle in Figure 3.1, the square of the target-to-receiver range can be expressed as

$$R_R{}^2 = R_T{}^2 - R_D{}^2 + 2R_D R_R \cos\Omega \tag{3.45}$$

where

$$\cos\Omega = \boldsymbol{\kappa}_\delta \left(\frac{\boldsymbol{p}_{TX} - \boldsymbol{p}_{RX}}{\|\boldsymbol{p}_{TX} - \boldsymbol{p}_{RX}\|}\right)^{\mathrm{T}} \qquad \boldsymbol{\kappa}_\delta = \begin{bmatrix} \cos\theta_\delta \sin\phi_\delta \\ \sin\theta_\delta \sin\phi_\delta \\ \cos\phi_\delta \end{bmatrix} \tag{3.46}$$

where $\boldsymbol{\kappa}_\delta$ is the vector corresponds to the DOA of target determined by the beamformer. The range of transmitter-target-receiver is defined as

$$R_A = R_T + R_R \tag{3.47}$$

Since R_T is unknown, it can be substituted by (3.47). R_R can be derived as

$$R_R = \frac{R_A{}^2 - R_D{}^2}{2\left(R_A - R_D\left(\boldsymbol{\kappa}_\delta \dfrac{\boldsymbol{p}_{TX} - \boldsymbol{p}_{RX}}{\|\boldsymbol{p}_{TX} - \boldsymbol{p}_{RX}\|}\right)^{\mathrm{T}}\right)} \tag{3.48}$$

As R_A is also equal to the combination of the direct-path and the path difference determined by the TDOA measurement, k_δ, the expression becomes

$$\begin{aligned} R_A &= c\frac{k_\delta}{f_s} + R_D \\ &= c\frac{k_\delta}{f_s} + \|\boldsymbol{p}_{TX} - \boldsymbol{p}_{RX}\| \end{aligned} \tag{3.49}$$

Therefore, by applying the target DOA obtained from the beamformer and R_R obtained from the TDOA measurement, the 3-D target position, $\boldsymbol{p}_\delta$, can be determined as

$$\boldsymbol{p}_\delta = R_R \boldsymbol{\kappa}_\delta = R_R \begin{bmatrix} \cos\theta_\delta \sin\phi_\delta \\ \sin\theta_\delta \sin\phi_\delta \\ \cos\phi_\delta \end{bmatrix} \tag{3.50}$$

For the case where more than 3 measurements are available, the localisation problem based purely on TDOA becomes overdetermined. In this case, a LSE can be used to determine the target position that minimises the mean square error (MSE) from all TDOA estimates. Using a linear exhaustive search process, the error estimated from this model in each trial position of target, $\hat{\boldsymbol{p}}_\delta$, using the sample delay given by l^{th} satellite is denoted as

$$\varepsilon_l(\hat{\boldsymbol{p}}_\delta) = \|\boldsymbol{p}_{TX} - \hat{\boldsymbol{p}}_\delta\| + \|\boldsymbol{p}_{RX} - \hat{\boldsymbol{p}}_\delta\| - R_D - \frac{ck_\delta}{f_s} \tag{3.51}$$

The MSE for each trial position of target is given by averaging the sum of squared errors for all satellites, such that

$$Y(\hat{\boldsymbol{p}}_\delta) = \frac{1}{L}\sum_{l=1}^{L} {\varepsilon_l}^2(\hat{\boldsymbol{p}}_\delta) \tag{3.52}$$

Based on the above estimator, the location of the target is obtained from the trial position that yields the smallest MSE since it best matches with the TDOAs which correspond to the multistatic scenario.

The above target localisation technique can be computationally inefficient when the smallest MSE is searched blindly across indefinite locations. The search range can be minimised if the process is initialised from the approximate location of the target followed by a linearly search across other nearby positions within a given range. In that case, equation (3.50) serves as a good option to determine this location. However, the search range should be expanded as the distance to the target increases.

The target's velocity vector can be estimated by utilising the corresponding FDOA information obtained from the BCAFs into model (3.34). The FDOA between the target scattering and direct-path signal can be denoted as

$$\begin{aligned} f_\delta &= \frac{1}{\lambda_0}\left(\frac{\boldsymbol{p}_{TX}-\boldsymbol{p}_\delta}{\|\boldsymbol{p}_{TX}-\boldsymbol{p}_\delta\|}+\frac{\boldsymbol{p}_{RX}-\boldsymbol{p}_\delta}{\|\boldsymbol{p}_{RX}-\hat{\boldsymbol{p}}_\delta\|}\right)\begin{bmatrix} v_{\delta x} \\ v_{\delta y} \\ v_{\delta z} \end{bmatrix} \\ &= \mathrm{X}\boldsymbol{v}_\delta \end{aligned} \tag{3.53}$$

where $\boldsymbol{v}_\delta$ is the instantaneous 3-D velocity vector of target relative to a stationary receiver. Simultaneous linear equations will be formed when multiple FDOAs are applied to the above model. In the case where more than 3 FDOAs are obtained from the detection process using L satellites, the LSE can provide the best estimate of the target's velocity vector as

$$\boldsymbol{v}_\delta = (\mathbf{X}^T\mathbf{X})^{-1}\mathbf{X}^T\boldsymbol{f}_\delta \tag{3.54}$$

where

$$\boldsymbol{f}_\delta = \begin{bmatrix} f_{\delta 1} \\ f_{\delta 2} \\ \vdots \\ f_{\delta L} \end{bmatrix} \qquad \mathbf{X} = \begin{bmatrix} \mathrm{X}_1 \\ \mathrm{X}_2 \\ \vdots \\ \mathrm{X}_L \end{bmatrix} \tag{3.55}$$

The above target velocity estimation model assumes that the position of the target is accurately estimated from the localisation process. If the position of target is unknown, a 3-D exhaustive linear position search can be applied in model (3.53) to determine the target velocity that corresponds to the smallest MSE.

This target velocity estimation technique only gives an average result over a snapshot of the correlation process. It is also possible to estimate the target's velocity from the target position variation over multiple coherent snapshots using the previously introduced localisation method.

3.5.4 Simulation Example of Target Parameters Estimation

This section will analyse and discuss simulation results for target tracking and parameter estimation for a GPS bistatic radar using the models that were discussed in Section 3.5.3. Using the phased-array receiver model that was applied in Section 3.5.2, this simulation includes 3 moving targets with identical 3-D velocity vectors within the search range of the receiver. Among these targets, the first two targets appear at the same DOA and different distances while the third target appears at separate DOAs. In order to demonstrate the capability of estimating the target position, the simulation also includes 4 satellite transmitters. These transmitters are widely separated in the same pattern as the constellation of GPS satellites and also use dedicated C/A code patterns in their broadcasts. The input SNRs of the direct-path signals from all the transmitters are also set to be identical in this simulation. The position of targets and transmitters relative to the radar receiver and their corresponding input SNR for this simulation is given in Table 3.2. Note that the transmitters are also moving following the satellites orbits. However, the direct-path signals are assumed to be removed prior to the target detection stage. Hence, the velocities of the transmitters do not need to be shown in the table.

Particular	**Position, $\boldsymbol{p}$ (m)**	**DOA, $[\theta; \phi]^\circ$**	**SNR (dB)**	**Velocity, $\boldsymbol{v}$ (m/s)**
Target 1	[100; 100; 100]	[45; 54.7]	−46	[50; 20; −10]
Target 2	[500; 500; 500]	[45; 54.7]	−52	
Target 3	[0; 150; 100]	[90; 56.3]	−46	
TX 1 (PRN04)	$[12.8; -5.29; 16.6] \times 10^6$	[−22.4; 39.9]	−26	
TX 2 (PRN12)	$[-7.4; -10.9; 16.7] \times 10^6$	[−124.5; 38.3]	−26	
TX 3 (PRN23)	$[-5.61; -9.10;17.9] \times 10^6$	[−121.7; 30.8]	−26	
TX 4 (PRN24)	$[-6.61; 6.09; 18.6] \times 10^6$	[137.4; 25.8]	−26	

Table 3.2: Positions of targets and transmitters relative to the radar receiver.

Following the modelling of the target scattered time delays in a discrete time manner as mentioned in model (3.43), the largest target position error in the simulation can be no more than half a sample. Hence, all the signals initially used a sampling rate 256 times higher than the real C/A code chipping rate. Then, the signal model of each target return is delayed by the number of sample delays rounded to the nearest integer relative to the direct-path signals as shown in Table 3.3. Prior to the detection process, a decimation filter is applied to the original data to reduce the sampling rate down to 4.092 MHz which is approximately equal to the sampling rate of the experimental receiver that will be described in Chapter 5.

Particular	**PRN04**	**PRN12**	**PRN23**	**PRN24**
Target 1	54 (210.9)	158 (617)	138 (539)	75 (293)
Target 2	269 (1051)	790 (3086)	688 (2688)	373 (1457)
Target 3	122 (477)	156 (609.3)	139 (543)	40 (156.2)

Table 3.3: Rounded number of samples (time in picoseconds) delays of target returns relative to direct-path signals.

At this stage, the decision for identifying the correlation peaks, which correspond to the target returns, were manually performed. In practice, this decision making process can be automated by sending the CCAFs through a Neyman-Pearson detector. Then, the detection threshold (3.5) is set to achieve the required detection performance for the radar receiver. The correlation peaks from the CCAFs that exceed the detection threshold will be identified as the presences of targets while those that fall below will be discarded from further process.

From the simulation, the normalised CCAF from PRN12 and PRN24 in the target detection process are selected as examples to identify the presence of targets as shown in Figure 3.16. From the observation of both CCAFs, there are several correlation peaks that exceed the detection threshold. Firstly, the direct-path signal appears as the strongest peak that is located at zero FDOA and sample delay. Also, the CCAF of PRN12 shows two returns at a frequency bin of −369 Hz and one return at −245 Hz while the CCAF of PRN24 shows one return at a frequency bin of −282 Hz and one at −159 Hz. There are also several returns at ±1000 Hz which are the correlation sidelobes from the correlation process between the direct-path signal and the locally generated C/A codes.

The DOA of each return is determined from the beampowers used to generate each CCAF. From Figure 3.16, each of the values in the CCAF corresponds to the maximum beampower for that particular TDOA or FDOA value. The beampowers for the target returns of PRN 12 and 24 are shown in Figure 3.17 and Figure 3.18 respectively. PRN12 has three distinct returns from each target, separated in Doppler or code phase. PRN24 only has two distinct returns because there is not sufficient delay separation to separate the returns from target 1 and 2 which have the same Doppler. The measurements from both PRN12 and PRN24 can be used to localise target 1 and 3 but PRN24 cannot be used for target 2 as the return is masked by target 1 which has stronger return with the same Doppler, TDOA and DOA. In summary, the measured parameters of each return from PRN12 and PRN24 are shown in Table 3.4, where

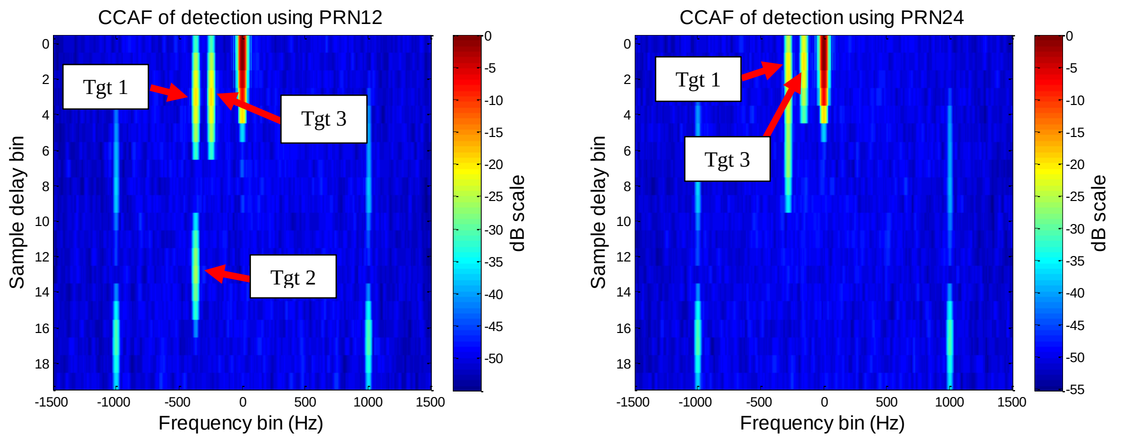

Figure 3.16: Normalised CCAF processed from simulation in a GPS bistatic radar multiple targets detection scenario using transmitter PRN12 (Left) and PRN24 (Right).

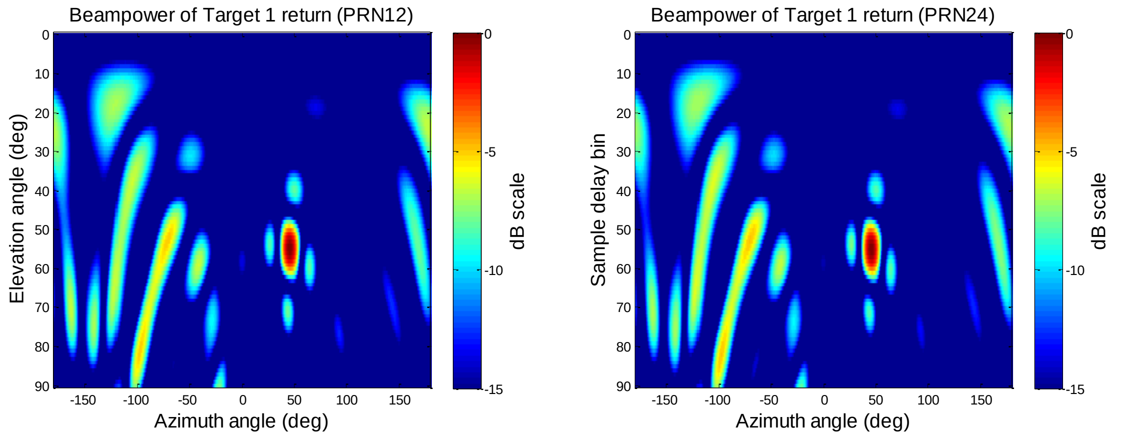

Figure 3.17: Beampower of target 1 return using detection from PRN12 and PRN24. The peaks of both results indicate the DOA of target at $\theta = 45°$ and $\phi = 55°$.

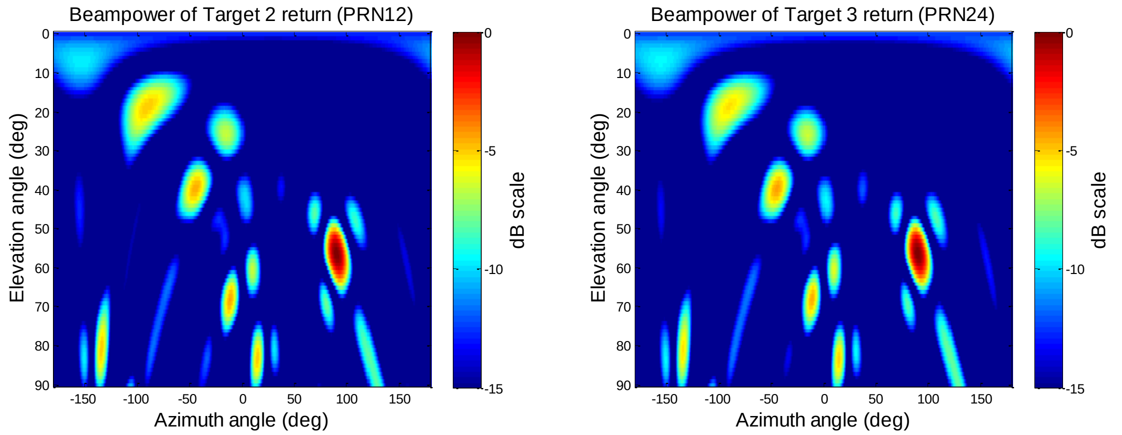

Figure 3.18: Beampower of target 3 return using detection from PRN12 and PRN24. The peak of both results indicate the DOA of target at $\theta = 90°$ and $\phi = 56°$.

the DOA of each return is obtained from the beampowers in Figure 3.17 and Figure 3.18 (Beampower of return 3 is not shown).

Particular	**Doppler (Hz) [PRN12;24]**	**Code phase (ps) [PRN12;24]**	**DOA, [θ; ϕ]°**
Target 1	[−369; −282]	[3 (750); 1 (250)]	[45; 55]
Target 2	[−369; No data]	[13 (3250); No data]	[45; 55]
Target 3	[−245; −159]	[3 (750); 1 (250)]	[90; 56]

Table 3.4: Measured parameters of each return from the detection process.

The sidelobes of the direct path signal can be much stronger than the target return. It can be identified and removed as they have the same Doppler as the direct-path signal. However, as shown in Figure 3.11, this signal can mask the weaker targets and should be removed.

When the DOA of targets are identified, the input signal at each channel can be passed through a beamformer to obtain a better estimate of the FDOA and sample delay of individual target, while discriminating other strong interference sources that appear at separate DOA such as the direct-path signals and their corresponding sidelobes. This simulation will demonstrate the performance of three beamforming techniques in processing the BCAF of each target with PRN12: conventional, MVDR and null-steering. Regardless of the technique, this process is unable to discriminate target 1 from target 2 as they both appear at the same DOA.

The BCAF results using the conventional beamforming technique are shown at Figure 3.19. These results indicate the existence of both the target at the desired DOA and the direct- path signal. This observation implies that the conventional technique does not suppress the power of strong interferences from undesired DOAs adequately. In comparison, both the BCAF results that are processed using MVDR and null-steering technique as shown in Figure 3.20 and Figure 3.21 respectively demonstrated only the existence of target return at the desired DOA. Hence, both of these techniques are adept at rejecting signals from undesired DOAs. However, the cancellation achieved by null steering will be compromised if the array has phase errors as is likely in real arrays.

From the computational perspective, the conventional beamforming technique is most efficient as it only requires the application of a single weight vector that corresponds to the DOA of the desired target. To overcome its weakness in suppressing the direct path signal, the direct-path signal suppressing technique can be applied to the input signal prior to conventional beamforming. The null-steering technique also requires a single weight vector that is adjusted based on the DOA of desired and non-desired directions. Its capability in rejecting signals from multiple DOAs is limited by the number of elements in the phased-array receiver. Therefore, it is well suited for use with a large antenna array. The MVDR beamformer is the least efficient

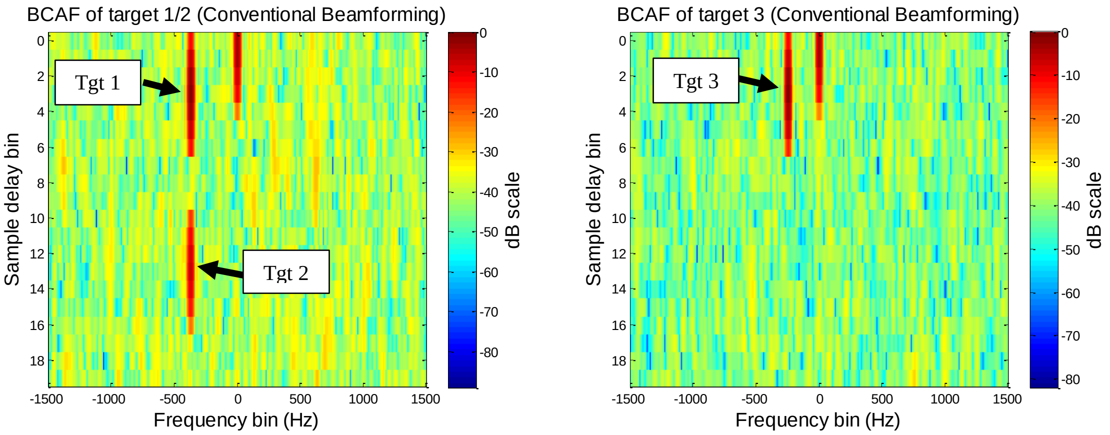

Figure 3.19: BCAF results (PRN12) of target 1/2 and 3 that are performed during the target tracking process using the conventional beamforming technique.

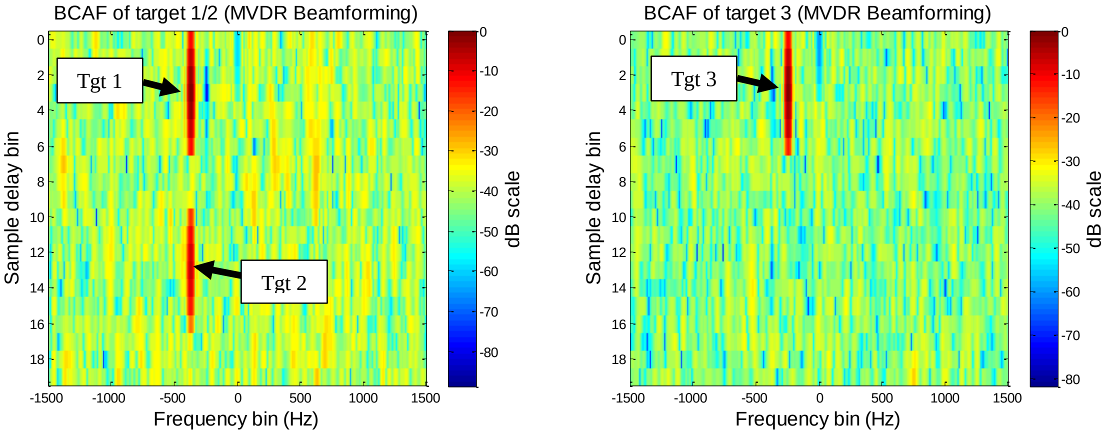

Figure 3.20: BCAF results (PRN12) of target 1/2 and 3 that are performed during the target racking process using the MVDR beamforming technique.

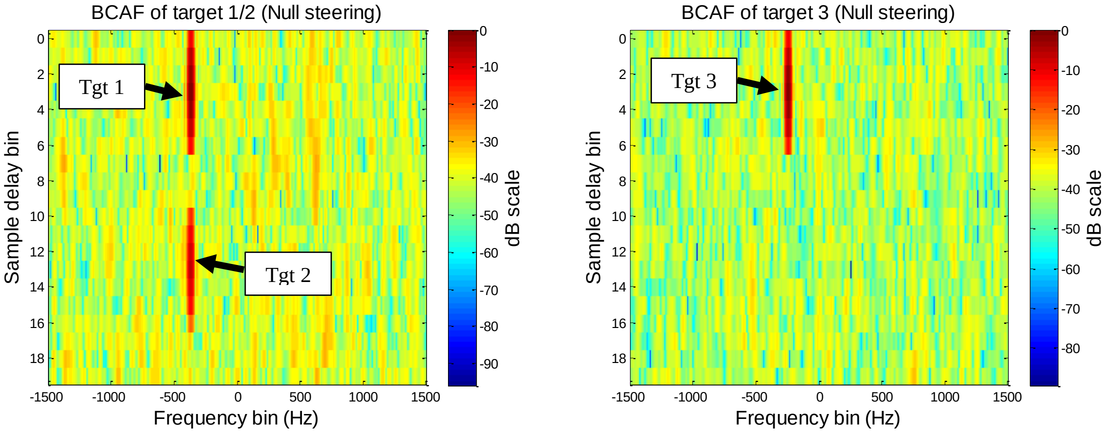

Figure 3.21: BCAF results (PRN12) of target 1/2 and 3 that are performed during the target tracking process using the null-steering technique.

technique as it requires an adaptive process that creates a unique weight vector based on an estimate of the array covariance matrix at each Doppler frequency offset and sample delay bin of the CAF results. The BCAF result for the l^{th} transmitter based on the MVDR technique can be expressed as

$$\mathcal{R}_{Bl}(k_{\delta l}, f_{\delta l}) = \left(\frac{\mathbf{Q}^{-1}(k_{\delta l}, f_{\delta l})\, \boldsymbol{a}(\boldsymbol{\kappa}_{\delta})}{\boldsymbol{a}^{\mathrm{H}}(\boldsymbol{\kappa}_{\delta})\, \mathbf{Q}^{-1}(k_{\delta l}, f_{\delta l})\, \boldsymbol{a}(\boldsymbol{\kappa}_{\delta})}\right)^{\mathrm{H}} \boldsymbol{\mathcal{R}}_{l}(k_{\delta l}, f_{\delta l}) \tag{3.56}$$

where $\boldsymbol{a}(\boldsymbol{\kappa}_{\delta})$ is the steering vector of the desired target.

When the desired target is properly tracked, its location can be estimated by incorporating the sample delays from the BCAF results of multiple transmitters into model (3.52). The resolution of localisation based on the BCAF result is only precise to within one sample delay bin. It can be improved by using a zero-padding FFT interpolating technique on the demodulated GPS signal at the output of the beamformer.

The localisation stage will be performed on target 3 as its correlation function is well separated from the direct-path signals and other target returns in frequency and time. These undesired signals are further suppressed by steering the beam at the DOA of target 3 using the weights determined by null-steering technique prior to interpolation up to 64 times of receiver's sampling rate on the input signals. The correlation functions between the interpolated target scattered signal and the locally generated C/A code samples from all available transmitters are shown in Figure 3.22. Since the interpolation was performed at the pre-matched filter stage where the AWGN dominates the desired signal, there are minor errors (i.e. max 1 bin) between the sample delay bins where the correlation peaks are located as given in the caption of Figure 3.22 and the delays given in Table 3.3.

Next, the acquired sample delay bins that correspond to the maximum peaks of the interpolated correlation result are applied into target positioning model (3.51) to linearly search for the corresponding target location. This process yields the MSE within the given position search range. However, for visual convenience the inverse MSE results will be illustrated instead. The 2-D inverse MSE that incorporated the delays from both the original and interpolated correlation results are illustrated in Figure 3.23. This outcome shows that the sample delays from the correlation process of the interpolated signals give a better estimation of the target location. While the accuracy of interpolation in estimating the delays can be affected by the SNR of the target return, the threshold set for the detection process will ensure that all detected signals will have sufficient SNR so that their parameters can be reliably applied for all forms of estimation.

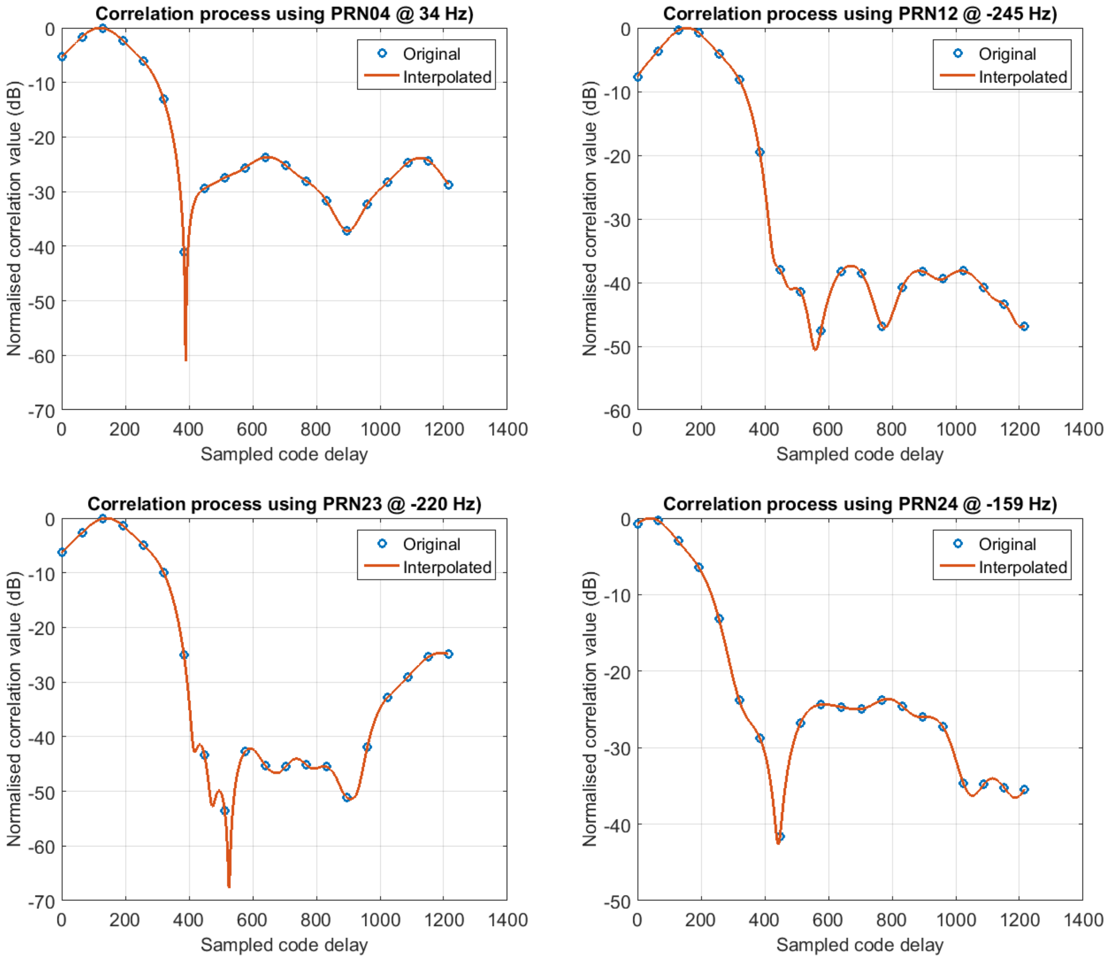

Figure 3.22: Correlation function that is performed using original vs. interpolated signals. Note that the correlation value is normalised and the sample delay axis is applied with the time scale of interpolated signals. The peak of correlation for PRN04, PRN12, PRN23 and PRN24 appear at sample delay bin of 123, 157, 140 and 41 respectively.

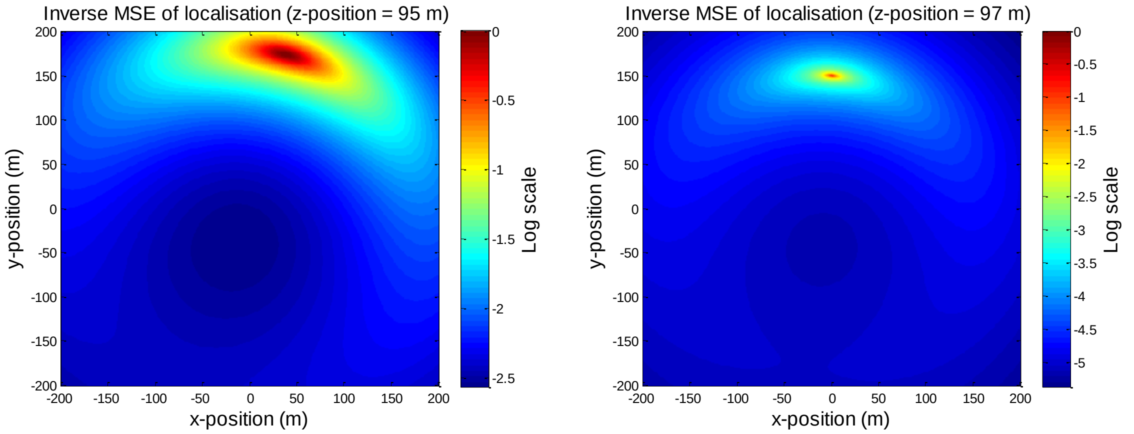

Figure 3.23: Inverse MSE of localisation for target 3 determined from model (3.51) using sampling delay from original (Left) vs. interpolated (Right) correlation results. The largest inverse MSE of these results appear at position of [38, 174, 95] and [0, 150, 97] metres relative to the radar receiver respectively.

In addition, the acquired Doppler and position readings of the target from the detection and localisation process respectively are applied in model (3.53) to estimate its corresponding velocity vector as shown in Table 3.5. An investigation has also been made to analyse the performance of the method for determining the position of target based on just the Doppler frequencies. This method works by finding the position that yields the smallest MSE through an exhaustive linear searching process. The inverse MSE results shown in Figure 3.24 suggested that the localisation technique using the target's Doppler readings will result in position ambiguity within an ellipsoid. Hence, this method is not recommended for performing target localisation.

Particular	**TX1 (PRN 04)**	**TX2 (PRN 12)**	**TX3 (PRN 23)**	**TX4 (PRN 24)**
Doppler bin (Hz)	31	−245	−220	−159
Sample delay (Original)	2	3	3	1
Sample delay (Interpolated)	123	157	140	41
DOA, [θ; ϕ] (degree)	[90; 56]			
Target position (m)	[0; 150; 97]			
Velocity vector (m/s)	[49.92; 19.82; −9.85]			

Table 3.5: Summary of parameters for target 3 from simulated detection and estimation.

The LSE 3-D velocity relative to the receiver at each position bin within the search range is also illustrated in Figure 3.24. It is observed that the velocity for z-component, $v_{\delta z}$, changes more erratically with position than the horizontal components as a result of the poor PDOP due to the orbital configuration of the GPS satellites which are widely separated horizontally but not vertically.

3.6 Conclusion

A feasibility study has been made for GPS bistatic radar in performing target detection and estimation. This study includes the investigation of the number of antenna elements in the phased-array receiver and the length of correlation process to achieve target detection for a given RCS at a given range.

A calibration technique using the phase information from multiple transmitters has been provided to remove phase errors in each channel of a phased-array receiver as well as estimating the attitude of the antenna array. Array processing techniques such as conventional, MVDR beamforming and null steering technique have been implemented in the detection process to exploit the capability of phased-arrays for estimating the DOA of the designated

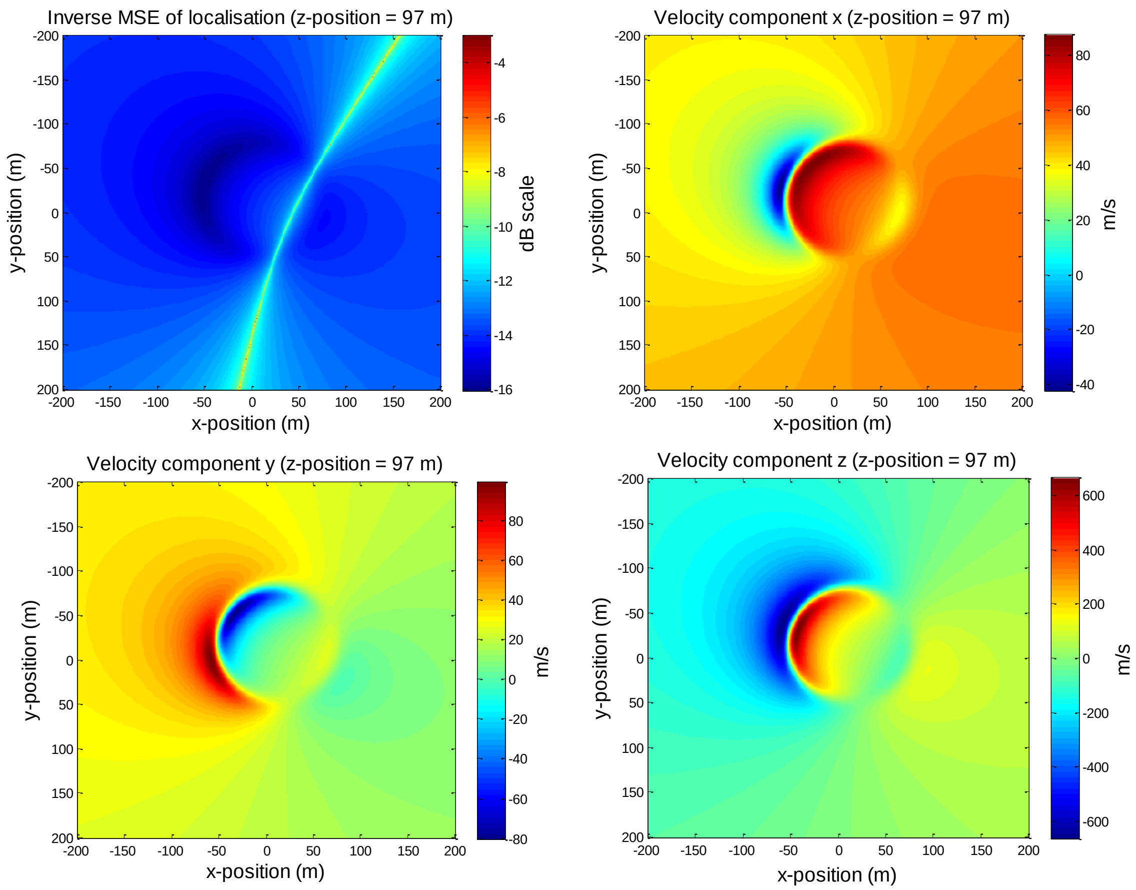

Figure 3.24: Inverse MSE of localisation for target 3 determined from model (3.53) using its corresponding Doppler readings from BCAF results (Top Left) and the 3-D velocity diagrams estimated by LSE at position bins within the search range.

target while rejecting non-desired signals. The DOA information helps greatly in reducing the ambiguities in the target parameter estimation process.

This chapter also investigates the proposed target detection and parameter estimation technique using computer simulation. The simulation results demonstrated the capability and limitation of GPS bistatic radar in detecting single and multiple targets. In addition, this simulation compares the performance of several array processing techniques in tracking the targets and several MSE location techniques. The comparison also shows the advantages and drawbacks of these techniques which can help in justifying their suitability for different detection cases or scenarios.

Many parameters such as the target scattering behaviour or RCS from different transmitter directions and the time varying nature of the Doppler components are complicated to accurately predict and model in a simulation. Therefore, it is important to provide further justification of the feasibility of GPS bistatic radar in performing air target detection by experimental work. Based on the specification mentioned in the simulations such as the number of elements and integration periods, the design of the large scale phased-array system for the experiment and the outcomes will be described in Chapter 5.

CHAPTER 4

GPS Bistatic Radar using MIMO Technique

4.1 Introduction

A bistatic radar can potentially detect a target that rebounds signals illuminated by multiple transmitters with multiple receive antenna elements. This concept can be achieved with the implementation of MIMO techniques that also exploit multiple transmitters and receivers. For GPS bistatic radar, it is important to improve the SNR of the target returns to guarantee more reliable parameter estimation. This chapter aims to demonstrate the idea of MIMO as a complement to other SNR improvement techniques such as extended signal integration times and array processing that have been previously discussed for GPS bistatic radar. In addition, this chapter will simulate a MIMO radar technique for GPS bistatic radar that tracks air targets while performing detection simultaneously.

Section 4.2 will discuss the modelling of a GPS MIMO radar technique for aircraft detection and demonstrate its potential to improve the detection performance. Section 4.3 will discuss the two major criteria to evaluate the performance of MIMO radar techniques for GPS bistatic radar. Firstly, the theoretical detection performance will be studied using the Neyman-Pearson detector. Secondly, the target localisation accuracy will be analysed for the GPS MIMO radar system using the Dilution of Precision (DOP) estimator. Also, the computational complexity of the MIMO radar techniques for GPS bistatic radar will also be discussed. Section 4.3.3 will evaluate GPS MIMO radar target detection performance based on simulations of the following systems: Single-input and Single-output (SISO), Multiple-inputs and a Single-output (MISO) and Multiple-inputs and Multiple-outputs (MIMO). Moreover, the results from detection of fast moving targets using tracking techniques such as the track-before-detect (TBD) and fragmentised data integration methods will also be demonstrated. Section 4.5 will conclude the discussion of MIMO radar technique for GPS bistatic radar.

4.2 MIMO Radar Target Detection Model for GPS Bistatic Radar

GPS bistatic radar can potentially apply the non-coherent MIMO radar technique for target detection and parameter estimation as the system is globally covered by large numbers of widely separated satellite transmitters. In Chapter 3, GPS bistatic radar target detection is performed based on the Doppler-delay search technique. This technique uses the signals transmitted by each satellite transmitter to detect the target. Then the parameters from the detection process of all transmitters are combined to estimate the target position using the MSE solution. In comparison, the MIMO radar technique aims to increase the cooperation between GPS satellite transmitters to detect and localise the target.

The MIMO radar detection model can be derived from the MISO model, which uses a single receiver to combine the target reflections of multiple satellites. This detection model can be simply implemented in a GPS bistatic radar receiver in the presence of multiple GPS satellites at any place. For a single phased-array GPS receiver, a bank of matched filters can be generated by using the expected velocities, TDOA and steering vector of target reflections from multiple satellite vehicles (SV) at each position bin as shown in Figure 4.1. Next, these matched filters are applied to the signals captured by the receiving elements. Then, multiple GPS signals are combined by summing the squared absolute correlation values at these matched filters outputs from each tentative position. The correlation values that exceed the desired detection threshold of the system will be identified as targets. Therefore, this detection process does not require further computations to determine the target position and velocity due to the tentative target parameters used by the matched filters during the position search process.

For a carrier and direct-path signal Doppler demodulated target return of the l^{th} satellite at the m^{th} element of a phased-array receiver, the signal can be modelled by the position and velocity vectors, $\boldsymbol{p}_\delta$ and $\boldsymbol{v}_\delta$, of the target respectively in the presence of AWGN, $n(k)$ as

$$\begin{aligned} x_{\delta ml}(k, \boldsymbol{p}_\delta, \boldsymbol{v}_\delta) &= \mu_{\delta l}\, a_m(\boldsymbol{p}_\delta)\, \mathcal{C}_l(k, \boldsymbol{p}_\delta)\, \mathscr{f}_l(k, \boldsymbol{v}_\delta, \boldsymbol{p}_\delta) + \sigma\, n(k) \\ &= \mu_{\delta l} \exp(j \boldsymbol{\kappa}_\delta \boldsymbol{u}_m)\, C_l(k - k_{\delta l}) \exp\left(j 2\pi \frac{f_{Dl} + f_{dl}}{f_s} k\right) + \sigma\, n(k) \end{aligned} \tag{4.1}$$

where δ is the number of targets, $\mu_{\delta l}$ is the amplitude of target return from the l^{th} satellite at the receiver. $\mathcal{C}_l(k, \boldsymbol{p}_\delta)$ is the C/A code sequence delayed by a discrete sample of $k_{\delta l}$ relative

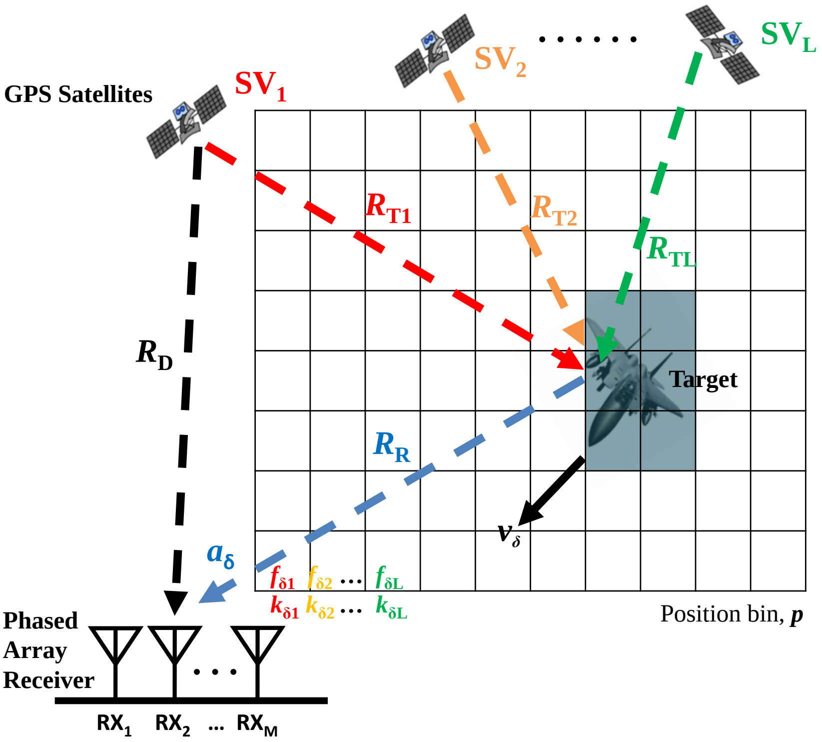

Figure 4.1: Illustration of target detection scenario for GPS MISO radar.

to the direct-path signal as derived in (3.43) and $\mathscr{f}_l(k, \boldsymbol{v}_\delta, \boldsymbol{p}_\delta)$ is the function of Doppler frequency of the target where f_{Dl} is the Doppler frequency of the satellite and f_{dl} is the target Doppler offset as derived in (3.53), $a_m(\boldsymbol{p}_\delta)$ is the spatial phase factor corresponding to the DOA of the target. This factor varies with the azimuth and elevation angles, such that

$$\theta_\delta = \operatorname{atan2}\left(p_{\delta y} - p_{Ry}, p_{\delta x} - p_{Rx}\right) \tag{4.2}$$

$$\phi_\delta = \operatorname{atan2}\left(p_{\delta z} - p_{Rz}, \sqrt{(p_{\delta x} - p_{Rx})^2 + \left(p_{\delta y} - p_{Ry}\right)^2}\right) \tag{4.3}$$

where atan2 is the four quadrants arc tangent.

The GPS MISO receiver uses a detection process as illustrated in Figure 4.2 to search for the presences of targets. Initially, it assumes that a target is moving at a position, $\boldsymbol{p}_\Delta$, and velocity, $\boldsymbol{v}_\Delta$. Then, a coherent integration process can be applied to the input signals using the locally generated matched filter expressed as

$$h_l(k, \boldsymbol{p}_\Delta, \boldsymbol{v}_\Delta) = \mathcal{C}_l(k, \boldsymbol{p}_\Delta)\, \mathscr{f}_l^{\,*}(k, \boldsymbol{v}_\Delta, \boldsymbol{p}_\Delta) \tag{4.4}$$

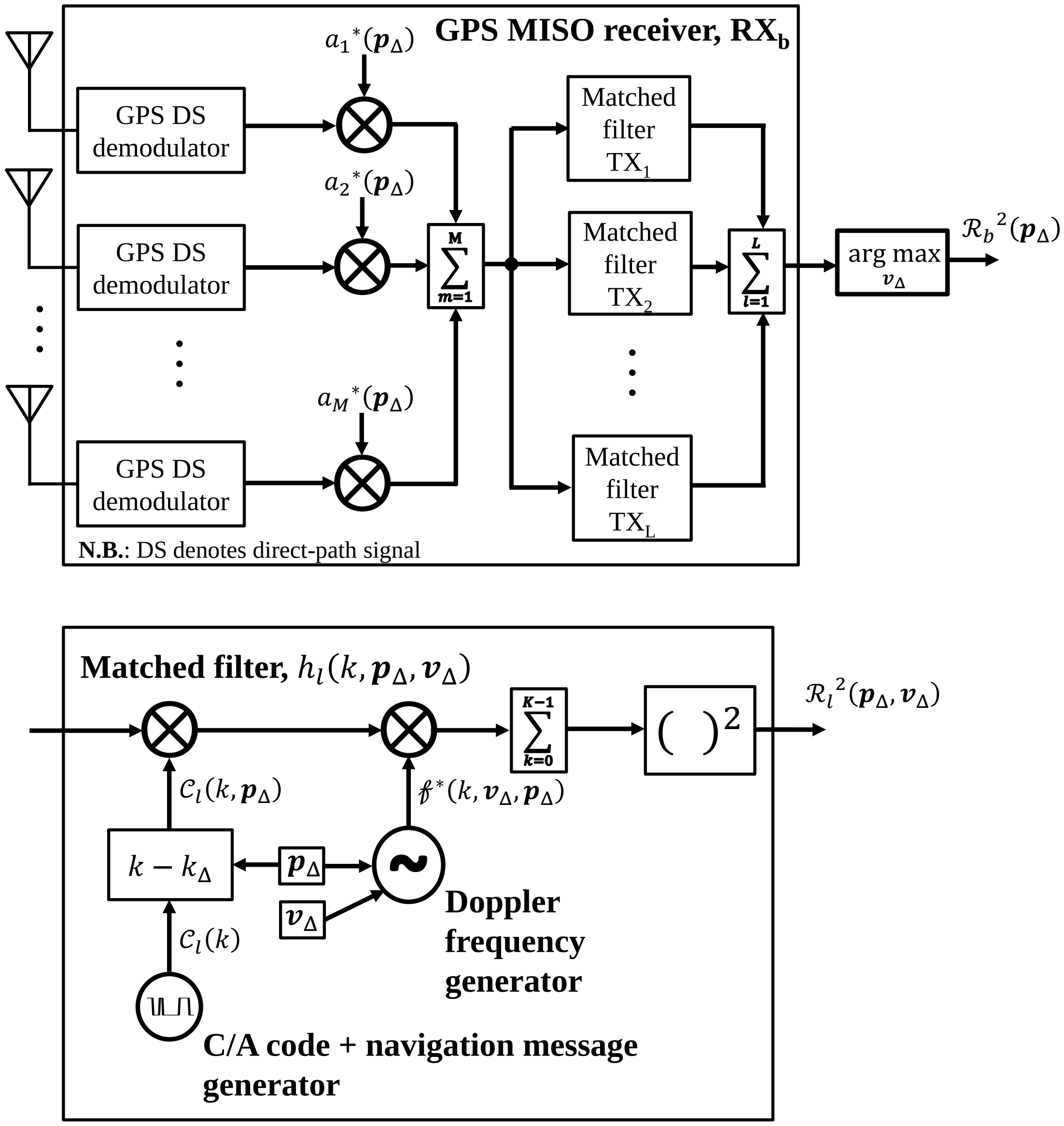

Figure 4.2: Block diagram of GPS MISO radar system (Top) that combines the output from *L* satellites. The function of the matched filters (Bottom) within the system is also illustrated.

By summing the matched filters outputs of every channel using the conventional beamforming technique, the correlation function becomes

$$\begin{aligned}\mathcal{R}_l(\boldsymbol{p}_\Delta,\boldsymbol{v}_\Delta) &= \sum_{k=0}^{K-1}\sum_{m=1}^{M} a_m{}^*(\boldsymbol{p}_\Delta)\, x_{\delta ml}(k,\boldsymbol{p}_\delta,\boldsymbol{v}_\delta)\, h_l(k,\boldsymbol{p}_\Delta,\boldsymbol{v}_\Delta)\\ &= \mathcal{R}_s(\boldsymbol{p}_\Delta,\boldsymbol{v}_\Delta)+\mathcal{R}_n(\boldsymbol{p}_\Delta,\boldsymbol{v}_\Delta)\end{aligned} \tag{4.5}$$

When the target appears within the LOS of *L* satellites, the MISO technique can be applied to the b^{th} receiver to jointly process the target returns by summing the squared correlation values of all the satellites. The velocity that corresponds to the largest summed correlation value is taken as the final correlation value of each searched position grid, $\boldsymbol{p}_\Delta$, such that

$$\mathcal{R}_b{}^2(\boldsymbol{p}_\Delta) = \max_{\boldsymbol{v}_\Delta} \sum_{l=1}^{L} |\mathcal{R}_l(\boldsymbol{p}_\Delta, \boldsymbol{v}_\Delta)|^2 \tag{4.6}$$

If the PBR system requires even greater spatial diversity of targets, the number of widely separated receivers can be increased to form the MIMO detection model. This would potentially improve the target detection threshold and localization accuracy at an increase of overall hardware and computational cost. Also, a timing alignment mechanism is required to synchronise the data capturing module at each receiving site prior to the integration process. PBR system such as GPS bistatic radar can simply overcome this issue by using the GPS signal itself as the synchronisation source.

For a MIMO radar system with B receivers as illustrated in Figure 4.3, each receiver's correlation output as a function of positions and velocity is non-coherently added together first. Then, the summed output of L x B matched filters for velocity, $\boldsymbol{v}_\Delta$, that gives the highest correlation value is taken as the correlation value of each position bin, $\mathcal{R}^2(\boldsymbol{p}_\Delta)$ as

$$\mathcal{R}^2(\boldsymbol{p}_\Delta) = \max_{\boldsymbol{v}_\Delta} \sum_{b=1}^{B} \sum_{l=1}^{L} |\mathcal{R}_{bl}(\boldsymbol{p}_\Delta, \boldsymbol{v}_\Delta)|^2 \tag{4.7}$$

4.3 Performance of MIMO Technique for GPS Bistatic Radar

For the detection process in a GPS bistatic radar, long C/A code integration periods and large scale antenna arrays are essential to improve the SNR of targets reflections. Moreover, non-coherent addition of single target reflections from multiple transmitters or receivers will further improve the output SNR of the radar system. This method is immune to any misalignment between the phases of the combined signals.

The objective of this section is to investigate the theoretical performance of GPS bistatic radar that applies MIMO/MISO technique using different numbers of transmitters and receivers. The investigation will consider two major criteria: target detection and position estimation performance.

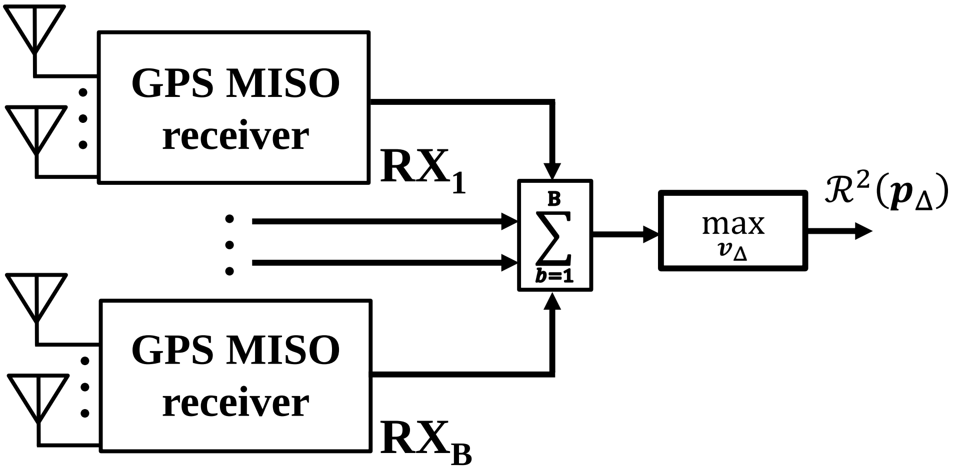

Figure 4.3: Block diagram of GPS MIMO radar system that combines the output from *B* MISO receivers.

4.3.1 Target Detection Performance

The analysis of target detection performance using the MIMO technique was again based on the 32-element phased-array receiver which was used for the simulations in Chapter 3 and experimental results in Chapter 5. By combining the target returns in AWGN using the MISO (4.6) and MIMO (4.7) model, the GPS bistatic radar target detection range model in (3.10) will be improved by the non-coherent integration gain, G_{NC}. Hence, the maximum target detection range of the GPS MIMO radar becomes

$$R_{\mathrm{R}} = \sqrt{\frac{P_{\mathrm{D}}\sigma_{\mathrm{B}}G_R G_{\mathrm{NC}}}{4\pi(\mathscr{k}\mathrm{T_A}f_{\mathrm{B}})G_{\mathrm{LOSS}}\mathrm{SNR_{out}}}} \tag{4.8}$$

G_{NC} can be determined using the CDF that is modelled as a non-central chi-squared distribution due to summing multiple squared variables with normal distributions. To be consistent with the receiver performance as indicated in Section 3.2.1, the detection threshold, τ, will be set to be less than 1% CFAR, $\mathbb{P}_{\mathrm{FA}}$ (3.6).

A comparison of the receiver's detection performance will be made between methods that use a single and the combination of multiple satellite returns. Ideally, this comparison assumes the target is non-fluctuating. Hence, the non-centrality parameter of the model becomes

$$\Lambda = \sum_{b=1}^{B}\sum_{l=1}^{L}\left(\frac{\mu_{bl}}{\sigma}\right)^2 = BL\frac{\mu^2}{\sigma^2} \tag{4.9}$$

where μ_{bl} is the post matched filter amplitude of the l^{th} signal at the b^{th} receiver and $\mu = \mu_{bl}\ \forall\ b\ \&\ l$.

From the above parameter, the receiver's probability of detection, $\mathbb{P}_\text{D}$, using different number of target returns can be determined using the CDF (cumulative distribution function) of the non-central chi-squared distribution (3.7). From Figure 4.4, the CDF plots demonstrate that as the L x B factor increases, the SNR at the input of the non-coherent integrator needed to achieve the same detection performance decreases. Hence, the non-coherent gain, G_NC, of the system can be determined by the SNR difference between a particular $\mathbb{P}_\text{D}$ value at a different number of non-coherent integrations.

An alternative yet more straightforward method to determine the theoretical non-coherent integration gain is to use the difference between SNR estimated by a mathematical model proposed by Alberhseim [99] at different number of integrations, L. This model is based on the results collected from the envelope detection samples performed in the Bell Laboratories. The non-coherent gain of this model is given as

$$G_{\text{NCA(dB)}} = -5\log_{10} L + \left(6.2 + \frac{4.54}{\sqrt{L+0.44}}\right)\log_{10}(\mathcal{F}_1 + 0.12\mathcal{F}_1\mathcal{F}_2 + \mathcal{F}_2) \tag{4.10}$$

where

$$\mathcal{F}_1 = \ln\frac{0.62}{\mathbb{P}_\text{FA}} \qquad \mathcal{F}_2 = \ln\frac{\mathbb{P}_\text{D}}{1-\mathbb{P}_\text{D}} \tag{4.11}$$

Besides, an optimum non-coherent integration gain model was given by Marcum [56] as

$$G_{\text{NCM}} = L^{0.76} \tag{4.12}$$

The integration gain factors of various models are summarised in Figure 4.5. It is shown that by using the same number of integrations, the performance of the non-coherent technique is inferior to the coherent counterpart, but better than the square root times the numbers of integrations, which lies within the range given in [56]. In addition, this figure shows that the gain factor analysed by the chi-squared model lies in between (4.10) and (4.12). Therefore, G_NC can be applied in model (4.8) to estimate the theoretical improvement of the receiver's detection range.

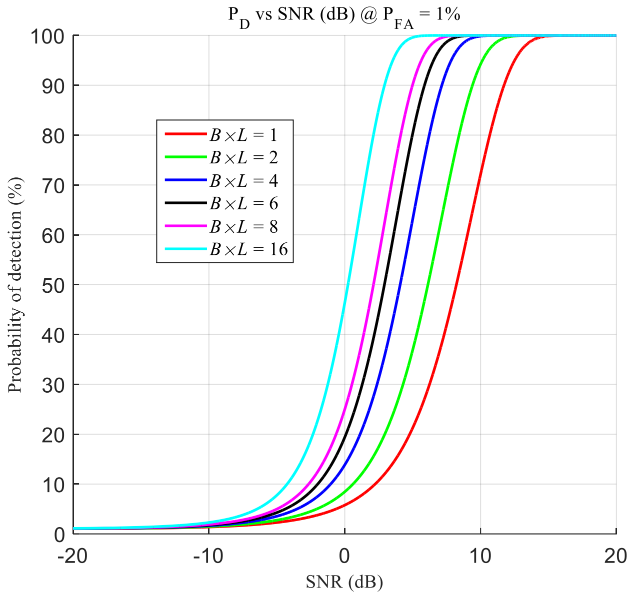

Figure 4.4: The probability of detection vs. pre-integrator stage SNR using different numbers of non-coherent integration.

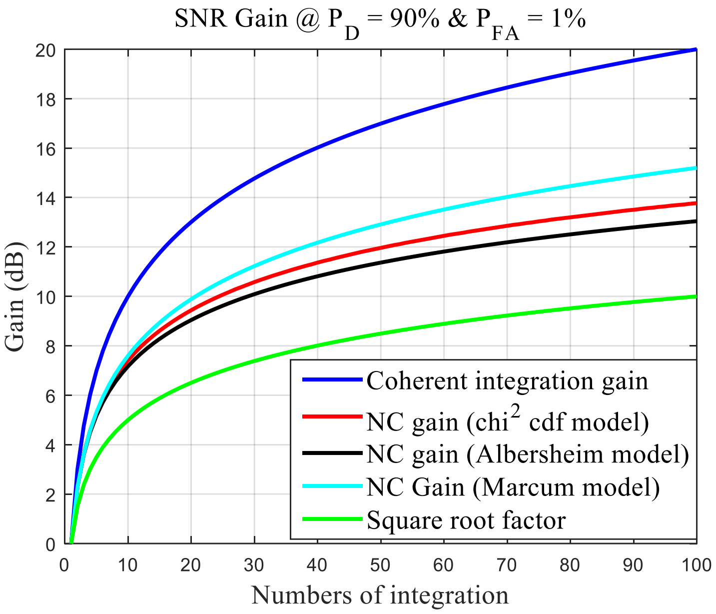

Figure 4.5: Comparison of gain level at different numbers of integration.

Assuming that the target is non-fluctuating, the above figure shows a significant improvement when a large number of target returns are used in the integration process. However, it is impossible to capture power returns from more than 10 GPS satellites within a region unless the PBR system uses more widely separated receivers or the target reflections of other navigation systems, such as the GLONASS, Galileo and BDS. On the other hand, it is highly unlikely to capture multiple uniform power target returns at the receiver in practice due to the complexity of the targets' shapes that causes the fluctuations of signal reflections. Hence, the non-coherent integration technique may not necessarily improve the target output SNR under such cases.

4.3.2 Target Location Estimation Accuracy

One of the factors that contribute to the accuracy of positioning for a navigation system is the satellite geometry [26]. The constellation of the navigation SVs are designed to have excellent spatial diversity to provide users accurate estimation of their positions. The parameter, known as dilution of precision (DOP), takes the positions of all the available navigation SVs into account to estimate the standard deviation of the position solution.

For a GPS bistatic radar, the location estimation technique is applied to determine the position of the air targets. Therefore, the positions of both the satellites and the receivers need to be considered in the DOP to estimate the accuracy of target positioning. The DOP of a GPS bistatic radar can be derived from the pseudorange, ρ, as

$$\begin{aligned}\rho &= R_{\mathrm{T}} + R_{\mathrm{R}} \\ &= \sqrt{(p_{\mathrm{S}x} - p_{\delta x})^2 + \left(p_{\mathrm{S}y} - p_{\delta y}\right)^2 + (p_{\mathrm{S}z} - p_{\delta z})^2} \\ &\qquad + \sqrt{(p_{\mathrm{R}x} - p_{\delta x})^2 + \left(p_{\mathrm{R}y} - p_{\delta y}\right)^2 + (p_{\mathrm{R}z} - p_{\delta z})^2} \\ &= f\left(p_{\delta x}, p_{\delta y}, p_{\delta z}\right)\end{aligned} \tag{4.13}$$

where R_{T} is the transmitter-to-target range, R_{R} is the receiver-to-target range, p_{Si}, p_{Ri} and $p_{\delta\mathrm{i}}$ are the true position elements of the satellite, receiver and target respectively.

For small errors $\Delta\rho$, the pseudorange estimate, $\hat{\rho}$, can be expressed as

$$f\left(p_{\delta x}, p_{\delta y}, p_{\delta z}\right) = f\left(\hat{p}_{\delta x} + \Delta p_{\delta x}, \hat{p}_{\delta y} + \Delta p_{\delta y}, \hat{p}_{\delta z} + \Delta p_{\delta z}\right) \tag{4.14}$$

Using the Taylor series expansion, the pseudorange becomes

$$\begin{aligned}\rho = f\left(\hat{p}_{\delta x}, \hat{p}_{\delta y}, \hat{p}_{\delta z}\right) &+ \frac{\partial f\left(\hat{p}_{\delta x}, \hat{p}_{\delta y}, \hat{p}_{\delta z}\right)}{\partial \hat{p}_{\delta x}} \Delta p_{\delta x} \\ &+ \frac{\partial f\left(\hat{p}_{\delta x}, \hat{p}_{\delta y}, \hat{p}_{\delta z}\right)}{\partial \hat{p}_{\delta y}} \Delta p_{\delta y} \\ &+ \frac{\partial f\left(\hat{p}_{\delta x}, \hat{p}_{\delta y}, \hat{p}_{\delta z}\right)}{\partial \hat{p}_{\delta z}} \Delta p_{\delta z}\end{aligned} \tag{4.15}$$

Hence, the pseudorange error becomes

$$
\begin{aligned}
\therefore \Delta\rho = \hat{\rho} - \rho = \; & \left(\frac{p_{\mathrm{S}x} - p_{\delta x}}{R_{\mathrm{T}}} + \frac{p_{\mathrm{R}x} - p_{\delta x}}{R_{\mathrm{R}}}\right)\Delta p_{\delta x} \\
& + \left(\frac{p_{\mathrm{S}y} - p_{\delta y}}{R_{\mathrm{T}}} + \frac{p_{\mathrm{R}y} - p_{\delta y}}{R_{\mathrm{R}}}\right)\Delta p_{\delta y} \\
& + \left(\frac{p_{\mathrm{S}z} - p_{\delta z}}{R_{\mathrm{T}}} + \frac{p_{\mathrm{R}z} - p_{\delta z}}{R_{\mathrm{R}}}\right)\Delta p_{\delta z}
\end{aligned}
\tag{4.16}
$$

In the presence of L transmitters and B receivers, the pseudorange errors can be expressed as

$$
\boldsymbol{\Delta\rho} = \mathbf{D}\boldsymbol{\varepsilon} = \begin{bmatrix} \boldsymbol{d}_{x1} & \boldsymbol{d}_{y1} & \boldsymbol{d}_{z1} \\ \boldsymbol{d}_{x2} & \boldsymbol{d}_{y2} & \boldsymbol{d}_{z2} \\ \vdots & \vdots & \vdots \\ \boldsymbol{d}_{xB} & \boldsymbol{d}_{yB} & \boldsymbol{d}_{zB} \end{bmatrix} \boldsymbol{\varepsilon}
\tag{4.17}
$$

where

$$
\boldsymbol{d}_{xb,yb,zb} = \begin{bmatrix} \dfrac{p_{S1x,y,z} - p_{\delta x,y,z}}{R_{\mathrm{T}1}} + \dfrac{p_{\mathrm{R}bx,y,z} - p_{\delta x,y,z}}{R_{\mathrm{R}b}} \\ \dfrac{p_{\mathrm{S}2x,y,z} - p_{\delta x,y,z}}{R_{\mathrm{T}2}} + \dfrac{p_{\mathrm{R}bx,y,z} - p_{\delta x,y,z}}{R_{\mathrm{R}b}} \\ \vdots \\ \dfrac{p_{\mathrm{SL}x,y,z} - p_{\delta x,y,z}}{R_{\mathrm{T}L}} + \dfrac{p_{\mathrm{R}bx,y,z} - p_{\delta x,y,z}}{R_{\mathrm{R}b}} \end{bmatrix} \qquad \boldsymbol{\varepsilon} = \begin{bmatrix} \Delta p_{\delta x} \\ \Delta p_{\delta y} \\ \Delta p_{\delta z} \end{bmatrix}
\tag{4.18}
$$

Taking the covariance of $\boldsymbol{\varepsilon}$, the equation becomes

$$
\begin{gathered}
E\{\boldsymbol{\varepsilon}\boldsymbol{\varepsilon}^{\mathrm{T}}\} = E\{\boldsymbol{\Delta\rho}\boldsymbol{\Delta\rho}^{\mathrm{T}}\}(\mathbf{D}^{\mathrm{T}}\mathbf{D})^{-1} \\
\begin{bmatrix} {\sigma_x}^2 & \sigma_{xy} & \sigma_{xz} \\ \sigma_{xy} & {\sigma_y}^2 & \sigma_{yz} \\ \sigma_{xz} & \sigma_{yz} & {\sigma_z}^2 \end{bmatrix} = \sigma_{\mathrm{UERE}}(\mathbf{D}^{\mathrm{T}}\mathbf{D})^{-1}
\end{gathered}
\tag{4.19}
$$

where σ_{UERE} is the user equivalent range error factor (UERE). Therefore, the DOP of each dimension can be expressed as follows

$$
\mathrm{HDOP} \times \sigma_{\mathrm{UERE}} = \sqrt{{\sigma_x}^2 + {\sigma_y}^2}
\tag{4.20}
$$

$$
\mathrm{VDOP} \times \sigma_{\mathrm{UERE}} = \sqrt{{\sigma_z}^2}
\tag{4.21}
$$

$$
\mathrm{PDOP} \times \sigma_{\mathrm{UERE}} = \sqrt{{\sigma_x}^2 + {\sigma_y}^2 + {\sigma_z}^2}
\tag{4.22}
$$

4.3.3 Computational Complexity

The computational complexity of MIMO detection technique for GPS bistatic radar is highly dependent on the length of integration process, sizes of the phased-array receiver and MIMO configuration. For a SISO radar system, only the correlation process is involved in the target detection at each tentative position, $\boldsymbol{p}_{\Delta}$. Hence, the computation is dominated by the integration length applied for the detection. As a result, it needs $\mathcal{O}(K)$ flops in total. If a phased-array receiver with dual-polarised elements is utilised, then the system requires to perform $2M$ of correlation process. This would increase the computational complexity to $\mathcal{O}(2MK)$. For a MISO/MIMO radar systems, the target detection is performed by non-coherently integrating the signal reflections from L GPS satellites at B receivers. This would result in the computational process of $\mathcal{O}(2BLMK)$.

Since the targets presences are unknown, the size of the 3-D search grids for the positions and velocities of targets also contribute to the computational complexity of the detection process. At each dimension, given the size of the position search range as P_{x}, P_{y}, P_{z} and the velocity search range as V_{x}, V_{y}, V_{z}, the overall computational complexity for a GPS MIMO radar will become $\mathcal{O}\left(2\mathrm{P}_x\mathrm{P}_y\mathrm{P}_z V_x \mathrm{V}_y \mathrm{V}_z BLMK\right)$.

4.4 Simulation of Target Detection Results for GPS MIMO Radar

This section will show the simulation results for a GPS bistatic radar system based on the MIMO detection technique as discussed in Section 4.2. These results were processed under different assumptions of target parameters and detection scenarios. Several properties of the simulated data for the MIMO detection scenarios are common to its phased-array counterpart considered in Section 3.5.4. Firstly, the signals are generated at a sampling rate 256 times higher than the real C/A code chipping rate. Prior to the MIMO detection process, a decimation filter is applied to the original data to reduce the sampling rate down to 4.092 MHz which is approximately equal to the sampling rate of the experimental receiver that will be described in Chapter 5. Then, the data is interpolated to 16.368 MHz for the detection process. The total data length is set as 100 ms. Also, each receiving site uses the conventional beamforming technique with a 32-element phased-array antenna to capture the target reflections. Theoretically, the 32-element array gain and 100 ms coherent integration increase the SNR by about 65 dB before non-coherent integration is applied.

4.4.1 Target Detection (SISO vs. MISO)

The use of signals from multiple GPS satellites for air targets detection is possible when the targets appear within the transmitters LOS. In this section, a comparison of a receiver's detection performance will be made between the use of a single (i.e. SISO configuration: 1×1) and multiple (i.e. MISO configuration: L×1) transmitters. This detection scenario includes a moving target within the search range of a 32-element phased-array GPS receiver. Also, this simulation assumes that 6 GPS satellites appear at different directions relative to the target. These transmitters are widely separated in the same constellation pattern of GPS satellites and also use independent C/A code patterns in their broadcasts. Among these satellites, TX1 to TX4 are located at a high elevation angle while TX5 and TX6 are situated at low elevation angle. The positions of the target, transmitters and radar receiver for this simulation case are illustrated in Figure 4.6.

In this simulation, target detection is performed using simulated data that contains 6 GPS signal reflections from a target with equal input SNR of −59 dB at the input of a receiver. Prior to applying non-coherent integration, this input SNR level is assumed to be enhanced by the aforementioned GPS bistatic radar system to achieve an output SNR of 6 dB. The reason for choosing such a weak input SNR level is to demonstrate the significance of the MISO technique in improving the target returns over the SISO technique. Therefore, a comparison of detection performance was made between the results that perform non-coherent integrations of target reflections from 1, 2, 4 and 6 GPS SVs. By applying the MISO target detection model, the normalised 2-D target detection results are shown in Figure 4.7. The dynamic range of the correlation values from these results is limited to a minimum of −15 dB relative to the highest peak.

From the analysis, the detection performance of the 6x1 configuration was superior to those that applied integration over fewer transmitters. Firstly, the correlation peak was narrower which results in a more accurate target position estimate (i.e. smaller deviation from the true target position). Besides, its overall noise floor is visually observed to be lower. This observation also implies that detection process using higher numbers of target reflections integrations achieve a better output SNR, hence reducing the fluctuations of target location estimation results. However, there is no significant improvement of the positioning accuracy between the results from 4×1 and 6×1 configurations. The reason is that the locations of the transmitters for 4×1 configuration has achieve good DOP and its output SNR is also sufficiently high. On the other hand, the target positioning result from the 2×1 configuration does not

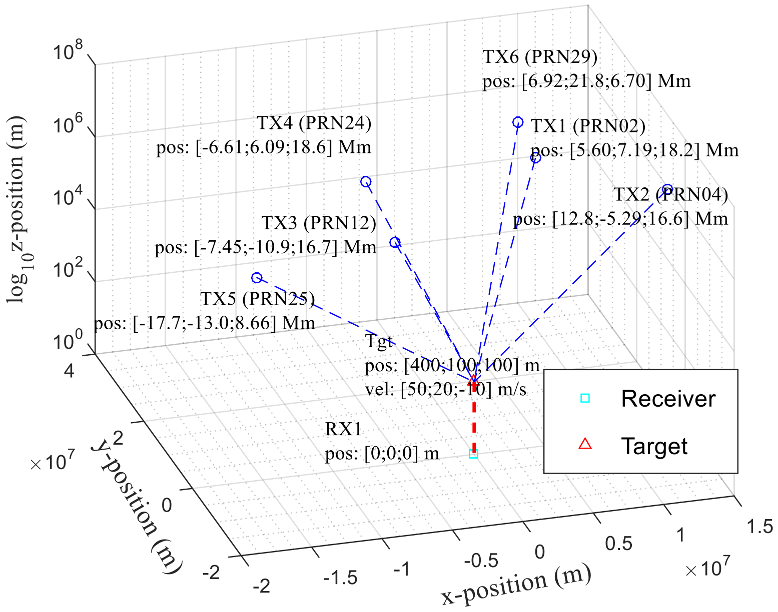

Figure 4.6: Simulated geolocation of target detection (4TX and 1RX). Note that the unit ‘Mm’ denotes Mega (10^6) metre.

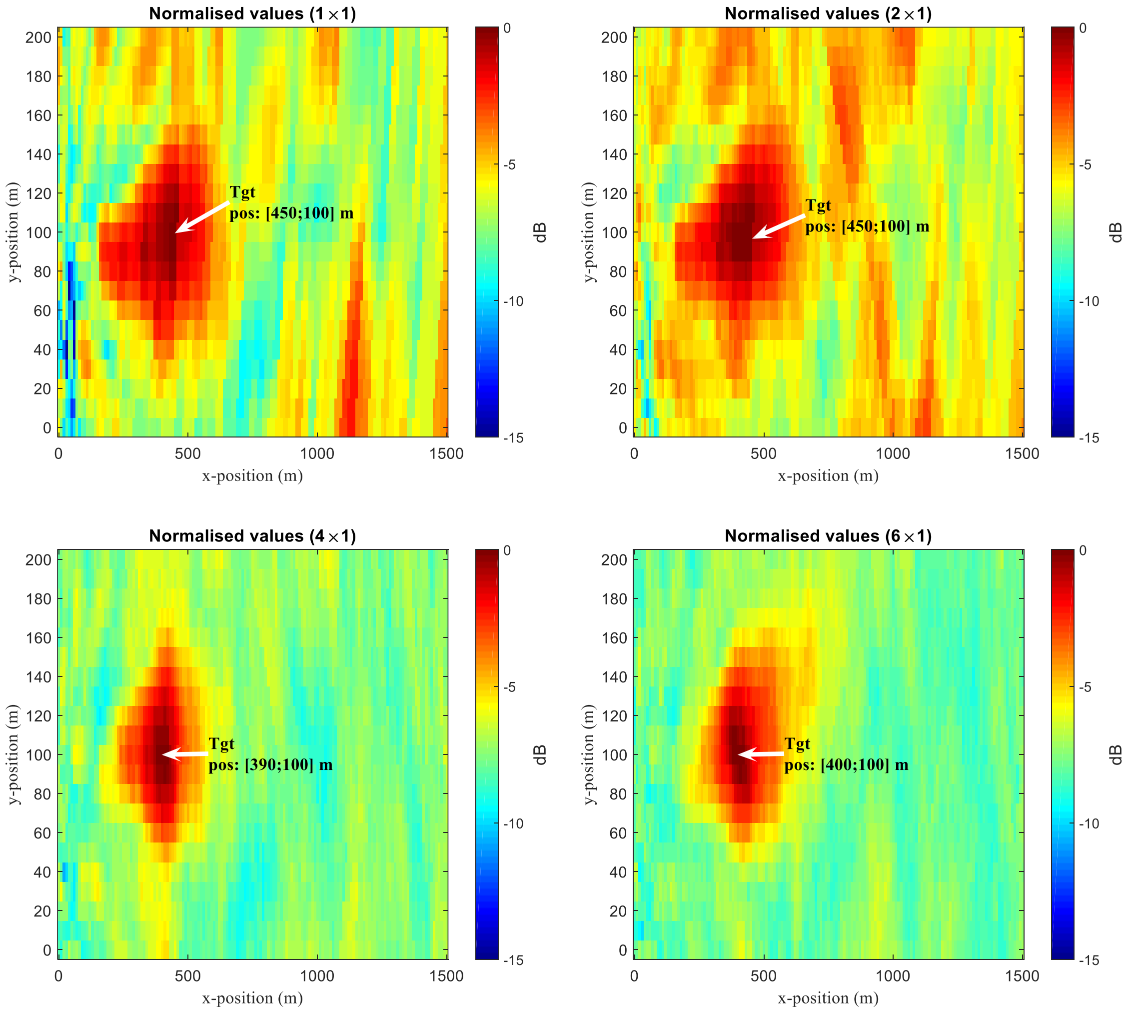

Figure 4.7: Target location estimation results (normalised) from L×1 GPS MISO radar systems with 10 m search resolution using integration of different numbers of SV.

demonstrate any significant improvement over the 1×1 configuration due to the poor DOP for the location of the additional transmitter relative to the target and receiver.

In addition, the velocity estimates from target returns using different number of non-coherent integrations are also obtained. To compare the accuracy of the simulation results, the error between the magnitudes of the true target velocity and the readings from the measurements at all searched position bins are given in Figure 4.8. From these results, the detection that integrated target reflections over 4 and 6 transmitters had virtually no error in the location corresponding to the target returns. In contrast, when using fewer number of integration, the velocity of the target cannot be determined accurately. In summary, these simulation results imply that the MISO technique benefits the GPS bistatic radar in achieving a higher SNR on the target return while also obtaining more precise target parameters.

Further analysis of target detection performance between different numbers of integrations was also made using Monte Carlo experiments (MCE). Using these experiments, the target detection using the MISO technique was performed repeatedly with randomly generated AWGN applied to the input signals at each consecutive run. Then the correlation value, target position and velocity estimated from each run are recorded.

The detection performance can be determined through the collection of correlation values from the detection performed in the MCE. Then, the correlation processes were made in two cases where the phases between the target reflection and the matched filter are: (i) misaligned, and, (ii) aligned. Hence, these outcomes represent the hypotheses of the absence of signals, $\mathcal{H}_0$, and the presence of signals, $\mathcal{H}_1$, respectively. The distribution of correlation values from these two hypotheses are represented by histograms. Hence, the probability of detection of the systems can be determined from $\mathcal{H}_1$ for a given CFAR applied to $\mathcal{H}_0$.

A comparison of the detection performance has been made between the theoretical benchmark of non-coherent integration shown in Figure 4.4 and the simulation results performed by 20,000 detection processes from the MCE. Initially, the input data for different GPS MISO radar configurations are applied with different levels of input SNR. The input SNRs and their corresponding matched filter output SNRs (i.e. before applying non-coherent integration) are recorded in Table 4.1. Note that the matched filter output SNRs are equal to the 90% $\mathbb{P}_\mathrm{D}$ case in Figure 4.4.

MISO configuration	1×1	2×1	4×1	6×1
Input SNR (dB)	−53.28	−55.60	−57.85	−59.13
Matched filter gain (dB)	65			
Matched filter output SNR (dB)	11.72	9.40	7.15	5.87

Table 4.1: Summary of the input and pre-integrator SNR for various MISO configurations.

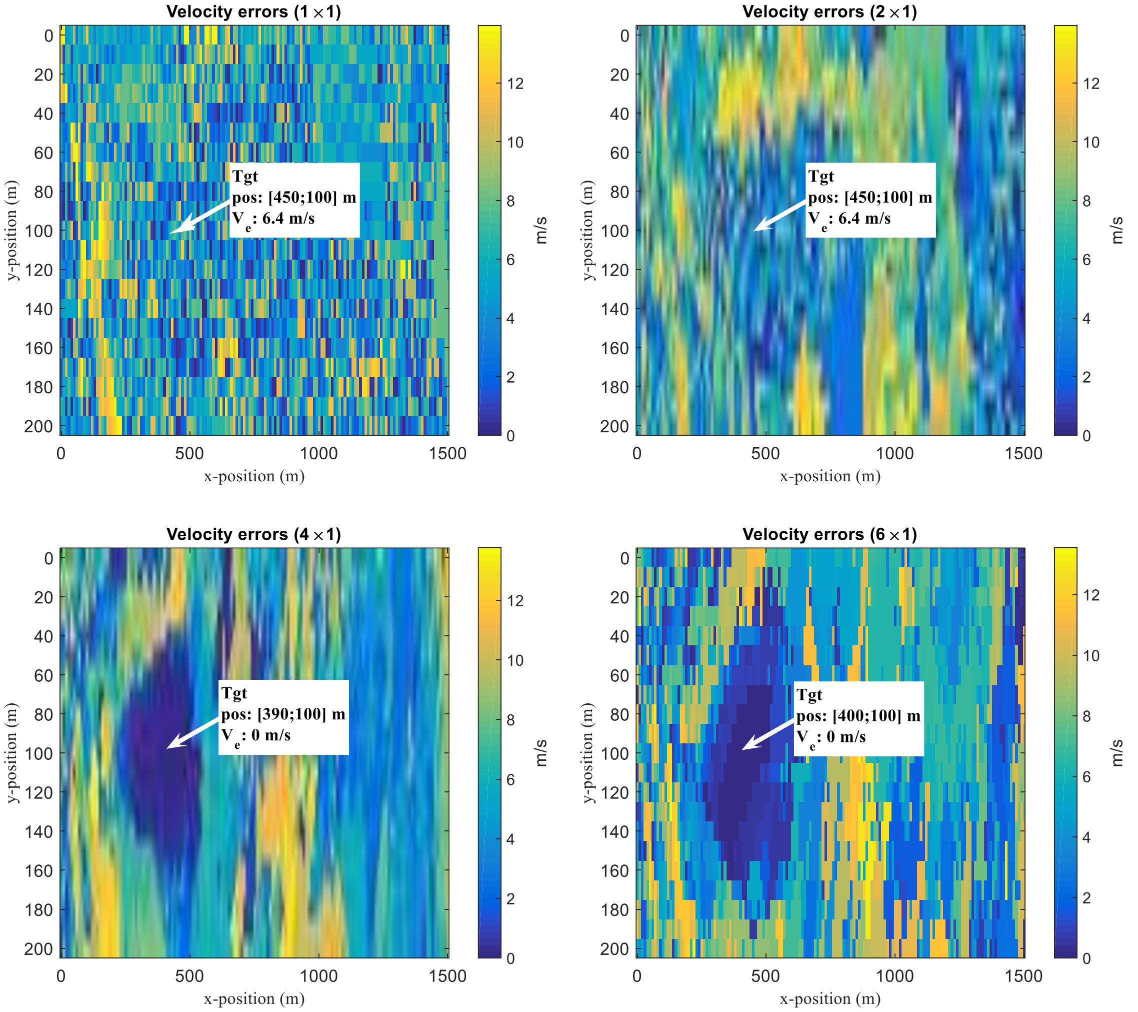

Figure 4.8: Errors between the magnitudes of true target velocity (i.e. 54.78 m/s) and the readings from the measurements of L×1 GPS MISO radar target location estimation results.

The histograms of the correlation value distribution at the output of the non-coherent integrators under both $\mathcal{H}_0$ and $\mathcal{H}_1$ from the MCE are compared with the theoretical standard and non-central chi-squared PDF in Figure 4.9. Given the required CFAR of 1%, it was observed that the statistical non-coherent integration output correlation values from all MISO configurations achieved the $\mathbb{P}_\mathrm{D}$ of approximately 90%. Besides, the histograms of these correlation values also fit well to the theoretical chi-squared PDF models.

The $\mathbb{P}_\mathrm{D}$ for a CFAR of 1% at the MCE receiver output is shown as a function of SNR in Figure 4.10 for several MISO configurations The simulated CDFs closely match the theoretical chi-squared CDF models from Figure 4.4 that are also shown on the same figure. These results indicate that the chi-squared CDF model gives a good approximation to the non-coherent integration gain, G_NC, for the MISO detection model.

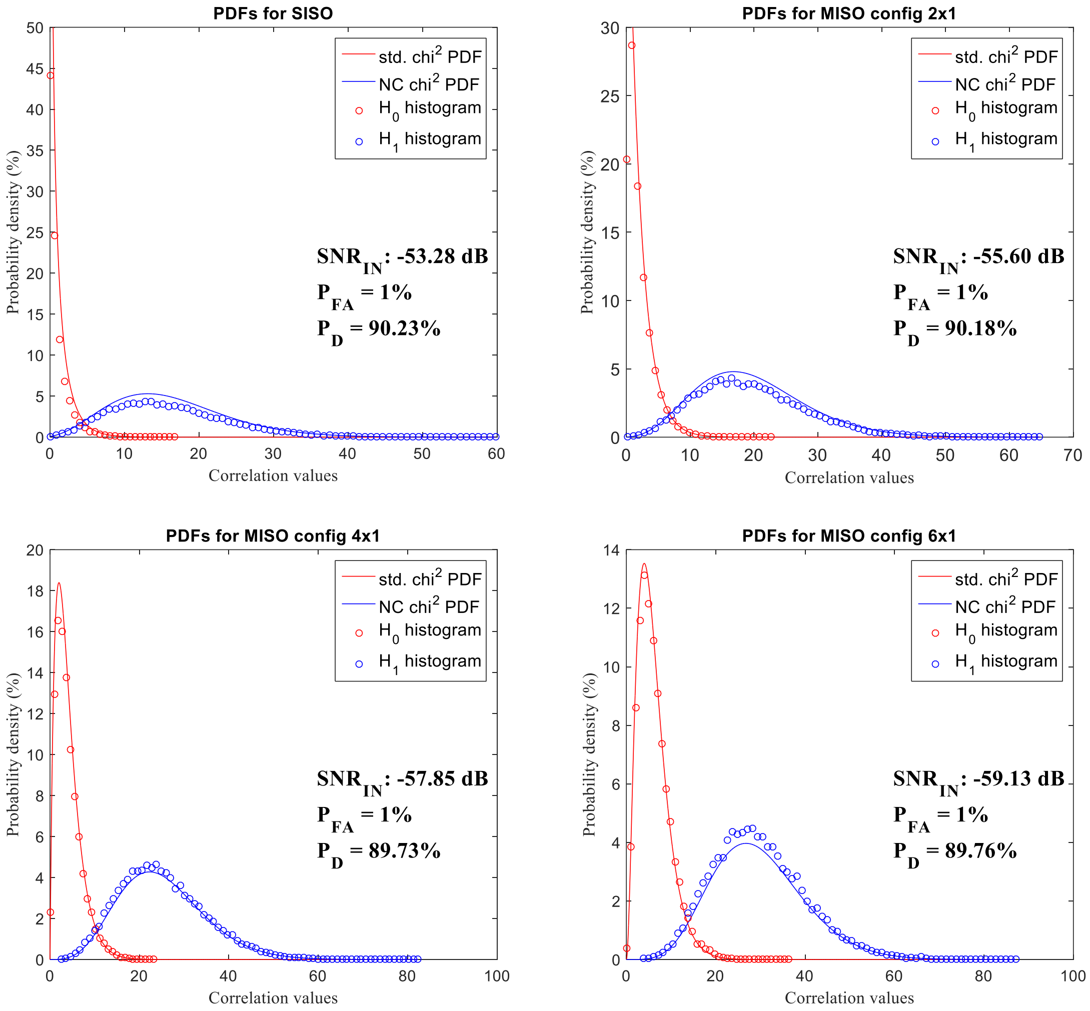

Figure 4.9: Histograms of $\mathcal{H}_0$ and $\mathcal{H}_1$ compared with the theoretical chi-squared and non-central chi-squared PDFs model respectively for L×1 GPS MISO configurations.

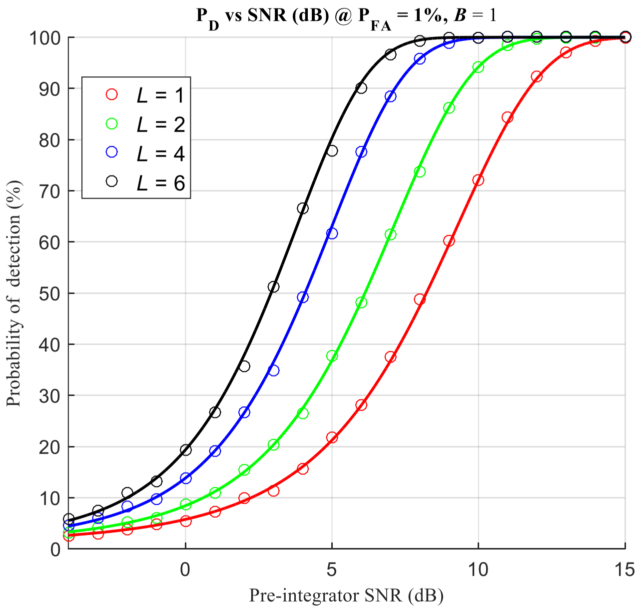

Figure 4.10: Comparison of CDFs for different numbers of non-coherent integration between the histograms given by the MCE of MISO detection results (o) and the theoretical chi-squared models (continuous lines).

The overall accuracy of the MISO technique for target positioning and velocity estimation can be determined by the root-mean-squared error (RMSE). The RMSE is measured by the RMS difference between the target parameters that correspond to the largest correlation values obtained from the MCE and the true target position and velocity. The RMSEs for both the 3-D position (pRMSE) and the velocity (vRMSE) can be measured as

$$\mathrm{pRMSE}_{\mathrm{SNR}} = \sqrt{\frac{1}{\mathcal{N}}\sum_{n=1}^{\mathcal{N}}\sum(\hat{\boldsymbol{p}}_n - \boldsymbol{p}_\delta)^2} \tag{4.23}$$

$$\mathrm{vRMSE}_{\mathrm{SNR}} = \sqrt{\frac{1}{\mathcal{N}}\sum_{n=1}^{\mathcal{N}}\sum(\hat{\boldsymbol{v}}_n - \boldsymbol{v}_\delta)^2} \tag{4.24}$$

where $\mathcal{N}$ is the total number of runs of the Monte Carlo experiment for a given input SNR.

The MCE used for estimating the accuracy of the target position and velocity was only performed using 1,000 runs due to the large computational complexity in searching for the largest correlation values at a given range. The search of target position and velocity for each run is initially performed using a resolution of 10 m and 1 m/s respectively. When the position and velocity bins that correspond to the largest correlation value is obtained, a second search of the target position is made at a finer resolution of 1 m while still retaining the velocity search resolution of 1 m/s. Finally, all the position and velocity bins corresponding to the largest correlation values are collected and used in the RMSE measurements.

Both the pRMSE and vRMSE measurements for different input SNR levels using various MISO configurations are summarised in Figure 4.11. From this figure, it is observed that at low input SNR, the pRMSE improved significantly with SNR level. The accuracy improvement reduces at stronger input SNR. Clearly, the receiver system that integrates over more transmitters achieves superior positioning accuracy over the lesser counterparts at equivalent SNR levels. The improvement also appears to be higher at low input SNR levels and gradually reduces as the input SNR level increases. The vRMSE measurement accuracy does not appear to change significantly with input SNR for the same MISO configuration. However, integrating over more transmitters also result in better accuracy for velocity estimation.

In summary, the target detection simulation results of GPS bistatic radar using L×1 MISO technique were presented in this subsection. These results demonstrate that the target detection and parameters estimation performance improves as the target reflections from a larger number of GPS satellite transmitters are incorporated at a single receiver. While no significant

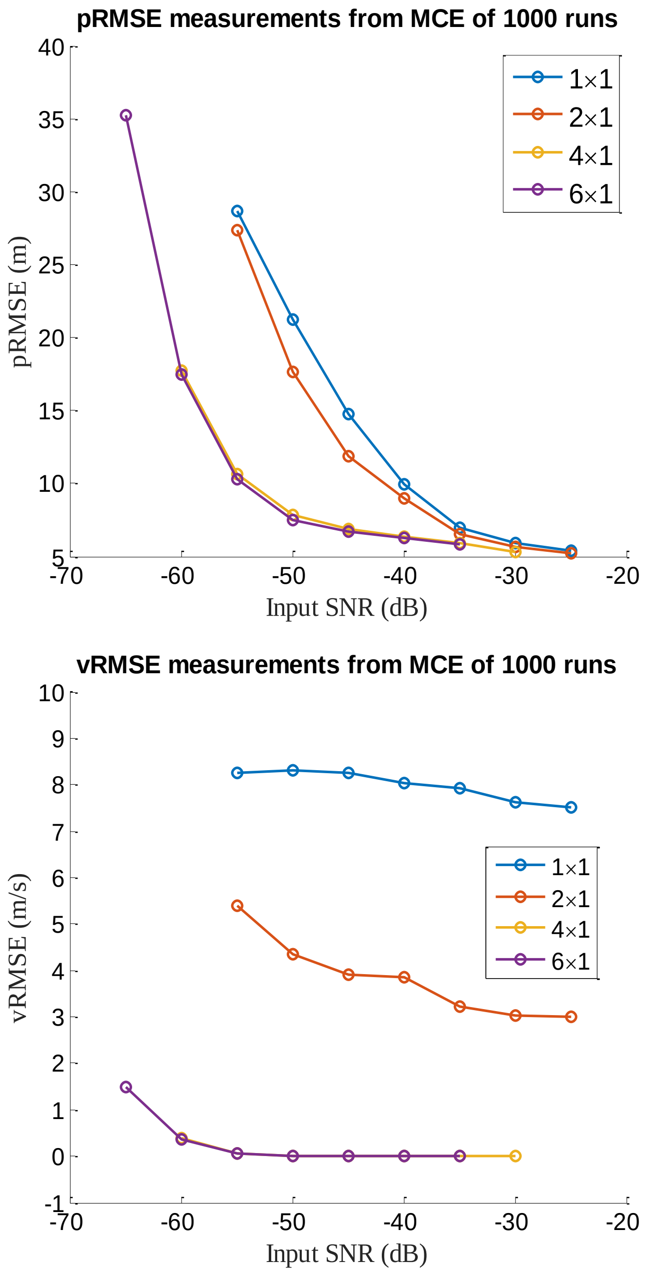

Figure 4.11: Comparison of pRMSE and vRMSE measurements obtained from the MCE between *L*×1 MISO configurations at different input SNR levels.

improvement of the positioning performance was observed between the results from 4×1 and 6×1 MISO configurations, it is suggested that a GPS bistatic radar should incorporate as many available satellites as possible to improve the SNR of target detection using the MISO technique.

4.4.2 Target Detection (MISO vs. MIMO)

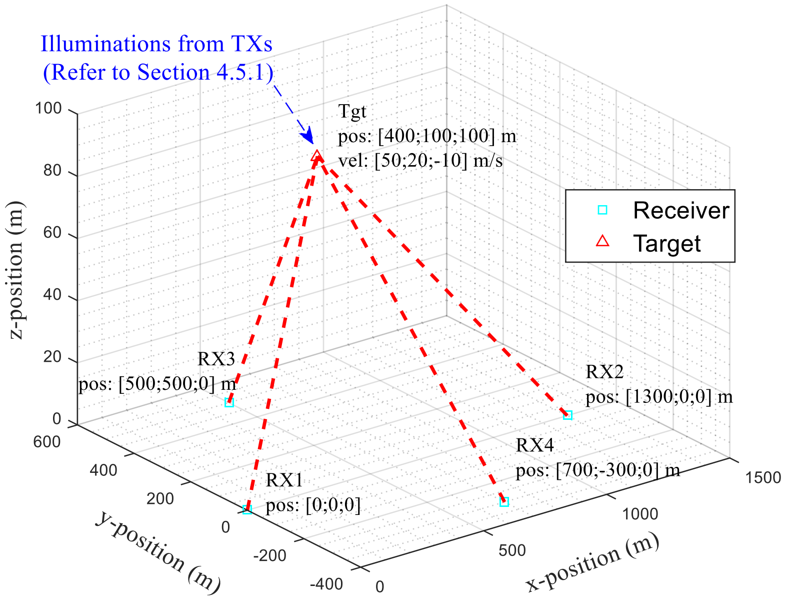

Figure 4.12: Simulated geolocation of target detection (4TX and 4RX).

While retaining the locations of the target and the first four transmitters (i.e. TX1 to TX4) as described in Section 4.4.1, the simulations in this subsection are extended to include multiple 32-element phased-array GPS receivers in the detection scenario. Hence, a comparison of detection performance is made between the use of single (MISO) and multiple receivers (MIMO). The receivers of the radar system are sparsely deployed to create good angular spreads between the target and receivers. The positions of the target, transmitters and radar receivers for this simulation are illustrated in Figure 4.12.

In this simulation, the target detection is performed using the simulated data that contains target reflections from 4 GPS satellites with equal input SNR of -59 dB at each receiver. A comparison of the detection performance will be made between the results from non-coherent integrations of target reflections using 1, 2 and 4 receivers. Each receiver is also assumed to be able to capture and perform integrations of target returns from 4 GPS SVs. By applying the MIMO target detection model, the 2-D target detection results are given in Figure 4.13. The dynamic range of the correlation values from these results is limited to a minimum of -15 dB relative to the highest peak.

From the analysis of the results, both MIMO configurations show the peak target returns at a position identical to the true target position, which demonstrates their better positioning performance over the MISO results that were shown in Figure 4.7. Two MIMO scenarios were considered: 4 transmitters and two arrays (4×2) & 4 transmitters and 4 arrays (4×4). The 4×4 configuration gives superior performance over the 4×2 configuration due to the comparatively lower noise floor being observed within the same dynamic range and the narrower target correlation peak. This implies that the positioning result using integrations from higher number of receivers will be less affected by noise fluctuations in the case where the input SNR is extremely weak.

The velocity estimated from the target returns are also obtained from the MIMO results. To compare the accuracy of the simulation results, the diagrams that show the error between the magnitudes of the true target velocity and the readings from the measurements at all searched position bins are shown in Figure 4.14. These results presented virtually no error at the location corresponding to the peak target returns. However, by using the correlation results in Figure 4.13 as a benchmark, the 4×4 configuration is likely to estimate the target velocity more accurately when the input SNR becomes lower.

Similar to the simulation case performed in Section 4.4.1, the correlation values from both hypothesis cases $\mathcal{H}_0$ and $\mathcal{H}_1$ are collected from the MCE to determine the detection performance of the MIMO systems. The detection results from 20,000 detection runs in the MCE are also compared with the theoretical benchmark of non-coherent integration in Figure 4.4. Initially, the input data for different GPS MIMO radar configurations are applied with different input SNRs. The input SNRs and their corresponding matched filter output SNRs are recorded in Table 4.2. Note that the matched filter output SNRs (i.e. before applying the non-coherent integration) are equal to the $\mathbb{P}_\mathrm{D}$ case of 90% in Figure 4.4.

MIMO configuration	4×1	4×2	4×4
Input SNR (dB)	−57.85	−60.02	−62.07
Matched filter gain (dB)	65		
Matched filter output SNR (dB)	7.15	4.98	2.93

Table 4.2: Summary of the input and pre-integrator SNR for MIMO configurations.

The histograms of the correlation values from the output of the non-coherent integrators for both $\mathcal{H}_0$ and $\mathcal{H}_1$ from the MCE are shown in Figure 4.15. These histograms are also compared with the theoretical standard and non-central chi-squared PDF. Given the required CFAR, $\mathbb{P}_\mathrm{FA}$ of 1%, it was observed that the statistical non-coherent integration output correlation values from all MIMO configurations achieved the $\mathbb{P}_\mathrm{D}$ of approximately 90% and also fitted well to the theoretical chi-squared PDF models.

The simulated $\mathbb{P}_\mathrm{D}$ as for a given $\mathbb{P}_\mathrm{FA}$ of 1% is also shown as a function of SNR in Figure 4.16 and closely matches the theoretical chi-squared CDF models from Figure 4.4. Similar to the comparison with the MISO models, these results also demonstrated that the chi-squared

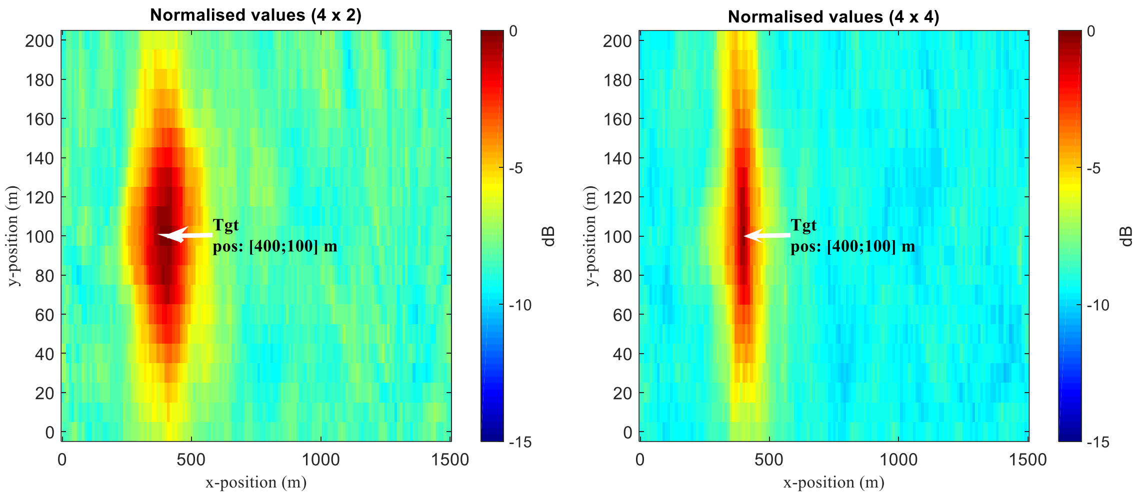

Figure 4.13: Target location estimation results (normalised) from GPS *L*×*B* MIMO radar with 10 m search resolution using integration of different numbers of receivers.

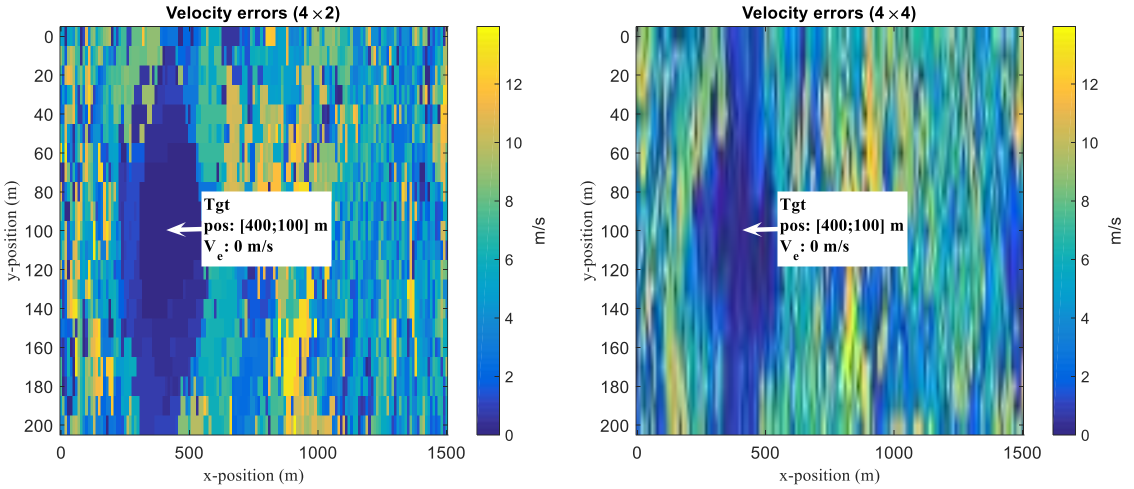

Figure 4.14: Errors between the magnitudes of true target velocity (54.78 m/s) and the readings from the measurements of *L*×*B* GPS MIMO radar target location estimates.

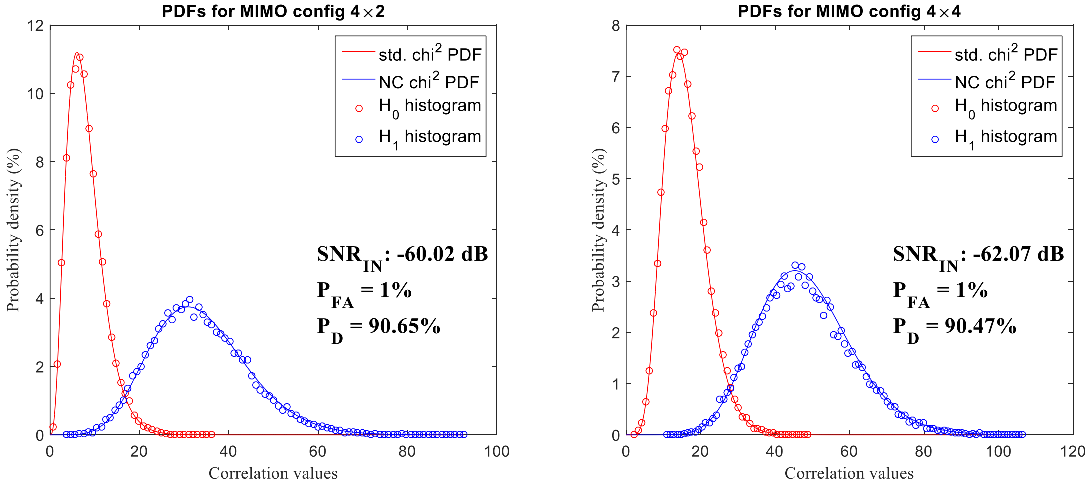

Figure 4.15: Histograms of $\mathcal{H}_0$ and $\mathcal{H}_1$ compared with the theoretical chi-squared and non-central chi-squared PDFs model respectively for *L*×*B* GPS MIMO configurations.

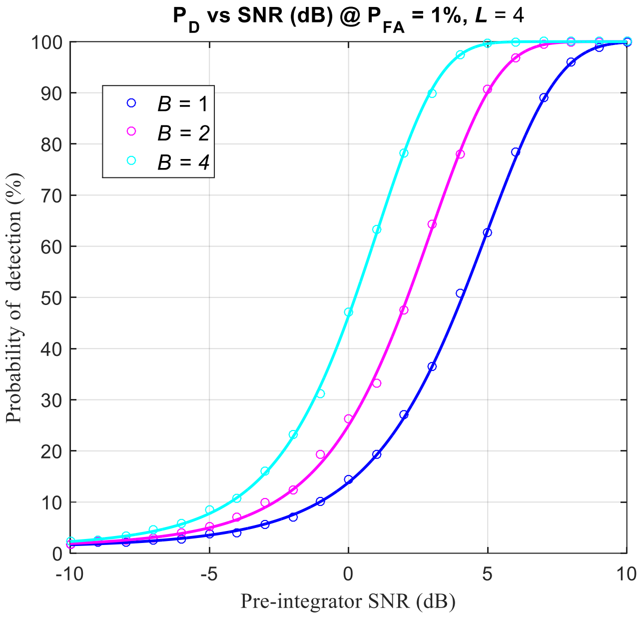

Figure 4.16: Comparison of CDFs for different numbers of non-coherent integration between the histograms given by the MCE of MIMO detection results (o) and the theoretical chi-squared models (continuous lines).

CDF model gives a good approximation to the non-coherent integration gain, G_{NC}, for the MIMO detection model.

The MCE used for estimating the accuracy of target position and velocity for MIMO detection technique was performed identically to Section 4.4.1 (i.e. same number of runs and search resolution). All the position and velocity bins correspond to the largest correlation values collected at the refine search from the MCE are used in the RMSE measurements (4.23) and (4.24) respectively.

Both the pRMSE and vRMSE measurements for different input SNR levels using the 4×1 MISO, 4×2 and 4×4 MIMO configurations are summarised in Figure 4.17. The system that integrates the target reflections with larger numbers of receivers achieves superior accuracy positioning performance over the lesser counterparts at the same SNR level. Note that the 4×4 configuration significantly improves the pRMSE value at a low input SNR. This configuration demonstrates superior accuracy in locating the target as the target distance is much shorter to the phased-array receivers RX3 and RX4, which significantly reduces the target position ambiguity. The rate of improvement gradually reduces as the input SNR level increases. Hence, the pRMSE result shows the MIMO technique gives a significant improvement in target positioning accuracy under very weak input SNR conditions. Besides, MIMO systems with more receivers achieved zero vRMSE with lower input SNRs, which implies that they performed the velocity estimation more accurately.

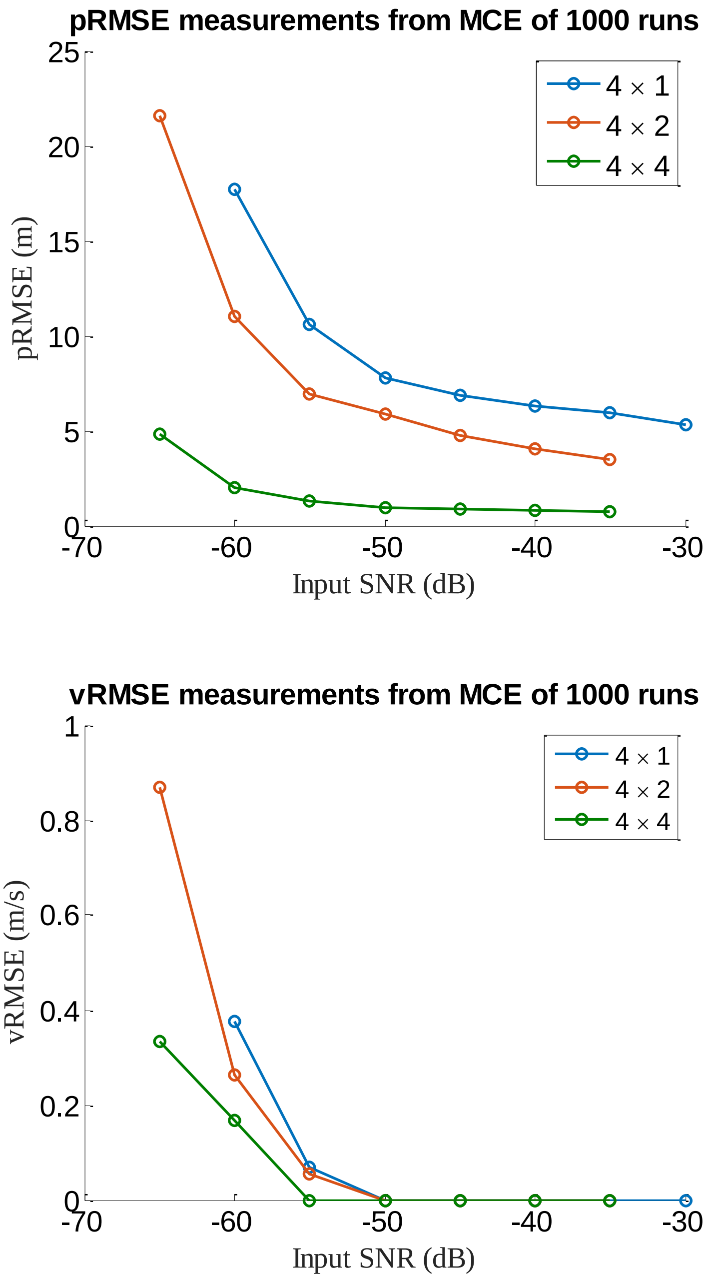

Figure 4.17: Comparison of pRMSE and vRMSE measurements obtained from the MCE between 4×1 MISO, 4×2 and 4×4 MIMO configurations at different input SNR levels.

In summary, the target detection simulation results of GPS bistatic radar using $L \times B$ MIMO technique were presented in this subsection. These results imply that with sufficient resources to increase the number of receivers, the target detection and parameters estimation performance can be improved by using multiple widely separated GPS receivers incorporated into a single radar system to capture the target reflections from multiple GPS satellite transmitters.

4.4.3 Detection for Multiple Targets (SISO vs MISO vs MIMO)

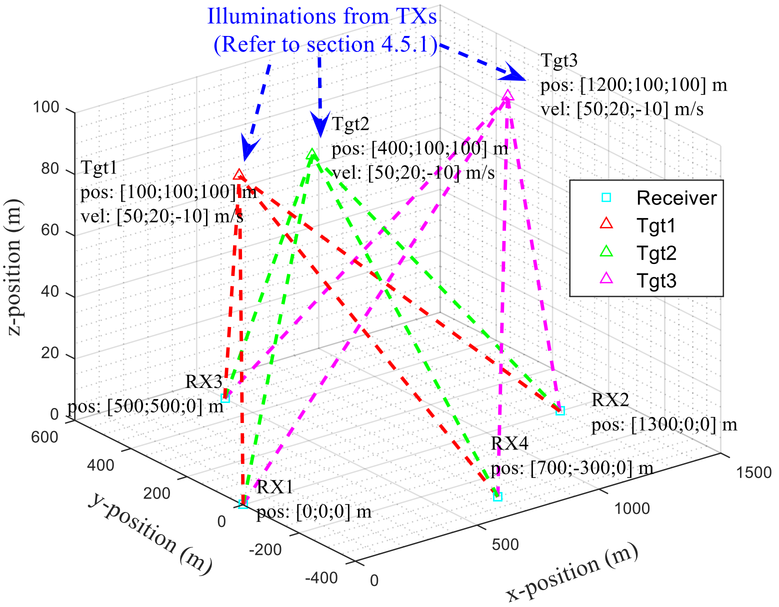

Figure 4.18: Simulated geolocation of target detection (4TX, 4RX and 3 targets).

The simulation performed for this section retains the transmitter and receiver configuration identical to Section 4.4.2, but extends the detection scenario with 3 targets moving at identical velocity. The positions of the targets, transmitters and radar receivers for this simulation are illustrated in Figure 4.18. The aim of this simulation is to analyse the target resolution produced by the radar in the detection scenario where multiple transmitters and receivers are utilised to search for multiple targets that are located within a relatively close proximity. This scenario will occur when a squadron of aircraft approaches the radar detection zone.

In this simulation case, the target detection is performed using the simulated data that contains 4 GPS signal reflections from 3 targets with equal SNR of −59 dB. A comparison of target positioning performance was made between the results produced by the 1×1, 2×1, 4×1, 4×2 and 4×4 systems. The detection results that show the 2-D target positioning and velocity estimation error given by the MISO and MIMO target detection models are shown in Figure 4.19 and Figure 4.20 respectively. Note that the dynamic range of the correlation values from these results is limited to a minimum of −15 dB relative to the highest peak.

From the analysis, the 1×1 system gave the correlation peaks of the 3 targets with comparatively high positioning and velocity estimation errors. Due to the relatively high noise floor compared to the target returns, some of the strong noise correlation values from the positioning results can be falsely identified as targets. The results improved when integration

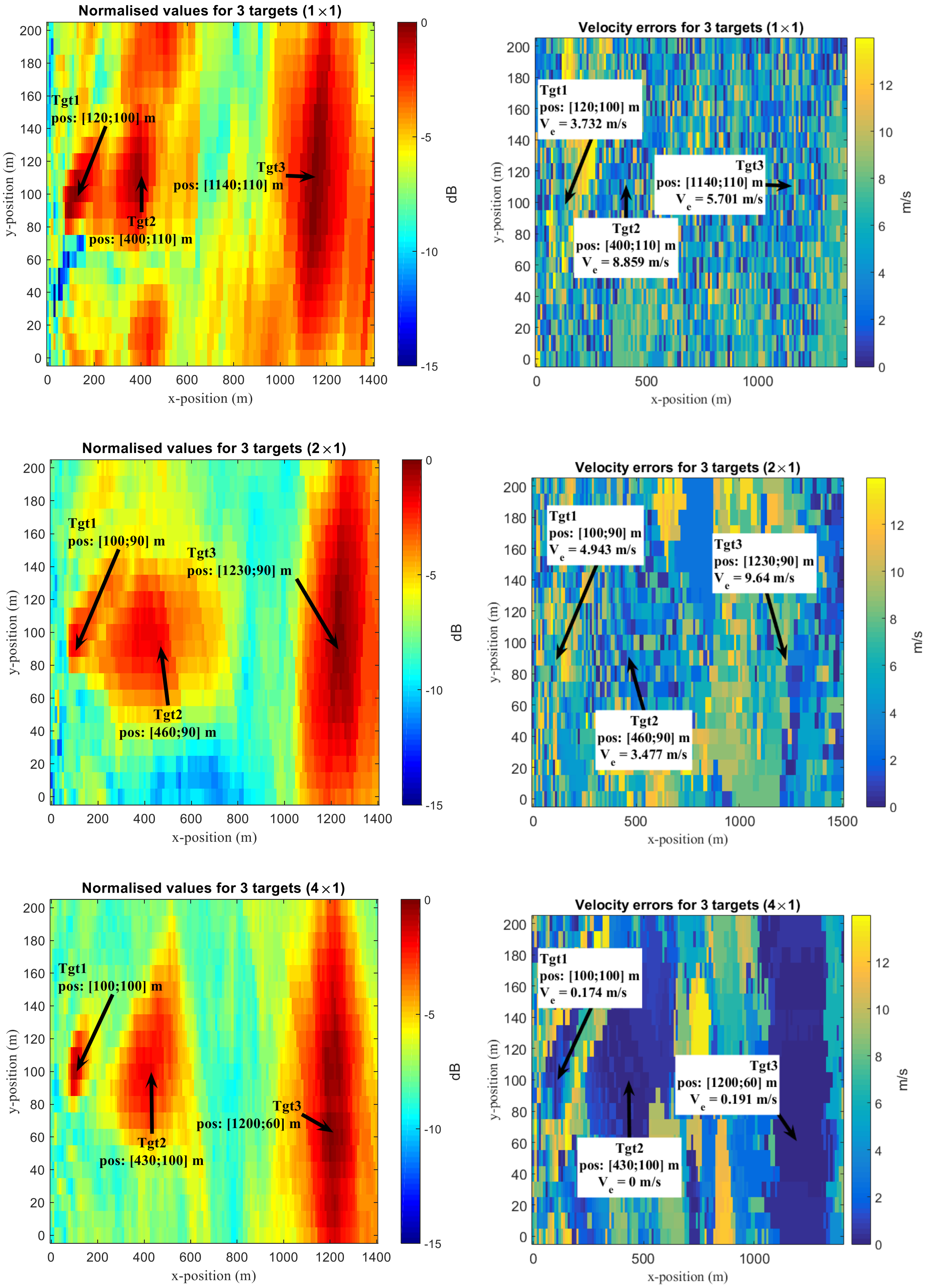

Figure 4.19: Position estimation and velocity error results of multiple targets (normalised) from GPS SISO/MISO radar systems with 10 m search resolution using the 1×1, 2×1 and 4×1 configurations.

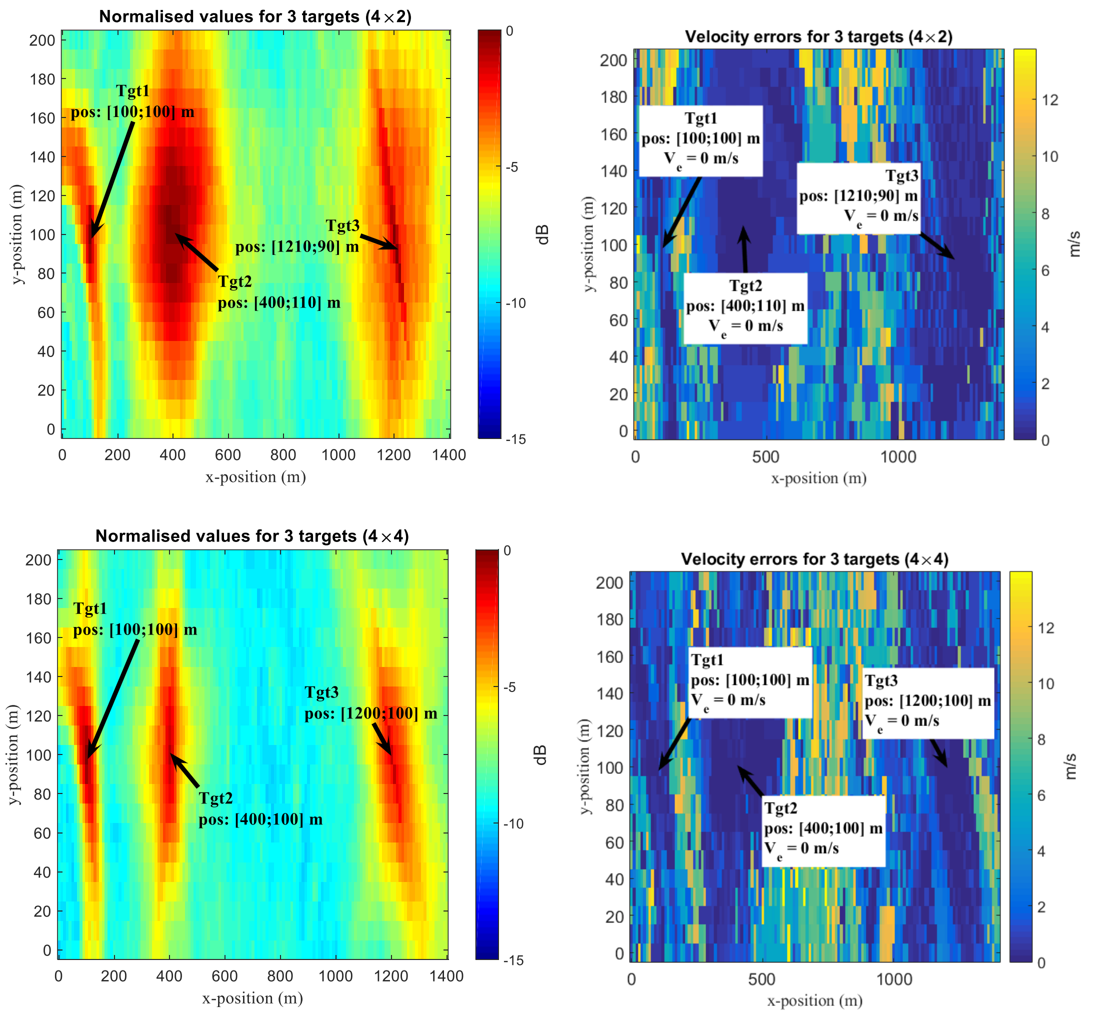

Figure 4.20: Position estimation results of multiple targets (normalised) from GPS MIMO radar systems with 10 m search resolution using the 4×2 and 4×4 configurations.

was performed over target reflections from multiple transmitters. For example, the result from the 4×1 system had a lower noise floor due to the improved output SNR, allowing the number of targets to be distinguished more clearly. Therefore, the location and velocity of targets are generally more accurately estimated by the 4×1 system compared to the lesser configurations.

Another common observation from the results of the 1×1, 2×1 and 4×1 systems is that the width of Tgt1's correlation peak is much narrower than the others. This is because the target is much closer to one of the phased-arrays where the DOA estimate is much more accurate. To improve the DOA estimation accuracy at larger ranges, a larger phased-array could be used.

Alternatively, the target resolution can be improved by applying the MIMO technique to the GPS bistatic radar system to jointly process the target reflections captured by phase array receivers at multiple sites. As demonstrated by the 4×2 and 4×4 systems, their results gave better output SNR and more accurate positioning and velocity estimation for all the targets than the MISO configurations. The reason is that RX2 is relatively close to Tgt 3 while RX3 and RX4 are relatively close to Tgt2.

In summary, the simulation results in this subsection show that the target resolution improves when the reflections from more GPS transmitters are jointly processed, and further improves when more sparsely deployed large scale phased-array receivers are incorporated into the system's detection process. These results also demonstrate that the number of aircraft in a squadron can be identified by the radar system when it has sufficient target searching resolution.

4.4.4 Target Tracking for GPS MISO/MIMO Radar

In the previous sections, the simulated target velocities were relatively low and the detection used a relatively short integration time. Hence, these simulations assumed that the target parameters such as Doppler frequency, the TDOA relative to the direct-path signal and the DOA relative to the receivers remain unchanged within the integration time. In practice, variations of these parameters become more significant as the target velocity increases or the integration time applied to the detection process increases. This section aims to demonstrate the capability of tracking targets that are cruising at high velocities. The detection scenario in this simulation includes 3 moving targets that appear at slightly more than 2 km apart from the radar receiver moving at different constant velocities: final approach speed at [50; 20; −10] m/s, subsonic cruising speed at [500; 200; −10] m/s and supersonic cruising speed at [2000; 2000; 0] m/s. The transmitter configuration is still identical to the previous scenarios. In this simulation, the initial positions of targets and a radar receiver are given in Figure 4.21.

Variations in the anticipated discrete target parameters, such as the positions, Doppler frequencies and sample delays relative to the direct-path GPS signals and DOAs relative to the receiver due to targets' motion are demonstrated in Figure 4.22. Due to the significant variations of these parameters, applying long integration periods for the receiver without a tracking technique will affect its detection performance. On the other hand, without using the matched filters with adequately long integration periods, it can be difficult to extract the target information due to the extremely weak input SNRs of the GPS reflections from the target. Hence, as illustrated in Figure 4.23, a TBD method can be applied by locally generating a matched filter that is adaptive to the target motion within the time frame of the detection. This approach maintains the SNR gain of a long integration period without being degraded by the samples phase variations. Since an aircraft spends the majority of its flight time in cruise speed

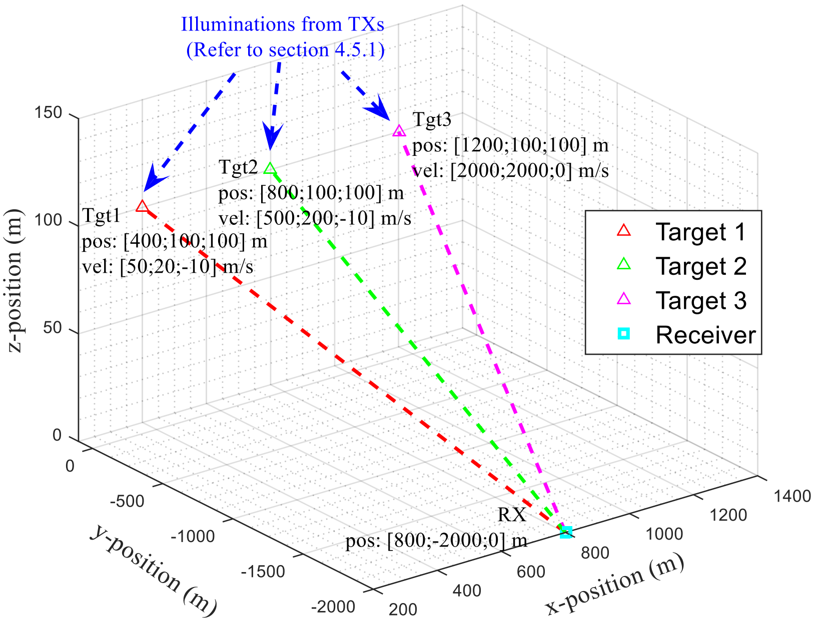

Figure 4.21: Simulated geolocation of target detection (4TX, 1RX and 3 targets).

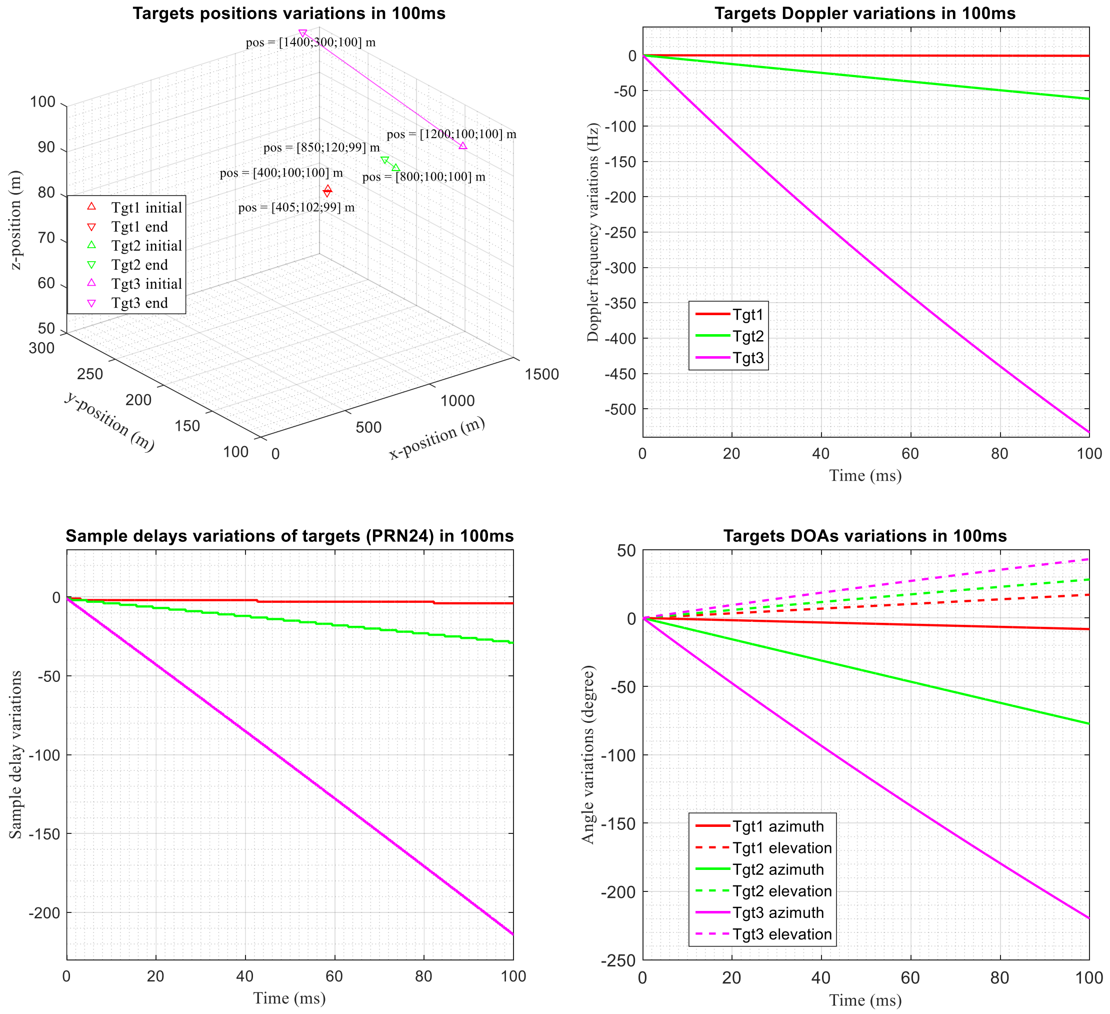

Figure 4.22: Variations in targets positions, Doppler frequency, sample delays and DOAs due to their corresponding motions in 100 ms.

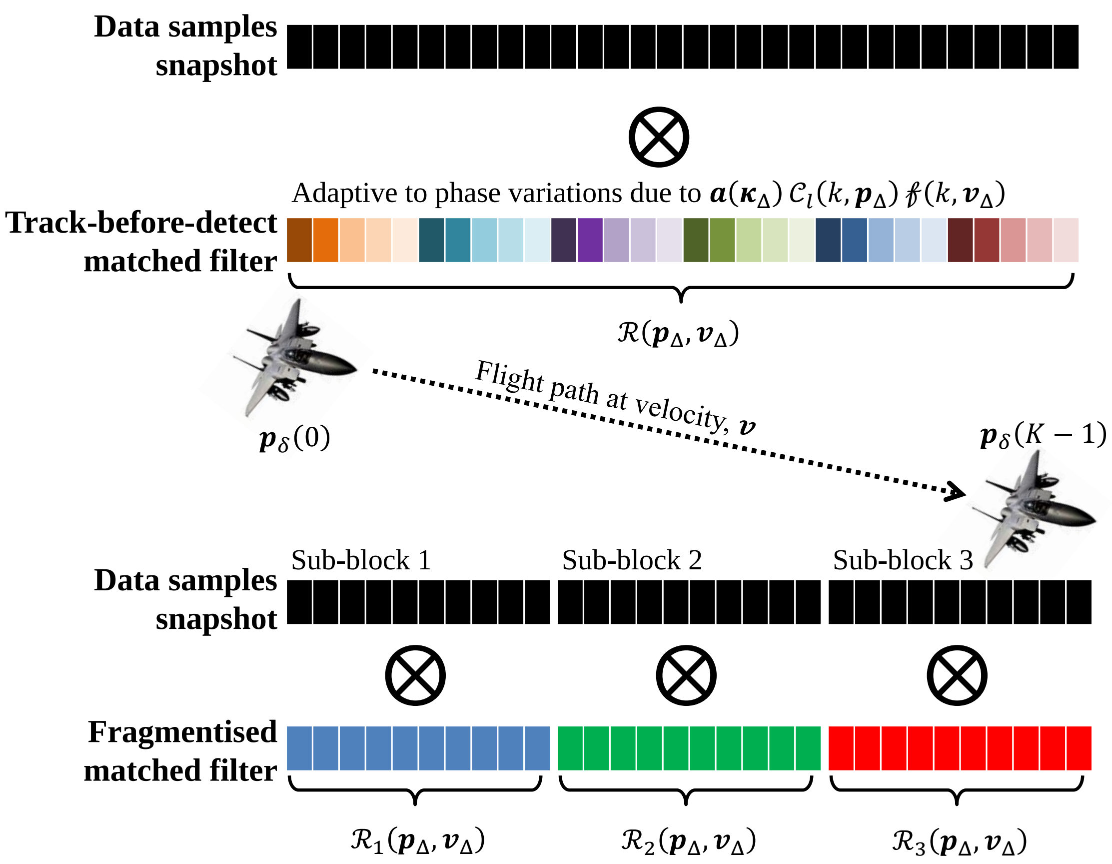

Figure 4.23: Illustration of matched filter for tracking target in the detection process using the TBD (Top) and integration with fragmentised data samples (Bottom) methods.

to maintain fuel efficiency, the TBD method can assume constant target velocity across the detection time frame. When the target returns at the matched filters output exceeds the detection threshold, the initial positions of these targets and their corresponding velocities will be positively identified, hence showing the flight paths within the processing time frame. This approach can also track and detect targets that performed complicated flight paths such as evasive manoeuvres or steep accelerations/decelerations during the flight's ascent/descent. However, the search process for non-linear motions is less practical as the search space greatly increases, resulting in a much higher computational load.

Another method to track targets with weak reflections is also illustrated in Figure 4.23. This method firstly fragments the captured data samples into shorter sub-blocks. Then, independent detection process is applied to each sub-block using individually generated matched filter. Due to the shorter integration period, the SNR gain of this method is inherently inferior to the TBD counterpart. However, the matched filters can be generated with constant phases across the detection frame in each sub-block since the shorter integration period is less vulnerable to phase variations and is therefore more computational efficient. The positive returns of matched filter outputs at each sub-block will indicate the discrete position shift of a target across the whole data blocks. Based on the detection model (4.5), the correlation function of integrating the data at sub-block time frame, $\Bbbk$, can be expressed as

$$\begin{aligned}\mathcal{R}_{l\Bbbk}(\boldsymbol{p}_\Delta,\boldsymbol{v}_\Delta) &= \sum_{k=(\Bbbk-1)\bar{K}}^{\Bbbk\bar{K}-1}\sum_{m=1}^{M} a_{m\Bbbk}{}^{*}(\boldsymbol{p}_\Delta)\, x_{\delta ml}(k,\boldsymbol{p}_\delta,\boldsymbol{v}_\delta)\, h_{l\Bbbk}(k,\boldsymbol{p}_\Delta,\boldsymbol{v}_\Delta) \\ &= \mathcal{R}_{s\Bbbk}(\boldsymbol{p}_\Delta,\boldsymbol{v}_\Delta) + \mathcal{R}_{n\Bbbk}(\boldsymbol{p}_\Delta,\boldsymbol{v}_\Delta)\end{aligned} \qquad (4.25)$$

where $\bar{K}$ is the length of each sub-block, $\Bbbk = 1,2,\dots,\mathbb{K}$.

A comparison of the detection performance will be made between the aforementioned tracking techniques. The target detection simulation is performed on simulated data that contains 4 GPS signal reflections from 3 moving targets with equal SNR of -50 dB and reflectivity. Using the MIMO target detection model, the individually normalised target detection results using: (i) TBD techinque is shown in Figure 4.24 while the detection results of (ii) non-tracking, and, (iii) with fragmentised data at various sub-block sizes are shown in Figure 4.25.

From Figure 4.24, the TBD result technique is able to accurately locate the initial positions of all 3 targets with relatively equal correlation values and their corresponding velocities. In addition, the search space for the target velocity in the next 100 ms can be reduced significantly by using the velocity estimate from the current detection. On the other hand, the widths of target returns are also affected by their corresponding velocities due to the Doppler sensitivities with respect to position variations. From the observation of the simulation result, the accuracy of location estimation for slower targets is readily affected by noise fluctuations while the faster targets require a higher search resolution to be located.

The effect of sub-block size on the fragmentised detection process is also analysed using sub-block sizes of 10 ms, 25 ms, 50 ms and 100 ms. While the slow moving Tgt1 can be detected by all techniques, the correlation value (not shown in the results) using the 100 ms integration is higher than for the fragmentised integration processes and comparable to the TBD results. This outcome demonstrates that longer integration periods improve the target SNR. However, it fails to identify the presence of all other faster targets. The subsonic cruising Tgt2 returns can be identified by all fragmentised integration processes. Its normalised correlation value is compared with Tgt1's results to show the integration losses due to the target motion.

From Table 4.3, it is observed that the integration losses for fast target returns is less significant for shorter integration times as it is less susceptible to the residual Doppler

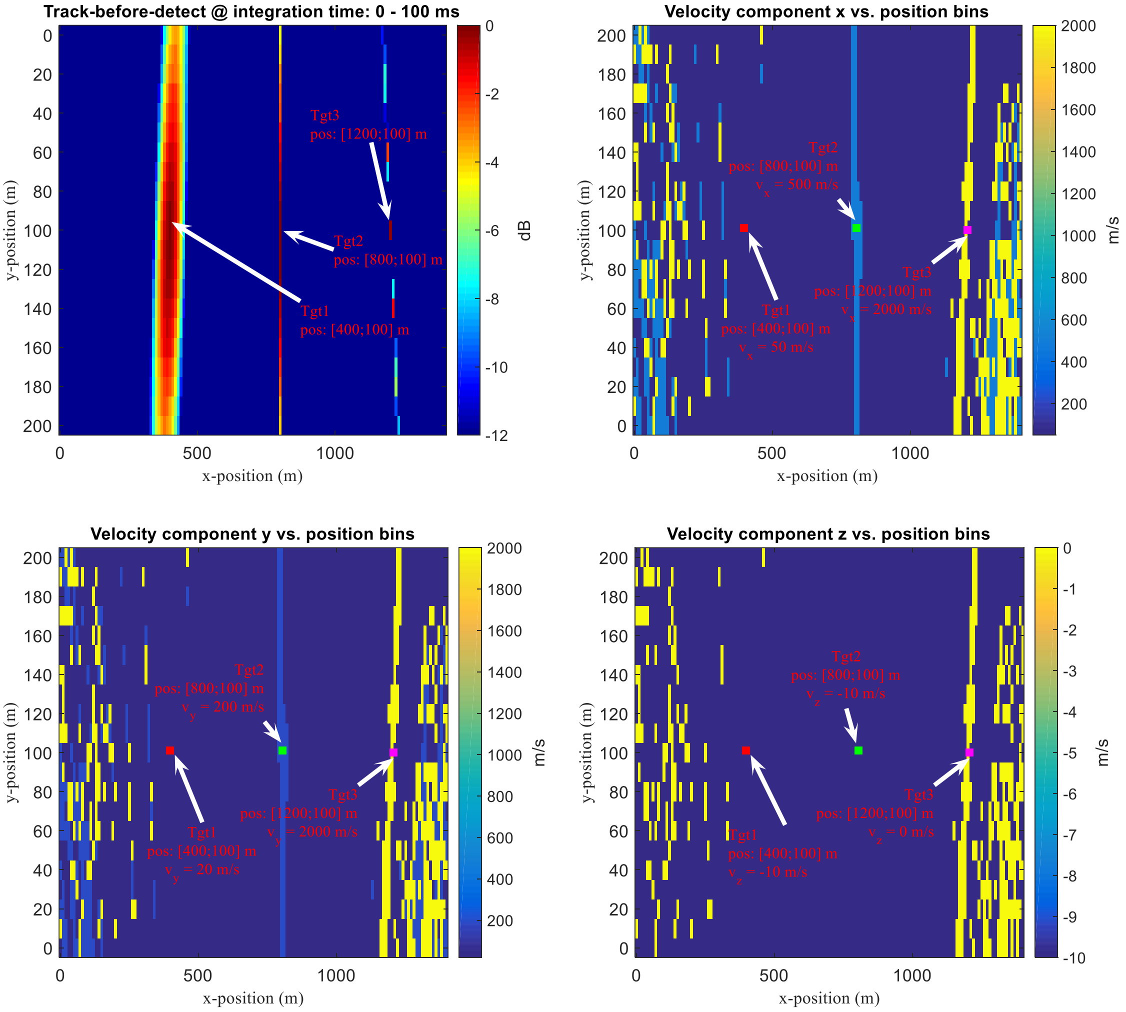

Figure 4.24: MIMO radar target location estimation results (normalised) at 10 m search resolution (Top Left) and their corresponding 3-D velocity components using the TBD technique. The velocity vector estimates for all identified targets are [50; 20; −10], [500; 200; −10] and [2000; 2000; 0] m/s respectively.

components. However, using shorter integration times makes it harder to resolve closely spaced targets as the correlation peaks get broader. The supersonic cruising Tgt3 fails to be identified by all the processes. Although this issue can be compensated by fragmentising the data to even shorter sub-block lengths, this will also result in a lower SNR.

Sub-block length (ms)	Tgt1	Tgt2
50	0	−3.155
25	0	−0.9
10	−0.078	0

Table 4.3: Summary of the normalised correlation values between Tgt1 and Tgt2 using the fragmentised integration process of various lengths.

Next, the tracking capability of the fragmentised integration process is analysed. This analysis ignores the tracking of Tgt1 as the effect of the position variation is minor due to its

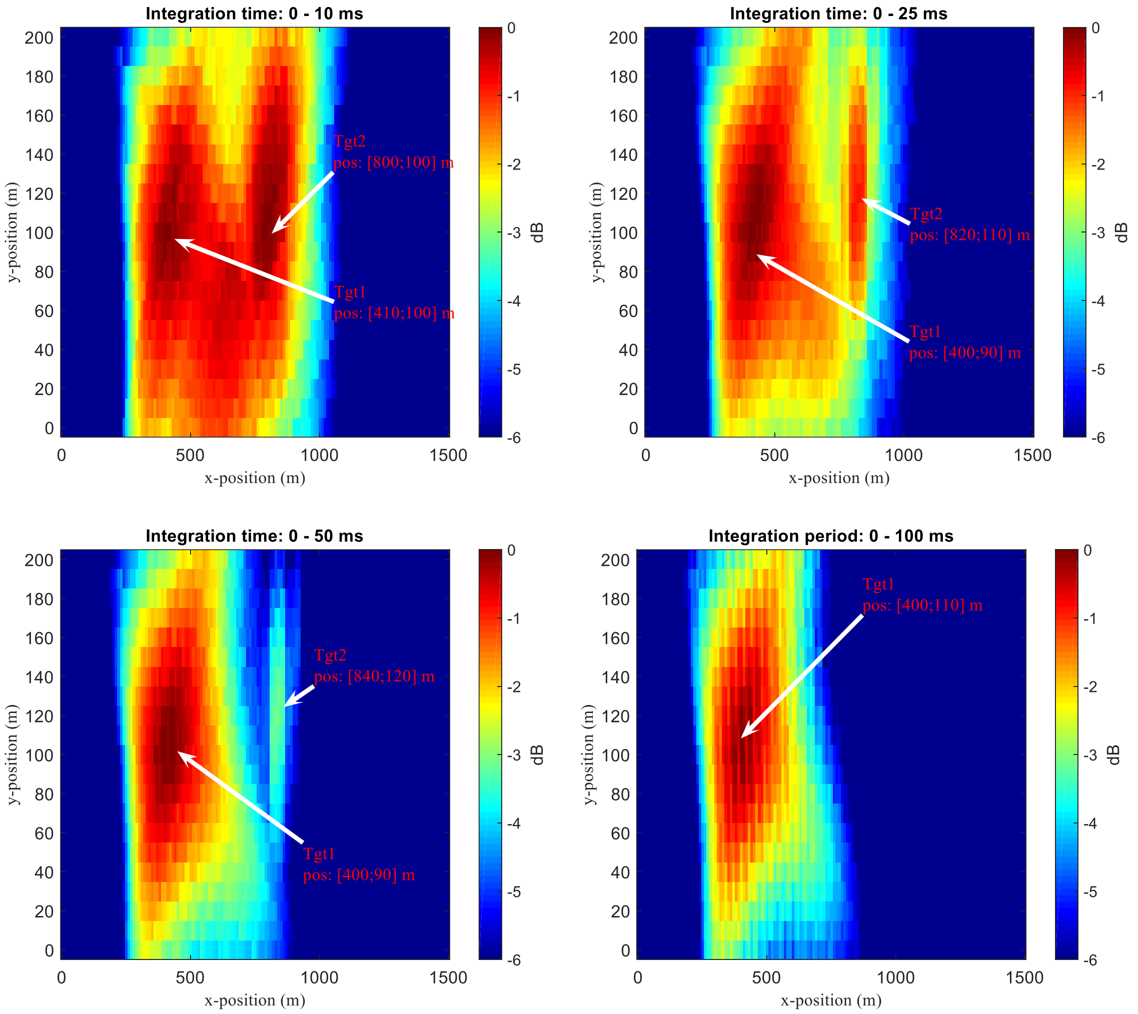

Figure 4.25: MIMO radar target location estimation results (normalised) at 10 m search resolution using the integration of the first sub-block fragmentised data of 10 ms, 25 ms, 50 ms and full integration process of 100 ms (i.e. no fragmentisation).

extremely low velocity and poor ambiguity function. In Figure 4.26, an example that used the sequence of locations estimated from the 25 ms sub-block integrations is shown. This sequence demonstrates the capability of tracking Tgt2 by observing the update of its position at individual time frames. Note that the target velocity measurements from the integration process are not required. However, it can still be used as supplementary tracking information for the detected target. An example of the 2-D velocity result taken from the integration process of fragmentised data sub-block 0 - 25 ms is shown in Figure 4.27. This result demonstrates that the target velocity readings can also be taken from each processed time frame.

The accuracy of Tgt2 position was analysed for various sub-block lengths taken from a 100 ms data snapshot. The accuracy of individual tracking results are measured by the tRMSE expressed as

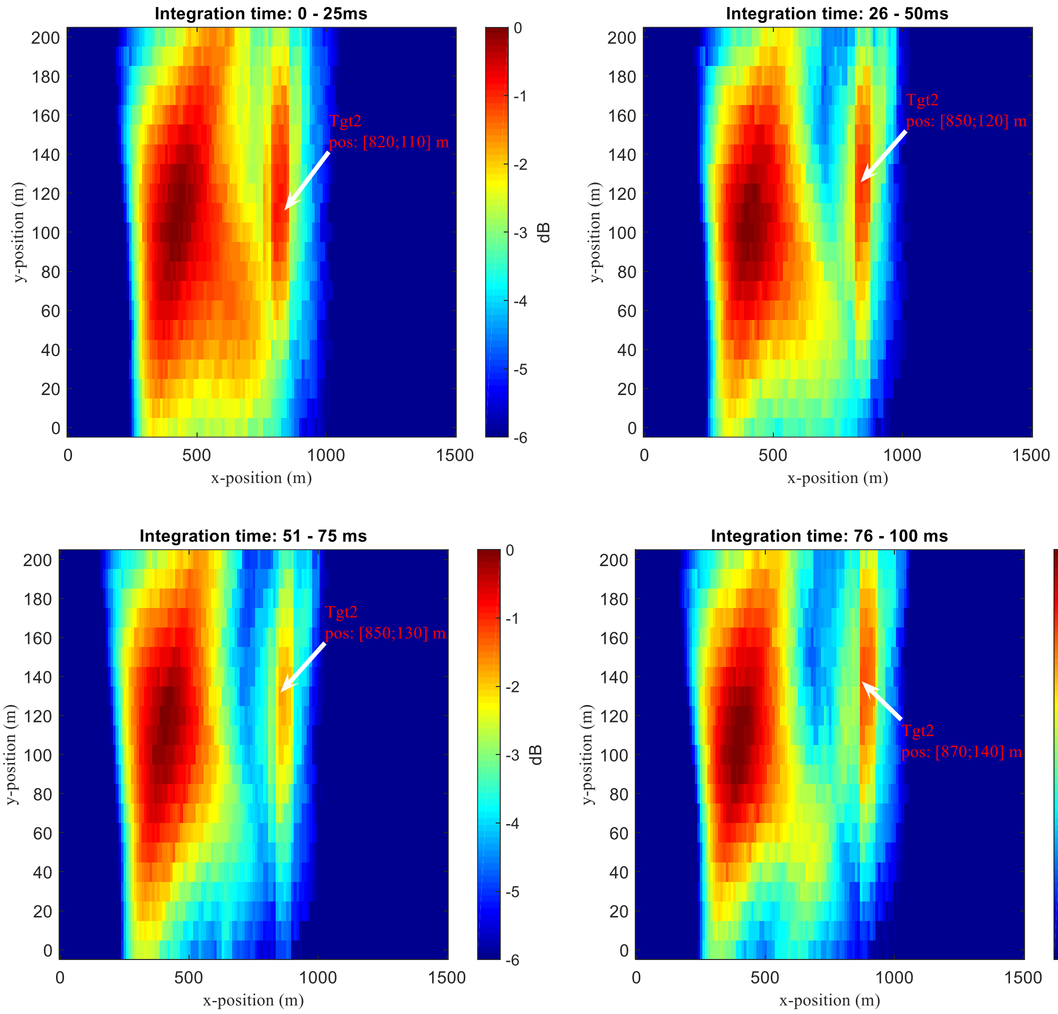

Figure 4.26: The sequence of MIMO radar target location estimation results (normalised) at 10 m search resolution using the integration of 25 ms fragmentised data sub-blocks out of 100 ms data snapshot.

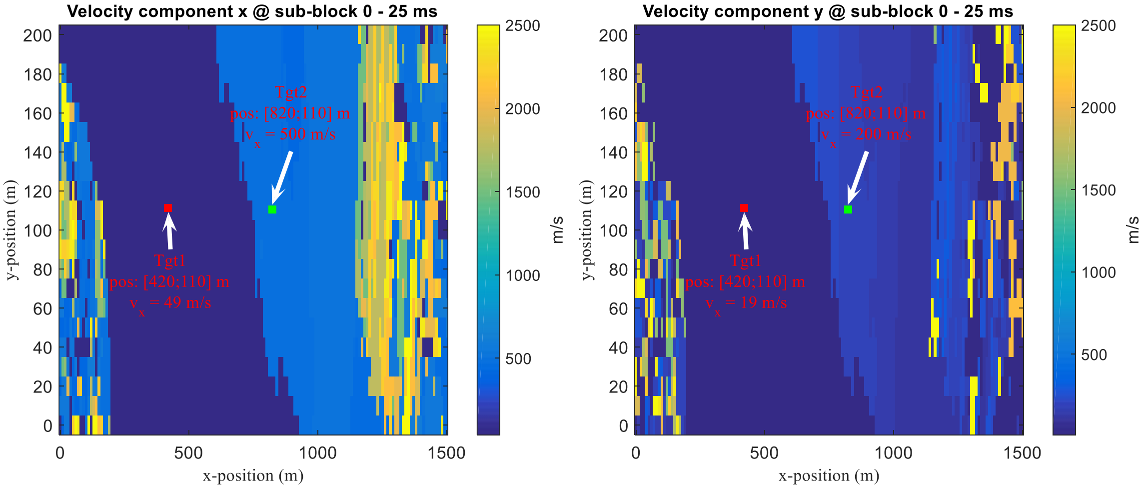

Figure 4.27: The 2-D velocity result corresponding to the integration of fragmentised data sub-block 0 - 25 ms.

$$\mathrm{tRMSE}_{\overline{K}} = \sqrt{\frac{1}{\mathbb{K}}\sum_{\Bbbk=1}^{\mathbb{K}}\sum\left(\boldsymbol{p}_{\delta\Bbbk} - \boldsymbol{p}_{\Delta_{max}\Bbbk}\right)^2} \tag{4.26}$$

where $\mathbb{K}$ is the total number of time frames applied for the process, $\boldsymbol{p}_{\delta\Bbbk}$ is the true initial target position at time frame $\Bbbk$ and $\boldsymbol{p}_{\Delta_{max}\Bbbk}$ is the position where the peak target return appeared at time frame $\Bbbk$.

Figure 4.28 shows the true target path and the recorded target (Tgt2) positions where peak returns appeared at all the time frames using the fragmentised data integration of various sub-block lengths out of 100 ms data snapshot. From the tRMSE performance chart summarised in Figure 4.29, it is observed that the RMSE measurements for the integrations with shorter sub-blocks are comparatively smaller. These measurements imply that using the shorter integration process is also able to localise the moving targets more accurately as it is less susceptible to error caused phase variations.

In summary, within the same hardware performance and data snapshot length, the TBD technique has the best performance in tracking fast moving targets if accurate target flight path models are used. This path modelling process uses the matched filters to align the phases of every data samples prior to integration, hence making the detection process computationally intensive. The fragmentised data integration process sacrifices integration gain since it applies matched filters that assume the phases of data samples remain constant within a shorter integration time. As the target position is tracked over multiple sub-blocks, this technique can also handle fluctuations in the power of target returns over several snapshots.

4.5 Conclusion

The background of MIMO radar has been reviewed at the beginning of the chapter. The background study briefly elaborated the advantages and feasibilities of both coherent and non-coherent MIMO radar techniques for different kinds of radar systems. From the study, the non-coherent MIMO radar technique was selected as a model suitable for GPS bistatic radar to perform air target detection. The choice is mainly due to the limitation that the system, like other PBRs, does not have any control over the transmitters. Secondly, non- coherent integration over multiple sources simplifies the detection problem as the phase shifts between transmitters can be ignored.

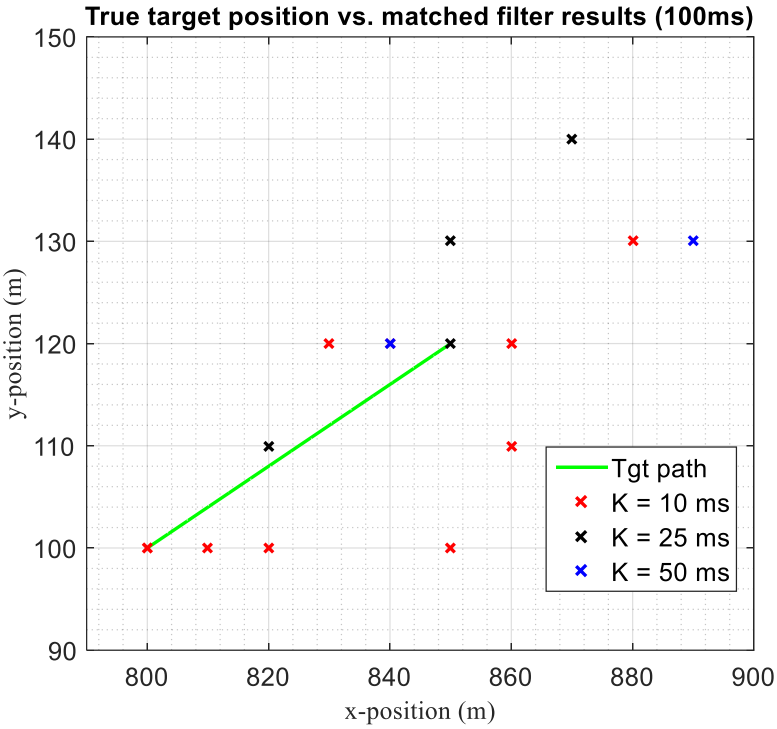

Figure 4.28: The true target path and the recorded target (Tgt2) positions where peak returns appeared at all the time frames using the fragmentised data integration of various sub-block lengths out of 100 ms data snapshot.

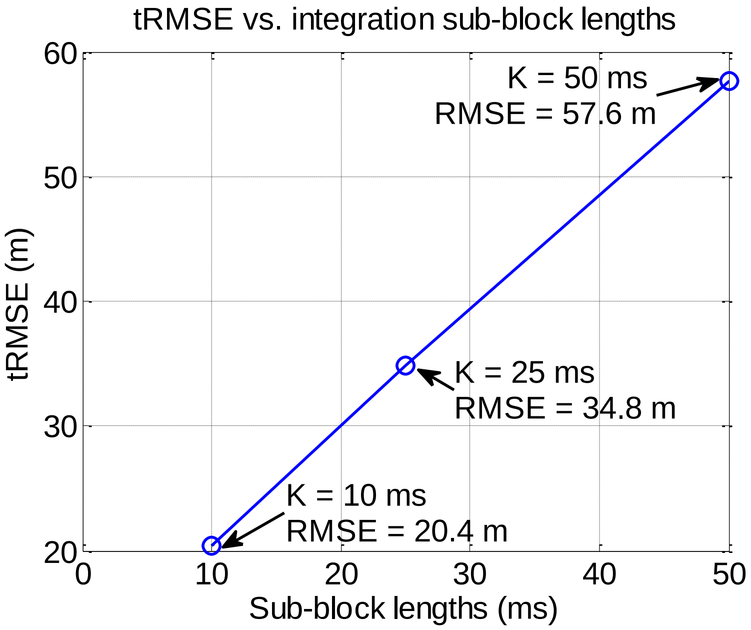

Figure 4.29: Performance chart of tRMSE vs. integration sub-block lengths.

The MISO/MIMO radar detection model was also developed for a GPS bistatic radar that detects the target reflections from multiple satellites using single/multiple phased-array GPS receivers. The detection performance of the GPS MIMO radar using different numbers of non-coherent integrations for target reflections with equal SNR was also investigated using both the standard and non-central chi-squared CDF models. These statistical models demonstrate that the system can achieve better detection performance under the same CFAR when more non-coherent integrations are applied. In addition, a DOP model was also developed for GPS MIMO radar to measure its accuracy for target positioning. This model extends the DOP model of conventional GPS positioning.

The detection performance and target resolution of SISO, MISO and MIMO techniques were compared using simulations with multiple sources. For the MISO technique, the detection and resolution improves as more transmitters are incorporated in the solution. The detection and resolution of MIMO technique improve as more transmitters and receive arrays are incorporated. Spacing the receive arrays further apart also improves the target resolution. The advantages of the MISO and MIMO techniques in detecting and estimating target parameters were evaluated based on the MCE and chi-squared distributions for several input SNR values.

Two target tracking techniques for GPS MIMO radar were also developed. These techniques are able to handle variations in the data samples' phase due to variation in the target position. From the target detection simulations, the TBD had the best performance among all techniques in detecting and tracking high velocity cruising targets. On the other hand, the fragmentised data integration technique is able to obtain the target position at different times and requires less computation time for the process. Hence, the decision of choosing either technique depends on the targets range and velocities, or the capabilities of radar receiver detection and computational performance.

The simulation results in this chapter demonstrated the capability of a MIMO technique for GPS bistatic radar to detect moving targets such as aircraft. However, the simulation assumes several ideal situations such as equal power target reflections from all the GPS satellites and input SNRs at all the receivers. So the final SNR improvement in practice may less than predicted by the simulations. Besides, each target in the simulation was assumed to appear at a single position bin whereas in reality, the size of a real aircraft may span several bins. Therefore, it is anticipated that the widths of the target correlation peaks would be wider than those from the simulations. Moreover, the DSI issue was still ignored in the simulation. A mitigation technique for the DSI will be introduced in the next chapter.

On the other hand, the GPS MISO/MIMO target detection and tracking models proposed in this chapter require a lot of computational time for the simulations to produce the position and velocity estimates. This is because these estimates are run through an exhaustive grid search across all position and velocity bins. These simulations are processed by MATLAB on a PC with reasonably powerful hardware specifications (i.e. Intel® Core-i7 3.40 GHz and 16GB DDR3 RAM), which took around an hour to complete the 1×1 SISO case, 16 hours to complete the 4×4 MIMO case and 72 hours to complete the TBD 4×1 MISO case. Hence, the time taken for the experimental detection process described in Chapter 5 using this computational platform will be much longer as the experimental data size is around ten times larger (i.e. approximately 1000 ms) than the simulated data (i.e. 100 ms).

In practice, the target search range and array size is much larger than the cases demonstrated by the simulation processes. For real-time radar applications, the target detection and parameter estimation results should be completed within a much shorter time. Therefore, the target searching and tracking algorithm must be handled by a more capable computational platform that is installed with dedicated processors such as DSPs or field-programmable gate arrays (FPGA) capable of handling the data using a parallel processing algorithm. It is also worth considering exploiting other techniques that can reduce the computational load for the detection process in the future.

CHAPTER 5

Experimental Target Detection Performance for GPS Bistatic Radar

5.1 Introduction

This chapter investigates the feasibility of GPS bistatic radar for target detection experimentally. An experimental system that consists of a receiver with a large scale antenna array was built and utilised to capture the GPS signal reflections from targets. The detection and parameter estimation techniques that were simulated in Chapters 3 and 4 were tested on the experimental data. However, prior to applying these algorithms, some additional pre-detection techniques were applied to calibrate the array and remove the DSI. The overall process for GPS bistatic radar to perform target detection experiment is summarised in the flow diagram in Figure 5.1.

Firstly, the details of the radar receiver's system design and its capturing module for performing the target detection experiments are described in Section 5.2. This section also considers the available GPS signal power on Earth and benchmarks the required performance of a GPS bistatic radar receiver for reliable target detection.

Section 5.3 explains the direct-path signal acquisition technique and its application to the experimental data. The direct-path signals are acquired for a number of purposes: (i) to calibrate the array so that the full array gain and accurate DOA estimates can be obtained (ii) to obtain an accurate estimate of the residual Doppler and navigation message over the entire data block, thus allowing enhancing the integration time (iii) to cancel the DSI by generating an accurate replica of the direct-path signal and using a Wiener filter to cancel it from the captured data on each antenna.

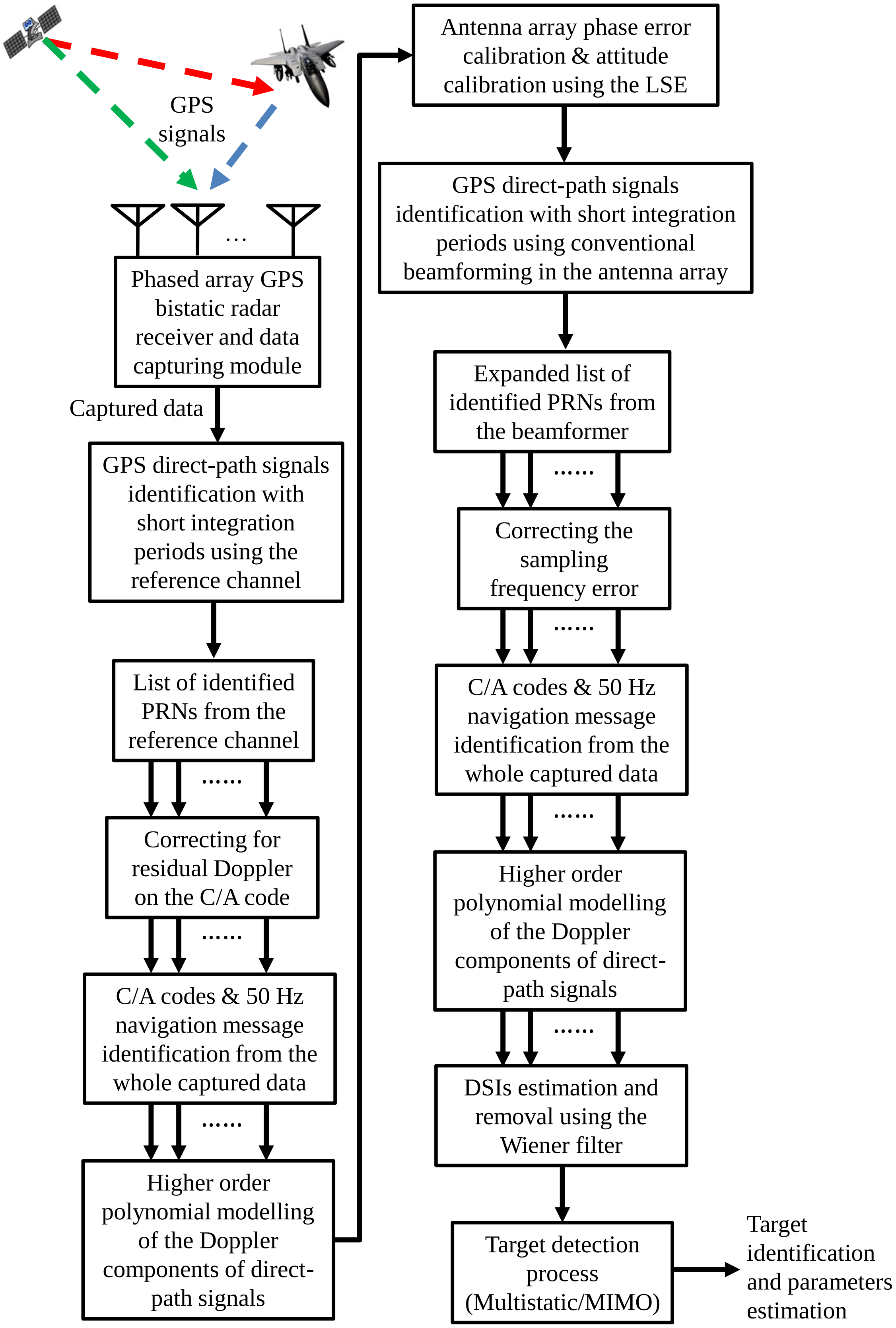

Figure 5.1: Overall process of GPS bistatic radar system for performing target detection.

To acquire the direct-path signals, firstly a short correlation between the data from the reference element (i.e. $m = 1$) and the locally generated C/A codes is used to identify the number of available GPS satellites within the LOS of the receiver. Note that this initial step only detects the most dominant direct-path signals. Then, an estimate of the Doppler shift on the C/A code signal is obtained based on the acquired direct-path PRNs. Next, the residual Doppler frequency, C/A code frequency and navigation message of each PRN is estimated across the entire captured data block.

Section 5.4 considers the results of estimating the phase errors due to non-idealities of electronic components and the variations in the antenna array's attitude using the proposed LSE model. Then, the direct-path signal acquisition process is repeated again by steering a beam at each satellite using the phased-array, thus estimating the modulation of the direct-path signals more accurately and also acquiring other PRNs that are too weak to be obtained previously.

The direct-path signals are treated as interferences (i.e. DSI) for the subsequent target detection process. Firstly, the copies of all the acquired direct-path signals are generated. Then, these generated copies are applied into a Wiener filter and subtracted from each front-end. Section 5.5 demonstrates the DSI cancellation technique applied to the GPS bistatic radar. The cleaned up signals are then presented to the target detection and parameter estimation algorithms.

An experiment was performed using the GPS bistatic radar to detect an aircraft. The results of the air target detection and parameters estimation using the phased-array and MIMO techniques previously simulated are analysed and presented in Section 5.6. This chapter's conclusion appears in Section 5.7.

The convention of angles used in the following sections in this chapter is defined here. The azimuth angles, θ, of 0°, 180°, 90° and −90° denote the directions to the East, West, North and South of the radar receiver respectively. The elevation angle, ϕ, is defined as the deviation of an angle from the z-axis. Hence, 0° refers to a direction directly above the receiver. The position estimates are expressed in Cartesian form and referred to coordinates relative to the receiver at origin point [0; 0; 0].

5.2 Experimental Receiver for Air Search GPS Bistatic Radar

The main purpose of this research is to study the feasibility of GPS bistatic radar for air target detection by analysing real experimental results. Therefore, an experimental phased-array receiver for this kind of radar was developed to meet the requirement of this research. From the discussions in the previous sections, it was decided that the scale of array must be sufficiently large to be capable of detecting weak GPS signals reflections from moving air targets. However, this study was mainly to obtain a benchmark since the receiver was only designed for detecting short range targets.

The experimental GPS bistatic radar receiver system consists of three major modules: RF front end, data acquisition and signal processing. To keep the hardware cost low, only the RF front end and data acquisition modules are performed by electronic hardware at the receiver while the signal processing module is implemented by computer software on a PC. The outline of the receiver system is given along with a description of the receiver's design in Figure 5.2. Also, a picture of the front-end's PCB is shown in Figure 5.3. The specification requirement of the radar receiver is recorded in Table 5.1.

Type	Parameters	Values
Front-ends allocation	Number of antennas per sub-array	8
	Total number of antennas	32
	Total number of front-ends	64
FPGAs allocation	Number of FPGA per sub-array	1
	Total number of FPGAs	4
	Number of front-ends per FPGA	16
Fundamental clock rate	GPS timing unit clock rate	100 MHz
	FPGAs clock distributor timing rate	16.667 MHz
RF components parameters	LO frequency of front-end's PLL	1575 MHz
	IF frequency of demodulator's output	420 kHz
	IF filter's bandwidth	2.5 MHz
ADCs parameters	ADCs sampling rate	4.167 MHz
	ADCs data resolution	2-bit for I & Q channels
Data streams parameter	Total number of data streams per FPGA	64
	Memory size per FPGA	32 MB
	Total time length per data stream	960 ms

Table 5.1: Specification chart for essential parameters of the experimental GPS bistatic radar.

5.2.1 Description of Receiver's Design

To achieve good reception for both the direct-path and target scattered signals while maintaining minimal mutual coupling effects in the array and the reception of ground clutter,

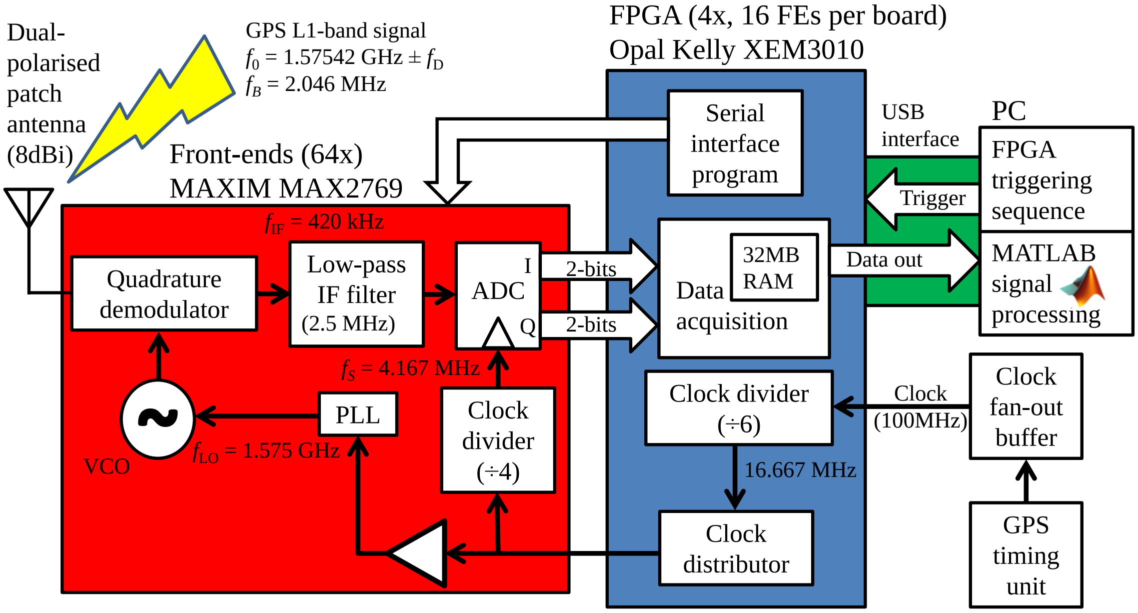

Figure 5.2: Outline of the experimental GPS bistatic radar receiver.

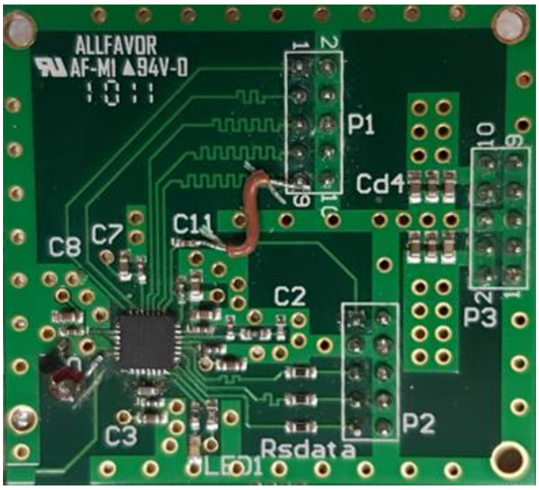

Figure 5.3: Picture of the front-end's PCB.

an Opt-Osl Systems designed patch type antenna with an air gap between the substrate of the element and a directivity of 8 dBi is utilised by the receive array. As the scattered GPS signals can be either left-hand, circularly polarised (LHCP) or linearly polarised (LP) [26], the antenna of the radar receiver must be able to capture signals from all polarisation aspects.

To cater for all polarisation states, antenna elements that consist of vertical (V) and horizontal (H) polarisation channels were chosen for the receiver. If both polarisation channels are processed independently, the polarisation mismatch will be less than 3dB on the best polarisation channel.

As shown in Figure 5.4, a 32-element phased-array receiver was built consisting of 4 sub-arrays that are configured in a square layout. The elements in each sub-array are configured in

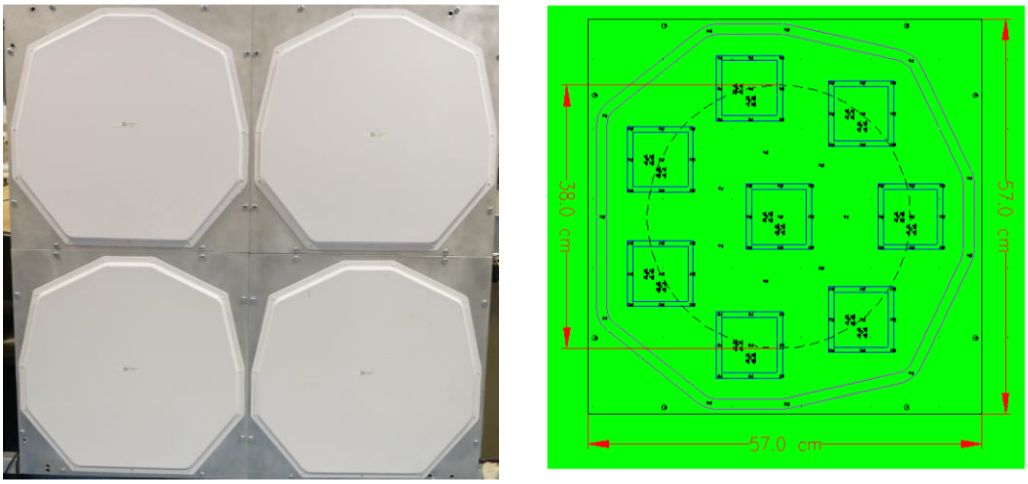

Figure 5.4: Picture of the 32-elements array and the schematic of the 8-element circular grid sub-array (Courtesy of Opt-Osl Systems).

a circular layout to maintain a large effective array aperture across all directions since the number of elements is reasonably small. To further mitigate the coupling between elements, the radius of the circular sub-array is also designed to be 0.19 m (i.e. λ_0 of GPS L1-band signal). However, this large spacing also increases the side-lobes of the beam pattern. The sidelobe levels are reduced by allocating 1 element in the centre of the circle and 7 elements uniformly around the circumference as illustrated by the schematic of sub-array in Figure 5.4. Placing an element in the circle helps to provide additional spatial lags, thus reducing the maximum sidelobe level. This can be seen by comparing the beam pattern of a conventional beamformer steered at $(\theta, \phi) = (0°, 45°)$ of this array with that of an 8-element circular array as shown in Figure 5.5. Also, the cascading of four sub-arrays into a square layout (Figure 5.4) further reduces the sidelobes as shown in Figure 5.6. Note that these aforementioned beam patterns were synthesised based on the antenna array that were formed by isotropic radiation pattern elements.

The output of each antenna polarisation (V/H) channel is connected to front-end circuitry. As a result, this 32-element receiver system requires a total of 64 front-end circuits. The front-end utilises a low cost MAXIM's MAX2769 programmable GPS chip containing all the essential components such as a low-noise amplifier (LNA), quadrature mixer, phase-locked loop (PLL), clock divider, intermediate frequency (IF) filter and two 2-bit ADC for both I & Q channels. Since the PLL is an integrated part of the chip, the demodulators for all the front-ends are not able to be driven by a common local oscillator. As a result, this design will cause phase misalignment between the data of each front-end. However, this issue is not a major

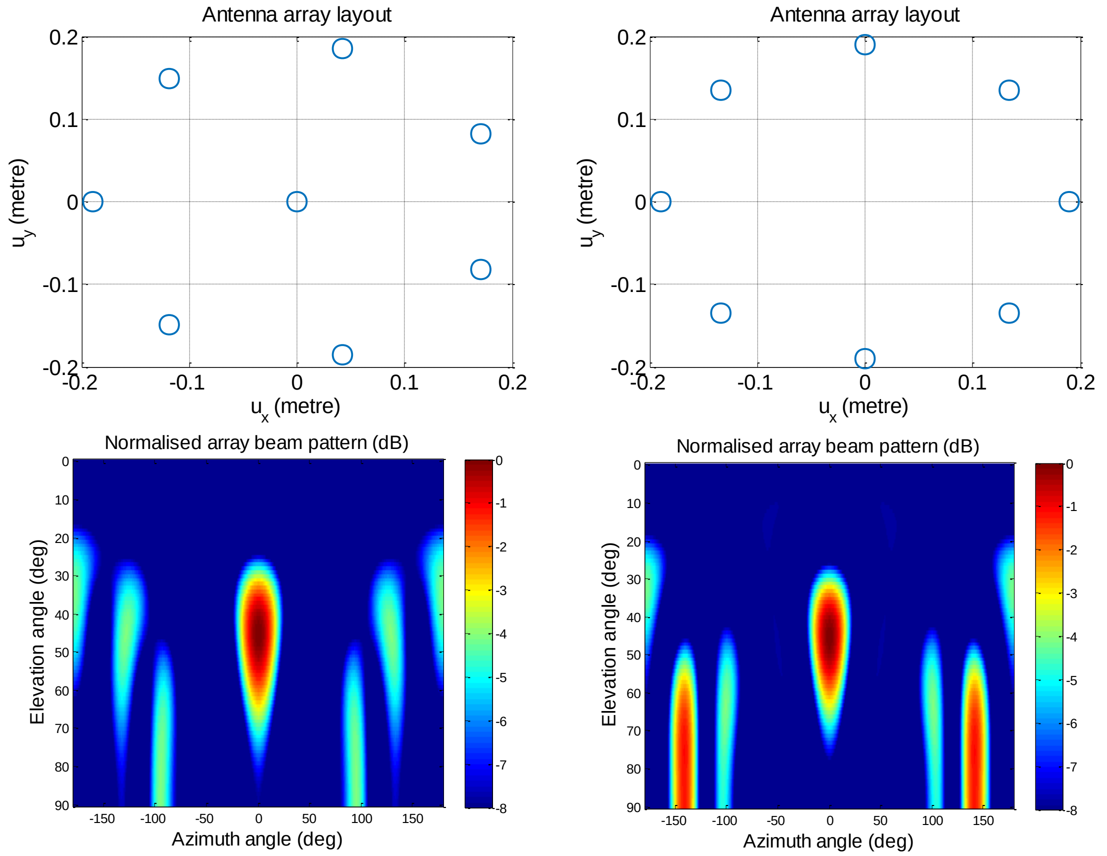

Figure 5.5: Comparison of beam pattern of 8-element sub-array ($\theta_s = 0°$, $\phi_s = 45°$).

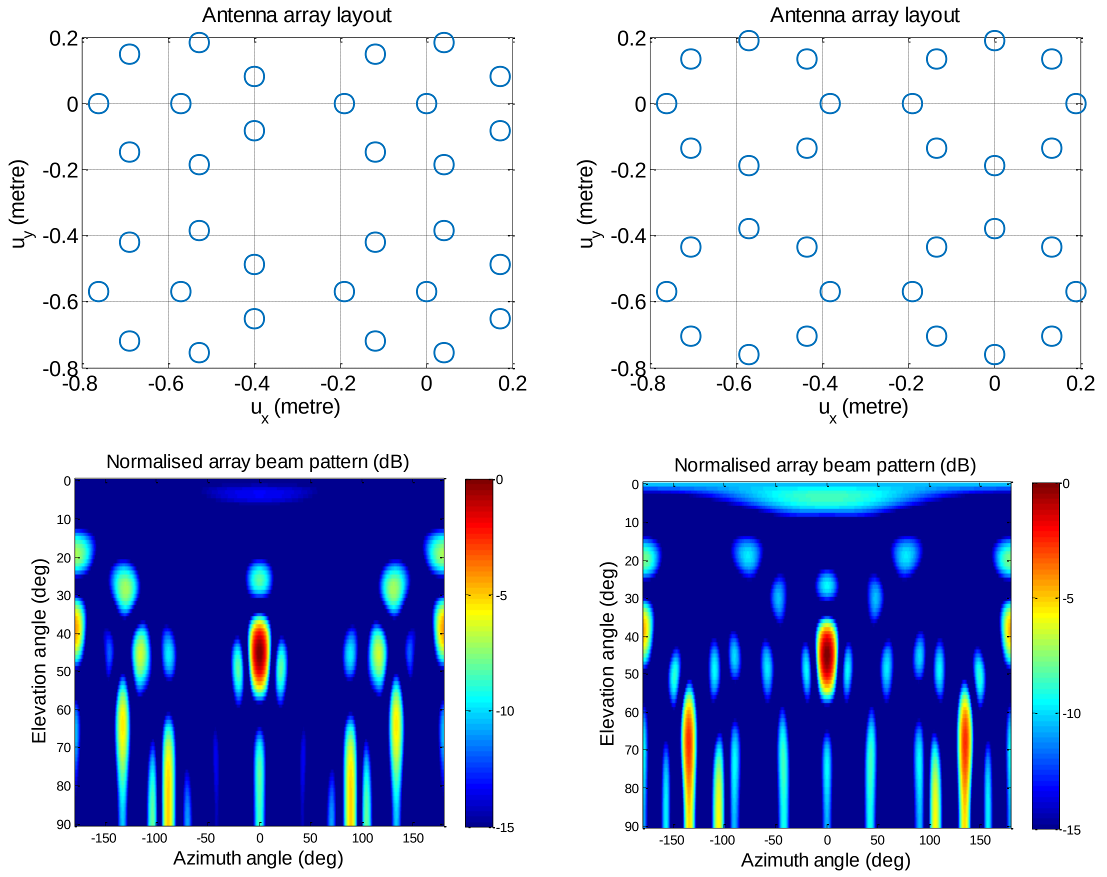

Figure 5.6: Comparison of beam pattern of 32-element antenna array ($\theta_s = 0°$, $\phi_s = 45°$).

concern to the experiment as it can be compensated by a practical phase-error calibration solution that will be presented in Section 5.4.

The chip thus includes both the down conversion and digitisation stages of the receiver. The downconversion process includes: (i) converting the input 16.667 MHz clock signal using the integrated PLL to become a 1.575 GHz local oscillator signal for the mixer, (ii) demodulating the input GPS L1-band signal down to an IF of 420 kHz, and, (iii) applying a low-pass filters with a 3-dB bandwidth of 2.5 MHz to the I & Q channels of the GPS IF signals. The digitisation process uses: (i) a clock divider to convert the 16.667 MHz input clock to become a 4.167 MHz sampling clock, and, (ii) 2-bit ADC for each I and Q channel. This 32-element array is made up of 4 sub-arrays with 8 dual-polarised elements each. Each sub-array uses a single Opal Kelly XEM3010 FPGA module to program the front-ends and collect the data from the ADCs.

VHSIC Hardware Description Languange (VHDL) is used in the receiver controller module to program the FPGAs. To control the operation of the front-ends at each sub-array, these FPGAs are triggered by a computer via a USB interface using a program designed from Microsoft Visual C++. To synchronise the timing between the FPGAs, these devices share a common 100 MHz clock source that is generated by a GPS disciplined oscillator via a clock fan-out buffer.

There are three functional modules implemented on the FPGA to control the operation of the front-ends. Firstly, a clock divider and 1-to-16 fan-out clock buffer are implemented on the FPGA to convert the frequency of the input clock to 16.667 MHz and replicate multiple clock signals to the front-ends. Secondly, a serial interface program is implemented on the FPGA to configure the registers of all the front-ends to the operating mode previously described. Lastly, the FPGA works as a data collector and buffer to facilitate the capture of large data blocks into memory from the ADC in each sub-array. A sychronisation signal between FPGAs in the receiver system is applied to synchronise the data acquisition process at each sub-array simultaneously. The data acquisition device works by filling up the FPGA’s 32MB synchronous dynamic random access memory (SDRAM) via a first in, first out (FIFO) buffer used for crossing clock domains at a clock rate of 100 MHz. A memory size of 32 MB allows the system to buffer approximately 1 second of real-time continuous data prior to streaming into a computer via the USB interface at a slower data rate. The final stage of the receiver system is carried out on a computer that communicates with the FPGAs in the receiver to control the front-ends and capture the data.

The data capturing process is illustrated in Figure 5.7. The SDRAM on the FPGA can only handle a word size of 16-bit for each write cycle. Hence, each FPGA in a subarray requires 4

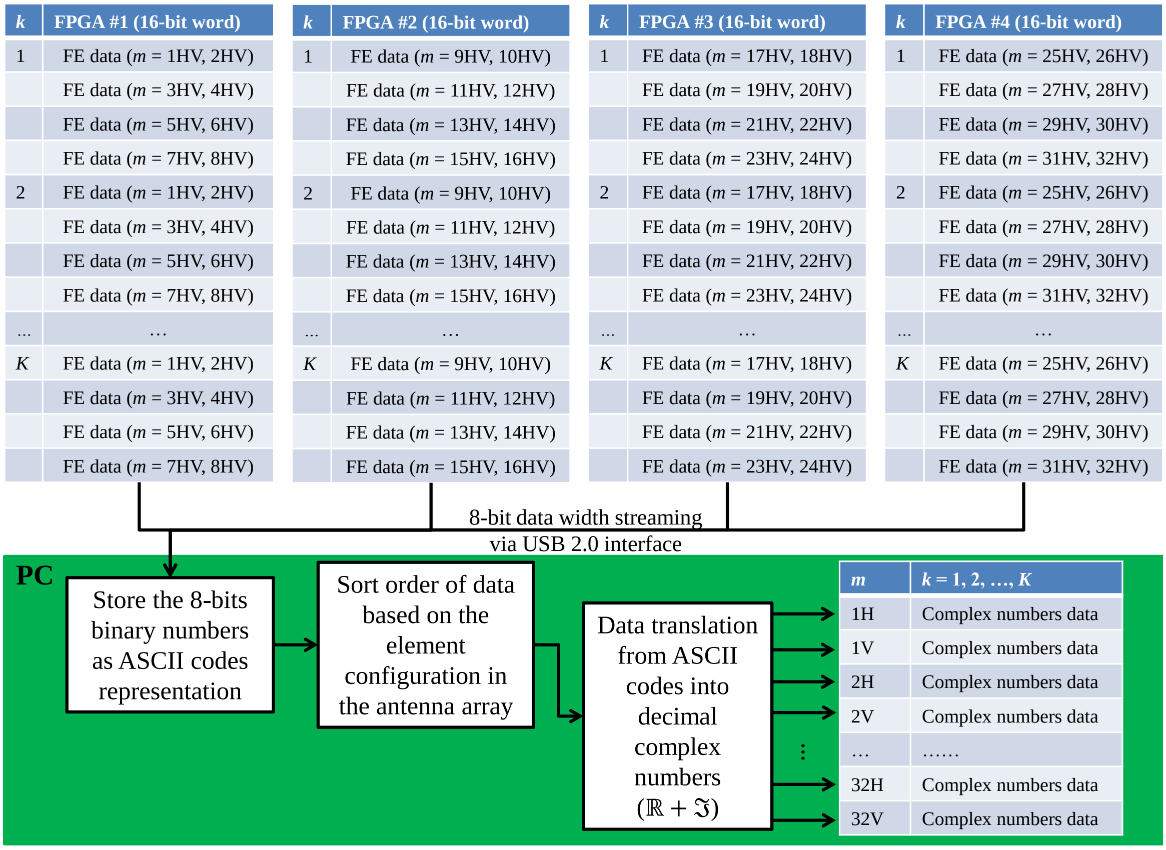

k	**FPGA #1 (16-bit word)**
1	FE data (*m* = 1HV, 2HV)
	FE data (*m* = 3HV, 4HV)
	FE data (*m* = 5HV, 6HV)
	FE data (*m* = 7HV, 8HV)
2	FE data (*m* = 1HV, 2HV)
	FE data (*m* = 3HV, 4HV)
	FE data (*m* = 5HV, 6HV)
	FE data (*m* = 7HV, 8HV)
…	…
K	FE data (*m* = 1HV, 2HV)
	FE data (*m* = 3HV, 4HV)
	FE data (*m* = 5HV, 6HV)
	FE data (*m* = 7HV, 8HV)

k	**FPGA #2 (16-bit word)**
1	FE data (*m* = 9HV, 10HV)
	FE data (*m* = 11HV, 12HV)
	FE data (*m* = 13HV, 14HV)
	FE data (*m* = 15HV, 16HV)
2	FE data (*m* = 9HV, 10HV)
	FE data (*m* = 11HV, 12HV)
	FE data (*m* = 13HV, 14HV)
	FE data (*m* = 15HV, 16HV)
…	…
K	FE data (*m* = 9HV, 10HV)
	FE data (*m* = 11HV, 12HV)
	FE data (*m* = 13HV, 14HV)
	FE data (*m* = 15HV, 16HV)

k	**FPGA #3 (16-bit word)**
1	FE data (*m* = 17HV, 18HV)
	FE data (*m* = 19HV, 20HV)
	FE data (*m* = 21HV, 22HV)
	FE data (*m* = 23HV, 24HV)
2	FE data (*m* = 17HV, 18HV)
	FE data (*m* = 19HV, 20HV)
	FE data (*m* = 21HV, 22HV)
	FE data (*m* = 23HV, 24HV)
…	…
K	FE data (*m* = 17HV, 18HV)
	FE data (*m* = 19HV, 20HV)
	FE data (*m* = 21HV, 22HV)
	FE data (*m* = 23HV, 24HV)

k	**FPGA #4 (16-bit word)**
1	FE data (*m* = 25HV, 26HV)
	FE data (*m* = 27HV, 28HV)
	FE data (*m* = 29HV, 30HV)
	FE data (*m* = 31HV, 32HV)
2	FE data (*m* = 25HV, 26HV)
	FE data (*m* = 27HV, 28HV)
	FE data (*m* = 29HV, 30HV)
	FE data (*m* = 31HV, 32HV)
…	…
K	FE data (*m* = 25HV, 26HV)
	FE data (*m* = 27HV, 28HV)
	FE data (*m* = 29HV, 30HV)
	FE data (*m* = 31HV, 32HV)

m	*k* = 1, 2, …, *K*
1H	Complex numbers data
1V	Complex numbers data
2H	Complex numbers data
2V	Complex numbers data
…	……
32H	Complex numbers data
32V	Complex numbers data

Figure 5.7: Illustration of data captured from 4 FPGAs stored into PC, translated into decimal complex numbers form and sorted into 64 blocks based on the configuration of antennas in the array.

write cycles to capture the 4-bit digital data from the 16 front-ends at each sample frame, *k*. The binary data from each FPGA was individually streamed via the USB interface using 8-bit data words into the PC and stored in ASCII representation. Then, the data was translated into decimal complex numbers and sorted into 64 chronological sample blocks based on the element configuration in the antenna array.

5.2.2 Receiver Performance Benchmark

This section considers the detection thresholds of the experimental GPS bistatic radar receiver described in Section 5.2.1. This detection threshold can be obtained from the expected SNR of a target return calculated in (3.4) based on the overall receiver gain, G_R, and loss, G_{LOSS}, as

$$\text{SNR}_{\text{out}} = \text{SNR}_{tgt}\frac{G_{\text{R}}}{G_{\text{LOSS}}} = \text{SNR}_{tgt}\frac{G_{\text{ANT}}G_{\text{ARR}}G_{\text{SP}}}{G_{\text{LOSS}}} \qquad (5.1)$$

where G_{R} consists of three gain components: G_{ANT} is the directivity of a single antenna element, G_{ARR} is the array gain, G_{SP} is the signal processing gain. Both G_{ANT} and G_{LOSS} are fixed for a given antenna type and receiver components. G_{ARR} can be increased by increasing the size of the phased-array while G_{SP} is predominantly dependent on the length of the coherent integration period applied at the receiver. Both of these parameters can be adjusted according to the required target detection range which is related to the SNR by an inverse square relationship. However, there are certain trade-offs involved in increasing both G_{ARR} and G_{SP}. Firstly, increasing the size of the array will result in higher array processing complexity and design cost. Secondly, prolonging the integration period might lead to further processing loss as a result of a changing Doppler shift of a non-cooperative target during the integration time.

The maximum received data length available for post processing is around 1 second for the system described above, which can theoretically provide a gain of 60 dB if coherent integration process is performed across the whole block of data. On the other hand, splitting the data into sub-blocks for which the Doppler search and integration process are performed individually enables the receiver to track the position variation of the target and makes it less susceptible to an integration loss due to a non-stationary Doppler shift. The proposed length of each sub-block is set to be 100 milliseconds for our system as this integration length is deemed a good trade-off between the above factors.

In setting the probability of detection and CFAR to be 90% and 1% respectively, the receiver's final SNR is required to be 11.7 dB. Based on (3.4) and (4.8), the detection range for various target sizes in terms of RCS using the experimental 32-element GPS bistatic radar receiver is summarised by the power budget estimation below.

Parameter	**Unit**	**Value**					
Direct-path signal power level	dBW	−160					
Directivity of a single patch antenna	dBi	8					
Array gain	dB	15 @ 32-element			25 @ 320-element		
Integration gain	dB	50@100 ms			60@1000 ms		
Noise level (T_A = 296 K, f_B = 2.5MHz)	dBW	−139					
Overall receiver loss	dB	3					
Final SNR requirement	dB	11.7					
RCS of target	dBsm	0	10	20	0	10	20
Max target detection range	m	23	73	232	72	232	734

Table 5.2: Summary of target detection range for a 32-element GPS bistatic radar receiver.

From Table 5.2, it is found that a 32-element GPS bistatic radar receiver is only capable of detecting a reasonably large aircraft such as an airliner at a distance suitable for experimentation. This table also serves as a benchmark for estimating the size of coherent integration periods, the scale of the phased-array receiver and the number of transmitters and/or receivers implementing the MISO/MIMO techniques required for detecting targets at a further distance.

5.3 Direct-path Signal Acquisition

The direct-path GPS signal needs to be extracted from noise to retrieve the phase and Doppler shift of its modulation information. This extraction can be made using the digital data from the front-end of an arbitrary element in the phased-array receiver. Then, a matched filter can be applied to this data using the locally generated PRN code that corresponds to the broadcast PRN code of the desired satellite using a code-Doppler search method as illustrated in Figure 2.3. Alternatively, the extraction of the direct-path signal information can also be done using the higher SNR data produced by the beamformer. This method can be realised by steering individual receive beams at each GPS satellite to capture these direct-path signals. However, this process can only be performed after the antenna array calibration process is applied to the receivers.

The modulation of the GPS signal consists of the addition modulo 2 of two components: (i) the C/A code sequence that repeats at every 1 millisecond, and, (ii) the time varying navigation message that provides GPS users the ephemeris and network information of the satellite at a 50 Hz chip rate. Therefore, the traditional Doppler-delay search technique can be feasibly performed for a short period, provided no navigation message transition occurs within the cross-correlation period. This approach is suitable for conventional GPS applications that do not require high sensitivity.

For a GPS bistatic radar, the modulation information on the GPS direct-path signal must be analysed for very long periods so that the local C/A code generator can replicate the code pattern accurately to perform bistatic target detection. While modulation over a short period can be accurately modelled based on the code-Doppler search, there are several issues that need to be addressed when capturing the modulation parameters over a longer period. The clock rate of the PC is not important as the replica is synthetically generated by adding the phase increments obtained from the assumed code frequency. This does not depend on the PC’s clock rate. Firstly, the Doppler on the C/A code needs to be compensated as a mismatch would begin to reduce the correlation coefficient of the matched filter when the cross-correlation process is extended.

The residual C/A code Doppler can be determined by performing a short period cross-correlation between the locally generated C/A code and the GPS signal at several separated discrete time frames, k, of the captured data's snapshot. For a misaligned sample rate, this process gives the rate of change of the correlation sample lag, k_τ, with time as shown in Figure 5.8. The residual Doppler, Δf_D, can be determined from K data samples using a simple linear regression method that estimates this discrete rate of change from the slope of the linear model, such that

$$\Delta f_\mathrm{D} = \frac{k_\tau(k) - k_\tau(k-1)}{K} \tag{5.2}$$

The second critical issue that needs to be considered when using long coherent integration periods for a GPS signal is the code transitions of the navigation message, $C_\mathrm{NAV}(k)$, which is unknown at this stage. This component will potentially invert the C/A code pattern, $C_\mathrm{C/A}(k)$ every 20 ms, and so needs to be replicated on the locally generated code. The PRN code sequence can be expressed as

$$C_s(k) = C_\mathrm{C/A}(k)\, C_\mathrm{NAV}(k) \tag{5.3}$$

Next, the non-linear motion of GPS satellite relative to the receiver will significantly vary the Doppler shift of GPS signal over longer signal acquisition periods as it follows an orbital trajectory. The Doppler shift of GPS signal is only coarsely estimated during the initial acquisition since the Doppler-delay search process is only performed for a short period of time and also assumes that the Doppler shift of the signal remains constant over the search period.

Due to the presence of navigation message and residual Doppler shift, the GPS direct-path signal after the Doppler-delay search process becomes

$$x(k) = \mu_S\, C_s(k)\, f_d(k) + \sigma_n n(k) \tag{5.4}$$

where $f_d(k)$ is the residual Doppler shift function and $n(k)$ is the complex WGN term.

After the C/A codes in the GPS signal are demodulated using the Doppler compensated replica, the remaining components in the GPS signal are the navigation message, $C_\mathrm{NAV}(k)$, such that

$$\begin{aligned} y(k) &= x(k)\, C_\mathrm{C/A}(k) \\ &= \mu_S\, C_\mathrm{NAV}(k)\, f_d(k) + \sigma_n\, C_\mathrm{C/A}(k)\, n(k) \end{aligned} \tag{5.5}$$

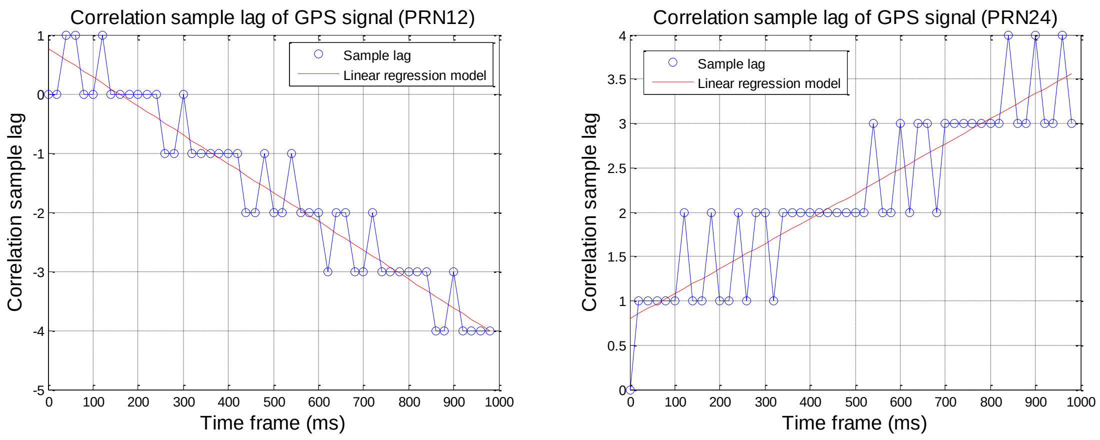

Figure 5.8: Analysis of GPS signal correlation sample lag across time and its rate of change modelling using linear regression method. Note that PRN12 and PRN24 possess a negative (-4.1 Hz) and positive (3.6 Hz) Doppler respectively.

As the noise power in (5.5) is much stronger than the signal, the navigation message and residual Doppler cannot be extracted directly. A decimation filter is applied to the GPS signal to reduce the bandwidth to 1 kHz, hence reducing the noise by 34 dB compared with the original signal bandwidth of 2.5 MHz. The decimated signals are indicated by using a k' index as

$$y(k') = \mu_S{}' \, C_{\mathrm{NAV}}(k') \, f_d(k') + \sigma_n{}' \, C_{\mathrm{C/A}}(k') \, n(k') \tag{5.6}$$

where

$$E\{|\mu_S{}' \, C_{\mathrm{NAV}}(k') \, f_d(k')|^2\} \gg E\left\{\left|\sigma_n{}' \, C_{\mathrm{C/A}}(k') \, n(k')\right|^2\right\} \tag{5.7}$$

After downsampling, each phase reading of the decimated GPS signal represents the phase of one C/A code period time frame. The phase of the decimated signals, $\angle y(k')$, for both GPS satellites are shown in Figure 5.9. The data transitions are clearly visible when the phase changes by approximately π radians.

When the navigation message is extracted, it can be combined with the locally generated C/A code to demodulate the GPS direct-path signal (5.4). The demodulated signal, $y'(k)$, is given by

$$\begin{aligned} y'(k) &= x(k) \, C_{\mathrm{C/A}}(k) \, C_{\mathrm{NAV}}(k) \\ &= \mu_S f_d(k) + \sigma_n \, C_{\mathrm{C/A}}(k) \, C_{\mathrm{NAV}}(k) \, n(k) \end{aligned} \tag{5.8}$$

Hence, the residual Doppler shift becomes the only signal component in the presence of noise. To improve the SNR of the residual Doppler component, a decimation filter is applied to (5.8). The decimated output demodulated signal becomes

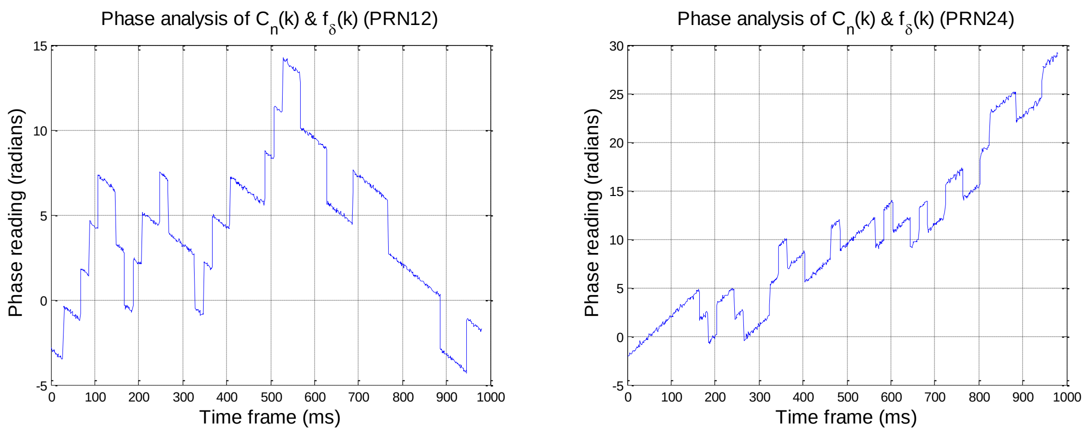

Figure 5.9: Phase analysis of GPS signal after the removal of C/A codes decimation filtering. Each phase change of π radians in the figures indicates a data-bit transition of the navigation message.

$$y'(k') = \mu_s' f_d(k') + \sigma_n' \, C_{\mathrm{C/A}}(k') \, C_{\mathrm{NAV}}(k') \, n(k') \tag{5.9}$$

In the case of constant residual Doppler frequency, this component can be estimated using a linear regression model that fits the equation of a line to the phase readings of $y'(k)$ against time. But in the presence of time varying Doppler shift, the accuracy of this estimation will be compromised unless the modelling is performed partially over shorter period data blocks. A more straight forward method to precisely determine $y'(k)$ in the presence of the time varying Doppler component is to use a higher order polynomial regression model, which becomes

$$\angle y'(k') = r_1 k' + r_2 k'^2 + \cdots + r_n k'^n \tag{5.10}$$

Using the coefficients from the above polynomial function (i.e. r_1, r_2 ... r_n), the residual Doppler component can be modelled as

$$f_d(k) = \exp\left\{ j\left(r_1\left(\frac{k}{\overline{K}}\right) + r_2\left(\frac{k}{\overline{K}}\right)^2 + \cdots + r_n\left(\frac{k}{\overline{K}}\right)^n \right) \right\} \tag{5.11}$$

where $\overline{K}$ is the length of one C/A sample code period.

The accuracy of the residual Doppler components for the polynomial regression models with various orders was investigated experimentally. Firstly, these components were extracted from two GPS direct path signals, PRN12 and PRN24. Their phase readings are shown in Figure 5.10 and Figure 5.12 respectively. Next, the phases of these components are individually modelled by (5.10) using various orders. Then, the phase reading variances of the GPS signals after the removal of the residual Doppler components and the PRN code sequence were analysed. From Figure 5.11, the polynomial model only improves the linear model by a small

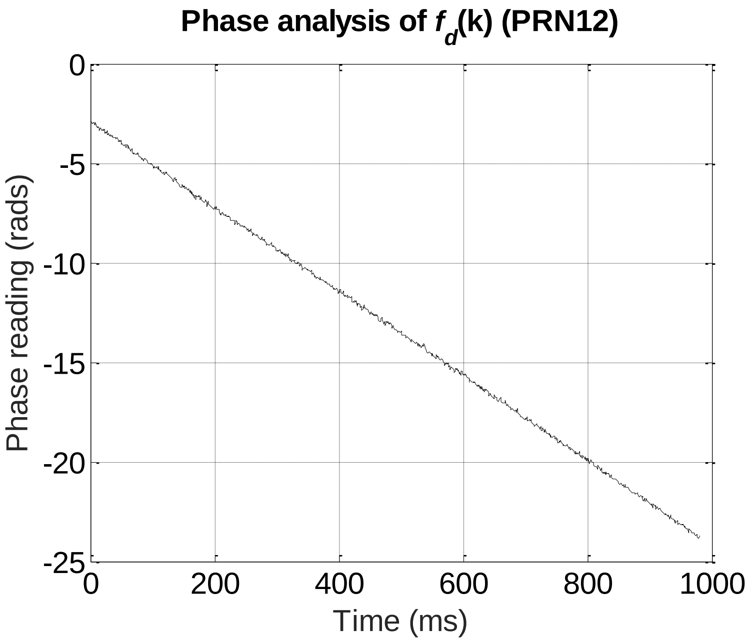

Figure 5.10: Phase reading of residual Doppler component in the GPS signal.

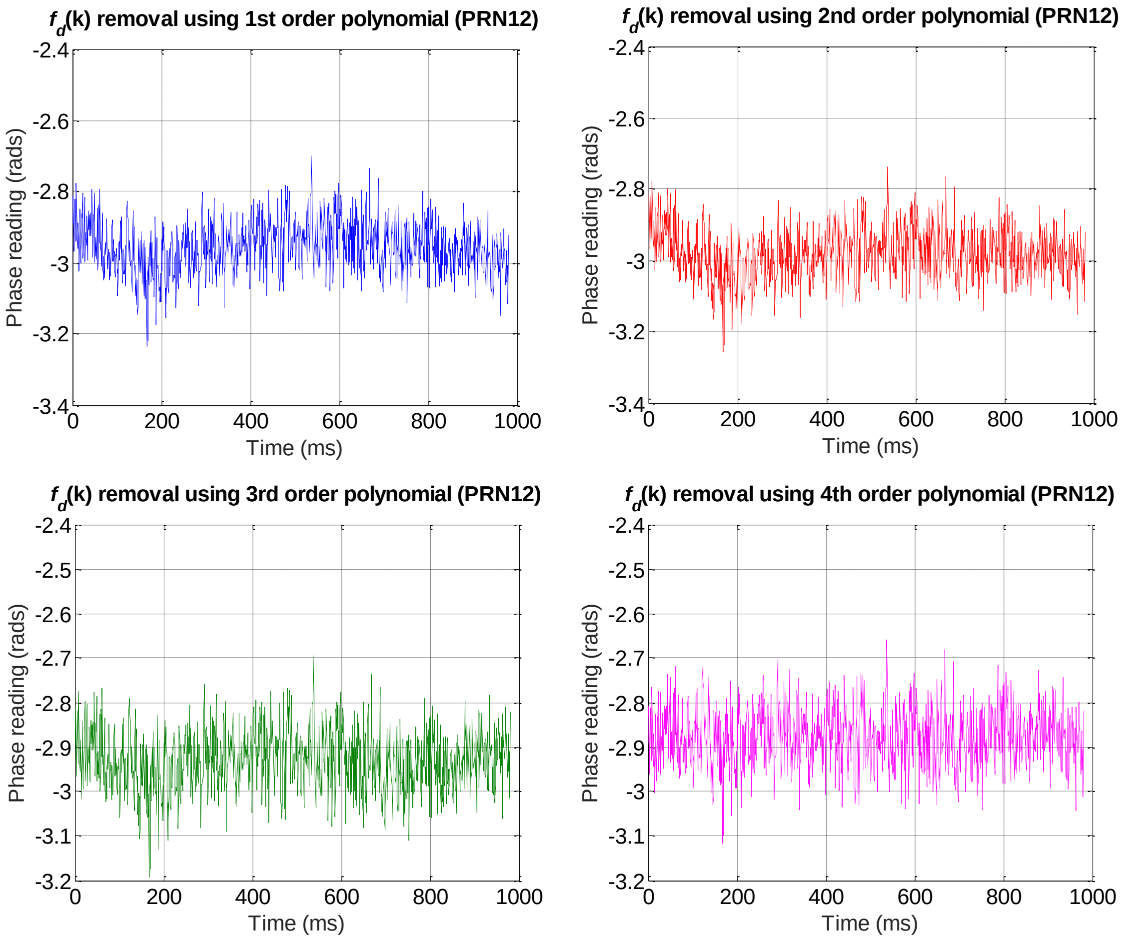

Figure 5.11: Comparison of the signal phase of PRN12 after residual Doppler removal modelled by various polynomial orders. The variances of these phase readings in the ascending polynomial order are 0.0051, 0.0049, 0.0046 and 0.0043. These parameters show that a slightly smoother phase reading is achieved as the time varying Doppler component is removed using higher order polynomial regression modelling.

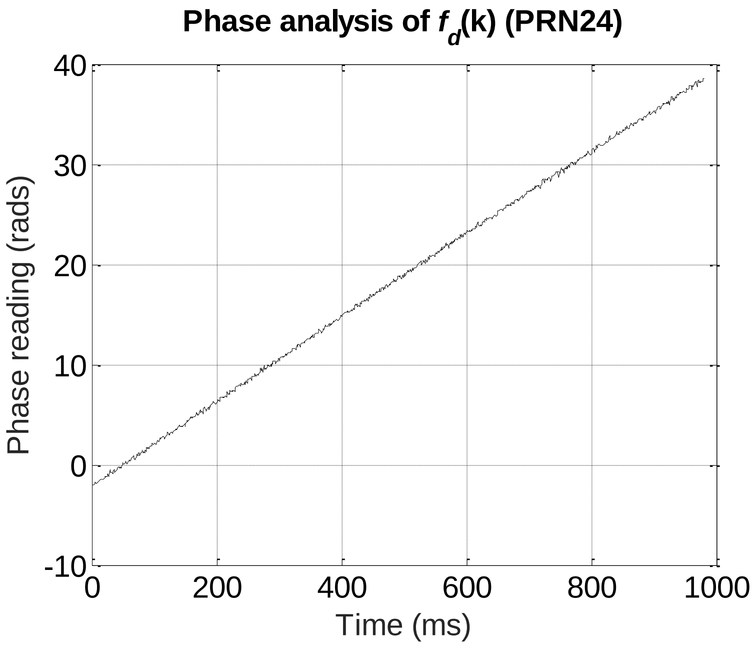

Figure 5.12: Phase reading of residual Doppler component in the GPS signal.

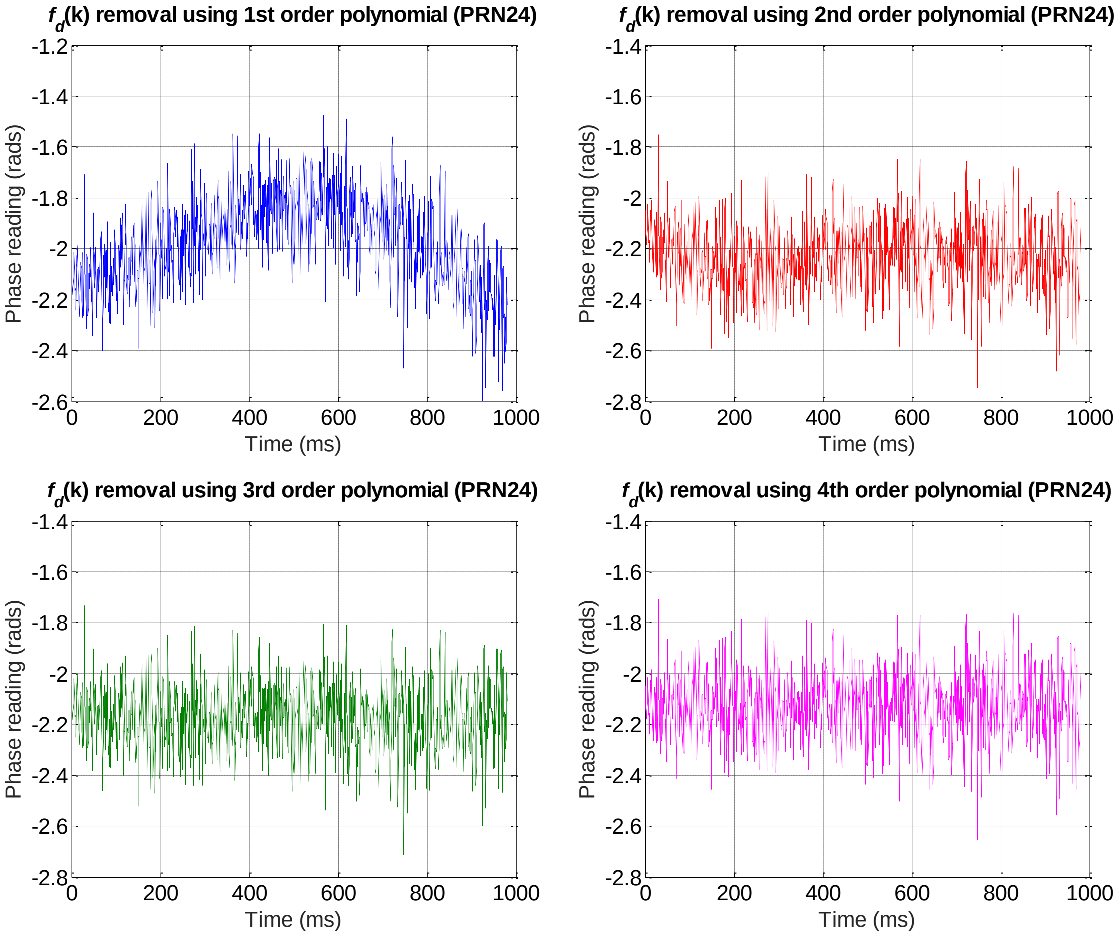

Figure 5.13: Comparison of the signal phase of PRN24 after residual Doppler removal modelled by various polynomial orders. The variances of these phase readings in the ascending polynomial order are 0.0307, 0.0175, 0.0170 and 0.0168. These parameters show a significantly smoother phase reading is achieved as the time varying Doppler component is removed using the polynomial regression modelling.

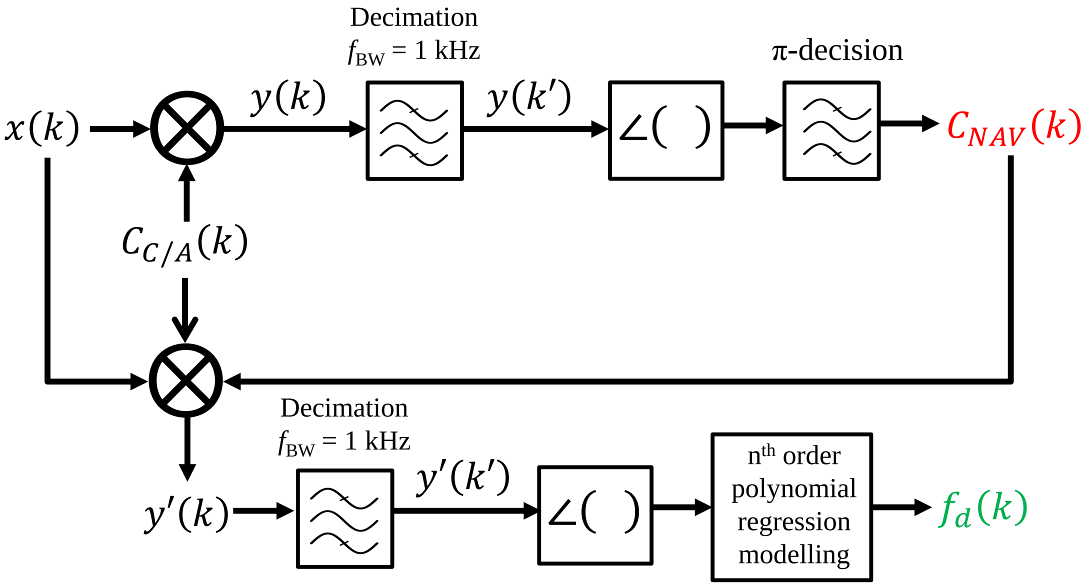

Figure 5.14: Block diagram of navigation message and residual Doppler component extraction from a GPS signal.

margin as the Doppler shift of PRN12 appeared to vary linearly within the given timeframe. On the other hand, it is observed in Figure 5.13 for PRN24 the polynomial model gives a significant improvement. Based on the experimental results, it is recommended to estimate the residual Doppler components using at least a 2nd order polynomial regression model to account for varying Doppler shifts in the GPS direct path signal.

As summarised in Figure 5.14, the direct-path signal acquisition process performs the extraction of the essential signal components such as the C/A code Doppler, navigation message and the time varying carrier Doppler. These parameters are then used to construct a matched filter that not only serves as a basis for searching the target scattering signal, but is also applied to the data captured by all the front-ends to determine the relative phases between them as required by the phase error calibration that was discussed in Section 3.4 for the phased-array receiver.

The above direct-path signals acquisition process can be repeated using the phased-array technique. Unlike the acquisition using a single (reference) element, the phased-array acquisition process steers a beam towards the direction of each GPS satellite using the conventional beamforming technique which greatly enhances the SNR of the direct-path signals. This technique improves the accuracy of acquiring the Doppler and code phase information of the direct-path signals. Also, the array processing technique improves the receiver's sensitivity that enables the extremely weak GPS signals to be extracted, hence increasing the availability of the passive illuminators to perform target detection. However, a phase error calibration process must be applied to the phased-array receiver before it can be used for direct-path signals acquisition. This technique will be discussed in the following section.

5.4 Experimental Antenna Array Calibration Results

This section applies the antenna array phase error calibration technique proposed in Section 3.4.3 to data from the experimental array. This section describes the antenna array deployment, the calibration process and outcome. The calibration results were applied to the phased-array receiver and verified using several methods: (i) comparing the correlation values between individual channels and the beamformer's output, (ii) demonstrating that the phased-array receiver is able to acquire weak direct-path signals which could not be acquired by a single element, and (iii) compare the DOA for each PRN obtained from the maximum beampower direction with the predicted DOA from the ephemeris.

5.4.1 Antenna Array Deployment

As described in the previous section, the experimental system is a 32-element phased-array receiver with dual polarised antenna elements. This gives 64 front-ends in total at the receiver. The broadside of the phased-array receiver must face the predicted landing flight path so that optimum reception of the target reflection from the airplane can be achieved. Hence in the experimental scenario illustrated in Figure 5.15, the antenna array panel was tilted westward at an unknown pitch angle and became diagonal relative to the ground.

5.4.2 Calibration Process and Outcome

The array calibration relies on the phase measurement of the direct-path signals captured by all the channels. Initially, the system acquires the direct-path signals acquisition of multiple GPS satellites using the element at the reference channel (i.e. $m = 1$). Then, the Doppler and code phase information obtained from this process is applied to remove the modulation of the direct-path signals from 5 GPS satellites captured by all the channels. The input data of the individual channel is then cross-correlated with the locally generated PRN codes over a long integration period and the phase of each signal is obtained from the correlation peak. From the

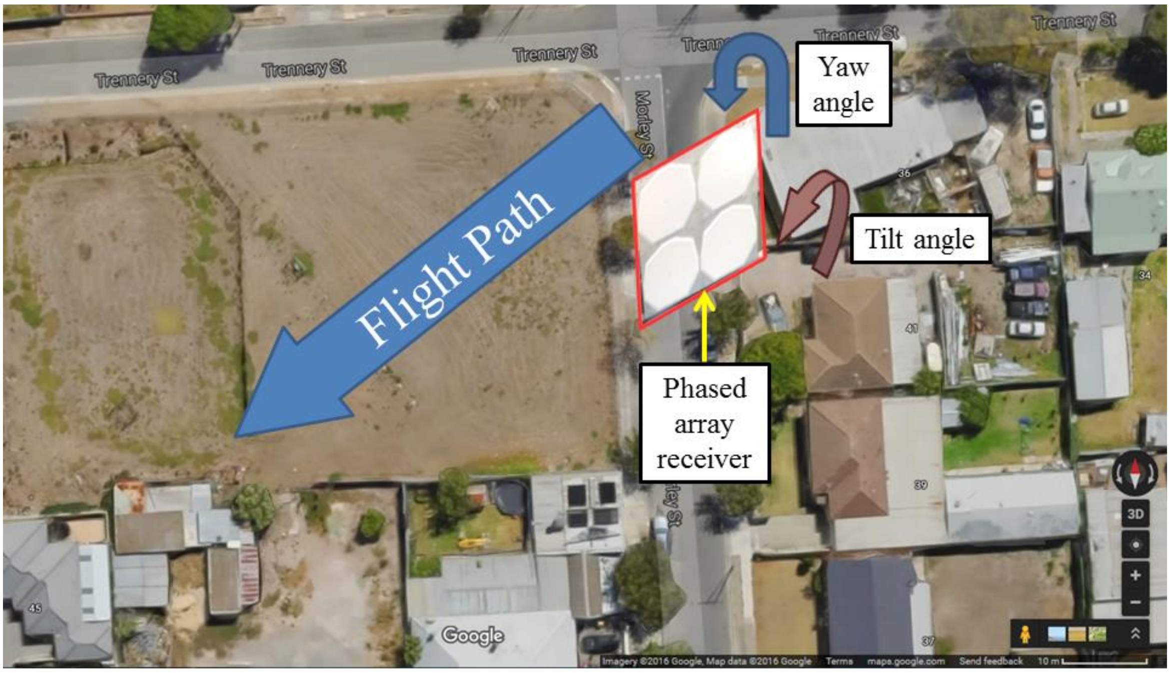

Figure 5.15: Illustration of the GPS bistatic radar receiver's deployment for the air target detection experiment (Courteousy Google Map's satellite view).

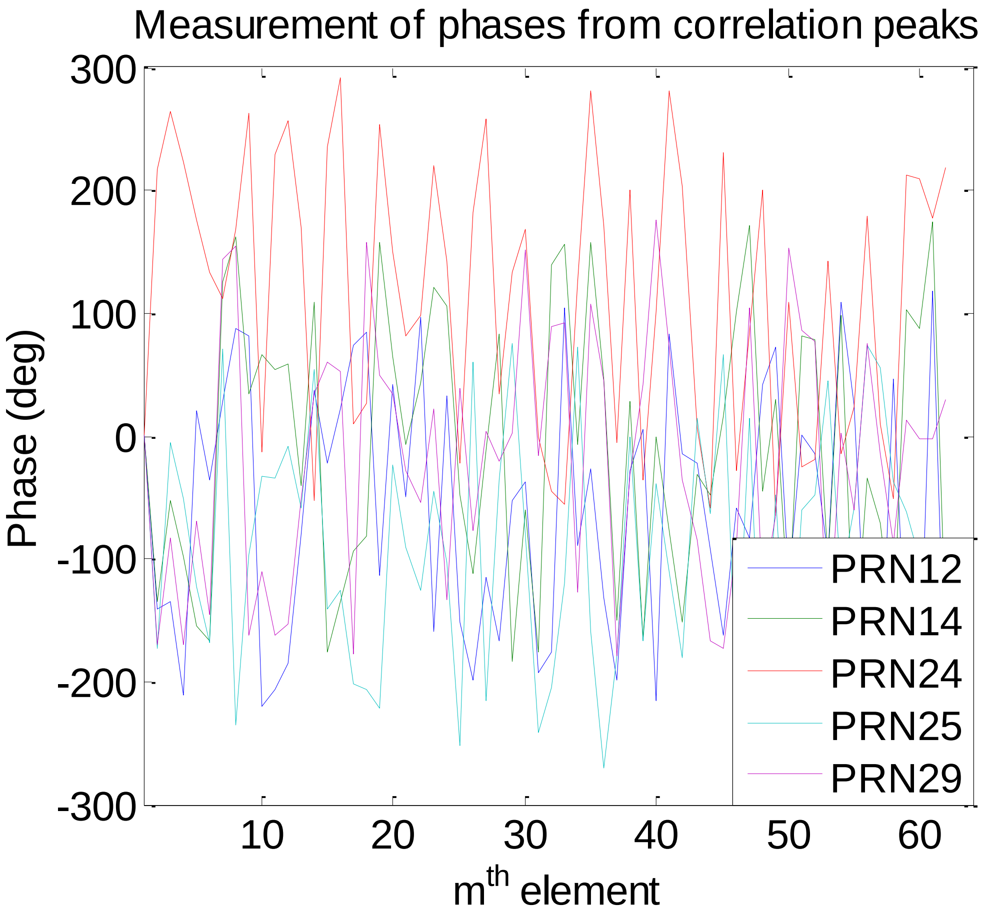

Figure 5.16: Phase measurement of direct-path signals correlation peaks at 62 channels from 5 GPS satellites (PRN12, 14, 24, 25 and 29).

measurement recorded in Figure 5.16, the phases between channels from this measurement were observed to be random. Note that during the experiments, 2 front-ends were diagnosed to have malfunctioned. Hence, only the data from 62 channels were used for the measurement.

An iterative search was made to search for the yaw and pitch angles that correspond to the attitude of the antenna array. Each search location used a different transformation $\boldsymbol{u}$ to $\boldsymbol{u}''$ of the antenna positions relative to the reference channel. By applying the measured phases of the correlation peaks , $\boldsymbol{\xi}_m$, and the spatial phase factors of the GPS satellites from directions as recorded in Table 5.3 relative to the phased-array receiver, $a_m(\boldsymbol{\kappa}_l)$, the phase error on each channel, ϵ_m, was determined from the calibration model in (3.27). Then the MSE of each channel's phase error at each attitude was determined. Ultimately, the sum of the MSE from all channels at all searched attitudes was determined from this phase error calibration process. The normalised, inverse MSE results are recorded in Figure 5.17.

Receiver location:	Lat: -34.94°	Lon: 138.55°
Date / Time:	9th April 2013 09:52:06 ACT	
Satellite PRN	**Azimuth (deg)**	**Elevation (deg)**
12	−124.51	38.35
14	−142.99	83.28
24	137.36	25.79
25	−143.68	68.47
29	158.13	82.42

Table 5.3: Summary of DOA of GPS satellites to the GPS bistatic radar receiver.

The highest inverse MSE value is located at $\phi_e = -42.5°$ and $\theta_e = 183.5°$, which corresponds to the attitude of the antenna array as shown in Figure 5.18. The phase errors corresponding to these angles were applied as phase offsets to each of the channels.

5.4.3 Verification of Calibration Results

To verify the accuracy of the calibration process, the direct-path signals acquisition process described in Secion 5.3 was repeated using the beamformed data. A comparison was made between the correlation results for PRN12 and PRN24 from each individual channel and the beamformer output. From Figure 5.19 and Figure 5.20, it was observed that at zero sample code phase offset, the beamformer output is 18.25 dB above the mean correlation values of all the channels. This gain value is very close to the theoretical SNR gain of 17.9 dB for coherent addition of signals from 62 channels.

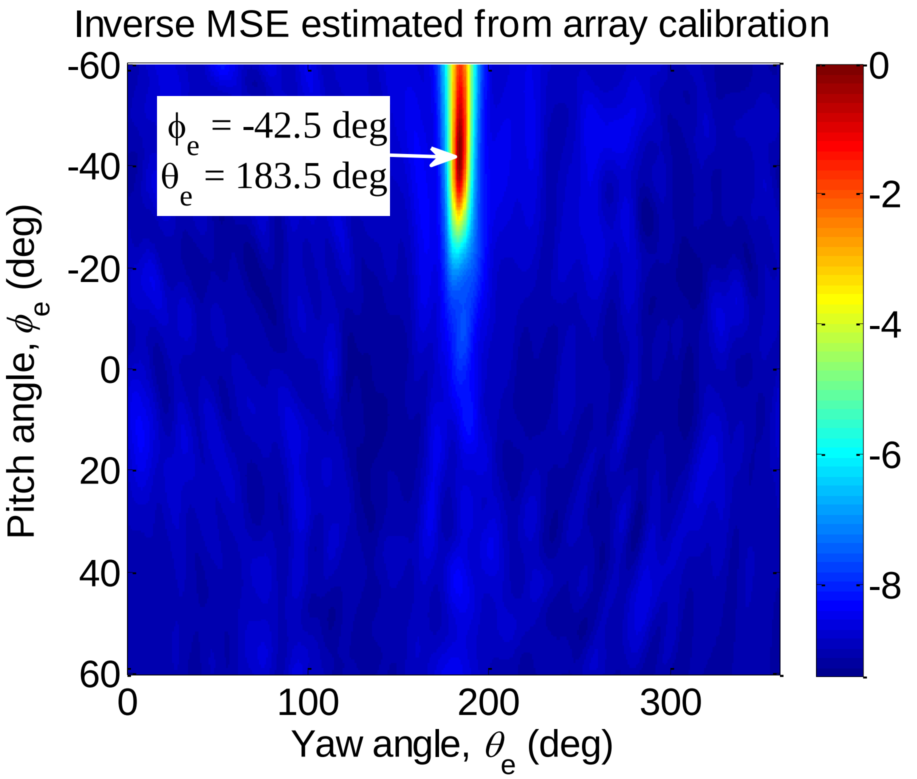

Figure 5.17: Normalised inverse MSE determined by the array attitude calibration process. The highest inverse MSE value was located at $\phi_e = -42.5°$ & $\theta_e = 183.5°$.

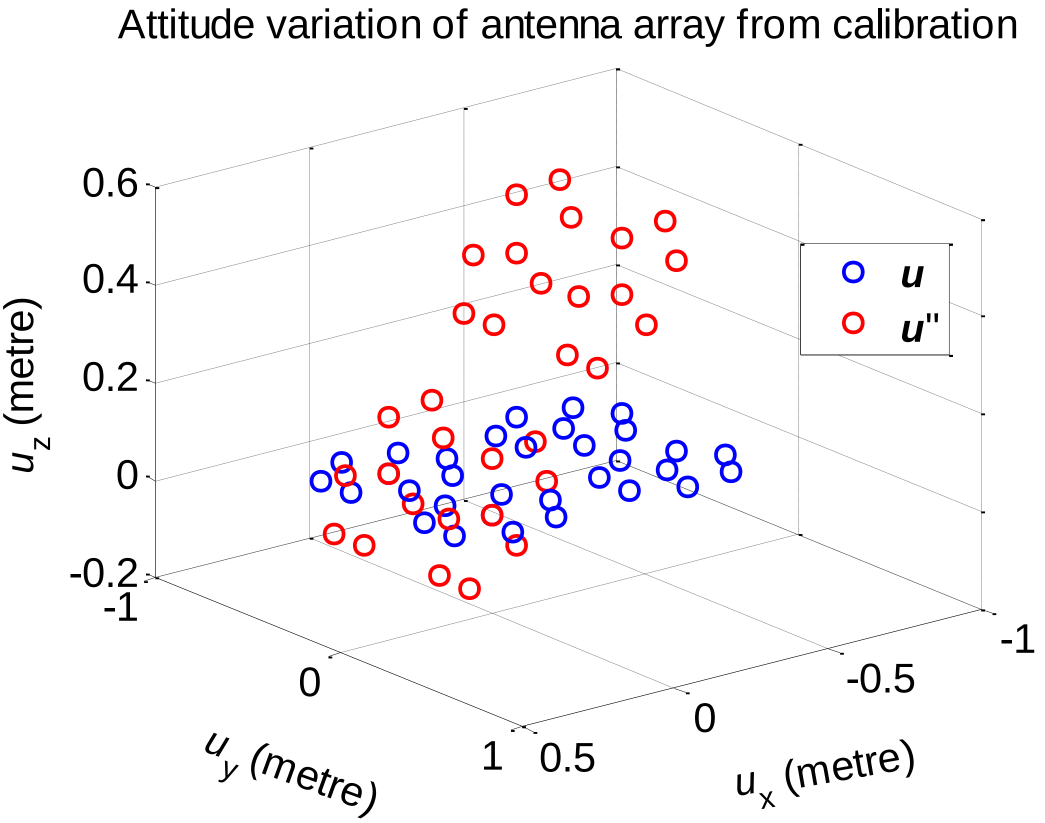

Figure 5.18: Antenna positions relative to the reference before attitude correction, ***u***, and after attitude correction, ***u***’’.

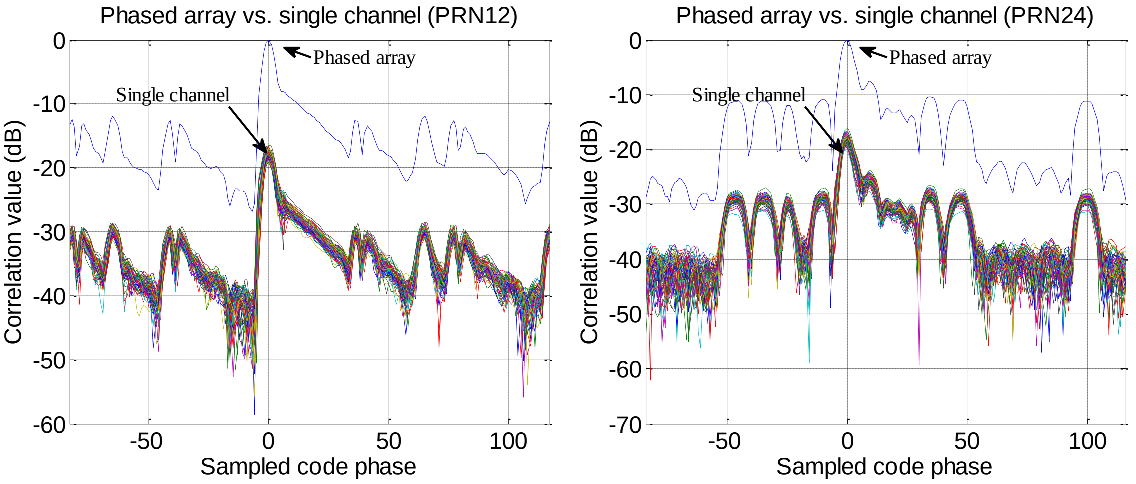

Figure 5.19: Normalised correlation values (dB scale) of phased-array receiver vs single channel from every element using an integration length of 980 ms (PRN12 & PRN24).

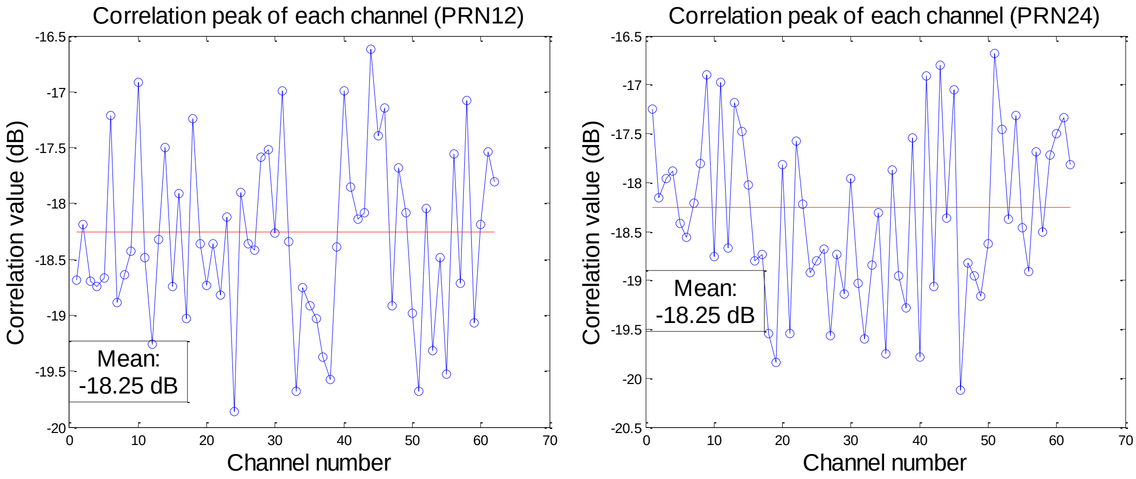

Figure 5.20: Peak correlation value (dB scale) of each channel relative to their phased-array correlation peak (PRN12 & PRN24) at zero sampled code phase.

The acquisition of an extremely weak GPS signals using a single element and the phased-array are compared in Figure 5.21. The phase of the moderately weak PRN02 had significant noise fluctuations for the single element which would cause problems in decoding the navigation message while the beamformer output has an extremely low noise level that resulted in successful identification of the navigation message. For the coarse acquisition of the extremely weak PRN04 signal using the code-Doppler search technique, the single element's result needed a 10 ms integration time to get the highest correlation peak at −1,150 Hz and was not able to demodulate the signal after acquisition. The beamformer's result also had the highest correlation peak at −1,150 Hz and the much lower sidelobes, but with an integration period of only 5 ms. The phased-array technique led to the eventual successful extraction of code and Doppler information from the direct-path signal.

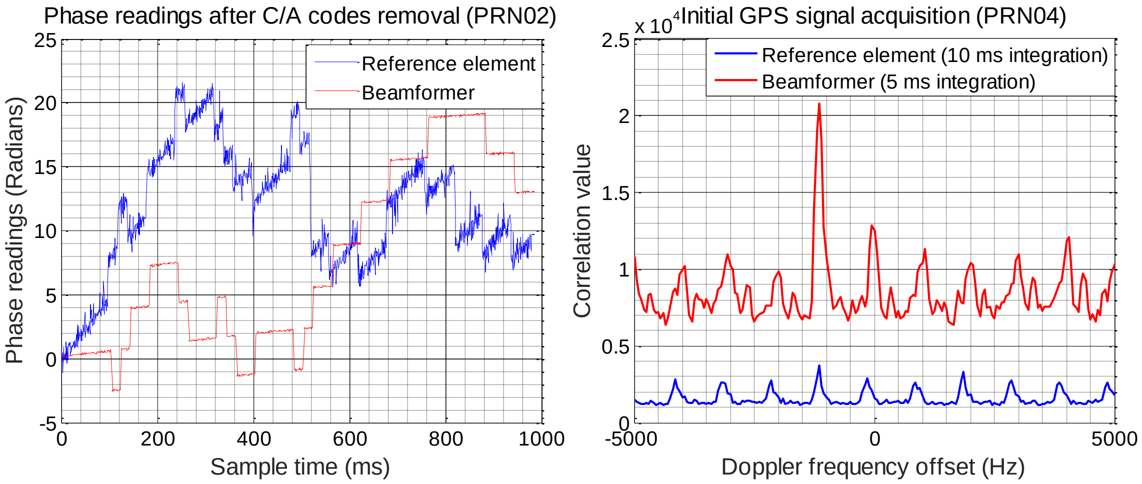

Figure 5.21: Comparison of direct-path signals acquisition results between a single (reference element) and beamformer: Phase readings of data after the removal of C/A codes PRN02 (Left); Coarse Doppler search for GPS signal PRN04 (Right).

Lastly, the DOAs of all available satellites are determined using the conventional beamforming technique. Examples of beampowers vs. DOA for PRN04, PRN12 and PRN14 from the beamforming searching process using an angle resolution of 1° for both θ and ϕ are shown in Figure 5.22. The estimation of the DOA for each satellite by the phased-array GPS receiver are indicated by the highest beampower and recorded below.

Receiver location:	Latitude: −34.94°	Longtitude: 138.55°
Satellite PRN	**Ephemeris info [θ; ϕ] (deg)**	**Max beampower [θ; ϕ] (deg)**
02	[52.12; 26.56]	[50; 25]
04	[−22.43; 39.90]	[−36; 36]
12	[−124.51; 38.35]	[−124; 38]
14	[−142.99; 83.28]	[−143; 84]
24	[137.36; 25.79]	[138; 24]
25	[−143.68; 68.47]	[−144; 68]
29	[158.13; 82.42]	[158; 83]

Table 5.4: Comparison of DOA readings between the results from ephemeris information and the beamformer’s search process.

Most DOA estimates are very accurate except PRN04, which arriving from a direction opposite to the broadside of the tilted array (i.e. facing west). Thus, PRN04 had a much lower signal power and a larger DOA error. This factor may not necessarily affects its ability to be utilised as one illuminator of opportunity for the GPS bistatic radar.

In summary, the results from the verification process demonstrated that the inter-channel phase errors and attitude were accurately determined from the LSE result using an iterative search over all attitude angles. This enabled the phased-array GPS receiver to acquire more GPS signals (i.e. added PRN02 and PRN04 from the previously acquired PRN12, 14, 24, 25 &

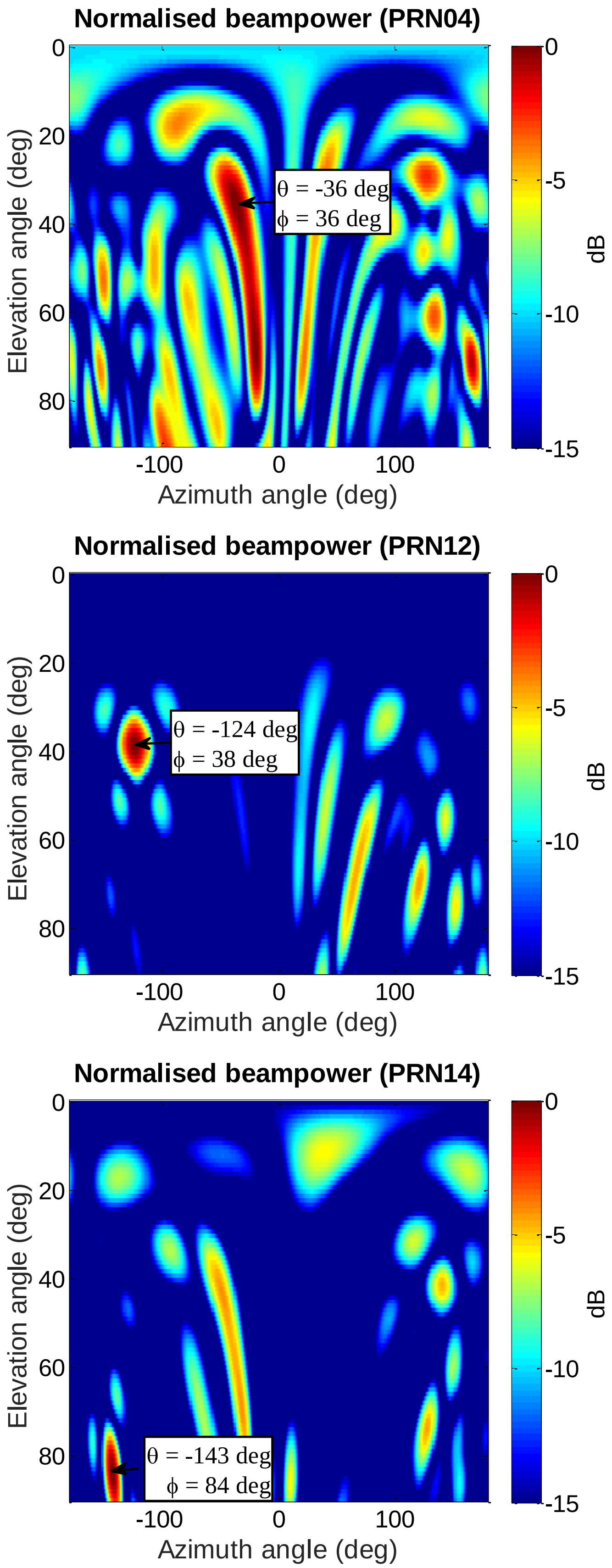

Figure 5.22: Normalised beampowers (dB scale) vs. DOA of PRN04, 12 and 14 from the phased-array GPS receiver DOA search process with an angle resolution of 1° for both θ and ϕ.

29). These parameters will be further used for the target detection process where array processing is required.

5.5 Direct-path Signal Interference Cancellation Technique

The DSI cancellation technique is an essential component for the pre-detection stage of PBRs. However, the target detection simulations for GPS bistatic radar from previous chapters did not cover this technique to simplify the simulation. Hence, the DSI cancellation technique will be introduced in this section. Initially, the background of this technique will be briefly covered at the beginning of this section. Then, the performance of the proposed DSI technique will be demonstrated using simple simulations and ultimately, the data captured from the target detection experiment.

5.5.1 Background

The PBR receivers can easily capture the direct-path signals while performing target detections. From the analysis in (3.2), the power levels of these signals are generally stronger than the target reflections due to the shorter propagation path. They were classified [100, 101, 102] as interferences for all PBRs, specifically termed DSI. These DSIs can produce strong Doppler and delay sidelobes if the correlation coefficients between the matched filter and these interferences are high. Therefore, these strong DSIs can affect the target detection and parameter estimation by masking the target reflections or be misidentified as target returns.

Several DSI cancellation techniques were proposed or performed for different types of PBR. For instance, the Extensive Cancellation Algorithm was performed on data captured by PBRs using the FM [103] and DVB-T [104] signals. Moreover, the least mean squares based filter for direct-path and clutter cancellation was also performed experimentally on the Global System for Mobile Communications (GSM) type PBR [101]. Also, there are DSI mitigation strategies proposed for DAB-based PBR from an antenna reception perspective using a cross polarisation approach or to locate the receiver at a place where the DSI is minimal [102].

The beamforming technique also allows a phased-array receiver to steer beams towards the DOAs of target reflections and rejecting the directions of the direct-path signals as well as their corresponding multipath from ground reflections. However for space-based PBR such as GPS bistatic radar, the direction of the transmitter may overlap with the air targets. Also, the large numbers of widely distributed GPS satellites further increases the likelihood of capturing both the direct-path signal and target reflection from a common direction. For a very large scale array with many more spatial degrees of freedom than the current experimental system and narrower null widths, the simpler null-steering technique to cancel the DSI may be more attractive.

DSI is a significant problem for GPS bistatic radar as the cross-correlation isolation between two PRN codes is only about 24 dB [26], which is much less than the power difference between the DSI and target reflections. Therefore, it is critical to apply a DSI cancellation technique for GPS bistatic radar.

Several techniques have been proposed for detecting weak GPS signals in the presence of much stronger ones, as the problem occurs in indoor GPS applications and the positioning standard for Enhanced E911 cellular phones [33]. One such technique uses the subspace projection [33, 105]. This technique assumes the desired signals and interferers are deterministic. Also, both of these signals are mutually uncorrelated and independent to the AWGN. The GPS bistatic radar also experiences similar circumstance to the abovementioned applications when performing target detection. Therefore, the subspace projection technique can be applied at its pre-detection stage to estimate the direct-path signals and then remove them from the captured data.

Assuming that only a single target appears within the radar receiver's coverage, the baseband data at a GPS receiver can be modelled as

$$x_{\text{base}}(k) = \left(\sum_{l=1}^{L} \mu_{\delta l}\, \mathscr{s}_{\delta l}(k) + \mathscr{s}_{il}(k) \right) + \sigma_n\, n(k) \tag{5.12}$$

where $\mathscr{s}_{\delta l}(k)$ and $\mathscr{s}_{il}(k)$ is the target reflection and interference from the l^{th} GPS satellite respectively while $n(k)$ is an AWGN. For the target detection mode of the GPS bistatic radar, the direct-path signals from the satellites are treated as interference, such that

$$\mathscr{s}_{il}(k) = \mu_{Dl}\, \mathscr{s}_{Dl}(k) \tag{5.13}$$

where $\mathscr{s}_{Dl}(k)$ is the direct-path signal. In the case where $\mu_D \gg \mu_\delta$, the DSIs will become disruptive to the target detection process.

The signal parameters of the DSIs were determined by the direct-path signals acquisition process described in Section 5.3. Following a successful acquisition process, the modulation of direct-path signals can be locally synthesised as

$$\mathscr{s}_{Dl}(k) = C_{Dl}(k)\, f_{Dl}(k) \tag{5.14}$$

where $C_l(k)$ is the PRN code sequence that consists of both the C/A code and navigation message while $f_{Dl}(k)$ is the Doppler frequency component of DSI from the *l*th GPS satellite. Hence, the projection onto the DSI subspace can be expressed as

$$\boldsymbol{\mathcal{P}} = \boldsymbol{\mathcal{S}}(\boldsymbol{\mathcal{S}}^H \boldsymbol{\mathcal{S}})^{-1} \boldsymbol{\mathcal{S}}^{\mathrm{H}} \tag{5.15}$$

where $\boldsymbol{\mathcal{S}}$ is a matrix composed of *L* signals, such that

$$\boldsymbol{\mathcal{S}} = [\boldsymbol{\mathscr{s}}_{D1} \quad \boldsymbol{\mathscr{s}}_{D2} \quad \cdots \quad \boldsymbol{\mathscr{s}}_{DL}] \tag{5.16}$$

The DSIs can be removed by applying an orthogonal projection to the DSI subspace:

$$\boldsymbol{y}_{base} = (\mathbf{I} - \boldsymbol{\mathcal{P}})\boldsymbol{x}_{\mathrm{base}} \tag{5.17}$$

It is critical to use an accurate replica of the direct-path signal for the subspace projection to ensure good cancellation of the DSIs. While the Doppler and code phase of the DSIs can be accurately determined from the direct-path signal acquisition, the multipath signals due to reflections from the ground or large stationary objects cannot be identified. Like the DSIs, these multipath signals can also be much stronger than the target reflections, which can mask targets. To include multipath in the projection, the expression for the DSI in (5.13) can be expanded as

$$\mathscr{s}_{il}(k) = \sum_{\mathfrak{m}=0}^{\mathfrak{M}} \mu_{\mathfrak{m}l}\, \mathscr{s}_{\mathfrak{m}l}(k) \tag{5.18}$$

where there are $\mathfrak{M}$ unknown multipath signals, $\mathscr{s}_{\mathfrak{m}l}(k)$, from the *l*th satellite, which can be expressed as

$$\mathscr{s}_{\mathfrak{m}l}(k) = \mathscr{s}_{Dl}(k - \mathfrak{m}) \tag{5.19}$$

The finite impulse response (FIR) Wiener filter was proposed as a solution for GPS applications to cancel the DSIs and their multipath components [106]. This method extends the functionality of the subspace projection technique to estimate the multipath signals. From Figure 5.23, this filter models the effects of both the direct-path signals and their corresponding multipath components by applying an FIR filter to the locally generated GPS baseband signal, such that

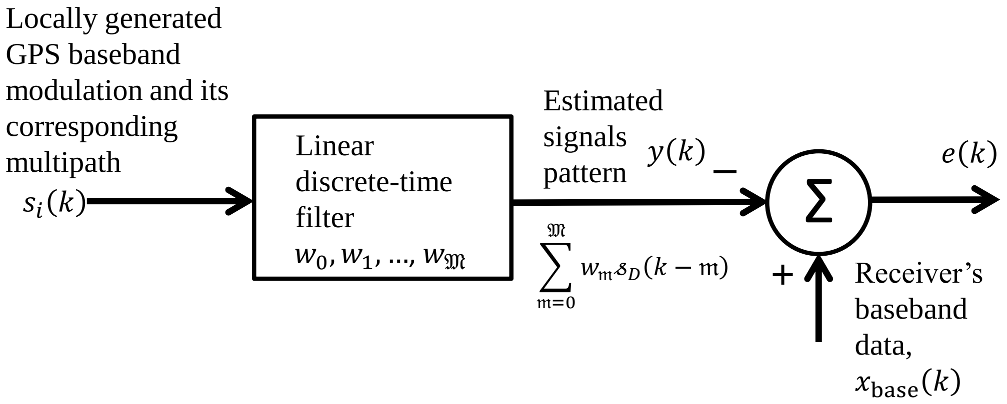

Figure 5.23: Illustration of a Wiener filter for estimating and cancelling the interferences from the captured data.

$$y(k) = \sum_{\mathfrak{m}=0}^{\mathfrak{M}} w_{\mathfrak{m}}\, s(k-\mathfrak{m}) \tag{5.20}$$

where $w_{\mathfrak{m}}$ denotes weight for $\mathfrak{m}^{\text{th}}$ delay. Using the minimum mean square error (MMSE) estimator, the weight vector for the Wiener filter can be determined as

$$\boldsymbol{w} = (\boldsymbol{S}^{\mathrm{H}}\boldsymbol{S})^{-1}\boldsymbol{S}^{\mathrm{H}}\boldsymbol{x}_{\text{base}} \tag{5.21}$$

where $\boldsymbol{S}$ in this section extends the previous model of (5.16), such that

$$\boldsymbol{S} = [\boldsymbol{S}_{i1} \quad \boldsymbol{S}_{i2} \quad \ldots \quad \boldsymbol{S}_{iL}] \tag{5.22}$$

where

$$\boldsymbol{S}_i = [s_0 \quad s_1 \quad \ldots \quad s_{\mathfrak{M}}] \tag{5.23}$$

Note that the total number of taps, $\mathfrak{M}$, assigned to the filter is finite. More taps would allow more discretely delayed multipath signals to be estimated from the baseband data at a cost of a higher computational load. The direct and multipath signals are suppressed at the output of the Wiener filter when a subtraction is made between the receiver's baseband data and the estimated signals.

5.5.2 Simulation Examples of DSI cancellation technique

A simple simulation was performed to investigate the performance of DSI cancellation technique using the Wiener filter for GPS bistatic radar. This simulation case assumes that the baseband data consists of direct-path signals from 2 GPS satellites that transmit signals PRN01 and PRN02, their corresponding multipath signals and a target reflection from PRN02. The Doppler frequency difference between the two direct-path signals at the receiver is 100 Hz. The Doppler frequency and delay of the target reflection relative to the direct-path signal PRN02 is also set to be 100 Hz (same as the direct-path signal of PRN01) and 4 delay samples respectively. The parameters of these signals prior to the matched filter stage are recorded below.

Sampling frequency:	4.092 MHz			
Integration time:	100 ms			
Signals	**PRN**	**SNR (dB)**	**Sample delay**	**Frequency (Hz)**
Direct-path signal 1	01	0	0	100
Direct-path signal 2	02	0	0	0
Multipath group 1	01	−40 to −20	0 to 100	100
Multipath group 2	02	−40 to −20	0 to 100	0
Target reflection	02	−30	4	100

Table 5.5: Summary of signal parameters for DSI cancellation simulation case.

The target searching process was performed by the Doppler-delay search technique using the correlation between the input data and the locally generated C/A codes from PRN02. The normalised CAF outcomes from three separate processes are shown in Figure 5.24: (i) no Wiener filter, (ii) Wiener filter cancelling only the DSI (i.e. $\mathfrak{M} = 0$) and (iii) Wiener filter cancelling both direct-path and multipath signals (i.e. $\mathfrak{M} = 100$). The CAF in the first case shows the presence of strong DSIs and their corresponding multipath for PRN01 at 0 Hz and PRN02 at 100 Hz. The target return cannot be clearly identified from this result as it was masked by these interferers. When the DSIs of both PRNs are estimated by the Wiener filter and removed in the second case, it is observed that the direct-path signal of PRN02 and its sidelobes no longer exist. However, the multipath of both PRN01 and PRN02 are still observable. The multipath of PRN01 corrupts the target return, interferes with the correlation values along the 100 Hz Doppler bin. When the DSIs and their corresponding multipath of both PRNs are estimated by the Wiener filter and removed, the resulting CAF shows only a strong correlation peak at the 100 Hz Doppler bin and 4 samples delay bin, which matches the target parameters in this simulation. These CAF results demonstrate over 60 dB cancellation of the DSI and its multipath components.

In summary, the Wiener filter achieves perfect cancellation of the DSI and its multipath using simulated signals. A more realistic study of the Wiener filter DSI cancellation technique using a Wiener filter using experimental data is described in the following section.

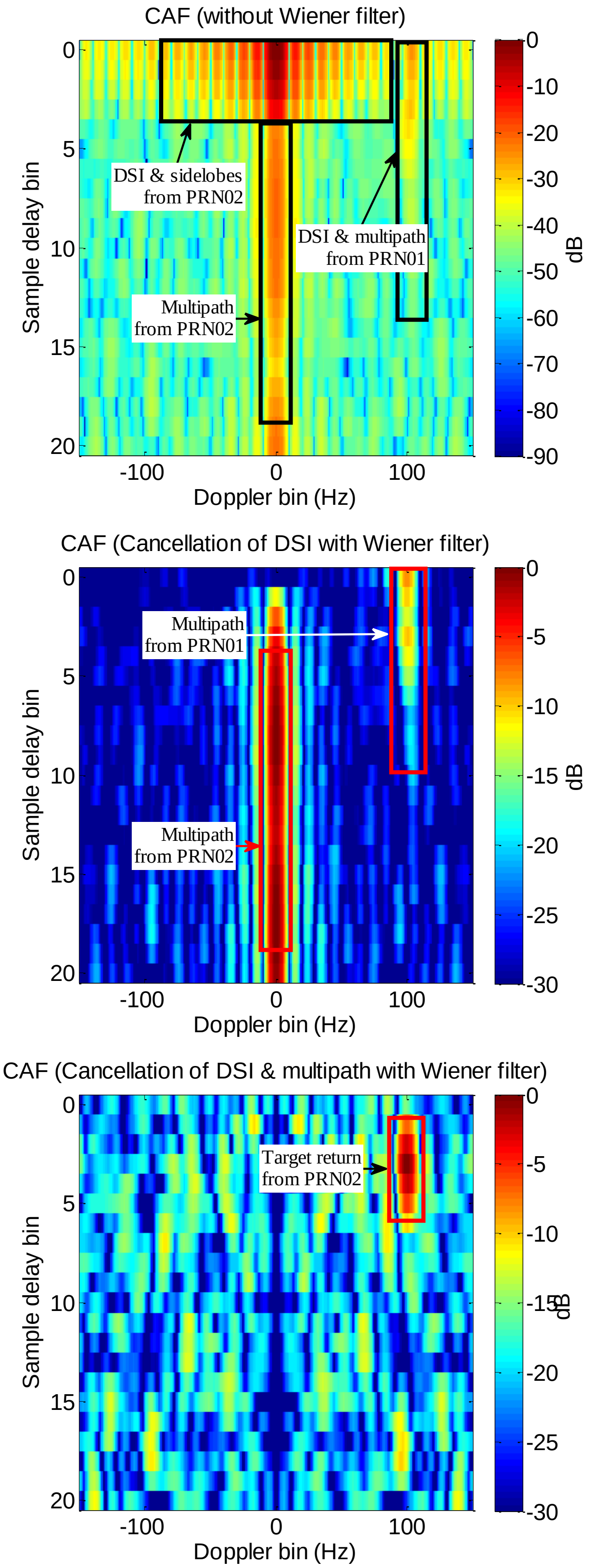

Figure 5.24: Normalised CAF results from a simulation detection process without Wiener filter (Top), with Wiener filter to remove the DSIs only (Middle) and to remove both DSIs and their multipath (Bottom). Both the CAFs from the Wiener filter are compressed to a dynamic range of 30 dB.

5.5.3 Experimental results using DSI cancellation technique

The performance for the GPS direct-path signals cancellation technique using the Wiener filter is investigated experimentally using the captured data by comparing the strength of DSIs before and after applying the filter. The signal power was measured from the cross-correlation between the data from the beamformer's output and the locally generated C/A code sequences for the weak PRN02 signal and the strong PRN24. Note that the direct-path's Doppler component, $f_{Dl}(k)$, and navigation messages, $C_{\mathrm{NAV}}(k)$, were removed from the data before the correlation processes.

The correlation results include the cases where (i) no filter is applied; (ii) applying a Wiener filter using number of taps, $\mathfrak{M} =$ (ii) 20, (iii) 40 and (iv) 60. The DSIs for the Wiener filter were obtained by applying their corresponding modulations extracted from the Section 5.3 direct-path signals acquisition technique, including the C/A code delay, navigation message and the polynomial Doppler model into the filter's estimator. The results are shown in Figure 5.25. The correlation values are squared and normalised to the peak level of the DSI case when no filter is applied to the data. From Figure 5.25, the DSI for PRN02 and PRN24 when no filter is applied (i.e. zero sampled code phase) is normalised to 0 dB. The multipath components are less than −20 dB and correlation sidelobes are around −25 dB relative of the DSI. These components would mask weak target returns. When the filter with 20 taps was applied for DSI estimation and cancellation, the direct-path signal peaks are suppressed to values less than −100 dB. However, the multipath and sidelobe components only attenuated to power levels that are comparable to the target reflections. The sidelobe cancellation improved considerably when a filter with 60 taps was applied. The residual sidelobe components (i.e. beyond 60 sampled code phase offset) remain at −50 dB or less, allowing much weaker targets to be detected. They became even less problematic if the DOAs of their transmitting satellites, Doppler and code phases do not coincide with the target parameters.

In summary, applying a Wiener filter to the replica signal obtained from the acquisition process was effective in attenuating the DSI and its multipath components by over 50 dB if sufficient taps are used in the filter. As a result, the Wiener filter DSI cancellation technique is applied to the real data prior to further target detection processing described in the next section.

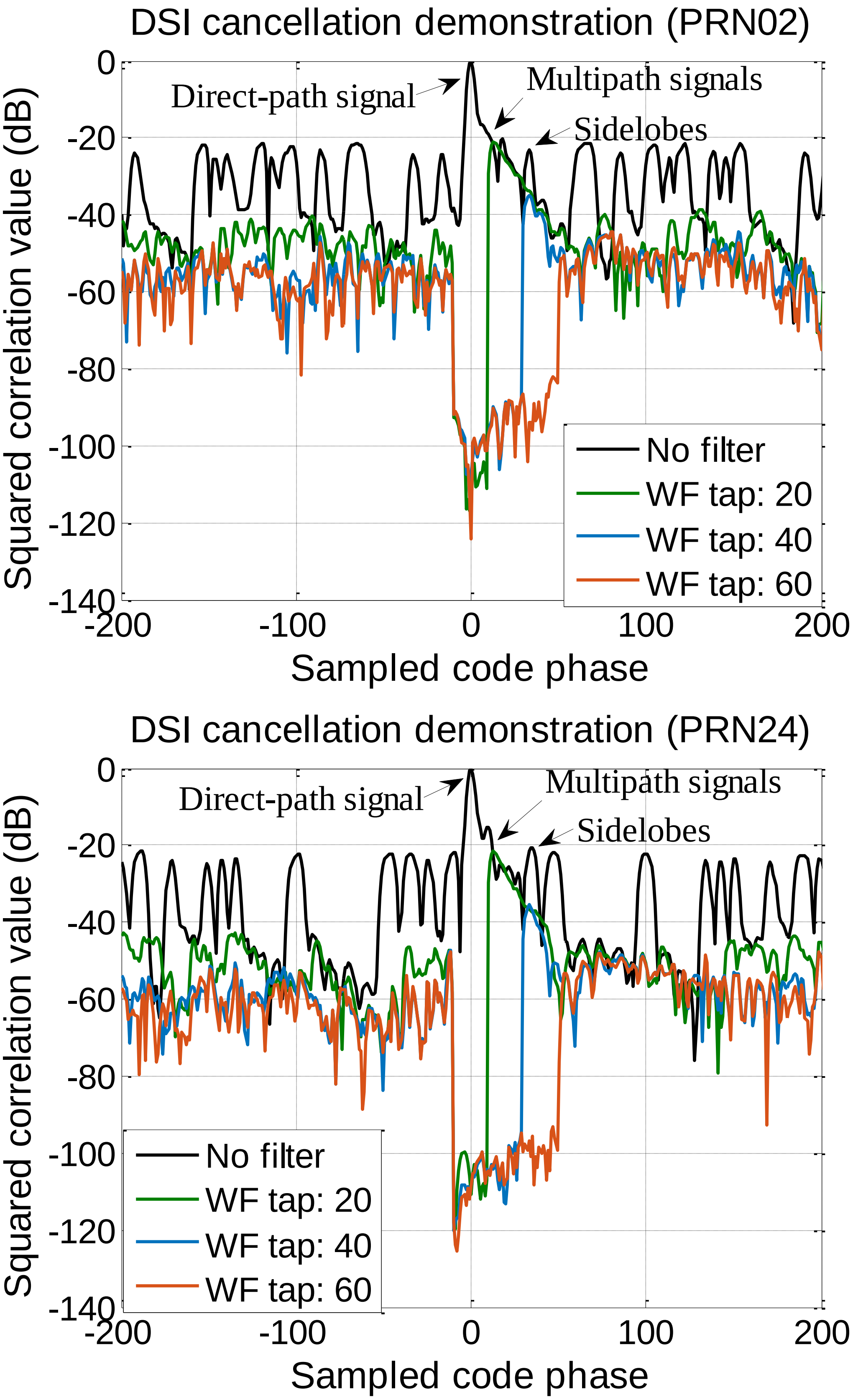

Figure 5.25: Squared correlation results (dB) for PRN02 and PRN24 from the beamformer's output applying (i) No filter; Wiener filter for DSI cancellation with number of taps, $\mathfrak{M} =$ (ii) 20, (iii) 40 and (iv) 60.

5.6 Experimental Results from Air Target Detection

This section describes an air target detection experiment performed by the GPS bistatic radar. The results of the air target detection and parameters estimation using the phased-array and MIMO techniques are also analysed and presented to demonstrate the feasibility of using illuminators of opportunity with weak transmitting powers for PBR in performing air target detection and localisation.

5.6.1 Experiment Scenario for Target Detection

According to Table 5.2, the detection range of our PBR is around 273 m. As the target is non-cooperative, the air target chosen for the experiment should have a predictable flight path and motion so that the detection and parameter estimation results can be verified. To meet with the above considerations, the experimental GPS bistatic radar system was deployed at Morley Street, South Australia to perform the target detection experiment. It is located outside the perimeter fence of the Adelaide Airport where many aircraft take off and land. Also, it is more desirable to perform detection on an aircraft which is on final approach due to its predictable flight path, constant velocity and low altitude. An illustration of the scenario is shown in Figure 5.26. This figure also shows the predicted flight path for final approaches aircraft with a heading of 228° bearing, towards the airstrip at Adelaide airport.

The phased-array receiver was deployed at 34°56'14.82"S latitude and 138°32'53.99"E longitude in an orientation described earlier in Section 5.4.1. As shown in Figure 5.27, the whole system was powered up by a fully charged lead-acid battery via a power inverter and the data captured by the FPGAs was streamed onto a laptop PC. During the experiments, the data acquisition command was triggered by the PC each time to capture a flyby aircraft when it flew past the aircraft approach landing lights. This ensures that the target is approximately 100 m away from the receiver, which lies within the detection range of the system.

An aircraft on its final approach is anticipated to be travelling at a constant ground speed between 70 and 75 m/s at a glide slope of 20:1. The descending speed of the aircraft is thus estimated to be between 3.5 to 3.75 m/s. As calculated by the Google Earth, a software package, the distance between the aircraft and the touchdown point at the airstrip is about 0.9 km. This means that the flyby aircraft is at an altitude of around 45 m relative to the ground.

The experimental results for the following detection process are obtained using a dataset that was captured during the arrival of an unknown model jet-powered regional airliner (flight

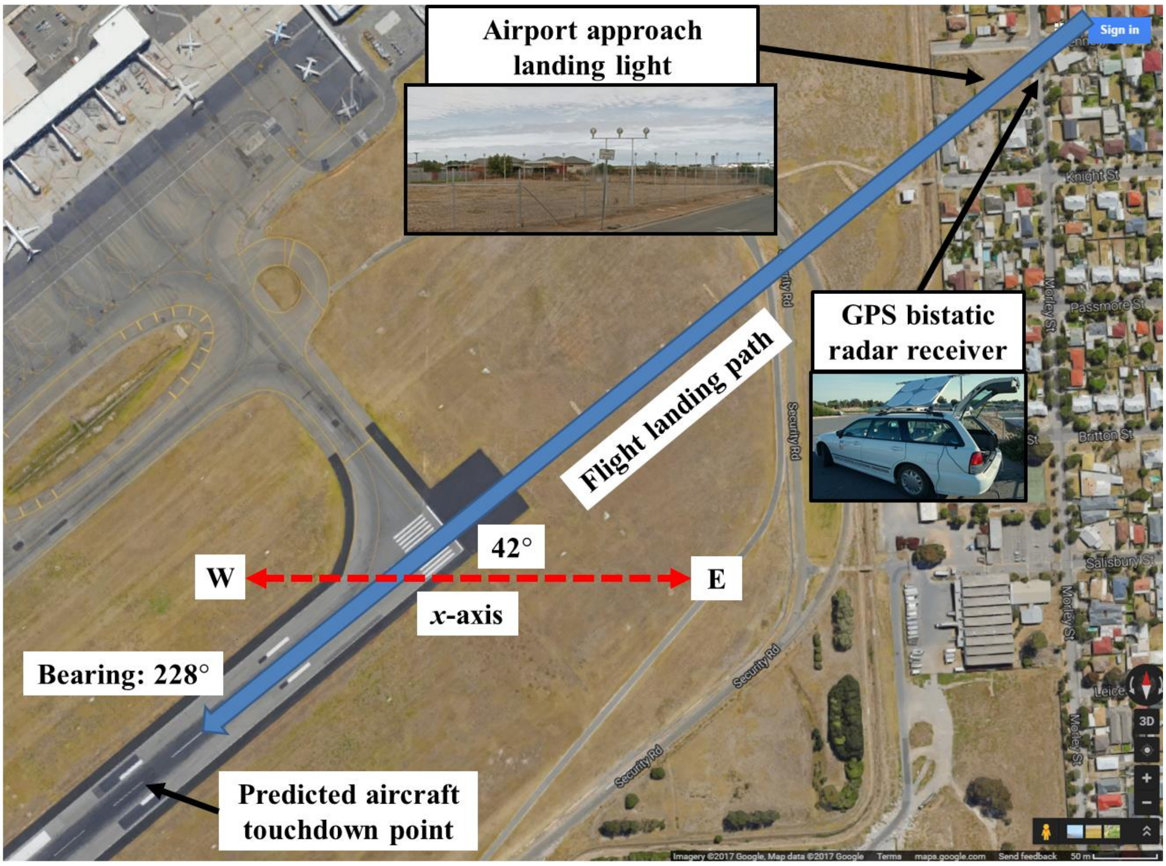

Figure 5.26: Experiment scenario (Courtesy Google Map's satellite view).

Figure 5.27: Deployment of phased-array receiver (Left); Power supply and data acquisition PC for the receiver system (Right).

SH462 according to the flight tracker). The footage of this flyby was recorded by a digital video camera. Three snapshots showing the aircraft's descent were taken from the video clip and shown in Figure 5.28. As this jet aircraft was the smallest among all other aircraft captured by the receiver, its RCS should also be comparatively smaller in theory. As recorded by the data acquisition PC that was synchronised with the internet server on the site, the experiment was performed at 9.52am CST on April 9th, 2013. This time stamp was applied to the satellite

Figure 5.28: Pictures of landing aircraft extracted from the footage recorded by a digital video camera at the target detection experiment site.

tracking tool to identify the locations of the GPS satellites relative to the radar receiver as shown in Figure 5.29 prior to performing the target pre-detection processing steps of direct-path signal acquisition, array calibration and DSO cancellation, described in the previous sections.

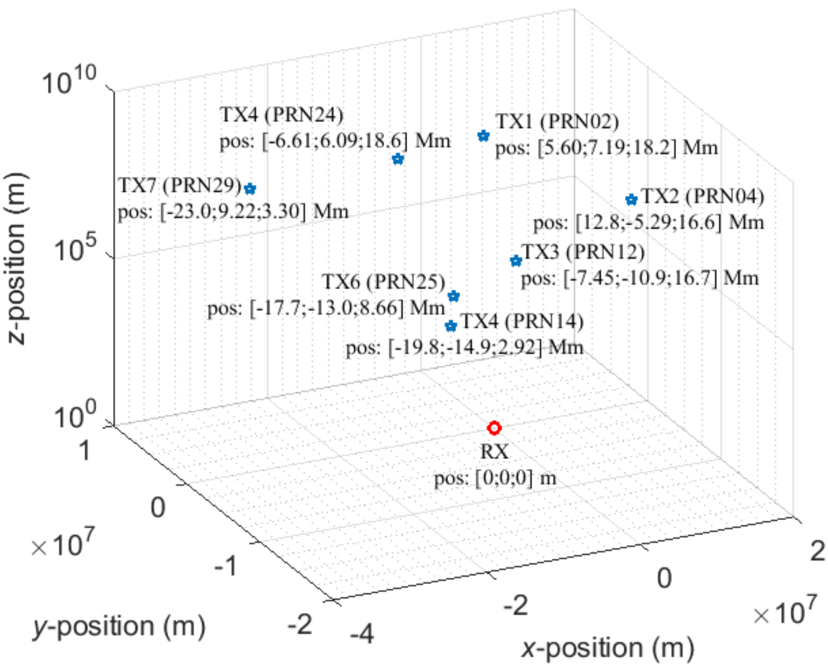

Figure 5.29: Positions of GPS satellites during the aircraft detection experiment.

5.6.2 Phased-array Detection Technique

Using the content of each PRN extracted from the direct-path signal acquisition process, the phased-array detection technique was performed on the data captured from the experiment using the same methods and data length (i.e. 100 ms) as described in Section 3.5. This means that the captured data with an approximate total length of 1000 ms was fragmentised into 10 sub-blocks and each of them was processed individually.

The detection process was performed by first obtaining the CAF result from every channel using the code-Doppler search technique. Then the correlation values from all the channels at each Doppler and sample delay bin were fed into a conventional beamformer, which performed a target search across all directions. The correlation value at the highest beampower from the search process was extracted and formed the CCAF result as a function of Doppler and sample delay.

The presence of strong peaks was discovered in the CCAF results of 4 satellites (i.e. PRN02, 04, 12 and 24). In Figure 5.30, the normalised CCAF results for these satellites at data time frame 200 to 300 ms are shown. These correlation peaks appeared at certain Doppler frequency offsets and between 1 to 2 sampled code phase delays relative to their corresponding direct-path signals. As the data is sampled at 4.167 MHz, these delays roughly resemble target ranges between 72 to 144 m from the receiver. Moreover, the SNRs of these correlation peaks were

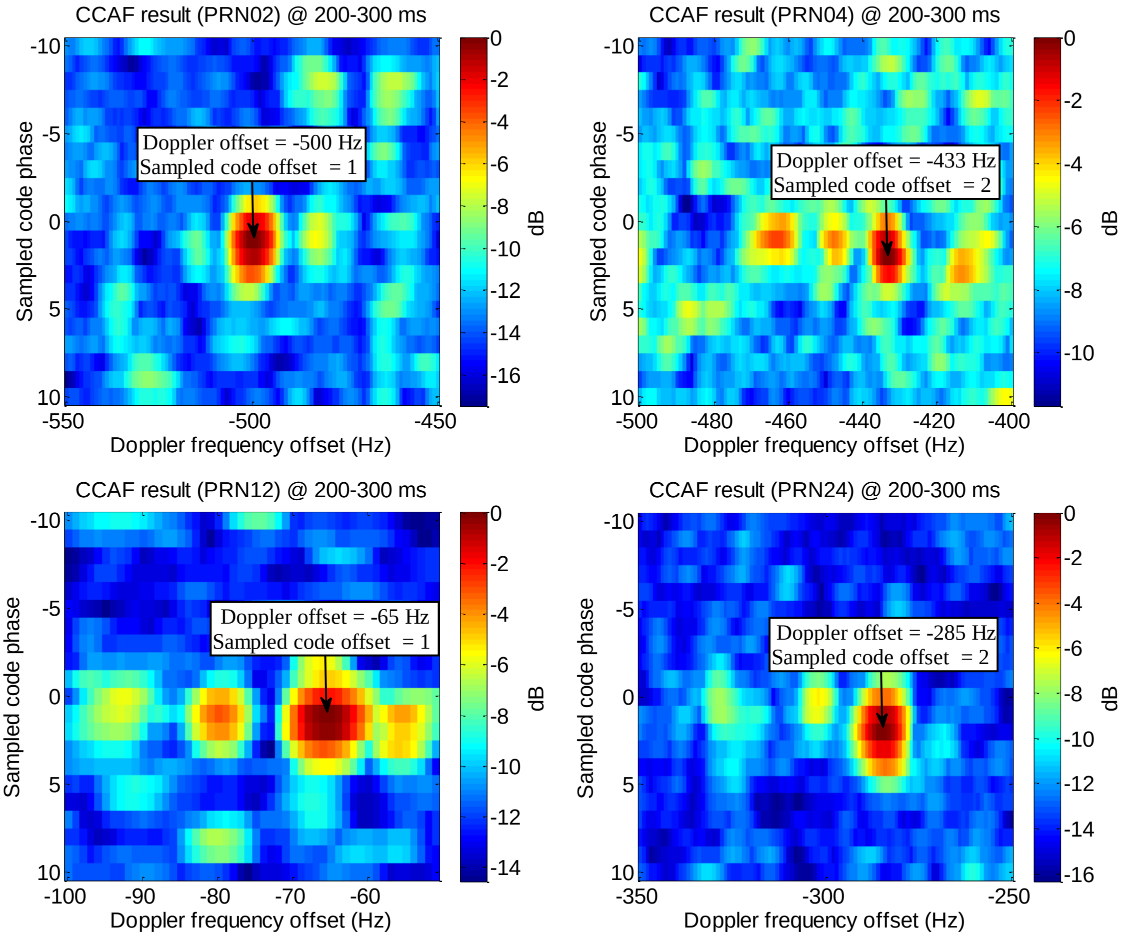

Figure 5.30: Normalised CCAF results of PRN02, 04, 12 and 24 from the experiment detection process for data period 200 - 300 ms.

also measured to be over 14 dB, which exceed the detection threshold set by the power budget calculation in Table 5.2 (i.e. 11.7 dB at 273 m). Hence, these peak values are suspected to be the reflections from the aircraft. There are also other lesser returns from each PRN at different Doppler offsets. Considering the size of the designated air target and its relatively close distance from the receiver, these returns are hypothetically believed to be the reflections of GPS signals from other parts of the aircraft.

The normalised beampower for these correlation peaks were extracted to verify the DOAs for these suspected signals. From the analysis of beamformer results at data time frame 200 - 300 ms in Figure 5.31, it can be observed that the DOAs from most reflected satellite signals were very close to each other. However, the azimuth angle of the reflected signal for PRN24 varies by about 10 degrees from the others. Further investigation was carried to observe the DOA of other signatures from PRN24. From Figure 5.32, the peak beampower of the third strongest signature (i.e. Doppler offset −328 Hz and sampled code phase 1) was observed to have lower signal-to-sidelobes ratio due to the poorer SNR of the arrival signal, but is located

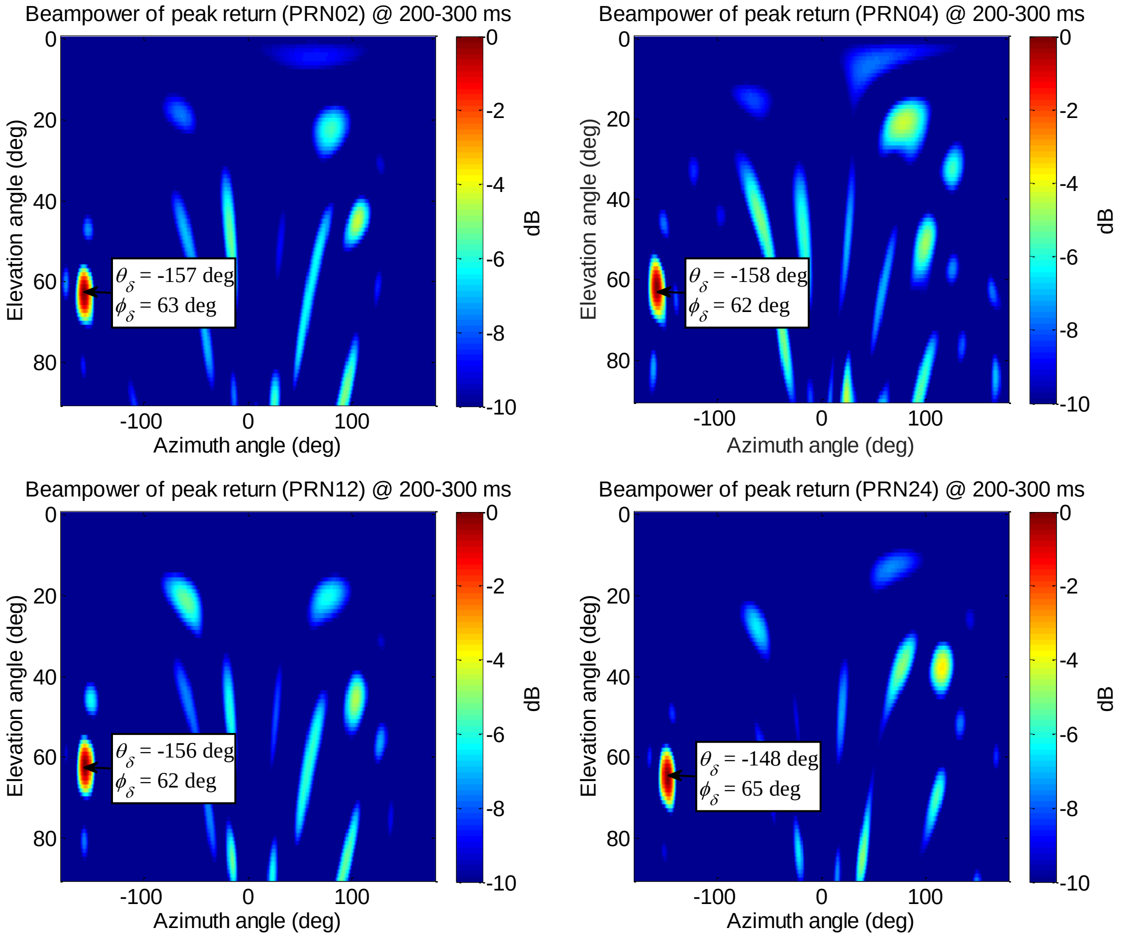
Beampower of peak return (PRN02) @ 200-300 ms

Beampower of peak return (PRN04) @ 200-300 ms

Beampower of peak return (PRN12) @ 200-300 ms

Beampower of peak return (PRN24) @ 200-300 ms

θ_δ = -157 deg
ϕ_δ = 63 deg

θ_δ = -158 deg
ϕ_δ = 62 deg

θ_δ = -156 deg
ϕ_δ = 62 deg

θ_δ = -148 deg
ϕ_δ = 65 deg

Figure 5.31: Normalised beampower of peak returns from the CCAF results of PRN02, 04, 12 and 24 for data period 200 - 300 ms.

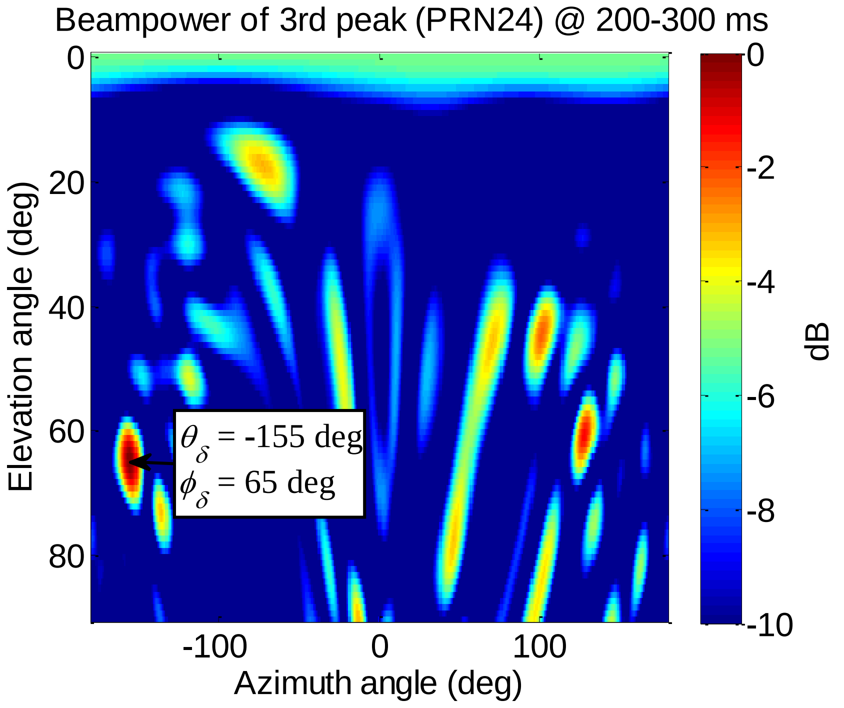
Beampower of 3rd peak (PRN24) @ 200-300 ms

θ_δ = -155 deg
ϕ_δ = 65 deg

Figure 5.32: Normalised beampower of 3rd peak return from the CCAF result of PRN24 for data period 200 - 300 ms. The DOA for the highest beampower is indicated.

at azimuth and elevation angles of −155° and 65° respectively. This DOA reading appears to be closer to the DOA of the reflections from the other satellites. These results indicate that there are multiple reflections of GPS signals which came from different DOAs.

Further investigation was carried to observe the DOA variation of this suspected signature over the full data block. Recall that the captured data was fragmentised into 10 frames, where each frame uses an integration length of 100 ms for the data. The peak signature from PRN02 within each data frame was selected for the observation and the beampowers corresponding to the strongest Doppler/delay bin are shown in Figure 5.33. These results demonstrate that the elevation angles relative to z-axis gradually increase, which implies that the altitude of the target was decreasing. The azimuth angle variation of the target is also compared with the landing flight path shown by Google Earth in Figure 5.34. From the analysis, it is observed the straight lines that follow the azimuth angles for both the initial and end result (i.e. frame 1 and 8) intersect with the flight path. In addition, the distance between these intersections is measured to be 75 m. This value is approximately equal to the distance predicted from the ground speed of an aircraft landing approach (i.e. 70 – 75 m/s). This evidence further justifies that these peak returns came from the reflections of the flyby aircraft in the experiment scenario.

The DOA of each time frame within the captured data is also obtained from the beamformer results of all other satellites and shown in Figure 5.35. Note that the result from PRN12 is not included as a clear peak could not be discerned in the CCAF. Both azimuth and elevation angle variations for the reflections from these satellites match well with the trend of the flight path. On the other hand, the azimuth angles of different PRNs are not as well matched as the elevation angles. This might be due to the fact that hulls of all commercial aircrafts have a large length-to-height ratio. As a result, the reflections from different parts of the body have a significantly wider spread of azimuth angles than elevation angles when the aircraft is close to the receiver.

Once the DOAs of the target reflections were obtained from the CCAF results, the beam of the receiver was steered in these directions and another code-Doppler search was applied to the beamformed data to form the BCAF results. This procedure aims to focus the reflections in a single direction while suppressing the interferences from other directions. After applying this second stage search process for the target at DOA $\phi_d = 63°$ and $\theta_d = -157°$, target reflections from 2 additional PRNs (i.e. PRN25 and 29) were identified. The normalised BCAF results at data period 200 to 300 ms, a time frame where the peak returns from all PRNs can be reliably obtained, are shown in Figure 5.36.

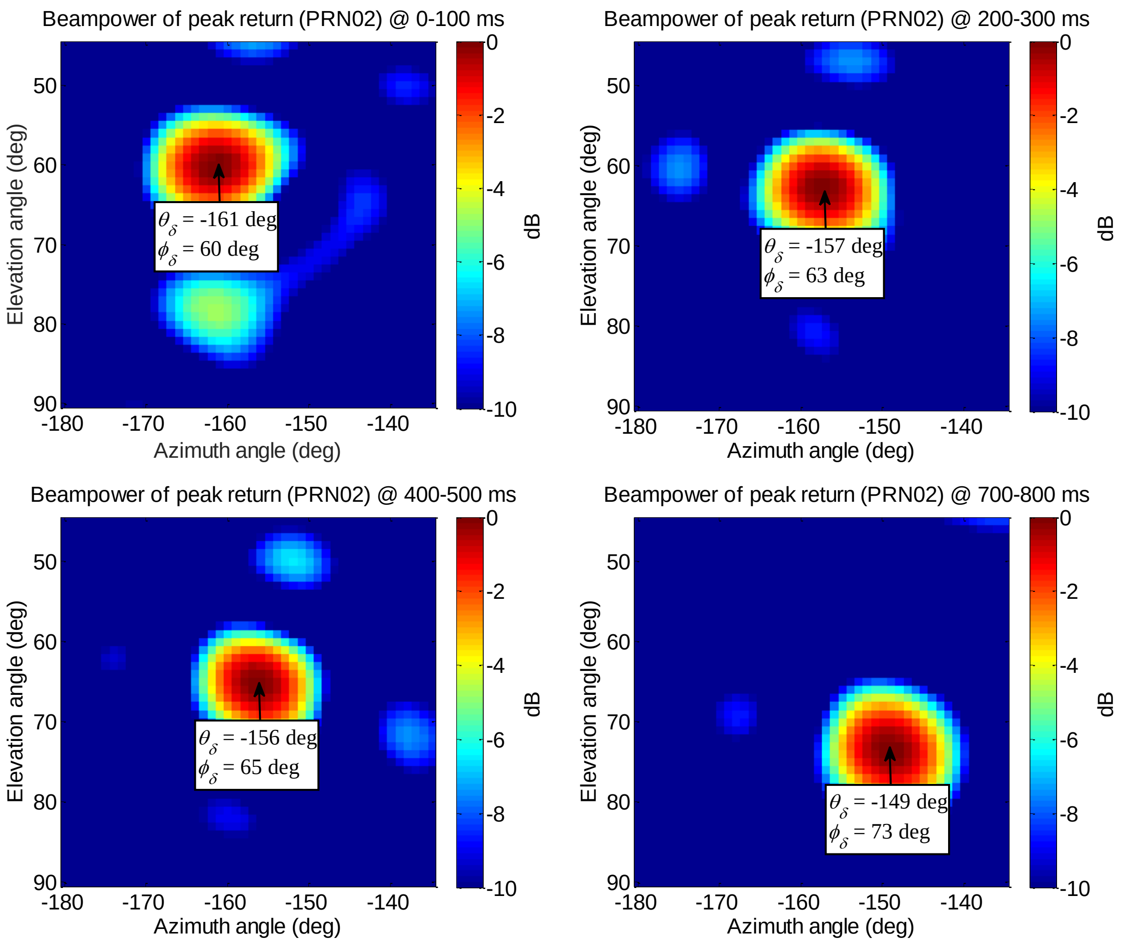

Figure 5.33: Normalised beampower results of peak return from the CCAF results of PRN02 along the captured data. Among the results are those from frame 1, 3, 5 and 8.

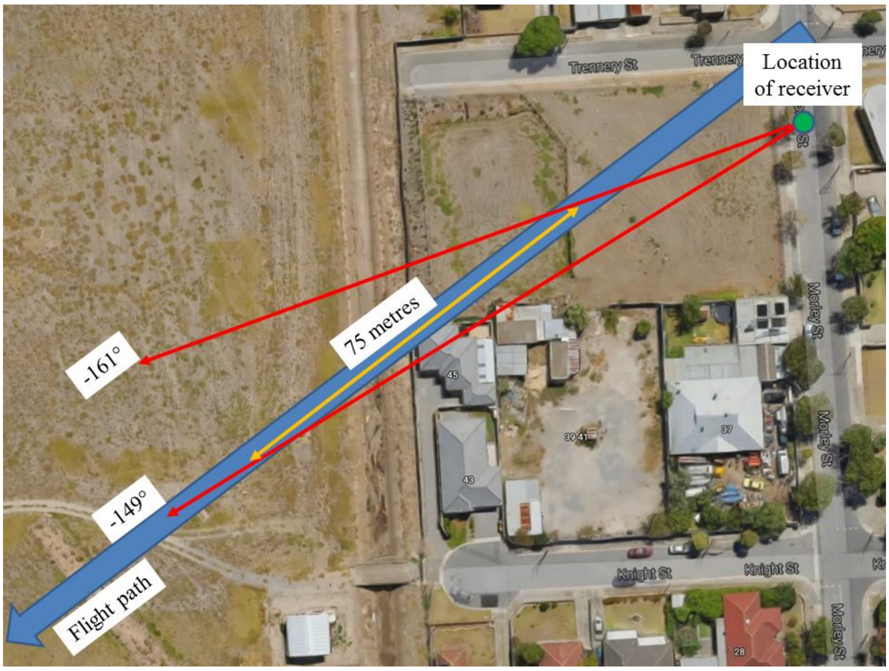

Figure 5.34: Comparison of flight path and the azimuth angles measured from the beamformer results of PRN02 along the captured data of approximately 1000 ms. Google Earth was used to perform the angles and distance measurements.

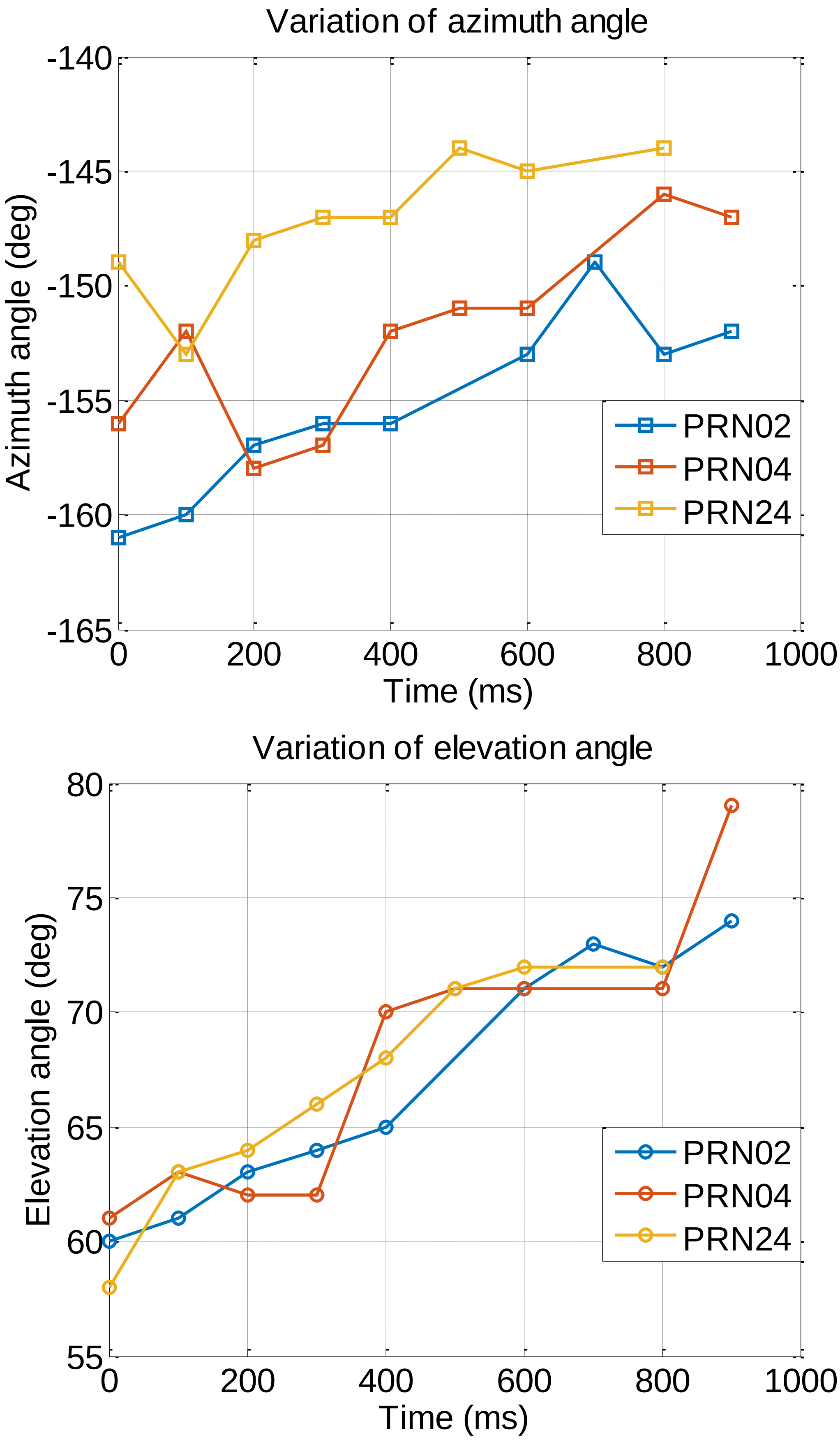

Figure 5.35: Variations of azimuth and elevation angles corresponding to the peak returns from PRN02, 04 and 24 at different time.

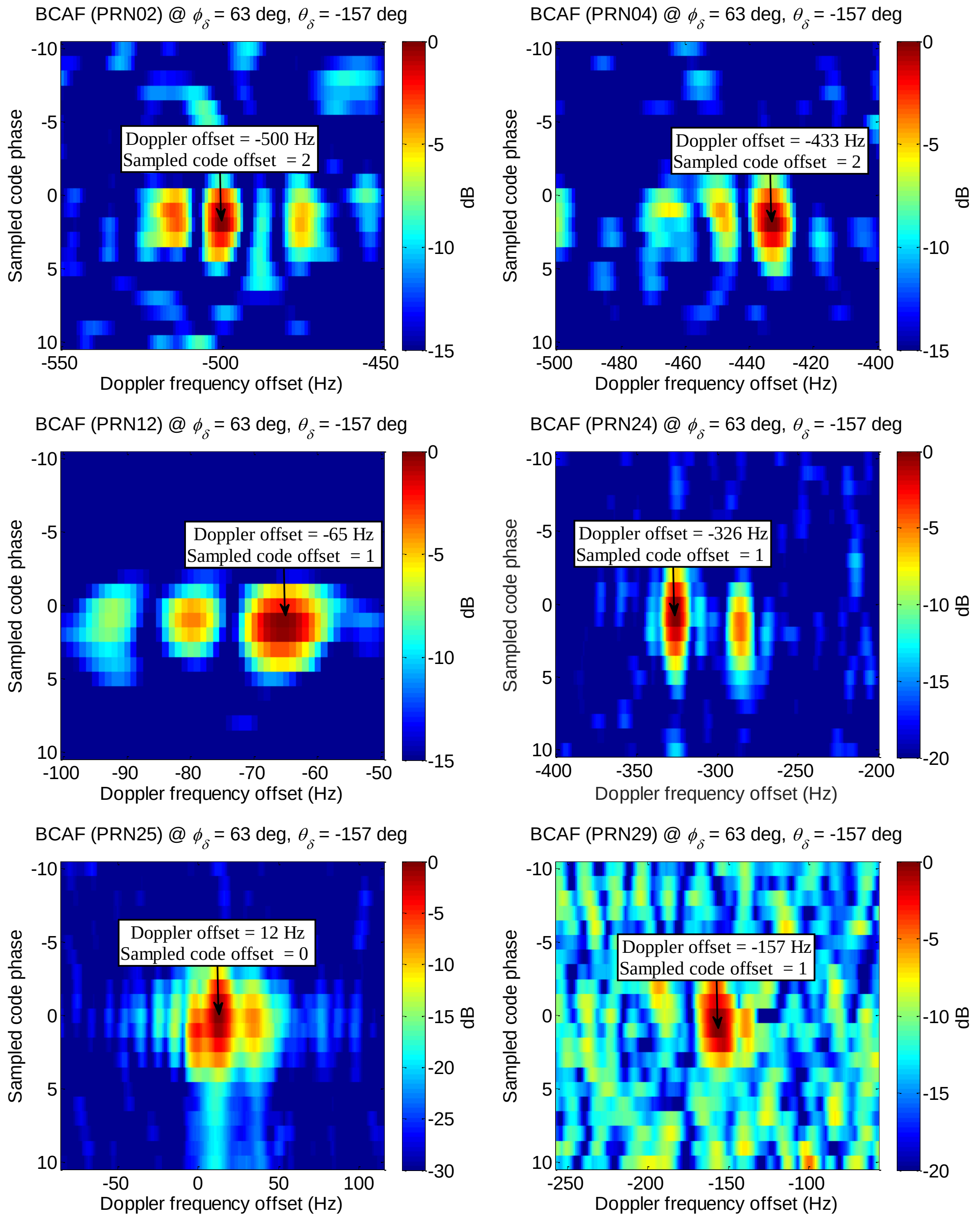

Figure 5.36: Normalised BCAF results of PRN02, 04, 12, 24, 25 and 29 from the experiment detection process for data period 200 - 300 ms at $\phi_d = 63°$ and $\theta_d = -157°$.

The BCAF results presented lower background noise compared to the CCAF results in Figure 5.30 as the correlation values from much fewer noise bins and sidelobe bins exceeded −15 dB. Moreover, it can be observed that the result from PRN24 had the strongest correlation peak at −326 Hz Doppler frequency offset followed by the second strongest peak at −285 Hz. Recall that from the observation of CCAF result, the signal at −326 Hz has comparatively poorer SNR than the signals at −285 Hz and −300 Hz, but its DOA is closer to the reflections from other PRNs. The outcome of the BCAF result further demonstrated that the beamformer retains the SNR of the signal at the desired DOA while effectively attenuated other reflections.

The BCAF result from PRN25 had a strong signal reflection with an SNR of around 28 dB at zero sampled code delay and 12 Hz Doppler frequency offset. It was observed that there is a small DOA difference between the target reflection and satellite PRN25 (i.e. $[\theta; \phi]_{\mathrm{PRN25}} = [-143.68°; 68.47°]$, which means that the location of the flyby aircraft approached the forward scatter path between this satellite and radar receiver. This observation shows that high SNR target reflections due to the increase in target RCS in the forward scatter path, can also be feasibly extracted, provided the power level of DSIs are sufficiently suppressed. On the other hand, the target reflection from BCAF result PRN29 had the highest noise floor among all other results due to its poor SNR of 12.2 dB, which is close to the detection threshold (i.e. 11.7 dB) set for the receiver.

The SNRs of the correlation peaks from the 6 PRNS at data time frame 200-300 ms are recorded in Table 5.6. Apart from PRN25 that experienced the forward scatter condition, the target SNR levels from all other PRNs are observed to be fairly constant with at an average 15.3 dB. From the power budget analysis performed for this experimental GPS bistatic radar, a 100 m^2 RCS target at 273 m relative to the receiver will achieve an SNR level of 11.7 dB. Assuming that the aircraft in the experiment also achieves an RCS of 100 m^2, the estimated target range for the receiver to achieve 15.7 dB SNR is 180 m. This value will be compared with the range estimated from the position results obtained later.

PRN	02	04	12	24	25	29
SNR (dB)	14.2	15.8	16.8	16.0	28	12.2

Table 5.6: SNR of target return peaks from 6 GPS satellites at data period 200-300 ms.

The sample delays of the correlation peaks from all the BCAF results are required to be incorporated into the MSE solution to locate the target position using model (3.51). A comparison was made between the accuracy of the target positioning results using the TDOA from 4, 5 and 6 satellites with the list of PRNs shown in Table 5.7.

No. of PRNs	**4**	**5**	**6**
List of PRNs	02, 04, 12, 24	02, 04, 12, 24, 25	02, 04, 12, 24, 25, 29

Table 5.7: List of PRNs applied for each MSE configuration.

The process assumed the target's altitude of 45 m above surface level since the inverse MSE values at different z-position did not vary significantly. The inverse 2-D position MSE results from these PRNs and the predicted flight path are shown in Figure 5.37. The position estimated by all of these MSE results indicated a target range of 135 m from the receiver, which is fairly close to the anticipated range of 180 m.

Among these results, the inverse position MSE produced by the TDOAs from 6 satellites gave the smallest difference between the target location and the predicted flight path. This outcome demonstrates the advantage of using multiple GPS satellites in performing target positioning. On the other hand, the azimuth angle of the target reflections relative to the receiver determined by the MSE position from different numbers of satellites were found to have 7° to 10° differences from the azimuth angle applied to the BCAF search process. However, the elevation angle determined by the MSE position from 6 satellites presented the smallest error among others compared to the elevation angle applied to the BCAF search process.

Apart from using the TDOAs, the target position and its corresponding velocity were also determined by model (3.53). This process estimates the MSE at each position based on the velocity vector obtained from the LSE that uses the Doppler offsets of the peak returns obtained from the BCAF results. The inverse 2-D position MSE results from 4, 5 and 6 satellites and the predicted flight path are shown in Figure 5.38. The target position determined by these results is not as consistent as the processing performed using the TDOA information. The processing that applied the Doppler offsets from 4 satellites pinpoints the target at a location nearby the receiver whereas others had ambiguous results across a wide area of position bins. This observation implies that the MSE solution based on Doppler offsets from the detection is not suitable for determining the target location. On the other hand, the target velocity was also estimated by the MSE solution. Since the MSE solution using Doppler offsets did not provide accurate position estimation, the velocity will be estimated directly from model (3.54) at the target location estimated by the TDOAs. From Table 5.8, it was observed that the velocity vector extracted from the estimation of 6 satellites has the smallest error in the horizontal component, including ground speed and bearing, compared to the predicted flight path. However, the aircraft vertical speed estimates, $v_{\delta z}$, from all the results showed positive values, which implies that the target was ascending. This might be due to the error in the Doppler

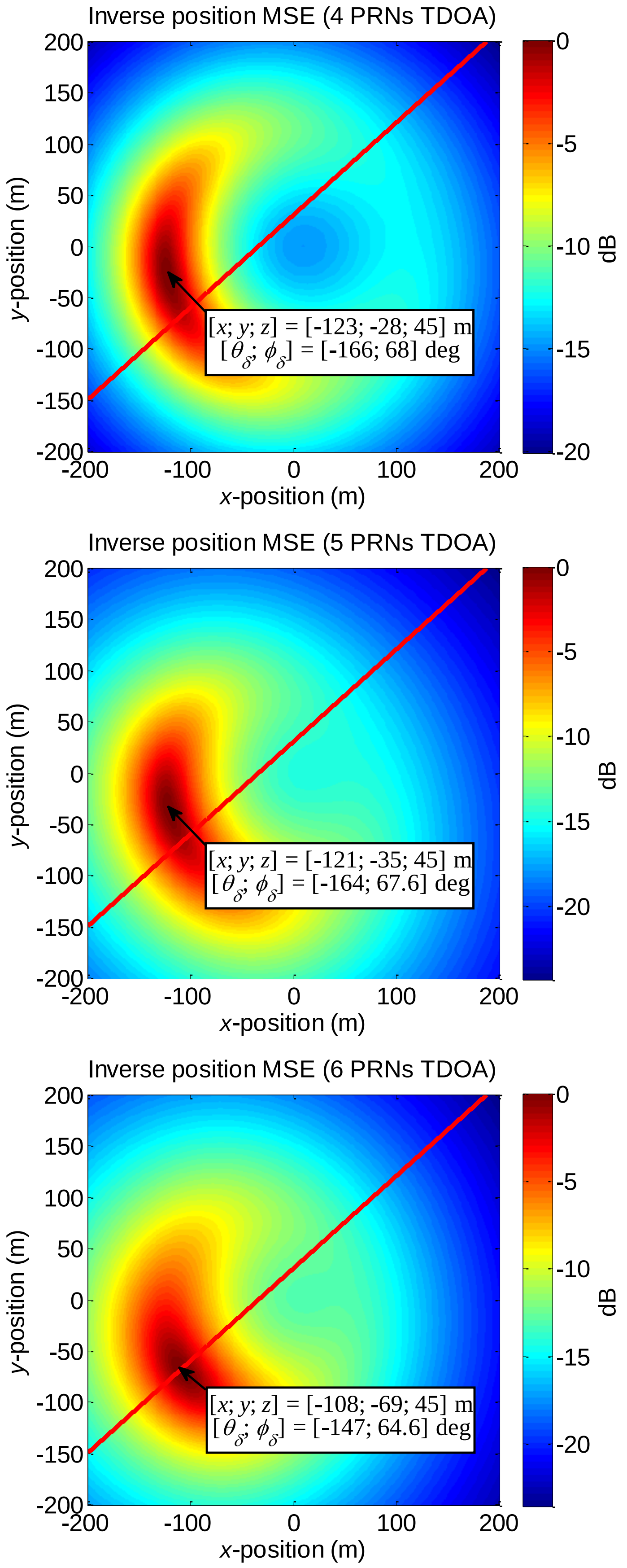

Figure 5.37: Normalised inverse 2-D position MSE results estimated by the TDOAs from 4, 5 and 6 satellites. The red lines resemble the flight path determined from Google Earth.

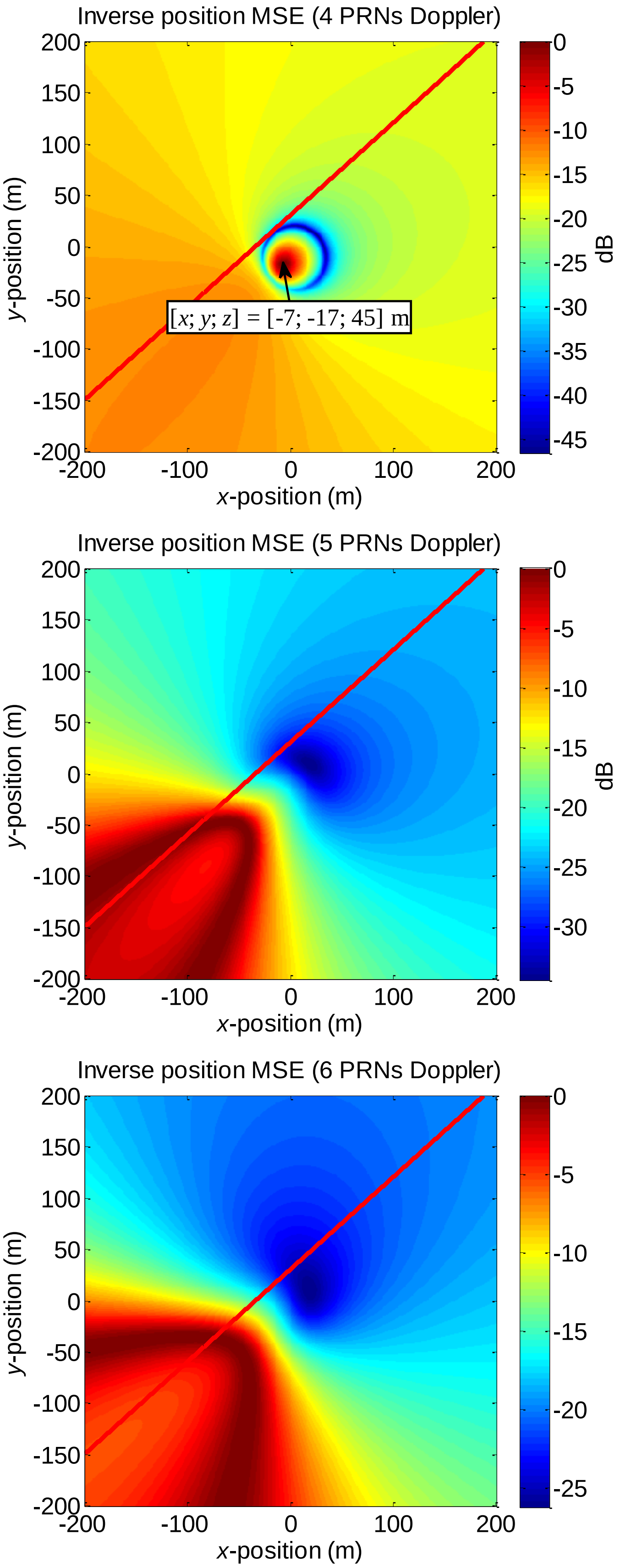

Figure 5.38: Normalised inverse 2-D position MSE results estimated by the Doppler offsets from 4, 5 and 6 satellites. The red lines represent the flight path determined from Google Earth.

frequency offsets obtained from the detection process which will have a greater impact on the vertical components.

Parameters	Flight path	4 PRNs	5 PRNs	6 PRNs
Position, $\boldsymbol{p}_\delta$ (m)	N/A	[-123; -28; 45]	[-121; -35; 45]	[-108; -69; 45]
Velocity, $\boldsymbol{v}_\delta$ (m/s)	[-52; -46.8; -3.5] to [-55.7; -50.2; -3.75]	[-56; -56.8; 3]	[-56; -54.2; 5.9]	[-52.8; -46.1; 5.7]
Ground speed (m/s)	70 to 75	79.8	77.9	70.1
Bearing	228°	224.6°	225.9°	228.9°

Table 5.8: Comparison of target velocity between the estimations from the predicted from the flight path and the results from the MSE solution.

Lastly, the target positions estimated by the TDOA information from 6 satellites at [−108; −69; 45] m and the predicted velocity of the flight path were applied to the simulator used to verify the detection algorithms in Chapter 3. The simulator was used to calculate the theoretical Doppler offsets and sampled code phase delay for the aircraft at the designated position. Then a comparison was made between these target parameters determined by simulation and the experimental results from the BCAFs in Figure 5.36. From Table 5.9, it is observed that apart from PRN12, there are smaller differences (< 20 Hz) between the Doppler frequency offsets from the experimental results and theoretical values that assumed the aircraft flew at a ground speed of 70 m/s. Moreover, the discrete sampled code delays from most PRNs, $\boldsymbol{k}_\delta$, between the simulation and experiment are also found to be identical. On the other hand, the position estimated by the MSE solution can only use the TDOA values that are rounded to the nearest sampled code delay. Therefore, the TDOA errors between the simulation and the experiment can be noticed from the following table. The TDOA rounding errors can be reduced by interpolating the captured data at a higher sampling rate. This would require more computation power to perform the target detection process.

In summary, the GPS bistatic radar using the phased-array receiver presented reasonable air target detection results from the experiment as it estimated the target at a location that is consistent with the flight path. There are only minor errors that slightly affect the accuracy of the experimental results compared to the theoretical estimation. It is also recommended to utilise as many transmitters as practicable from the GPS constellation to perform the target detection and parameter estimation as it gives more tolerance to measurement errors.

Target position, $\boldsymbol{p}_\delta$ (m)	[−108; −69; 45]					
Satellite PRN	02	04	12	24	25	29
Doppler frequency offsets						
Simulation (70 m/s) $\boldsymbol{f}_\delta$ (Hz)	−514	−452	−129	−337	0	−178
Simulation (75 m/s) $\boldsymbol{f}_\delta$ (Hz)	−551	−484	−138	−362	0	−190
Experiment $\boldsymbol{f}_\delta$ (Hz)	−500	−433	−65	−326	12	−157
TDOA (*f*s = 4.167 MHz)						
Simulation TDOA (ns)	510	506	93	276	1.19	191
Simulation $\boldsymbol{k}_\delta$ (*f*s sample)	2	2	0	1	0	1
Experiment $\boldsymbol{k}_\delta$ (*f*s sample)	2	2	1	1	0	1
Experiment TDOA (ns rounded to $\boldsymbol{k}_\delta$)	480	480	240	240	0	240

Table 5.9: Comparison between the target parameters determined by simulation and experiment.

5.6.3 MISO Radar Detection Technique

The MISO/MIMO radar detection technique works by aligning the Doppler frequency and sampled code offsets relative to the direct-path signals from multiple GPS satellites/receivers to form a combined matched filter at every searched 3-D position and velocity as described in model (4.5). The matched filter output from a certain velocity vector that corresponds to the highest sum of the squared correlation values from multiple satellites (i.e. non-coherent integration) will be stored in each position bin. The highest combined correlation values among all the searched position bins will be identified as the target.

Since only a single phased receiver was built for the experiment, the radar system can only implement the MISO technique that incorporates all the available transmitters in performing target detection. The MISO radar detection requires a higher computational complexity to search for targets compared to the previously described phased-array TDOA based technique since it performs the target tracking process by generating a bank of matched filters on each position bin prior to the detection stage. Therefore, the target searching process for this MISO detection experiment was only performed using a position resolution of 10 m. However, it does not require additional stages to classify targets from multiple peak returns of each PRN and extract their TDOAs to determine the target position.

From the study in Section 4.3.1, the MISO technique can improve the radar detection performance by at least the square root factor of the number of satellites used in the position solution, assuming an equal power level between the target reflections from all the transmitters. Therefore, the captured data with an approximate total length of 1000 ms was able to be fragmentised into twice (i.e. 20) the total number of sub-blocks compared to the phased-array counterpart, which enables finer target position tracking results while retaining the receiver's detection performance through individual integration processes on each sub-block.

The MISO target searching process for this experiment was performed using 4×1, 5×1, 6×1 and 7×1 MISO configurations from the available GPS satellites as illustrated before in Figure 5.29. The list of satellite PRNs applied for each MISO configuration is recorded in Table 5.10. Example 2-D MISO target position tracking results from 6 selected data frames at 50 m altitude using the 7×1 MISO configuration along with the predicted flight path (red lines) were shown in Figure 5.39. It was observed that the positions of the peak target returns approached the predicted flight path and shifted towards the Southwest direction relative to the receiver in increasing order, which appears to be a good resemblance of the flyby aircraft.

MISO config	List of PRN	Average SNR (dB)
4×1	02, 04, 12, 14	16.69
5×1	02, 04, 12, 14, 24	17.25
6×1	02, 04, 12, 14, 24, 25	23.06
7×1	02, 04, 12, 14, 24, 25, 29	23.07

Table 5.10: List of PRNs applied for each MISO configuration and their average SNRs.

The target reflection SNRs from the position results at different data time frames using various MISO configurations and 50 ms integration are also shown in Figure 5.40. The average SNR results are also compared with the SNRs from the phased-array detection results recorded in Table 5.6 that use 100 ms integration. It is observed that the average target SNR from 4×1 detection is higher than the SNRs from most single PRN detection. It is slightly lower than the target SNR from PRN12 (i.e. 16.8 dB). From the theoretical calculation, the 50 ms integration time would lose 3 dB integration gain compared to the 100 ms counterpart while the non-coherent integration of 3 transmitters (i.e. leaving out PRN14 as it fails to show any sign of target reflections) would increase the SNR by 2.4 dB. Hence, it would result in the overall gain of −0.6 dB, which explained the reason for getting slightly lower SNR values. Also, the average target SNR from the 4×1 detection is lower than the SNR from PRN25 (i.e. 28 dB) which experienced the forward scatter path condition.

The average SNR from the 5×1 case is 0.56 dB higher than the 4×1. Under the condition where the SNRs of PRN02, 04, 12 and 24 were found to be relatively constant, the theoretical non-coherent integration gain difference between applying 3 and 4 transmitters (i.e. leaving out PRN14) would be at least 0.62 dB, which is close to the value of 0.56 dB from the experiment. On the other hand, the 6×1 results indicated significant SNR improvement (i.e. 5.81 dB) over the 5×1 due to the high target SNR from PRN25. Since the overall SNR is dominated by the result from PRN25 and the target SNR from PRN29 is the weakest among all PRNs, the 7×1

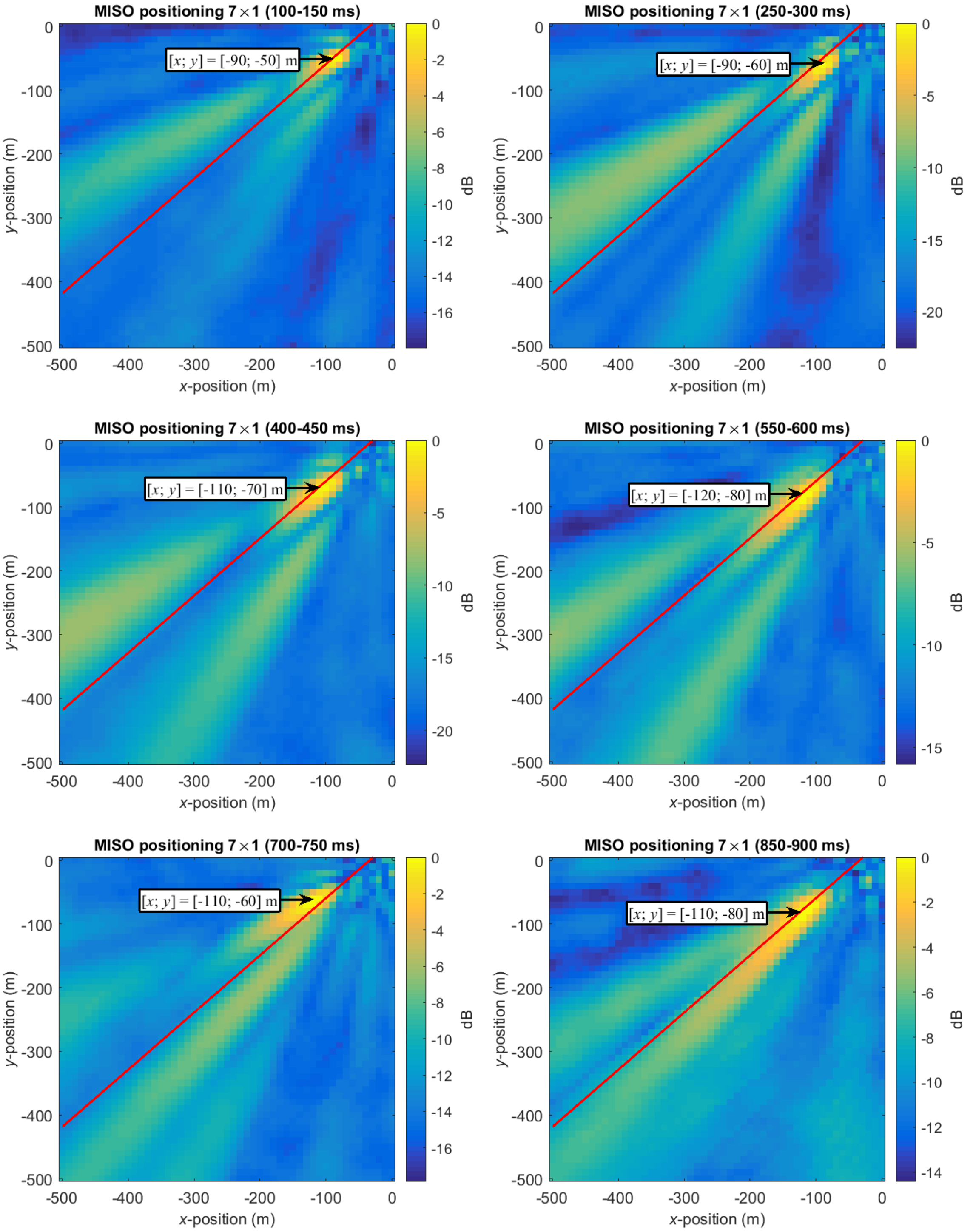
MISO positioning 7 × 1 (100-150 ms)

MISO positioning 7 × 1 (250-300 ms)

MISO positioning 7 × 1 (400-450 ms)

MISO positioning 7 × 1 (550-600 ms)

MISO positioning 7 × 1 (700-750 ms)

MISO positioning 7 × 1 (850-900 ms)

Figure 5.39: Normalised 2-D target positioning results from frame 3, 6, 9, 12, 15 and 18 at 50 m altitude using 7×1 MISO configuration (i.e. PRN02, 04, 12, 14, 24, 25 and 29). Each frame represents the result processed from the data integration process of 50 ms and 10 m search position resolution. The red lines represent the predicted flight path.

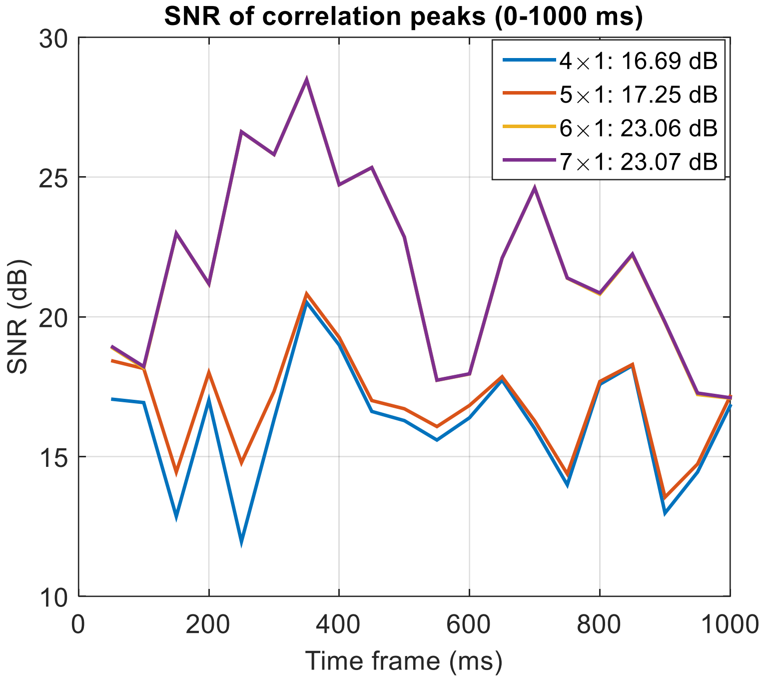

Figure 5.40: SNR of target return peaks at different time for MISO configurations: 4×1, 5×1, 6×1 and 7×1. Note that the 6×1 results are overlapped by the 7×1 results due to their extremely small SNR differences across the whole data block. The average SNR for each configuration is recorded in the legend box.

result no longer gives any significant SNR improvement over its 6×1 predecessor. The overall SNRs from all configurations were also found to reach the highest point at 350 ms after which they dropped off again.

While a 3-D search was performed to locate the target, it was observed that the size of the peak returns at different *z*-position did not show any significant differences due to the poor DOP in the vertical direction. Hence, the target position tracking were calculated from the 2-D positions that correspond to the peak target returns from different time frames at a 50 m altitude using various MISO configurations. From Figure 5.41, it was observed that the peak returns shifted towards the Southwest direction at close proximity to the predicted flight path (red lines), which is a good indication of the flight path. In addition, the positions determined by both 4×1 and 5×1 processes are nearly identical and more widely spread along the flight path. The positions determined by both 6×1 and 7×1 processes are identical and more concentrated. There is no way to compare which of these results are more accurate since the exact positions of the aircraft are unknown.

A simple comparison was also made between the positions determined by the MISO and the phased-array TDOA technique. From the data process at time frame 200 to 250 ms, both the 4×1 and 5×1 processes located the target at [−90; −50] m while both the 6×1 and 7×1

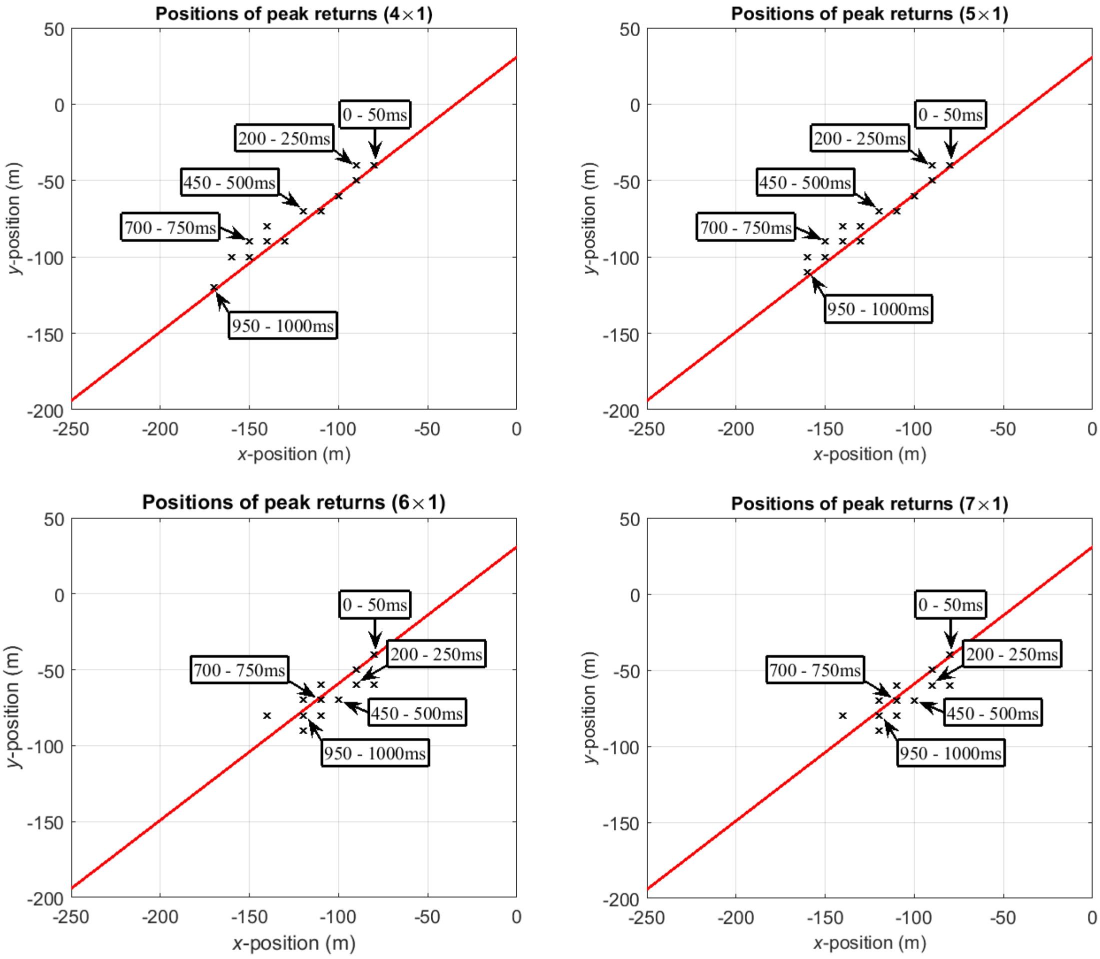

Figure 5.41: Results of various MISO configurations showing the 2-D positions of peak target returns from different time frames at 50m altitude. The red lines represent the predicted flight path.

located the target at [−90; −60] m. At time frame 250 to 300 ms, both the 4×1 and 5×1 processes located the target at [−100; −60] m while both the 6×1 and 7×1 located the target at [−110; −60] m. These results are also close to the location at [−108; −69] m obtained from the TDOA positioning solution using 6 satellites at 200 to 300 ms. Therefore, the position results obtained from both techniques are consistent with each other.

MISO config	**Position @ 0 to 50 ms (m)**	**Position @ 950 to 1000 ms (m)**	**Ground speed (m/s)**	**Bearing (deg)**
4×1	[−80; −40]	[−170; −120]	120	228.4
5×1		[−160; −110]	106	228.8
6×1		[−120; −80]	56.6	225
7×1		[−120; −80]	56.6	225

Table 5.11: Target velocity determined by the MISO positioning results.

The target velocity can be determined from the MISO positioning results using the position determined at the first and last time frame and are recorded in Table 5.11. It was observed that both the 4×1 and 5×1 gave a higher ground speed while both the 6×1 and 7×1 gave a lower ground speed relative to the expected ground speed between 70 to 75 m/s. However, the bearing of the target motion from the estimation matched well with the bearing of the predicted flight path of 228°.

In summary, the MISO detection results demonstrated its capability to track the position of target by processing the data at different time frames individually. Using more satellites was found to improve the SNR of the combined target return, which demonstrates that the MISO technique can improve the detection performance of the receiver by combining the reflected power from each satellite. However, the target velocities were less accurately determined from the MISO detection process than the phased-array TDOA technique. But this velocity was determined by subtracting positions rather than from the Doppler.

5.7 Conclusion

The feasibility of GPS bistatic radar for target detection using the phased-array MISO radar technique was investigated using the experimental data. An experimental 32-element phased-array receiver was designed and built to perform this experiment. A power budget study that investigates the available GPS signal power on Earth that benchmarks the required performance for reliable target detection was also made based on the parameters of this experimental system.

Experimental results from the pre-detection stages were also presented. These stages include the direct-path signal acquisition, inter-elements phase error estimation and DSI cancellation. Initially, the direct-path signals acquisition technique was performed by the reference element in the receiver and the signal was used to identify the Doppler component and C/A code delay across the whole captured data block. Then the signal phase extracted from the long period correlation process at each element and the DOA information obtained from the satellite tracking tool were incorporated to remove the inter-element phase errors within the antenna array. The results from this calibration process were checked by comparing the SNR of the phased-array receiver output with a single element. The properly calibrated phased-array receiver also enables the system to acquire direct-path signals from additional satellites that are too weak to be captured by a single element, especially those that are located beyond the main beam of the individual antenna element. Finally, the replica generated based on the direct-path signal information acquired by the phased-array receiver was passed through a Wiener filter to estimate and remove the DSIs that can potentially affect the target detection process. The experimental result from the Wiener filter stage demonstrated its capability to suppress the DSI and its corresponding multipath signals to a minimal level when a large number of filter taps were applied.

The GPS bistatic radar using the phased-array detection technique was applied on the data captured by the receiver to detect the aircraft and estimate its position and velocity. This technique involves performing a code-Doppler search technique to form the CCAF results from multiple satellites that identify the Doppler offset and discrete TDOA of the target reflection relative to the direct-path signals. The DOA results were also acquired from the CCAF results to form the BCAF results using the conventional beamformer, which produces more robust target returns. The position and velocity of the designated target was eventually identified from the MSE solution. The results from the phased-array technique were also verified by comparing their outcomes with the predicted flight path. The results from the x-y components were found to be consistent with the aircraft behavior.

The target detection process was also performed on the captured data using the MISO technique. This technique effectively combined the power returns of the aircraft reflection from multiple satellite transmitters and demonstrated superior SNRs compared to the phased-array detection technique. The presence of target was also tracked using the 2-D positions determined from the data at different time frames and is also found to be consistent with the predicted flight path. The target velocity estimated from the MISO detection results was found to be less accurate than the phased-array technique that used the target Doppler information.

In summary, the GPS bistatic radar presented satisfactory target detection and parameter estimation results overall. Several techniques such as the MIMO radar and the adaptive TBD process were not performed in this experiment and would be good topics for future research.

CHAPTER 6

Conclusion

6.1 Summary and Contributions

This thesis investigated the feasibility of using GPS satellites as the illuminators of opportunity for PBR using both simulations and an experiment. The investigations analyse the performance of GPS bistatic radar in performing air targets detection and estimation for parameters such as the position and velocity. This research was motivated by advantage offered by the GPS system which utilises a relatively large number of widely separated transmitters and being globally available to accurately locate the position of a user. The GPS bistatic radar can easily synchronise the signals from transmitters and/or receivers at multiple locations in the detection process since GPS system itself is a good source for time synchronisation.

The greatest challenge is that GPS signals are extremely weak, and such low power levels are insufficient for performing target detection. This issue can be compensated by applying techniques that greatly enhance the sensitivity of the receiver. Hence, a key part of this research investigated methods such as long coherent integration, beamforming using large scale antenna array and non-coherent integration of the power returns from the reflections of multiple satellites for improving the signals strength. A land-based experimental 32-element phased-array receiver was developed to investigate the performance of GPS bistatic radar including these enhancements. A power budget estimation study was also conducted to analyse the performance and capability of this radar system. Based on this study, the experiment module was deployed nearby the Adelaide Airport to capture the reflections from an aircraft during its final approach where its flight path can be precisely predicted and compared with the experimental results.

A number of techniques at the pre-detection stage were modelled and demonstrated experimentally to enhance target detection. Firstly, the direct-path signals were acquired from a reference element in the array to obtain the Doppler components and phase information of GPS signals from multiple satellites relative to the receiver. A polynomial regression model was used to estimate the varying Doppler component across the captured data due to the motions of the orbiting satellites, hence enabling precise C/A code replicas to be generated locally for the detection process. The carrier phase of each of the GPS signals on each antenna element could then be extracted by cross-correlating each corresponding replica with the input signal.

Secondly, the LSE technique was applied in an iterative search loop to calibrate the inter-element phase errors and attitude of the antenna array. The successful estimation and removal of these errors from the antenna array enabled beamforming technique to be applied, which not only allowed the receiver to search for the DOAs of target at the detection stage, but also assisted the direct-path signals acquisition process in capturing and estimating the C/A code replicas from more GPS satellites, where the power levels of their direct-path signals were insufficiently strong to be captured by a single element.

Lastly, a Wiener filter model was applied to remove the DSIs from affecting the detection stage. Simulation and experiment results are presented and demonstrated that the power levels of DSIs were suppressed to minimal levels which no longer affect the detection.

Initially, target detection was carried out using a conventional phased-array technique that processes the reflections from each satellite independently. This is a two stage process consisting of a code-Doppler search for each GPS signal reflection followed by a multilateration process based on the resulting delays and Doppler shifts of each reflection. This technique was evaluated in simulation and the experimental data captured from the landing aircraft. Simulation results demonstrated the use of these techniques for estimating the position and velocities of multiple targets, while the real data focused on a single target. In the experimental data, the reflections from six satellites were sufficiently strong to be detected by the code-Doppler search after the phased-array processing. More interestingly, the DOAs of some of these signals were common while others deviated slightly, which was suspected to be due to reflections from different parts of the aircraft. These issues were believed to be less likely to happen if the detection experiment was performed on an aircraft that was much further away from the receiver.

The sampled code delay and Doppler frequency offsets from the reflections of multiple satellites with a common DOA were then used to determine the position and velocity of the aircraft respectively using the multilateration technique. In comparison with the predicted flight path, the 2-D results from the process that incorporated the most transmitters were found to be highly consistent with the aircraft behaviour. The Doppler frequency offsets and sampled code delay of the target obtained from these results were also very similar to the parameters determined by the simulations. The greatest achievement for the phased-array detection technique is that its experimental results not only demonstrated the feasibility of GPS bistatic radar to detect extremely weak GPS signals from air target reflections, but also exhibited reasonably good performance in acquiring the target location and velocity using the parameters obtained from the detection.

The sensitivity of the target detection process can be improved further by combining the power of several GPS signals in the code-Doppler search. This is achieved by using MISO and MIMO techniques that non-coherently added the expected returns from multiple satellites based on an assumed target position. This target detection process is implemented by a matched filter stage for multiple satellites and/or receivers at each searched position bin as a function of the corresponding sampled code delay, Doppler frequency offsets related to all possible velocities and the receiving element's spatial phase factor. Then the correlation values from these transmitters and/or receivers were summed non-coherently as a function of the position bins. The target detection performance for both the MISO and MIMO techniques were evaluated using simulations for various scenarios. The SNR and position accuracy of multiple targets were evaluated with different MISO/MIMO configurations and techniques for tracking high velocity targets were evaluated using techniques such as generating matched filters which are adaptive to target motion and doing correlation processing on fragmentised data.

Only the MISO technique could be evaluated on the experimental data, as only a single phased-array receiver was built for this research project. The greatest achievement for the implementation of MISO detection technique for GPS bistatic radar is that its experimental results demonstrated the average output target reflections SNRs were improved by increasing the number of transmitters incorporated into the radar system. The SNR gain exhibited by this technique was also comparable to the chi-squared PDF model that was predicted earlier. Besides, the results also presented the 2-D target positions at different time frames. These position estimates were observed to follow the trend of the predicted flight path, which was another significant achievement demonstrated by the GPS bistatic radar.

6.2 Further Recommendations

With the experimental results demonstrated the feasibility of GPS bistatic radar in performing air target detection and parameters estimation with reasonably reliable outcomes, this application can potentially be used to complement existing PBRs in military technology. Besides, the achievement presented by the experimental results from the pre-detection stage of GPS bistatic radar in this research exhibits its usefulness in other GPS applications that are required to detect GPS signals which power levels might be degraded significantly due to the environmental factors. The reliability of the detection results from the existing study can be improved significantly if a larger amount of resources can be applied to this research.

The existing experimental module is only capable of capturing about 1000 ms of data due to the storage limit for the RAMs in the FPGAs. The rapid advancement in the FPGA performance and its interfacing speed with the PCs in recent years can potentially allow the system to acquire much larger data blocks in real-time. This would also allow further studies of the target tracking process with other techniques such as the Kalman filter or enable further improvement for the SNR of the target reflections by using longer integration periods.

The 32-element phased-array receiver for the experiment only provides reliable detection performance on aircrafts which were located at a range of less than 300 m. Hence, the experiment was only performed on an aircraft which was within visual range. It is recommended that the size of the phased-array receiver and/or MIMO configurations to be further expanded at the expenses of higher building cost. This solution would allow the detection of air targets at further and most importantly, practical ranges. It would also be interesting to build and deploy multiple phased-array receivers in a widely separated configuration, so that the study for aircraft detection using the MIMO radar technique can be further investigated.

While high performance home/office PCs were applied to process the data with both the phased-array and MISO detection models using MATLAB, the time taken for obtaining the results were extremely long. Moreover, the technique such as tracking the targets with matched filters which are adaptive to target motion cannot be performed by this research due to the limitation on the PC available to the research project. Therefore, an extremely powerful computation platform is mandatory for this application, so that the results of target reflections at much further and practical ranges using one or multiple much larger scale antenna array can be acquired within a practical time frame.

References

[1] N. J. Willis, Bistatic radar, 2nd ed., NC: SciTech, 2005.

[2] M. I. Skolnik, "An analysis of bistatic radar," *IEEE Transaction on Aerospace and Navigational Electronics,* vol. 8, pp. 19-27, 1961.

[3] P. Howland, "Editorial: Passive radar systems," *IEE Proceedings in Radar, Sonar and Navigation,* vol. 152, no. 3, pp. 105-106, 2005.

[4] N. J. Willis, "Bistatic radar," in *Radar Handbook*, New York, McGraw-Hill, 1990, pp. 1-35.

[5] J. I. Glaser, "Fifty year of bistatic and multistatic radar," *IEE Proceedings - Communications,* vol. 133, pp. 596-603, 1986.

[6] P. E. Howland, H. D. Griffiths and C. J. Baker, "Passive bistatic radar systems," in *Bistatic Radar: Emerging Technology*, West Sussex, England, John Wiley & Sons Ltd, 2008, pp. 247-313.

[7] H. D. Griffiths and C. J. Baker, "Passive coherent location radar systems. Part 1: Performance prediction," *IEE Proceedings of Radar, Sonar and Navigation,* vol. 152, no. 3, pp. 153 - 159, 2005.

[8] A. G. Westra, "Radar versus stealth: Passive radar and the future of U.S. military power," *National Defence University Journal,* vol. 4th quarter, no. 55, pp. 136-143, 2009.

[9] H. D. Griffiths, "From a different perspective: Principles, practice and potential of bistatic radar," in *IEEE Proceedings of the International Radar Conference,* Adelaide, Australia, 2003.

[10] J. Palmer, S. Palumbo, T. V. Cao and S. Howard, "A new illuminator of opportunity bistatic radar research project at DSTO," DSTO, South Australia, 2009.

[11] D. Poullin, "Passive detection using digital broadcasters (DAB, DVB) with COFDM modulation," *IEE Proceedings of Radar, Sonar and Navigation,* vol. 152, no. 3, pp. 143 - 152 , 2005.

[12] R. Saini and M. Cherniakov, "DTV signal ambiguity function analysis for radar application," *IEE Proceedings of Radar, Sonar and Navigation,* vol. 152, no. 3, pp. 133-142, 2005.

[13] C. J. Coleman, R. A. Watson and H. J. Yardley, "A practical bistatic passive radar sysem for use with DAB and DRM illuminators," in *IEEE Radar Conference,* Rome, Italy, 2008.

[14] H. Sun, D. K. P. Tan and Y. Lu, "Aircraft target measurements using A GSM-based passive radar," in *IEEE Radar Conference,* Rome, Italy, 2008.

[15] P. Falcone, F. Colone, C. Bongioanni and P. Lombardo, "Experimental results for OFDM WiFi-based passive bistatic radar," in *IEEE Radar Conference*, Washington, D.C., 2010.

[16] K. Chetty, G. Smith, H. Guo and K. Woodbridge, "Target detection in high clutter using passive bistatic WiFi radar," in *IEEE Radar Conference,* Pasadena, CA, 2009.

[17] D. Cristallini, M. Caruso, P. Falcone, D. Langellotti, C. Bongioanni, F. Colone, S. Scafe and P. Lombardo, "Space-based passive radar enabled by the new generation of geostationary broadcast satellites," in *IEEE Aerospace Conference,* Big Sky, MT, 2010.

[18] H. D. Griffiths, "Passive bistatic radar and waveform diversity," Information for the Defense Community, Shrivenham, United Kingdom, 2009.

[19] H. Griffiths, "Passive bistatic radar," in *Communications and Radar Signal Processing*, Waltham, MA, Elsevier, 2014, pp. 813-855.

[20] J. Homer, K. Kubik, B. Mojarrabi, I. D. Longstaff, E. Donskoi and M. Cherniakov, "Passive bistatic radar sensing with LEOS based transmitters," in *IEEE International Symposium of Geoscience and Remote Sensing*, Toronto, Canada, 2002.

[21] J. B. Y. Tsui and R. L. Shaw, "Passive ranging through Global Positioning System". U.S. Patent 5,187,485, February 16 1993.

[22] H. D. Griffiths, C. J. Baker, J. Baubert, N. Kitchen and M. Treagust, "Bistatic radar using satellite-borne illuminators," in *RADAR 2002,* Edinburgh, U.K., 2002.

[23] Coverttrack Group Incoporation, "Civilian GPS Applications," Coverttrack Group Incoporation, 2012. [Online]. Available: http://www.gpsintel.com/civilian-applications.php. [Accessed 12 June 2014].

[24] US Government, "GPS Accuracy," National Coordination Office for Space-Based Positioning, Navigation, and Timing, 17 March 2014. [Online]. Available: http://www.gps.gov/systems/gps/performance/accuracy/. [Accessed 12 June 2014].

[25] American Institute of Aeronautics and Astronautics, Inc., Global Positioning System: Theory and Applications, vol. I, B. W. Parkinson and J. J. Spilker, Eds., Washington, DC: American Institute of Aeronautics and Astronautics, 1996.

[26] E. D. Kaplan and C. J. Hegarty, Understanding GPS principles and applications, 2nd ed., Norwood, MA: Artech House, 2006.

[27] J. M. Kim, H. J. Song and Y. B. Kim, "Design and implementation of L1-band C/A-code GPS RF front-end chip," in *ICVC'99 6th International Conference on VLSI and CAD*, Seoul, 1999.

[28] R. E. Rouquette, "Axonn LLC," 23 July 2008. [Online]. Available: http://common.globalstar.com/doc/axonn/GPS-L1-Link-Budget.pdf. [Accessed 19 June 2014].

[29] J. Mehaffey, J. Yeazel, S. Penrod and A. Deiss, "How much POWER do the GPS Satellites output on the 1575mhz L1 frequency?," gpsinformation.net, 19 June 2014. [Online]. Available: http://www.gpsinformation.net/main/gpspower.htm. [Accessed 19 June 2014].

[30] D. Akopian, "Fast FFT based GPS satellite acquisition methods," *IEEE Proceedings - Radar, Sonar and Navigation*, vol. 152, pp. 277-286, 2005.

[31] W. de Wilde, "New fast signal acquisition unit for GPS/Galileo receivers," in *ENC-GNSS*, Manchester, UK, 2006.

[32] V. J. R. Van Nee and A. J. R. M. Coenen, "New fast GPS acquisition technique using FFT," *Electronic Letter*, vol. 27, no. 2, pp. 158-160, 1991.

[33] E. P. Glennon and A. Dempster, "A review of GPS cross correlation mitigation techniques," in *International Global Navigation Satellite Systems (IGNSS)*, Sydney, Australia, 2004.

[34] V. Koch and R. Westphal, "New approach to a multistatic passive radar sensor for air/space defense," *IEEE: Aerospace and Electronic Magazine,* vol. 10, no. 11, pp. 24-32, 1995.

[35] E. P. Glennon, A. G. Dempster and C. Rizos, "Feasibility of air target detection using GPS as a bistatic radar," *Journal of Global Positioning Systems,* vol. 5, no. 1-2, pp. 119-126, 2006.

[36] J. C. McIntosh, "Passive three dimensional track of non-coooperative targets through opportunistic use of Global Positioning System (GPS) and GLONASS signals". United States Patent 6,232,922, 2001.

[37] C. Clemente and J. J. Soraghan, "Passive bistatic radar for helicopters classification: A feasibility study," in *IEEE Radar Conference,* Atlanta, 2012.

[38] T. Thayaparan, S. Abrol, E. Riseborough, L. Stankovic, D. Lamothe and G. Duff, "Analysis of radar micro-Doppler signatures from experimental helicopter and human data," *IET Radar, Sonar & Navigation,* vol. 1, no. 4, pp. 289-299, 2007.

[39] M. M. Neira, "Altimetry method". United States of America Patent 5,546,087, 13 August 1996.

[40] D. Masters, P. Axelrad, V. Zavorotny, S. J. Katzberg and F. Lalezari, "A passive GPS bistatic radar altimeter for aircraft navigation," in *14th International Technical Meeting of the Satellite Division of the Institute of Navigation,* Salt Lake City, UT, 2001.

[41] M. de Vries, "GPS based bistatic radar - Beyond specular reflection," in *The 24th International Digital Avionics Systems Conference,* Crystal City, WA, 2005.

[42] J. L. Garrison, A. Komjathy, V. U. Zavorotny and S. J. Katzberg, "Wind speed measurement using forward scattered GPS signals," *IEEE Transactions on Geoscience and Remote Sensing,* vol. 40, no. 1, pp. 50-65, 2002.

[43] V. Zavorotny and A. G. Voronovich, "Scattering of GPS signals from the ocean with wind remote sensing application," *IEEE Transactions on Geoscience and Remote Sensing,* vol. 38, pp. 951-964, 2000.

[44] M. B. Rivas, J. A. Maslanik and P. Axelrad, "Bistatic scattering of GPS signals off arctic sea ice," *IEEE Transactions on Geoscience and Remote Sensing,* vol. 48, no. 3, pp. 1548-1553, 2010.

[45] V. Zavorotny, D. Masters, A. Gasiewski, B. Bartram, S. Katzberg, P. Axelrad and R. Zamora, "Seasonal polarimetric measurements of soil moisture using tower-based GPS bistatic radar," in *IEEE Proceedings of International Geoscience and Remote Sensing Symposium,* Toulouse, France, 2003.

[46] D. Masters, P. Axelrad and S. Katzberg, "Initial results of land-reflected GPS bistatic radar measurements in SMEX02," *Sciencedirect,* vol. 92, pp. 507-520, 2004.

[47] A. Brown and B. Mathews, "Test results from a novel passive bistatic GPS radar using a phased sensor array," in *Proceedings of the National Technical Meeting of The Institute of Navigation,* San Diego, 2007.

[48] J. W. Mo and S. Ouyang, "Study on imaging algorithm of bistatic inverse synthetic aperture radar based on reflected GPS signals," in *Proceedings of the Second International Conference on Modelling and Simulation*, Manchester, U.K., 2009.

[49] A. Lazarov, V. C. Chen and J. Passos Morgado, "Bistatic SAR system with GPS transmitter," in *IEEE Radar Conference,* Ottawa, Canada, 2013.

[50] C. Rizos, "Multi-constellation GNSS/RNSS from the perspective of high accuracy users in Australia," *Journal of Spatial Science,* vol. 53, no. 2, pp. 29-63, 2010.

[51] C. Rizos, M. B. Higgins and S. Hewitson, "New global navigation satellite system developments and their impact on survey service providers and surveyors," in *Spatial Sciences Conference,* Melbourne, Australia., 2005.

[52] M. Mojarrabi, "Power budget study for passive target detection and imaging using secondary applications of GPS signals in bistatic radar systems," in *2002 IEEE International Geoscience and Remote Sensing Symposium,* Toronto, Canada, 2002.

[53] L. Liu, W. Yuan, S. Wu and X. Sun, "Bistatic radar system based on GPS illumination," *Chinese Journal of Radio Science,* no. 1, 2004.

[54] T. Pany, B. Riedl, J. Winkel, T. Wörz, R. Schweikert, H. Niedermeier, S. Lagrasta, G. López-Risueño and D. Jiménez-Baños, "Coherent integration time: The longer, the better," *InsideGNSS: The Golden Age of GNSS,* vol. 4, no. 6, pp. 52-61, 2009.

[55] D. K. Barton, "Simple procedures for radar detection calculations," *IEEE Transactions on Aerospace and Electronic Systems,* Vols. AES-5, no. 5, pp. 837-846, 1969.

[56] J. C. Toomay and P. J. Hannen, Radar principles for the non-specialist, 3rd ed., Norwich, NY: Scitech Publishing Inc., 2004, p. 59.

[57] M. I. Skolnik, Introduction to radar systems, New York: McGraw-Hill, 1980.

[58] G. W. Ewell and S. P. Zehner, "Bistatic radar cross section of ship targets," *IEEE Journal of Oceanic Engineering,* vol. 5, no. 4, pp. 211-215, 1980.

[59] W. I. Kock, "Related experiments with sound waves and electromagnetic waves," *Proceedings of the IRE,* vol. 47, no. 7, pp. 1192-1201, 1959.

[60] J. E. Palmer, H. A. Harms, S. J. Searle and L. M. Davis, "DVB-T passive radar signal processing," *IEEE Transactions on Signal Processing,* vol. 61, no. 8, pp. 2116-2126, 2013.

[61] P. Knott, H. Kuschel and D. O'Hagan, "Antenna array geometry optimization for a passive coherent localisation system," in *9th International Conference on Mathematical Problems in Engineering, Aerospace and Sciences*, Vienna, Austria, 2012.

[62] D. Poullin and M. Flecheux, "Passive 3D tracking of low altitude targets using DVB (SFN broadcasters)," *IEEE Aerospace and Electronic Systems Magazine,* vol. 27, no. 11, pp. 36-41, 2012.

[63] A. B. Gershman and N. D. Sidiropoulos, Space-time processing for MIMO communications, Chichester, England: John Wiley & Sons Ltd, 2005.

[64] G. San Antonio, D. R. Fuhrmann and F. C. Robey, "Generalized MIMO radar ambiguity functions," in *MIMO Radar Signal Processing*, Hoboken, NJ, John Wiley & Sons, 2009, pp. 123-152.

[65] A. Paulraj, R. Nabar and D. Gore, Introduction to space-time wireless communications, Cambridge, U.K.: Cambridge University Press, 2003.

[66] H. Godrich, A. Haimovich and R. Blum, "Concepts and applications of a MIMO radar system with widely seperated antennas," in *MIMO Radar Signal Processing*, Hoboken, NJ, John Wiley & Sons, 2009, pp. 365-410.

[67] K. W. Forsythe and D. W. Bliss, "MIMO radar: Concepts, performance enhancements, and applications," in *MIMO Radar Signal Processing*, Hoboken, NJ, John Wiley & Sons, 2009, pp. 65-121.

[68] J. Li and P. Stoica, "MIMO radar with collocated antennas: Review of some recent work," *IEEE Signal Processing Magazine,* vol. 24, no. 5, pp. 106-114, 2007.

[69] E. Fishler, A. Haimovich, R. Blum, D. Chizhik, L. Cimini and R. Valenzuela, "MIMO radar: An idea whose time has come," in *IEEE Proceedings of Radar Conference*, Philadelphia, PA, 2004.

[70] E. Fishler, A. Haimovich, R. Blum, D. Chizhik, L. Cimini and R. Valenzuela, "Performance of MIMO radar systems: Advantages of angular diversity," in *38th Asilomar Conference on Signals, Systems and Computers*, Pacific Grove, CA, 2004.

[71] E. Fishler, A. Haimovich, R. Blum, L. Cimini, D. Chizhik and R. Valenzuela, "Spatial diversity in radars - Models and detection performance," *IEEE Transactions on Signal Processing,* vol. 54, no. 3, pp. 823-838, 2006.

[72] H. D. Griffiths, C. J. Baker, S. P. F and M. Rangaswamy, "MIMO as a distributed radar system," in *MIMO Radar Signal Processing*, Hoboken, NJ, John Wiley & Sons, 2009, pp. 339-384.

[73] W. K. Forsythe, D. W. Bliss and G. S. Fawcett, "Multiple-input multiple output (MIMO) radar: Performance issues," in *Proceeding of the 38th Asilomar Conference in Signals, Systems and Computers*, Pacific Grove, CA, 2004.

[74] D. W. Bliss and K. W. Forsythe, "Multiple-input multiple-output (MIMO) radar and imaging: Degrees of freedom and resolution," in *Proceeding of the 37th Asilomar Conference in Signals, Systems and Computers*, Pacific Grove, CA, 2003.

[75] I. Bekkerman and J. Tabrikian, "Spatially coded signal model for active arrays," in *IEEE International Conference in Acoustics, Speech, and Signal Processing*, Montreal, Canada, 2004.

[76] J. Li and P. Stoica, "On parameter identifiability of MIMO radar," *IEEE Signal Processing Letter,* vol. 14, no. 12, pp. 968-971, 2007.

[77] P. F. Sammartino, C. J. Baker and H. D. Griffiths, "Target model effects on MIMO radar performance," in *IEEE Proceedings of the 2nd International Conference on Acoustics Speech and Signal Processing*, Toulouse, France, 2006.

[78] N. Lehmann, A. M. Haimovich, R. S. Blum, Cimini and L, "MIMO-radar application to moving target detection in homogenous clutter," in *Proceeding of the 14th IEEE Workshop on Sensor Array and Multi-channel Processing,* Waltham, MA, 2006.

[79] N. Lehmann, A. M. Haimovich, R. S. Blum and L. Cimini, "High resolution capabilities of MIMO radar," in *Proceedings of the 40th Asilomar Conference on Signals, Systems and Computers,* Pacific Grove, CA, 2006.

[80] J. J. Zhang and A. Papandreou-Suppappola, "MIMO radar with frequency diversity," in *International Waveform Diversity and Design Conference,* Kissimmee, FL, 2009.

[81] M. Radmard, S. M. Karbase, B. H. Khalaj and M. M. Nayebi, "Data association in multi-input single-output passive coherent location schemes," *IET Radar, Sonar & Navigation,* vol. 6, no. 3, pp. 149-156, 2012.

[82] M. M. Chitgarha, M. Radmard, M. N. Majd, B. H. Khalaj and M. M. Nayebi, "The detector's output SNR as a criterion for receiver placement in MIMO DVB-T based passive coherent location," in *4th International Congress on Ultra Modern Telecommunications and Control Systems and Workshops (ICUMT),* St Petersburg, Russia, 2012.

[83] M. N. Majd, M. M. Chitgarha, M. Radmard and M. M. Nayebi, "Probability of missed detection as a criterion for receiver placement in MIMO PCL," in *IEEE Radar Conference (RADAR),* Altanta, GA, 2012.

[84] D. E. Hack, L. K. Patton, B. Himed and M. A. Saville, "Centralized passive MIMO radar detection without direct-path reference signals," *IEEE Transaction on Signal Processing,* vol. 62, no. 11, pp. 3013-3023, 2014.

[85] M. Cherniakov, D. Nezlin and K. Kubik, "Air target detection via bistatic radar based on LEOs communication signals," *IEE Proceedings - Radar, Sonar and Navigation,* vol. 149, no. 1, pp. 33-38, 2002.

[86] S. M. Kay, Fundamentals of statistical signal processing: Detection theory, vol. II, Upper Saddle River, NJ: Prentice Hall, 1998.

[87] W. Wulf-Dieter, Radar techniques using array antennas, London: The Institution of Engineering and Technology, 2013, p. 457.

[88] A. J. Fenn, D. H. Temme, W. P. Delaney and W. E. Courtney, "The development of phased-array radar technology," *Lincoln Laboratory Journal,* vol. 12, no. 2, pp. 321-340, 2000.

[89] J. Capon, "High-resolution frequency-wavenumber spectrum analysis," *Proceedings of the IEEE,* vol. 57, no. 8, pp. 1408-1418, 1969.

[90] H. M. Aumann, A. J. Fenn and F. G. Willwerth, "Phased array antenna calibration and pattern prediction using mutual coupling measurements," *IEEE Transactions on Antennas and Propagation,* vol. 37, no. 7, pp. 844-850, 1987.

[91] C. Shipley and D. Woods, "Mutual coupling-based calibration of phased array antennas," in *International Symposium on Phased Array Systems and Technology*, Dana Point, CA., 1996.

[92] A. Agrawal and A. Jablon, "A calibration techniques for active phased array antennas," in *IEEE International Symposium on Phased Array Systems and Technology*, Boston, MA, 2003.

[93] S. Backén, D. M. Akos and M. L. Nordenvaad, "Post-processing dynamic GNSS antenna array calibration and deterministic beamforming," in *Proceedings of the 21st International Technical Meeting of the Satellite Division of The Institute of Navigation*, Savannah, GA, 2008.

[94] Z. Xu, M. Trinkle and D. A. Gray, "A maximum-likelihood based mutual coupling calibration algorithm in the presence of multipath for GPS antenna array," in *Proceedings of the 24th International Technical Meeting of The Satellite Division of the Institute of Navigation*, Portland, OR, 2011.

[95] M. Trinkle, E. Celtin, R. J. R. Thompson and A. G. Dempster, "Interference localisation within the GNSS Environmental Monitoring System (GEMS) - Initial field test results," in *Proceedings of the 25th International Technical Meeting of the Satellite Division of the Institute of Navigation*, Nashville, TN, 2012.

[96] U. S. Kim, D. S. De Lorenzo, D. Akos, J. Gautier and P. Enge, "Precise phase calibration of a controlled reception pattern GPS antenna for JPALS," in *Position Location and Navigation Symposium*, Monterey, CA, 2004.

[97] D. S. De Lorenzo, S. Alban, J. Gautier and P. Enge, "GPS attitude determination for a JPALS testbed: Integer initialization and testing," in *Position Location and Navigation Symposium*, Monterey, CA, 2004.

[98] S. Gano, "JSatTrak," gano.name, 13 February 2008. [Online]. Available: http://www.gano.name/shawn/JSatTrak/. [Accessed 22 October 2014].

[99] W. J. Alberhseim, "A closed-form approximation to Robertson's detection characteristics," *Proceedings of the IEEE,* vol. 69, no. 7, p. 839, 1981.

[100] P. E. Howland, D. Maksimiuk and G. Reitsma, "FM radio based bistatic radar," *IEE Proceedings in Radar, Sonar and Navigation,* vol. 152, no. 3, pp. 107-115, 2005.

[101] D. K. P. Tan, H. Sun, M. Lesturgie and H. L. Chan, "Passive radar using Global System for Mobile communication signal: theory, implementation and measurements," *IEE Proceedings in Radar, Sonar and Navigation,* vol. 152, no. 3, pp. 116-123, 2005.

[102] C. Coleman, "Mitigating the effect of direct signal interference in passive bistatic radar," in *IEEE International Radar Conference on Surveillance for a Safer World*, Bordeaux, France, 2009.

[103] F. Colone, D. W. O'Hagan, P. Lombardo and C. J. Baker, "A multistage processing algorithm for disturbance removal and target detection in passive bistatic radar," *IEEE Transactions on Aerospace and Electronic Systems,* vol. 45, no. 2, pp. 698-722, 2009.

[104] H. K. Brustad, "Direct signal cancellation in passive bistatic DVB-T based radar," Norwegian Defense Research Establishment (FFI), Norway, 2014.

[105] Y. T. J. Morton, J. B. Y. Tsui, D. M. Lim, L. L. Liou, M. M. Miller, Q. Zhou, M. P. French and J. Schamus, "Assessment and handling of CA code self-interference during weak GPS signal acquisition," in *Proceedings of the 16th International Technical Meeting of the Satellite Division of The Institute of Navigation,* Portland, OR, 2003.

[106] Z. Xu, M. Trinkle and D. Gray, "Weak interference direction of arrival estimation in the GPS L1 frequency band," in *IEEE International Conference on Acoustics, Speech and Signal Processing (ICASP)*, Brisbane, Australia, 2015.